NATURAL CIRCULATION IN THE UPPER PLENUM OF A SCALED MODEL OF A VERY HIGH TEMPERATURE REACTOR IN THE EVENT OF LOSS-OF-COOLANT ACCIDENT

A Dissertation

by

JAE HYUNG PARK

Submitted to the Office of Graduate and Professional Studies of
Texas A&M University
in partial fulfillment of the requirements for the degree of

DOCTOR OF PHILOSOPHY

Chair of Committee,	Nagamangala K. Anand
Co-Chair of Committee,	Yassin A. Hassan
Committee Members,	Hamn-Ching Chen
	Sai Chuen Lau
Head of Department,	Andreas A. Polycarpou

August 2016

Major Subject: Mechanical Engineering

ABSTRACT

The very high temperature reactor (VHTR) is one of the most promising next generation reactors which will be commercialized in 2030. A loss-of-coolant accident (LOCA) is a major accident scenario in which the primary coolant loop is broken, resulting in a loss of forced circulation of helium into the reactor vessel. With the onset of natural circulation, coolant flow reverses and is driven by buoyancy forces. The goal of the research is to simulate this accident condition on a $1/16^{th}$ scaled model and visualize the flow behavior in the upper plenum of the VHTR. The facility was designed and constructed from a set of scaling parameters and outfitted with various instrumentation to characterize the depressurized conduction cooldown (DCC) event. Particle image velocimetry (PIV) is a nonintrusive optical laser technique used to obtain an instantaneous velocity field and was successfully applied to this system. Throughout the preliminary tests, the number of frames to be averaged to reach a statistically steady state was obtained from 1,000 images. The performance of the PIV method is validated with a flowmeter and analytic flowrate equation. The uncertainty of PIV system was also quantified.

Single jet tests are performed to provide a basic understanding of the simplest turbulent buoyant jet mixing in the upper plenum. By the Morton length scale, it was observed that the buoyant jet behaves like a plume and self-similarity is obtained for the axial velocity profiles. Q criterion is applied to identify the eddy structures of the turbulent jet mixing as a way to characterize the mechanism of vortex-pair mixing on the dome surface. Subsequent triple jet experiments are performed and compared with the results

from single jet tests. Velocity distributions along the concave wall show that higher wall shear stress is obtained in single jet tests. The experiment results will provide the benchmark data for the PIV validation.

DEDICATION

This dissertation is dedicated to my parents, Tae Youn Park and Kyung Ai Song; my wife, Heesun Kim; and my adorable son, James Seojun Park.

ACKNOWLEDGEMENTS

I am grateful to the Department of Energy to have this research opportunity. It was a wonderful research project that I could explore both experiments and CFD at the same time. I would like to thank my committee chairs, Dr. N.K Anand and Dr. Yassin Hassan, for their guidance and patient support throughout the course of my study. I am deeply grateful to those who gave me the opportunity to come here and be a part of this important and bountiful field of research and supported me along the way. I have grown tremendously, not just as a researcher, but as an academic and human being during my time here at Texas A&M University and has become one of the defining chapters of my life.

Thanks to my colleague Dr. Saya Lee who helped me with the experiments from the beginning of the research to the end. I would like to thank Kyle McVay who spent most of his time building the test facility and performing the preliminary tests with me. Without him I could not reach this far. Also thanks to Anas Alwafi who assisted me all the time whenever I needed help. I appreciate my two close Korean friends, Sam and Sero, who always stayed awake until the midnight and brainstormed with me to develop the research ideas. Last but not least I thank to Mark Silberberg who came to the lab to assist me and helped me until the end. I really appreciate your kindness and courtesy.

Finally, thanks to my mother and father for their devotion. They are the people who guide me to become who I am now. Thanks to my wife and son for her patience and love. I love you all.

NOMENCLATURE

A	Corresponding interrogation windows
$A_{Coolant}$	Coolant channel flow area (m^2)
$a_m(t)$	Temporal POD coefficient
B	Corresponding interrogation windows
B	Jet width (cm)
C_{ij}	Correlation matrix
c	Cross correlation function
c_p	Specific heat capacity (J/kg·K)
D_{Hole}	Coolant channel diameter (m)
D_{CID}	Core barrel inner diameter (m)
D_m	Model hydraulic diameter (m)
D_p	Prototype hydraulic diameter (m)
D_{RV}	Reactor vessel inner diameter (m)
d	Pipe outlet diameter (m)
d_p	Diameter of the particle (m)
f	Characteristic puffing frequency (Hz)
g	Gravity (m/s^2)
H	Height of upper plenum (m)
L	The integral length scale (m)
L_{CB}	Bottom of the core (m)

L_{CT}	Top of the core (m)
L_H	Height of upper plenum (m)
l_M	Morton length scale (m)
L_{RB}	Bottom of the lower reflector (m)
L_{RT}	Top of the upper reflector (m)
L_T	Top of the upper plenum shield (m)
M	Number of tests (number)
m	Test number
m	Shift locations in horizontal direction
$\dot{m}$	Mass flow rate (kg/s)
n	Maximum number of points in the PIV field (i, j)
n	Shift locations in vertical direction
N	Number of frames (number)
$N_{coolant}$	Number of coolant channels (number)
N_J	Number of jets
P	Coolant channel pitch (m)
P/D_{Hole}	Pitch-to-Diameter ratio
P	Invariants of the velocity gradient tensor
Q	Heat input to core piping (W)
Q	Invariants of the velocity gradient tensor
R	Invariants of the velocity gradient tensor
$R(x, x')$	Two point spatial correlation function

Ra	Rayleigh number
S	Strain tensor
St	Stokes number
q	Normalized diameter
r	Location vector (m)
Re	Reynolds number (= DV/ν)
Ri	Richardson number (= $g\alpha\Delta TD/V^2$)
r	Radial direction
S	Jet spacing (m)
St	Stokes number (= $(1/18)(\rho_P/\rho_f)(d_P/\eta)^2$)
T	Characteristic puffing period (s)
T_i	Temperature at core inlet (K)
T_o	Temperature at core outlet (K)
ΔT	Temperature gradient (= $T_0 - T_i$) (K)
Δt	Time interval of successive images (s)
$t_{upper,lower}$	Lower and upper threshold (m/s)
TI	Turbulence intensity (= $v_{rms}/\overline{v}^N$)
U_p	Particle velocity (m/s)
U	Fluid velocity (m/s)
u	x-velocity (m/s)
u	Radial velocity (cm/s)

u'	Coordinate transformed x'-velocity (cm/s)
u^+	Dimensionless velocity
V_m	Model velocity (m/s)
V_p	Prototype velocity (m/s)
V'	Resolved fluctuation velocity magnitude (cm/s)
v	y-velocity (m/s)
$\boldsymbol{v}$	velocity vector (m/s)
v'	Turbulent fluctuations of y-velocity (m/s)
v'	Coordinate transformed y'-velocity (cm/s)
v''	Resolved fluctuation velocity
$\bar{v}$	Mean velocity (cm/s)
v_θ	Azimuthal velocity
v_{ave}	Average y-velocity between the Tests (m/s)
v_{rms}	Turbulence strength in y direction averaged between the Tests (m/s)
$\bar{v}^N$	Average y-velocity for N frames (m/s)
w	Axial velocity (cm/s)
w_c	Centerline axial velocity (cm/s)
w_0	Axial velocity at the inlet (cm/s)
ΔX	Displacement of particle images (px)
x'	Coordinated transformed x direction (cm)
y^+	Wall coordinate
y'	Coordinated transformed y direction (cm)

z	Axial direction
z_0	Virtual origin (cm)

Greek alphabet

α	Magnification factor (mm/px)
α_G	Entrainment coefficient
β	Thermal expansion coefficient (1/K)
β_S	Spreading rate
Δ	Delta criterion
δ	Boundary layer thickness (cm)
δu	Experiment uncertainty factor (mm/s)
δ_{mn}	Kronecker delta
ε	Average rate of dissipation of turbulence kinetic energy per unit mass (m^2/s^3)
η	Kolmogorov length scale (m)
η	Similarity variable
Θ	Rotation angle (°)
λ	Wavelength of the incident light (nm)
λ	Eigenvalues
$\xi_{\dot{m}}$	Mass flow rate uncertainty (kg/s)

μ	Dynamic viscosity of the fluid (Pa·s)
ν	Kinematic viscosity (m^2/s)
ρ	Density of fluid (kg/m^3)
ρ_f	Density of fluid (kg/m^3)
ρ_P	Density of tracer particle (kg/m^3)
ρ_0	Reservoir fluid density (kg/m^3)
$\Delta\rho$	Density fluctuation ($=\rho-\rho_0$) (kg/m^3)
σ_V	Standard deviation of $\bar{v}$
σ_{Ti}	Thermocouple error at core inlet (K)
σ_{To}	Thermocouple error at core outlet (K)
τ_s	Relaxation time constant (s)
τ_v	Particle viscous relaxation time (s)
τ_w	Wall shear stress (Pa)
τ_η	Kolmogorov time scale (s)
ϕ_m	Individual POD eigenfunctions
Ψ	Set of eigenvalues
Ω	Vorticity tensor
ω	Vorticity ($=\partial v/\partial x-\partial u/\partial y$) (1/s)

Subscripts

m	Model
MA	Moving average
p	Prototype
std	Standard deviation

Acronyms

CFD	Computational Fluid Dynamics
CLAHE	Contrast Limited Adaptive Histogram Equalization
DCC	Depressurized Conduction Cooldown
DCC	Direct cross-correlation
DFT	Discrete Fourier transform
DOE	Department of Energy
FOV	Field of View
GIF	Generation IV International Forum
IEA	International Energy Agency
INEEL	Idaho National Engineering and Environmental Laboratory
INL	Idaho National Laboratory
LOCA	Loss of Coolant Accident
LOFA	Loss of Flow Accident

MHTGR	Modular High Temperature Gas-Cooled Reactor
NGNP	Next Generation Nuclear Plant
NRMSD	Normalized root-mean-square deviation
NRC	Nuclear Regulatory Commission
P2P	Plenum-to-Plenum
PCC	Pressurized Conduction Cooldown
PIRT	Phenomena Identification and Ranking Table
PIV	Particle Image Velocimetry
POD	Proper Orthogonal Decomposition
RCCS	Reactor Cavity-Cooling System
RMSD	Root-mean-square deviation
RMS	Root-mean-square
ROI	Region of Interest
RT	Rayleigh-Taylor
V&V	Verification and Validation
VHTR	Very High Temperature Reactor

TABLE OF CONTENTS

Page

LIST OF FIGURES

LIST OF TABLES

1. INTRODUCTION

Energy is the "ability of a system to perform work." We use this energy to drive a car, cook a fancy dinner, run machines in a large factory, and do various other activities. There are numerous forms of energy such as chemical energy, mechanical energy, nuclear energy, and thermal energy. People in the world use these types of energy constantly increasing the consumption/production rate every year (Figure 1.1). According to the 'BP Statistical Review of World Energy June 2015 [1],' global primary energy consumption increased by 0.9% in 2014. It was reported that the nuclear power was the only power source to grow at an above-average rate (1.8%), which is significantly greater than the 10-year average of 0.8% (Figure 1.2). This was the second consecutive annual increase in nuclear power use and the first time it has a gained global market share since 2009. In addition, consumption increased for all power sources types except nuclear power. Still, most of the world's primary energy consumption comes from fossil fuels such as oil, coal and natural gas. However, these fuel types emit significant amounts of carbon dioxide (CO_2) while nuclear power produces almost no greenhouse gases and is considered form of clean, sustainable energy.

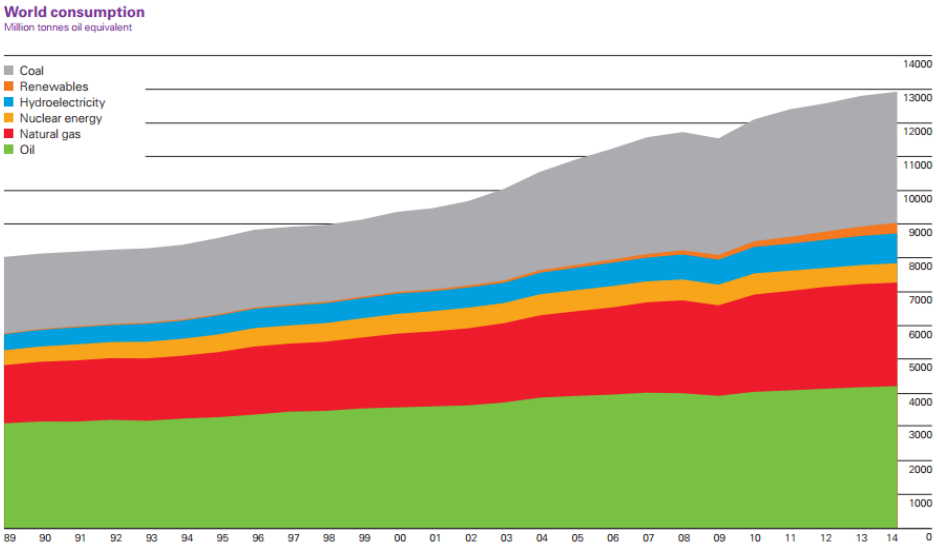

Figure 1.1. World primary energy consumption grew. X-axis = year; Y-axis = million tonnes oil equivalent [1].

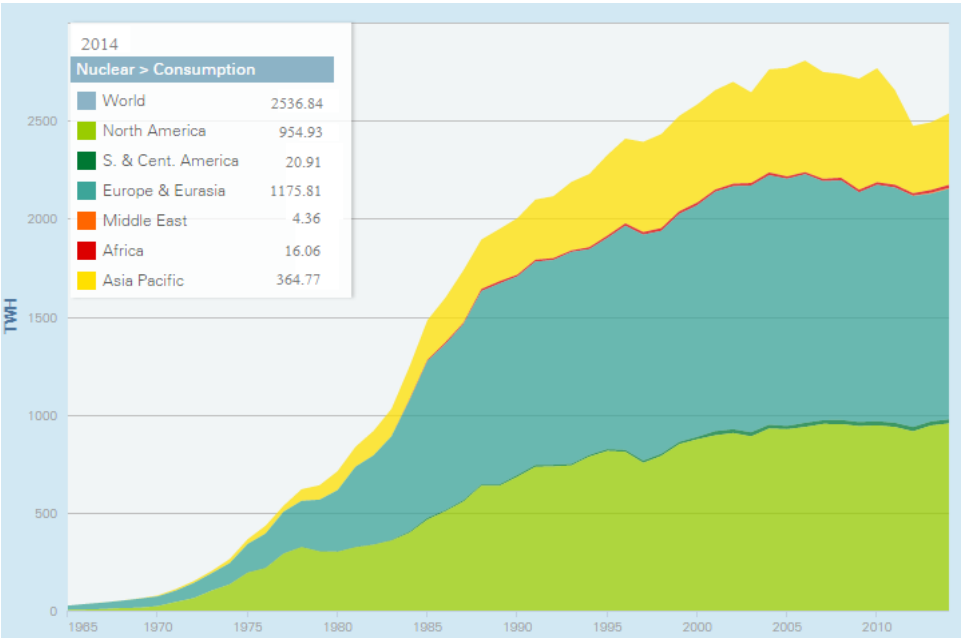

Figure 1.2. Nuclear energy consumption by region (TWh). X-axis represents year [1].

The gross US electricity generation was 4,092 TWh (million MWh) in 2014 according to International Energy Agency (IEA) report where the share of nuclear power was 19.47% (797 TWh). Annual electricity demand is expected to increase to 5,000 TWh in 2030 with a corresponding increase in nuclear power. Today, 16 countries depend on nuclear power for at least 25% of its total electricity. IEA released a technology roadmap for nuclear energy in 2015 which provided the future vision of nuclear power deployment up to 2050 [2] (Figure 1.3). According to the report, growth in nuclear power capacity and its share of global electricity production continuously increases reaching 930 GW in 2050 with annual electricity production of nearly 7,000 TWh. One of the key milestones during the next 10 years is to demonstrate the ability to build the most advanced nuclear plant designs on time and within budget where the regional investment needs for nuclear power generation from 2010 to 2050 are 883 USD bn for US and Canada, and 893 USD bn for China.

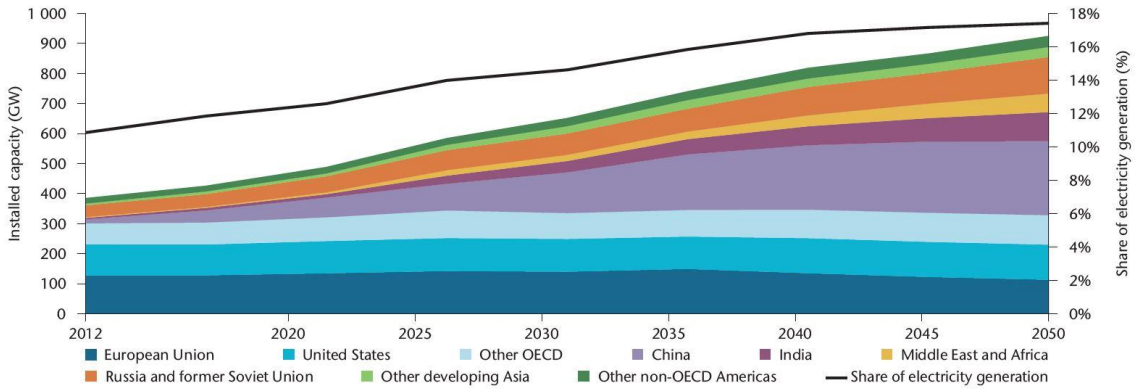

Figure 1.3. Growth in nuclear power capacity and its share of global electricity production [2].

In the near future, the US and other industrialized countries will need larger energy resources and an upgraded energy infrastructure to meet constant increasing demands for electricity. The Generation IV International Forum (GIF), an international research and development framework of the next generation nuclear energy power generation system, was founded in 2001 by Argentina, Brazil, Canada, France, Japan, the Republic of Korea, South Africa, the United Kingdom and the United States. The goals of the GIF nuclear energy system is required to provide future energy demand as well as meet four goals of sustainability, safety and reliability, superior economics, and proliferation resistance and physical protection [3]. In 2002, GIF selected six nuclear energy systems with nearly 130 reactor concepts for further development as Generation IV technologies: Gas-cooled Fast Reactor (GFR), Lead-cooled Fast Reactor (LFR), Molten Salt Reactor (MSR), Supercritical Water-cooled Reactor (SCWR), Sodium-cooled Fast Reactor (SFR), and Very High Temperature Reactor (VHTR). Commercial construction, deployment, and operation of Generation IV prototypes is expected before 2030 as shown in Figure 1.4. Currently, the US and South Korea are signed to participate in developing SFR and VHTR as a Generation IV rector.

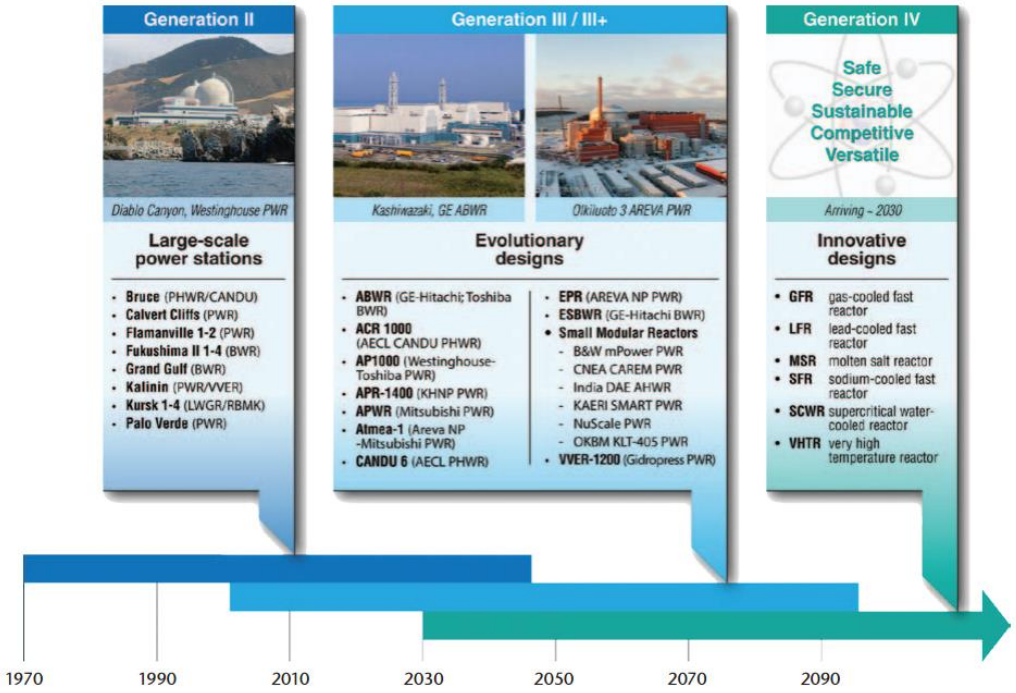

Figure 1.4. Evolution of fission reactor technology [2].

Among those Generation IV reactors, the Department of Energy (DOE) has selected the Very High Temperature Gas Cooled Reactor (VHTR) for the Next Generation Nuclear Power (NGNP) Project. The VHTR refers to any reactor design that has coolant outlet temperatures of at least 1000 ºC. As shown in Figure 1.5, it is one type of high-temperature gas-cooled reactor (HTGR) design (the terms commonly used inter-changeably) [4]. The HTGR is a graphite-moderated nuclear reactor with a flexible uranium/plutonium fuel cycle using helium as a coolant. The reactor core can be designed either as a prismatic block or a pebble-bed core. The high temperature enables the application of high efficiency electricity production as well as process heat and hydrogen production through the thermochemical sulfur-iodine cycle. The core design inherently enables the safety characteristics of the reactor and an air-cooled Reactor Cavity-Cooling

System (RCCS) provides a passive safety system to remove the decay heat from the reactor vessel. The reference design of the VHTR is a Modular High Temperature Gas-Cooled Reactor (MHTGR) designed by General Atomics. The detail parameters and features of the MHTGR are listed in Table 1.1. Figure 1.6 shows the primary and secondary (steam generator) vessels, and annual reactor core of MHTGR. The Idaho National Engineering and Environmental Laboratory (INEEL) will construct the VHTR as a part of NGNP in near future. However, the current stage of the development is conceptual and not ready to perform any validation process for computational simulations.

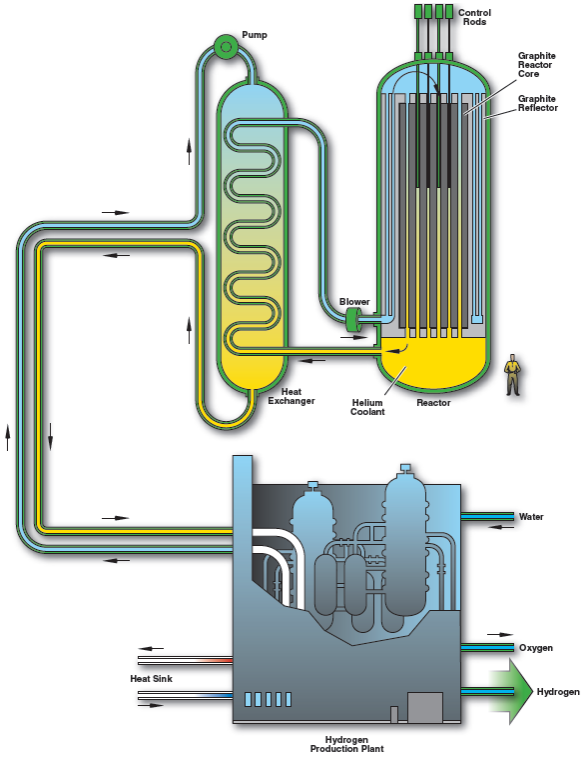

Figure 1.5. Schematics of Very High Temperature Reactor (VHTR) [5].

Table 1.1. Key operating parameters for the MHTGR [6].

Major Reactor Parameters	**MHTGR**
Thermal power (MWt)	350
Primary coolant	Helium
Moderator	Graphite
Average power density (MW/m^3)	5.9
Core inlet temperature/pressure (°C/MPa)	259/6.4
Core outlet temperature/pressure (°C/MPa)	687/6.4
Total temperature rise (°C)	428
Core Geometry	Annular
Safety Design Philosophy	Passive
Fuel Max Temp – Normal Operation (°C)	1250
Fuel Max Temp – Emergency Conditions (°C)	1600

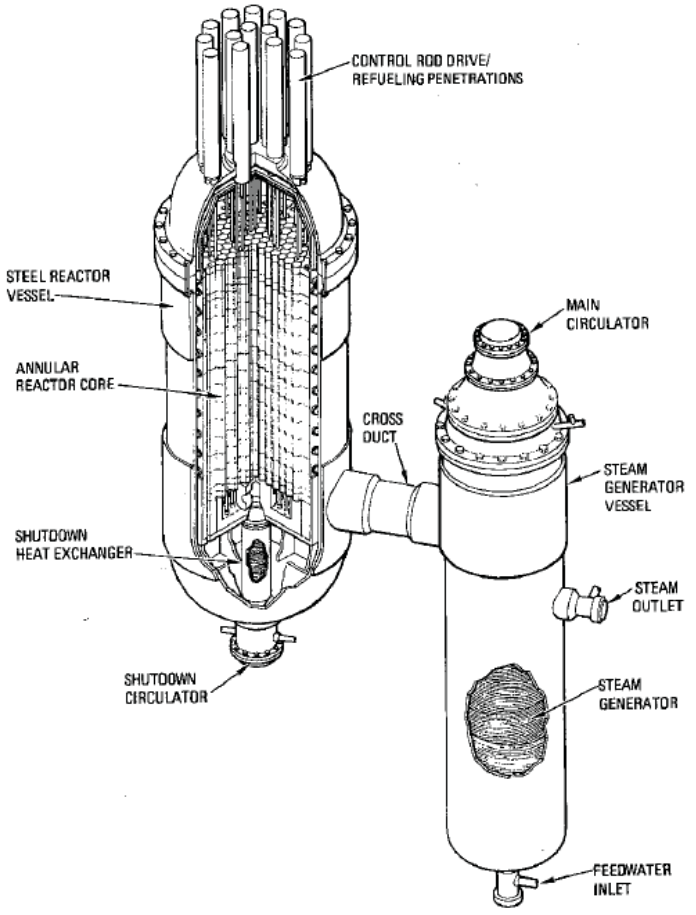

Figure 1.6. MHTGR module (DOE 1986).

The primary loop of the VHTR starts from the helium coolant entering the core, proceeding upward to the reactor vessel through an annual passage in the cross duct, and divided into distinct coolant inlet channels that exist between the peripheral duct wall of the core region and the inner diameter of the reactor vessel wall [6]. The helium coolant is redirected in the upper plenum by 180 degrees and enters the annular core and inner and outer reflector region and flows downward. The helium exits into the lower plenum and is gathered into a single stream which flows through the cross duct to the steam generator.

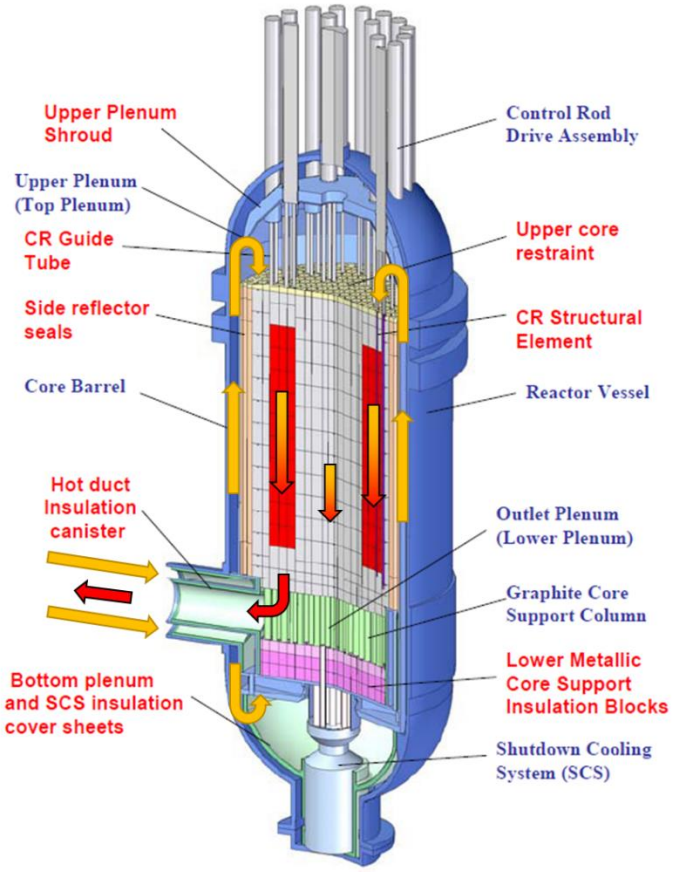

Figure 1.7. A typical prismatic VHTR concept: internal structure, core, control rod guide tubes (modified from KAERI [7]).

The Phenomena Identification and Ranking Table (PIRT) provides identification on safety-relevant phenomena associated with the NGNP during normal operations, transients, and postulated accidents. Based on the relative importance of these phenomena and an assessment of the knowledge level, each phenomena is ranked and listed in table. The most important safety-related accident is loss-of-forced-cooling (LOFC) events and is classified into two categories: the Depressurized Conduction Cooldown (DCC) and Pressurized Conduction Cooldown (PCC) event. The PCC event assumes a flow coast-down and scram while the RCCS is operating constantly. Buoyancy forces do not significantly establish helium coolant recirculation while the chimney effect increases the core temperatures near the top. The DCC event assumes a rapid depressurization of the primary coolant and scram with the passive RCCS system operating and assuming no air ingress [8]. Once natural circulation is achieved during the DCC and PCC event, the reversal flow will arise and thermal stresses on the ceiling of the upper plenum and the control rods become a critical concern [9]. To understand how the plume/jet mixing in the upper plenum of the VHTR influences the structure of the reactor and provides for a better reactor design is the purpose of this study.

Haque et al. [9] numerically calculated the thermal-hydraulic response of the VHTR during the PCC and DCC event using THERMIX (see from Figure 1.7 to 1.9). The normal flow direction was reversed as the buoyancy forces dominated to the system. The study showed that the core maximum temperature reached 1214 °C in 48 hours for the PCC event whereas it reached 1587 °C (near limiting temperature of the fuel) in 70 hours for the DCC case. It is noted that the DCC event has higher temperature distribution than

the PCC event because the natural circulation of the pressurized helium coolant within the core makes the uniform temperature distribution in which the natural recirculation is not significant [8].

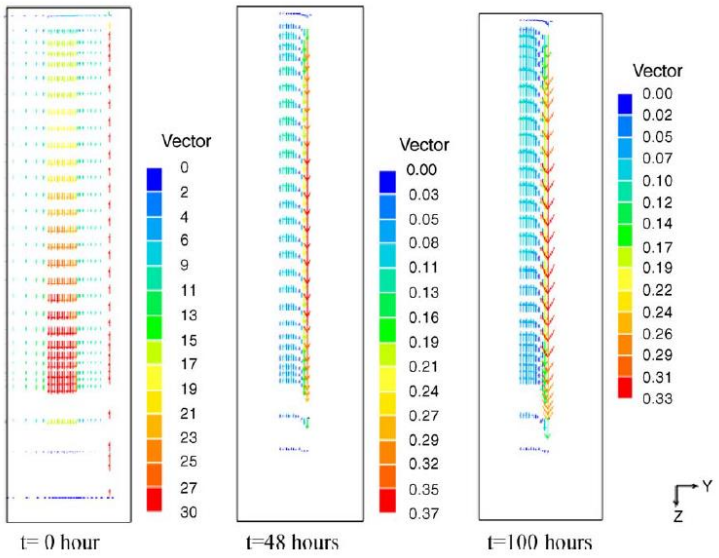

Figure 1.8. VHTR velocity vector in the core for a PCC event [9].

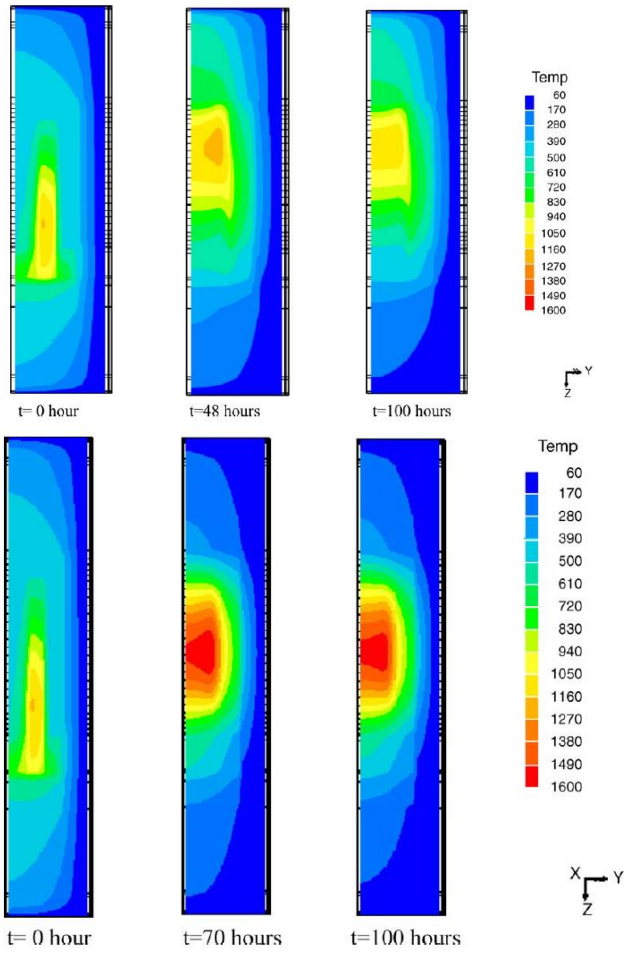

Figure 1.9. VHTR temperature distribution in the reactor for a PCC (top) and DCC (bottom) event [9].

The experiments performed in this study will provide the validation data for the majority of the challenging accident analysis in the commercial CFD software and system analysis [6]. In general a validation pyramid approach is used for the basis of constructing the NGNP thermal-fluids validation matrix as shown in Figure 1.10. The foundation of the pyramid is made up with validation data from basic experiments designed to study fundamental phenomena which are ideal for the university environment [6]. In other

words, to study complex mixing behavior between numerous gas jets, the study of a single jet and the interaction between two jets should be delivered in advance for a basic experiment as a foundation of the validation pyramid.

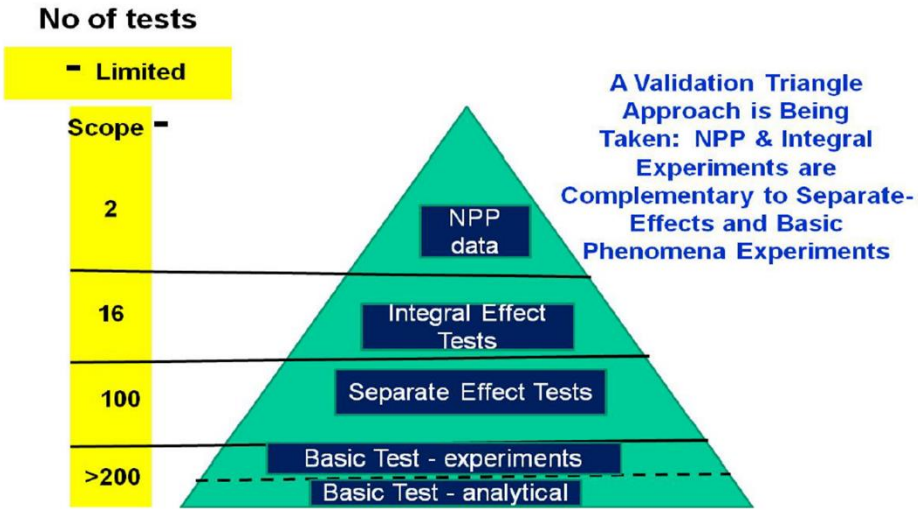

Figure 1.10. A validation pyramid approach [6].

The NGNP experimental verification and validation (V&V) program includes thermal-fluids experiments that will be used to provide validation data for systems analysis and Computational Fluid Dynamics (CFD) software for major accident scenarios [6, 10]. As a foundation of the validation pyramid approach, a relatively large number of basic experiments will be performed to better design the reactor system. Several experiment plans are proposed including integral facility, upper/lower plenum experiment, plenum-to-plenum experiment, MIR experiment, and air ingress experiments (Figure 1.11). Among those experiment plans, the study chosen to design a plenum-to-plenum (P2P)

experiment. This P2P experiment will be used to study the natural convection heat transfer that will occur during the LOFC event.

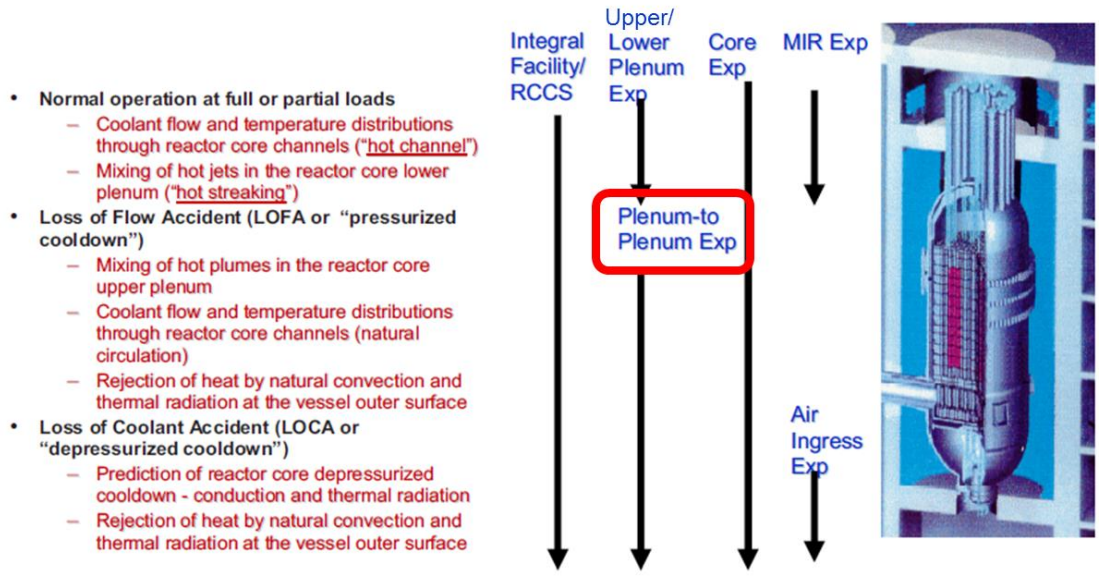

Figure 1.11. Thermal hydraulic phenomena experiment planning [6].

The primary goal of Texas A&M University (TAMU) VHTR facility is to perform the experiments to understand the phenomenon during both the PCC and DCC events. Starting from a single jet mixing behavior to the interactions between multiple jets, the P2P experiment will provide a basic understanding of the VHTR accident conditions. The particle image velocimetry (PIV), a non-intrusive optical measurement technique, will be performed to capture the complex behavior of the fluid flow which will happen in the upper plenum of the reactor vessel. While the TAMU VHTR facility is capable of simulating the PCC and DCC events, the dissertation focuses on a loss-of-coolant accident

(LOCA), i.e. the DCC event. The benchmark data will be compared to simulation results to determine the fidelity of particular turbulent models.

1.1 Research Objectives

The primary objective of this research is to investigate the fundamental physical phenomena associated with internal coolant flow in a prismatic core VHTR vessel during normal operation and under accident scenarios. Previous studies have revealed the importance of complex jet/plume flows in each plenum, with the potential to generate recirculation zones that can lead to formation of hot spots within the lower plenum. It is therefore of interest to ensure that adequate mixing is promoted, but the complexity of the internal flow fields (characterized by structures spanning multiple orders of magnitude in time and length scales) makes rational design challenging. These difficulties are further compounded by limited availability of data for validation of predictive models.

Here we propose to overcome these limitations by uniquely combining state-of-the-art experimental and computational capabilities of the project team. Experimentally, a geometrically scaled test facility incorporating a faithful 3D representation of the prismatic core VHTR vessel upper and lower plenum will be constructed to overcome difficulties encountered in previous attempts to capture the complex flow field using configurations incorporating a symmetry plane. This facility will be supplemented by the use of innovative high-speed high-resolution imaging capabilities that enable the multi-scale of fluid motion (velocity and temperature) to be probed with unprecedented spatial and temporal resolution. Computationally, we will employ the use of high performance cluster computing to simulate the flows using advanced computational fluid dynamics (CFD) techniques to capture the velocity and temperature fields, both globally and locally

in recirculation zones. Current modeling approaches typically rely on multi-scale averaging processes that impose serious constraints when unsteady phenomena must be captured. This limits the ability of commercial CFD codes to capture unsteady turbulence multi-scales encountered here. A distinguishing feature of this work will be the unique ability to perform direct cross-validation between experiment and simulation, enabling more accurate and rational prediction of the coolant flow field characteristics than is currently possible.

1.2 Outline of the Dissertation

This section describes the introductory background for the very high temperature reactor and shows its potential accident scenarios. Section 2 will provide the scaling analysis and show the design of $1/16^{th}$ scaled model of the VHTR. In this section, the process of fabrication and test assembly are described. Section 3 will show each PIV measuring instruments and preliminary test results. CFD results are provided to validate the PIV results. Section 4 will show experiment modification and calibration processes for each instrument. Section 5 will provide single jet experiment results and several analyses are made to describe the turbulent buoyant jet mixing. Section 6 will show triple jet experiments and similar analyses are made. Here, the proper orthogonal deposition is introduced and shear stress comparison is made. Section 7 will conclude the dissertation and summarize the entire sections.

2. EXPERIMENTAL TEST FACILITY

In this section, we introduce the background of the research; the history of the VHTR, two important safety related accident scenarios (the DCC and PCC events), scaling from the reference MHGTR design, fabrication and construction with methods of watertight integrity, installation of the measuring instruments and a PIV setup. The contents of this section were published in a journal [11]*.

2.1 The Very High Temperature Reactor

The Very High Temperature Reactor (VHTR) has been selected as one of the Next Generation Nuclear Plant (NGNP). It is an evolved Generation IV gas cooled reactor design that allows for a 1,000 °C coolant outlet temperature [4, 12-14]. The design has high fuel efficiency for electricity generation, and because of the high outlet temperature it is optimal for industrial applications or commercialized hydrogen production [15, 16]. There are two reactor designs being developed; the pebble bed and prismatic VHTR. The pebble bed reactor has graphite-moderated spherical fuel compacts stacked in a critical configuration together in a reactor pressure vessel. In a prismatic core the fuel compacts are placed into hexagonal graphite fuel blocks that are then loaded into an annular core with separate regions for the fuel and reflector. Many studies are being performed for both normal operation and accident scenarios for both designs. There are two major accident scenarios of interest; Depressurized Conduction Cooldown (DCC), and Pressurized

Conduction Cooldown (PCC) [9, 17]. A DCC event involves the depressurization of the main core coolant loop, generally through a Loss of Coolant Accident (LOCA). This results in an air ingress to the lower plenum where it slowly diffuses into the core and oxidizes with the fuel accelerating the heating of the core and releasing fission products [18]. As there is no heat sink for the core the primary heat removal is through radiation, and the core may reach the failure temperature of 1600 °C. In a PCC scenario there is loss of forced coolant but the main loop stays pressurized, this may be a result of a loss of power. During normal operation the helium is circulated into the upper plenum and down through the core with a blower. Because the loop stays pressurized in a PCC scenario the helium coolant has a high density differential resulting in large buoyancy forces. Over time these forces will overcome the initial inertial forces, reversing the circulation of the coolant to go up through the core into the upper plenum, and down between the reflector and the core. This natural circulation removes sufficient heat from the core so the core will not reach the failing temperature of the fuel, but may cause thermal stresses on the internal support structures in the upper plenum.

There are several nuclear system codes currently being developed as computational tools to conduct performance and safety analyses of the VHTR. Experimental models are needed for the validation of these codes. Idaho National Laboratories (INL) has collaborated with Korean and American universities to develop codes as well as experimental models to validate them [17, 19]. Primarily normal operation and air ingress following a DCC scenario were evaluated. To model this, a multi-dimensional gas mixture analysis code was created to predict chemical reaction and

thermo-fluid behaviors for an air ingress following a DCC scenario for both pebble bed and prismatic core designs. The Codes were validated with the water pool Reactor Cavity Cooling System (RCCS) test facility, and an inverse U-tube experiment that modeled the temperature and chemical reaction behavior of a gas mixture. Additionally Oregon State University has constructed a high temperature test facility that can model a VHTR during a DCC accident scenario which can provide benchmark data for existing safety analysis codes [18].

Currently there have been many studies and experimental models evaluating the core and lower plenum for normal operation [10, 14, 20] and DCC accident scenario [9, 18]. There has been CFD analysis for the upper plenum following a PCC Scenario [21]. As there are no experimental models to produce benchmark data for validation, a scaled experimental model of a VHTR is necessary to provide benchmark data in the upper plenum following a DCC or PCC accident scenario. The $1/16^{th}$ scaled test facility constructed in this study can fulfill this deficiency of data. The test facility is a closed loop that uses heated pipes to induce natural circulation through the system without the use of pumps, this may be used to model a DCC event. A pump may be added along with a heat exchanger to simulate a PCC event. Particle Image Velocimetry (PIV) is used to obtain the velocity field in the upper plenum. In order to produce benchmark data, the PIV system must first be validated for simpler test conditions. This study uses PIV to record the turbulent mixing of three adjacent naturally convective jets. The results are validated by comparing the PIV vector field with an ultrasonic flowmeter analytic flow rates.

2.2 Scaling and Design

The reference prismatic reactor design is the Modular High Temperature Gas Reactor (MHGTR) designed from General Atomics (GA). Its reactor power is 350 MW and helium inlet/outlet temperatures of 258.6 ºC and 687 ºC, respectively. The coolant flow rate is 157.05 kg/s and its RCCS heat removal is 0.7 MW. As a part of the plenum to plenum experiment from INL, the current VHTR design is geometrically scaled down ($1/16^{th}$ scale) from the MHGTR. Detailed geometrical parameters are listed in Table 2.1. The total number of coolant channels was chosen to be 25 to maintain both the symmetrical hexagonal array pattern and the scale area ratio of the core flow area in the prototype.

The design obtained from INL is shown in Figure 2.1 and 2.2. The experiment facility is capable of operating at both PCC and DCC event under steady-state conditions. The objective of each accident scenario is following:

1) During the PCC event experiment, the natural circulation through the loop, i.e. from the reactor vessel to the steam generator and back to the reactor vessel, is investigated.

2) During the DCC event, the natural circulation between the reactor vessel and the containment is investigated.

3) In both PCC and DCC event, the natural circulation within the reactor vessel only, i.e., natural circulation between the lower and upper plena through the core region, is

investigated. The VHTR test facility is currently assembled to simulate the DCC event, therefore a water reservoir system was installed.

Table 2.1. Dimensions of scaled VHTR geometry provided by INL and nomenclature.

Variables	Nomenclature	MHTGR (m)	$1/16^{th}$ scaled VHTR (m)
Bottom of the lower plenum	Reference	-2.88255	0
Bottom of the lower reflector	L_{RB}	-1.9825	0.05625
Bottom of the core	L_{CB}	0.0	0.18016
Top of the core	L_{CT}	7.93	0.6758
Top of the upper reflector	L_{RT}	9.516	0.7749
Top of the upper plenum shield	L_T	12.6656	0.9718
Height of upper plenum	L_H	3.1496	0.197
Reactor vessel inner diameter	D_{RV}	6.534	0.4083 (= 16.07 in)
Core barrel inner diameter	D_{CID}	5.95	0.370 (= 14.57 in)
Coolant channel diameter	D_{Hole}	0.01588	0.01905 (= 0.75 in)
Number of coolant channels	$N_{coolnat}$	11000 5/8 in diameter	25
Coolant channel flow area (m^2)	$A_{Coolant}$	2.177 (considering only 5/8-in channels)	0.00713
Coolant channel pitch	P	0.0322	0.03861 (= 1.52 in)
Pitch-to-Diameter ratio	P/D_{Hole}	2.03	2.03

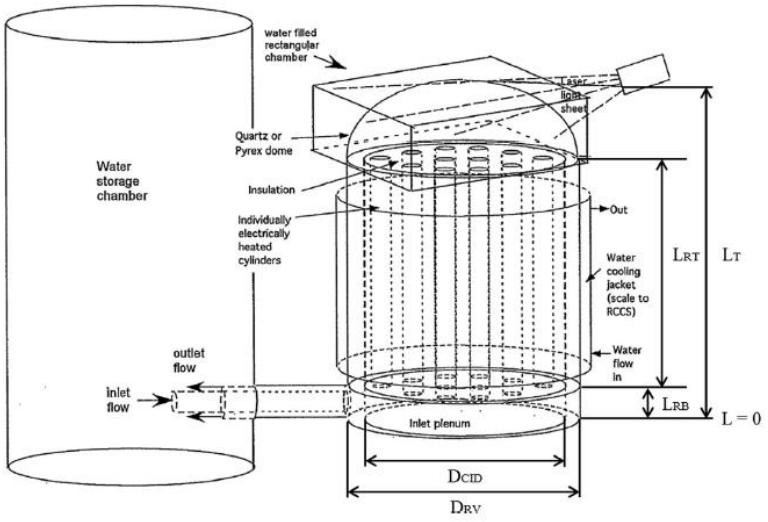

Figure 2.1. Water flow natural circulation apparatus configured for the study of DCC event.

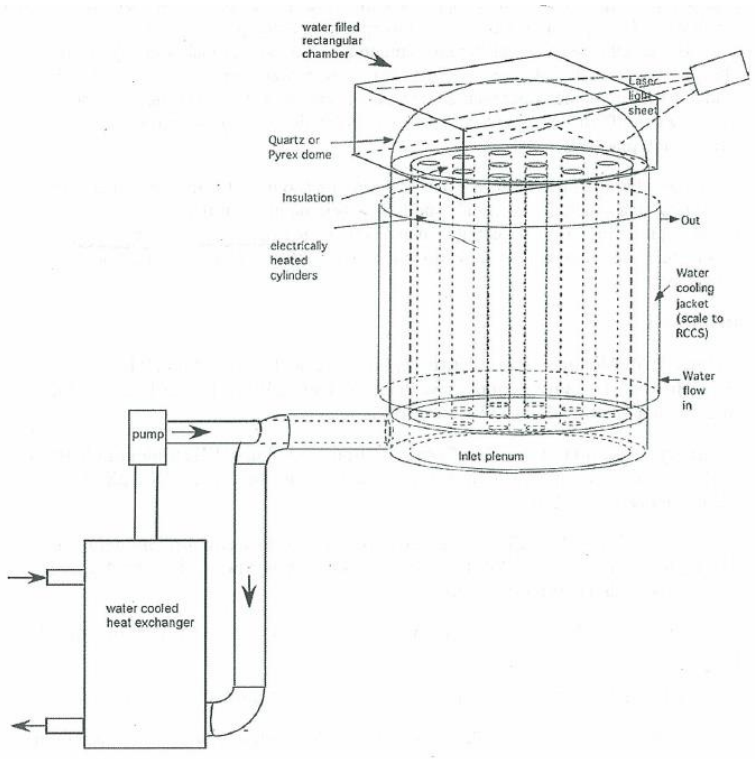

Figure 2.2. Water flow natural circulation apparatus configured for the study of PCC event.

This experiment is a preliminary testing of the PIV system, but is designed to have the capabilities to produce benchmark data for DCC and PCC accident scenarios after reaching steady state. The prototype fuel decay heat is modeled with individually electrically heated cylinders. When scaling an experiment to model the natural circulation in the prototype plenums, the main approach is matching the Richardson number (Ri), the ratio of the buoyancy force to inertial force, and the Reynolds number (Re), the ratio of inertial to viscous forces, for the model and the VHTR prototype [14]. This may be achieved once the systems have reached steady state. The Richardson ratio is shown in Equation (2.1).

$$\mathrm{Ri} = \frac{g\beta\Delta T D}{V^2} \rightarrow \frac{\mathrm{Ri}_m}{\mathrm{Ri}_p} = \frac{\left(\frac{\Delta\rho}{\rho}\right)_m}{\left(\frac{\Delta\rho}{\rho}\right)_p} \frac{V_p^2 D_m}{V_m^2 D_p}. \tag{2.1}$$

The ratio is currently in terms of density, but the Boussinesq approximation may be applied to set the ratio in terms of temperature. The Boussinesq approximation relates the density variation to be a function of temperature rise, as shown in Equation (2.2).

$$\rho = \rho_0 + \Delta\rho \rightarrow \Delta\rho = -\beta\rho_0\Delta T. \tag{2.2}$$

$$\frac{\mathrm{Re}_m}{\mathrm{Re}_p} = \frac{V_m D_m \nu_p}{V_p D_p \nu_m} = \left[\frac{\left(\frac{\Delta\rho}{\rho}\right)_m}{\left(\frac{\Delta\rho}{\rho}\right)_p}\right]^{1/2} \left[\frac{D_m}{D_p}\right]^{3/2} \frac{\nu_p}{\nu_m}. \tag{2.3}$$

If the Richardson numbers match then the velocity ratio may be extracted from Equation (2.1). This may be substituted into the Reynolds number ratio to make the ratio a function of density variation or temperature rise shown in Equation (2.3). Using these ratios the

independent variables of the experiment are determined. When modeling a DCC experiment, the independent variables would be the core heat input and distribution. For a PCC experiment a pump would be added, so the flowrate and core heat would act as the independent variables. Since this is just a preliminary testing maximum power was supplied to the active pipes. Since the model will be operating at much lower temperatures and pressures than the prototype, matching Re and Ri is not possible with the same working coolant. If the working coolant for the model was replaced with water, the density and viscosity for cold and hot water (approximately 20 and 46 ºC) are appropriate to match the Richardson and Reynolds number of the high temperature and pressure helium in the prototype.

Using the scaled geometry in Table 2.1 and Figure 2.1 a design for the experimental facility was generated, shown in Figure 2.3. The grey parts are polycarbonate, and the blue parts are stainless steel chosen for high thermal conductivity. The dimensions without the wall thickness of the geometry were matched with the INL provided ones. The diameter of the main coolant inlet and outlet are 1 in and 3 in, respectively with a length of 1.94 m. The basis for the design was a closed loop system where the flow is driven purely by natural circulation. The coolant enters the lower plenum from the inlet pipe, and is drawn up through heated pipes by natural convection. The water then leaves the pipes as slow jets into the upper plenum, the region of interest. The water exits the upper plenum through the downcomer, the region between the core containment and outer containment. A heat sink would need to be built that removes heat as the flow goes through the downcomer to the outlet pipe of the system. The outlet pipe leads to a

reservoir tank which then leads back to the inlet pipe completing the coolant loop. Next the pipe layout for the core was needed. Through collaboration with INL a final design of 25 pipes with a 1.905 cm inner diameter arranged in an octagonal pattern equidistant from each other was chosen, shown in Figure 2.4. Initially an annular pattern was considered, but was overruled as having the pipes be equidistant was priority. The pipes would be heated with heating tapes which were sorted in groups of five. These five groups would then be connected to five voltage variable transformers which could control the power to the heating tapes, and the resulting heat input. For this study, only T group was run for the tests. Multiple design parameters were considered during the design process, the largest being: waterproof access to the core for wiring, ease of assembly and disassembly, data acquisition, and fabrication limitations.

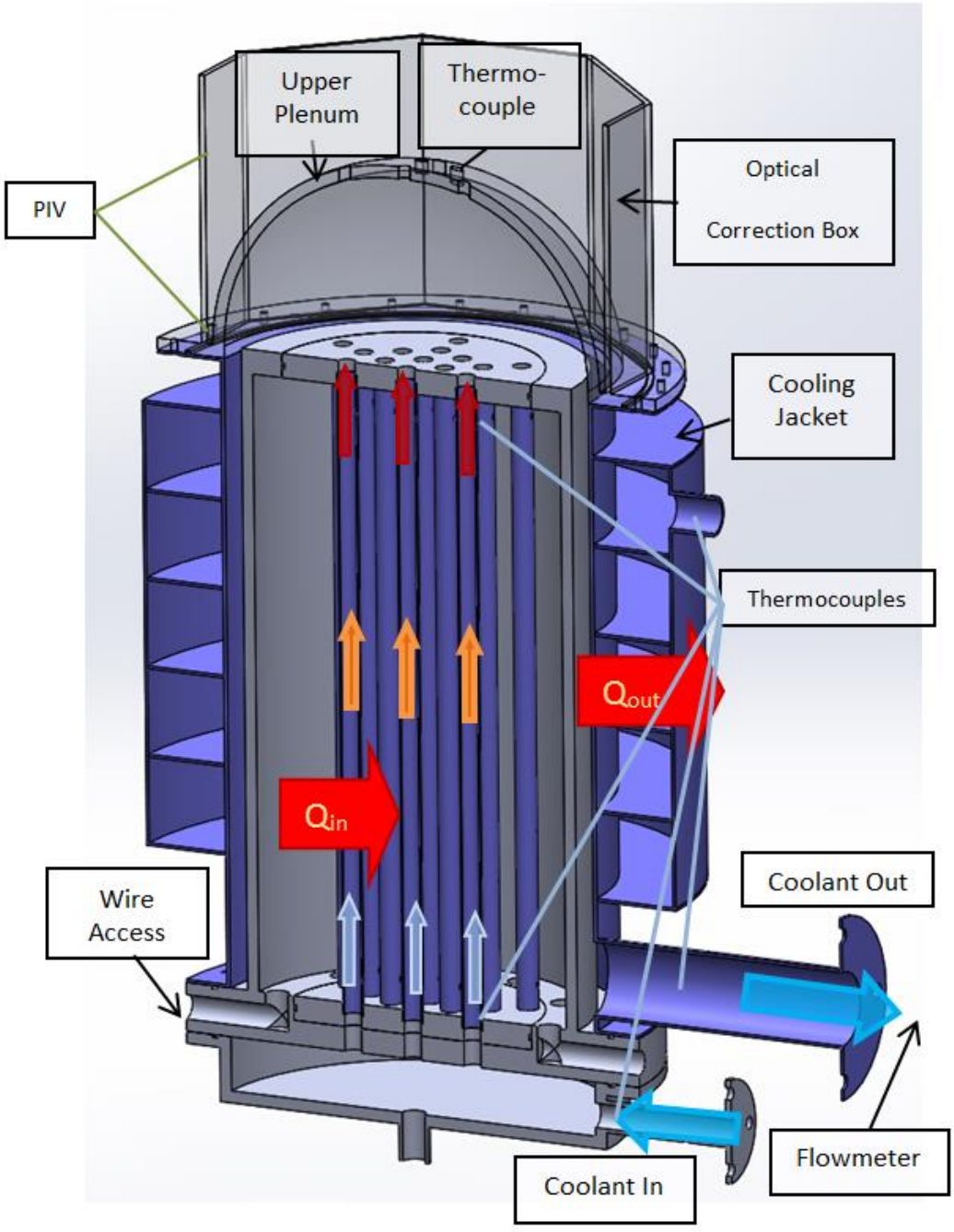

Figure 2.3. Experimental facility schematic.

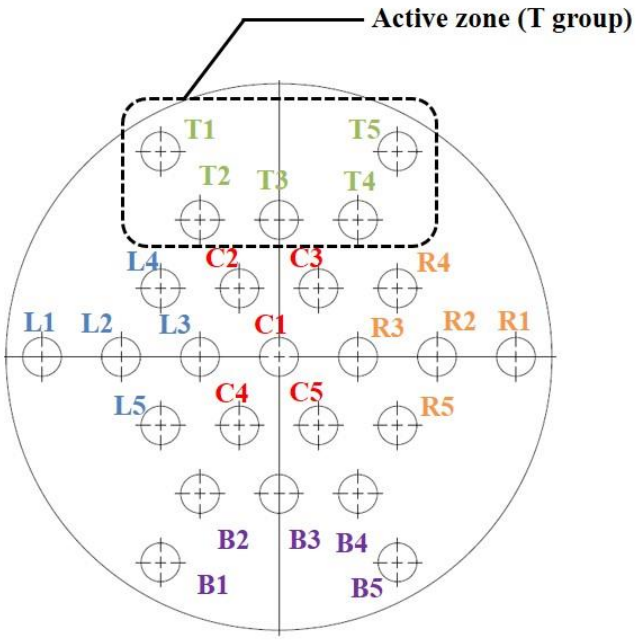

Figure 2.4. Core piping.

A heat sink is needed to remove the majority of the heat input to reach steady state and help induce natural circulation. Since the DCC simulation is driven through natural circulation any large pressure drops in the system would inhibit the flow and the resultant data may not be representative. Instead an external non-intrusive cooling jacket was needed that would be connected to the outer containment and remove heat. The cooling jacket and reservoir removes sufficient heat from the system so that it may achieve steady state, without impacting the flow in the upper plenum where data is recorded. This effectively acts as the RCCS for the prototype. Because the reservoir is much larger than the test vessel, there would be no significant reservoir temperature rise during a test. To simulate a PCC scenario, an in-line heat exchanger is needed to remove sufficient heat to reach steady state. The cooling jacket design shown in Figure 2.5 has five rows of baffles.

Water is pumped into the lowest baffle where it circles the containment and then rises 8.89 cm. This process is repeated until it reaches the cooling jacket outlet.

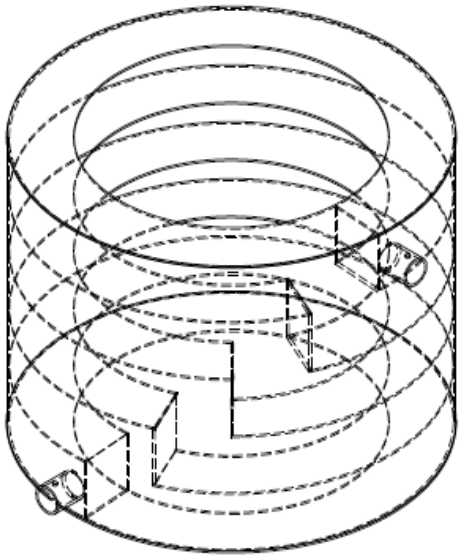

Figure 2.5. Cooling jacket design.

2.3 Fabrication and Construction

Figure 2.6 shows the assembly procedure. First the core containment and outer containment are lowered onto the lower plenum and their flange is bolted and sealed with O-rings. Next the core is assembled with the 25 pipes sealed into two plates with O-rings. The core is then dropped into the core containment where O-rings seal the plates with the containment. Finally the upper plenum is dropped and bolted onto the outer containment and sealed with either an O-ring or gasket. An arc welder was used to create T-type thermocouples which have an accuracy of ±0.5 °C, that were then calibrated using a certified thermometer with an accuracy of ±0.3 °C, installed at the centerline of the core piping and test vessel inlet and outlet. The combined accuracy of the measured temperature was calculated by taking the square root of the sum of the squares and was estimated ±0.58 °C. As shown in Figure 2.3 the thermocouples will measure the temperature rise for each pipe in the core, the temperature rise of the main coolant loop, and the temperature rise in the cooling jacket. The thermocouples enter the fluid through compression fittings, which are welded to the 25 pipes. To prevent leaks through the thermocouple locations, the thermocouples were inserted into fine steel tubing and both ends were sealed with ultraviolet epoxy as shown in Figure 2.7 (top); this also protects the thermocouple tips from corrosion. The temperature was measured at the center of the steel tubing as shown in Figure 2.7 (bottom). There are nine ports for thermocouples in the upper plenum that may be inserted vertically above the pipe outlets to measure the temperature field. The thermocouples are connected to a National Instruments SCXI-1600

data acquisition system and measured with LabVIEW. An ultrasonic flowmeter, Krohne Optisonic 6400, measures the outlet flow rate of the main coolant loop with an accuracy of ±1% reading value for flow greater than 0.5 m/s, and a paddlewheel flowmeter measures the cooling jacket flow rate with an accuracy of ±0.227 L/min.

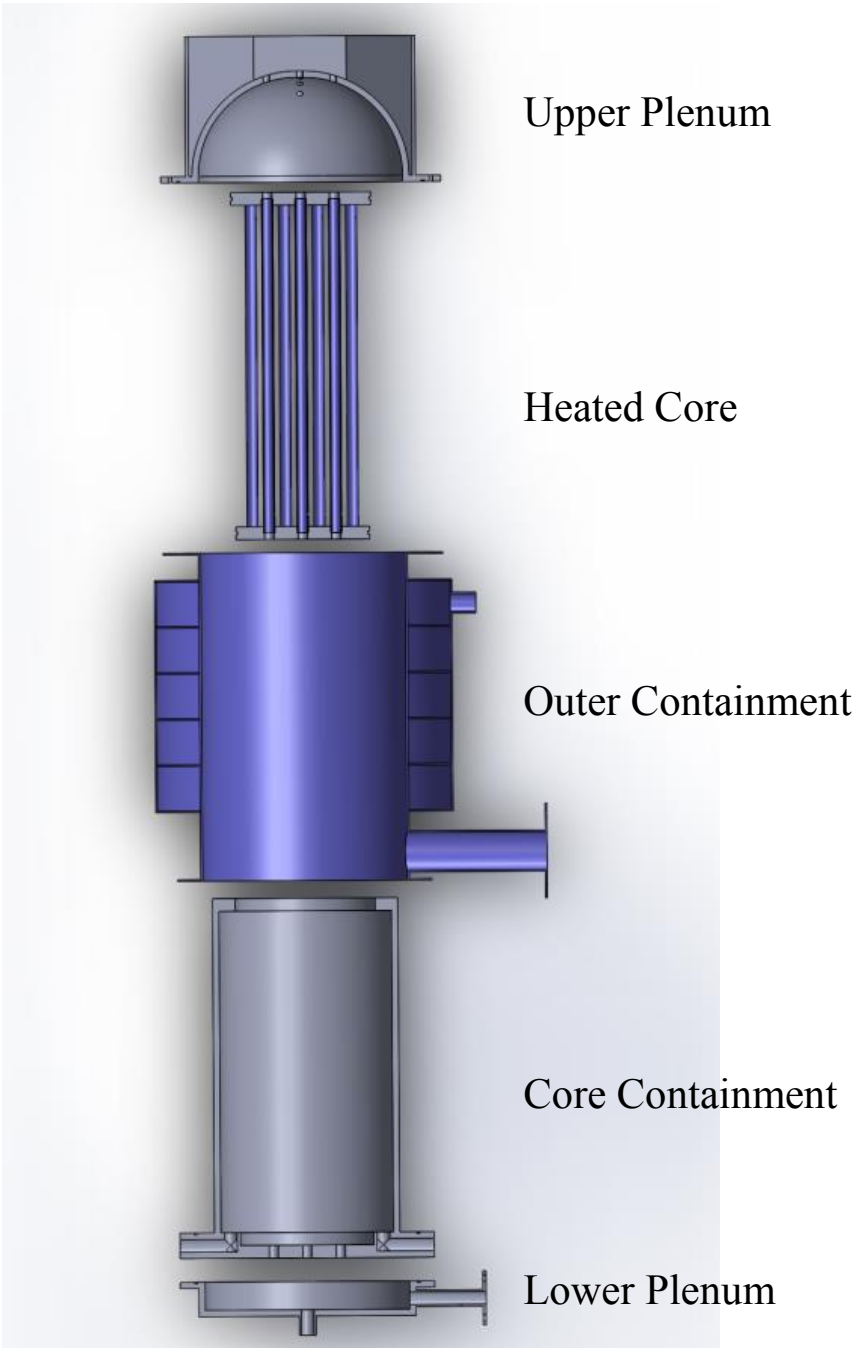

Figure 2.6. Exploded assembly cross section.

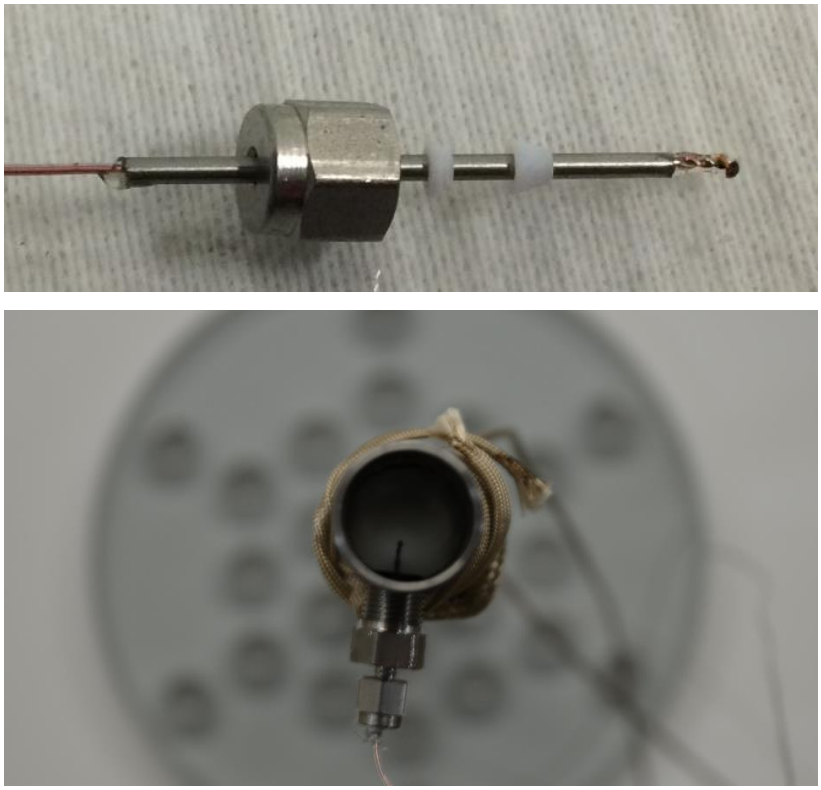

Figure 2.7. Thermocouple with tubing, epoxy, and ferrules (top) and its location for the temperature measurement inside the steel tubing (bottom).

PIV is used to measure a planar velocity field in the upper plenum. PIV involves seeding the working fluid with particles of equal density, and firing a laser sheet pulse that illuminates a plane of particles. The illuminated particles are then captured with a high speed camera in sync with the laser pulse; a sample is shown in Figure 2.8. Two laser pulses are fired in quick succession and both particle images are captured. A program then uses cross-correlation to track the patterns of particles between the two images, and using the time between the pulses a velocity vector field can be generated [15]. For this study a Vlite series dual laser pulse system was used, which operated at a wavelength of 532 nm with a pulse width of approximately 1 mm. A high speed camera MEMRECAM GX-3

was used for the imaging, and connected to the laser with a waveform generator. A lens Zeiss 2/50 Makro-Planar ZF.2 Macro Lens was used for the test. For the particle seeding fluorescent orange polyethylene microspheres were used. Their diameter ranged from 53-63 μm, and had a density of 1.002 g/cm^3. Fluorescent particles reflect the laser light at a different wavelength, so an optical filter was used for the camera that blocked the wavelength of the laser and consequently removing all light noise and producing clear particle images. As shown in Figure 2.3 a correction box is built around the upper plenum; when a curved surface is filled with water there is an optical distortion caused by refraction. The correction box presents a flat viewing plane, and the medium between the plane and curved surface is filled with water so that the images may be recorded on a flat surface without refraction. An optical test was performed in Figure 2.9 to confirm there were no distortions. The heating tapes were sealed individually with silicon tubing for waterproofing and insulation. Figure 2.10 shows the assembly procedure of the test facility. Figure 2.11 and 2.12 show the completed test facility and its schematic design, respectively.

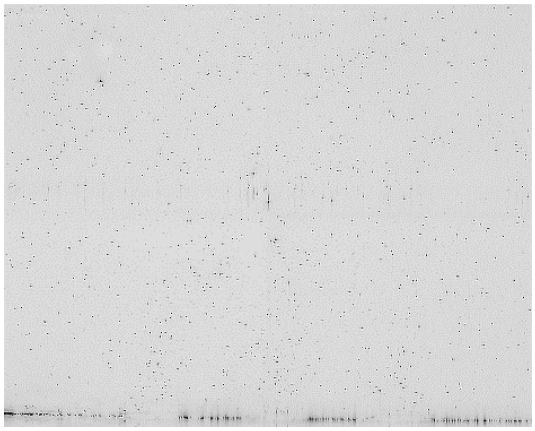

Test 1

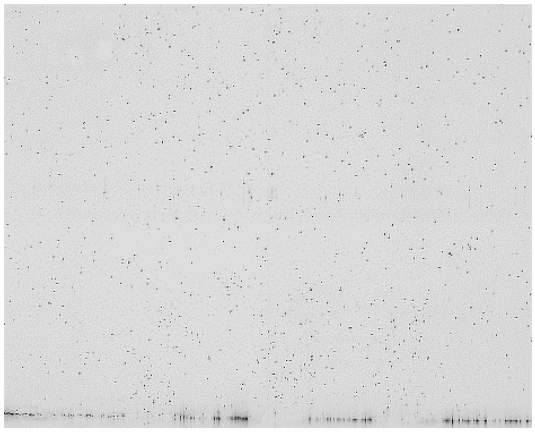

Test 2

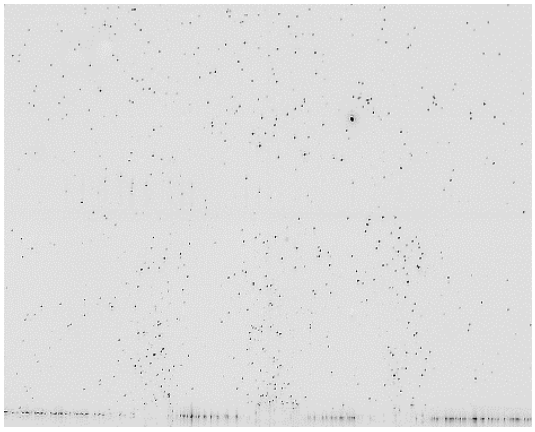

Test 3

Figure 2.8. Particle images for PIV with black and white inversion.

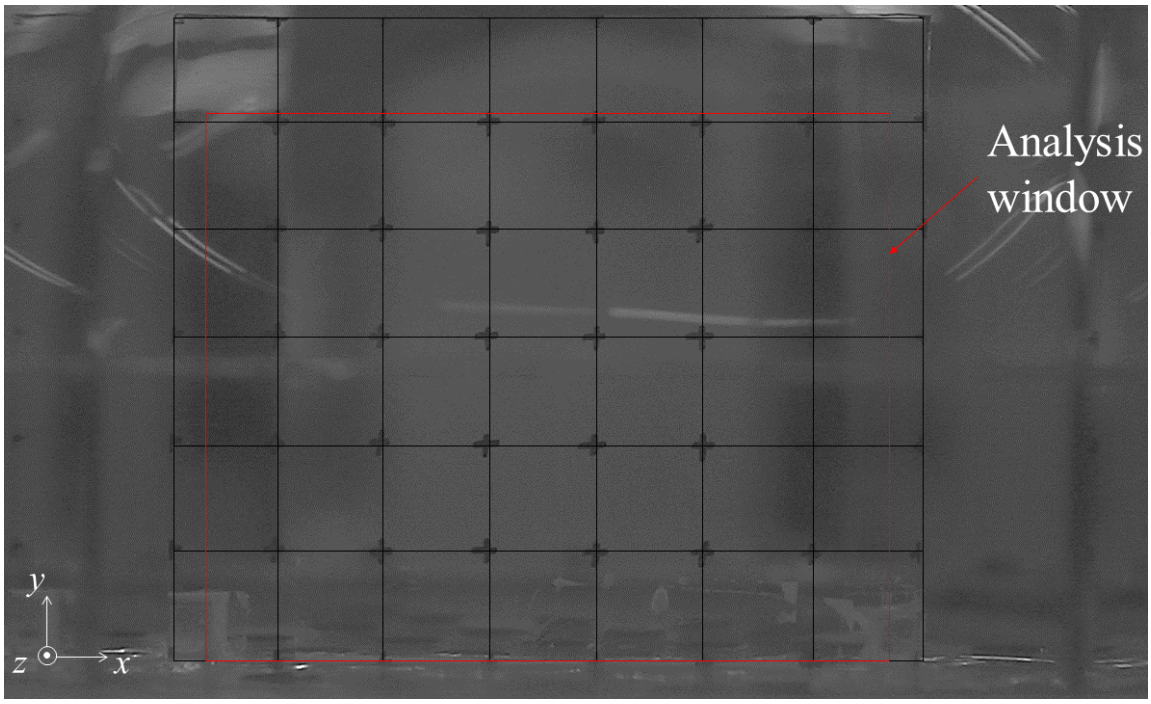

Figure 2.9. Optical distortion test.

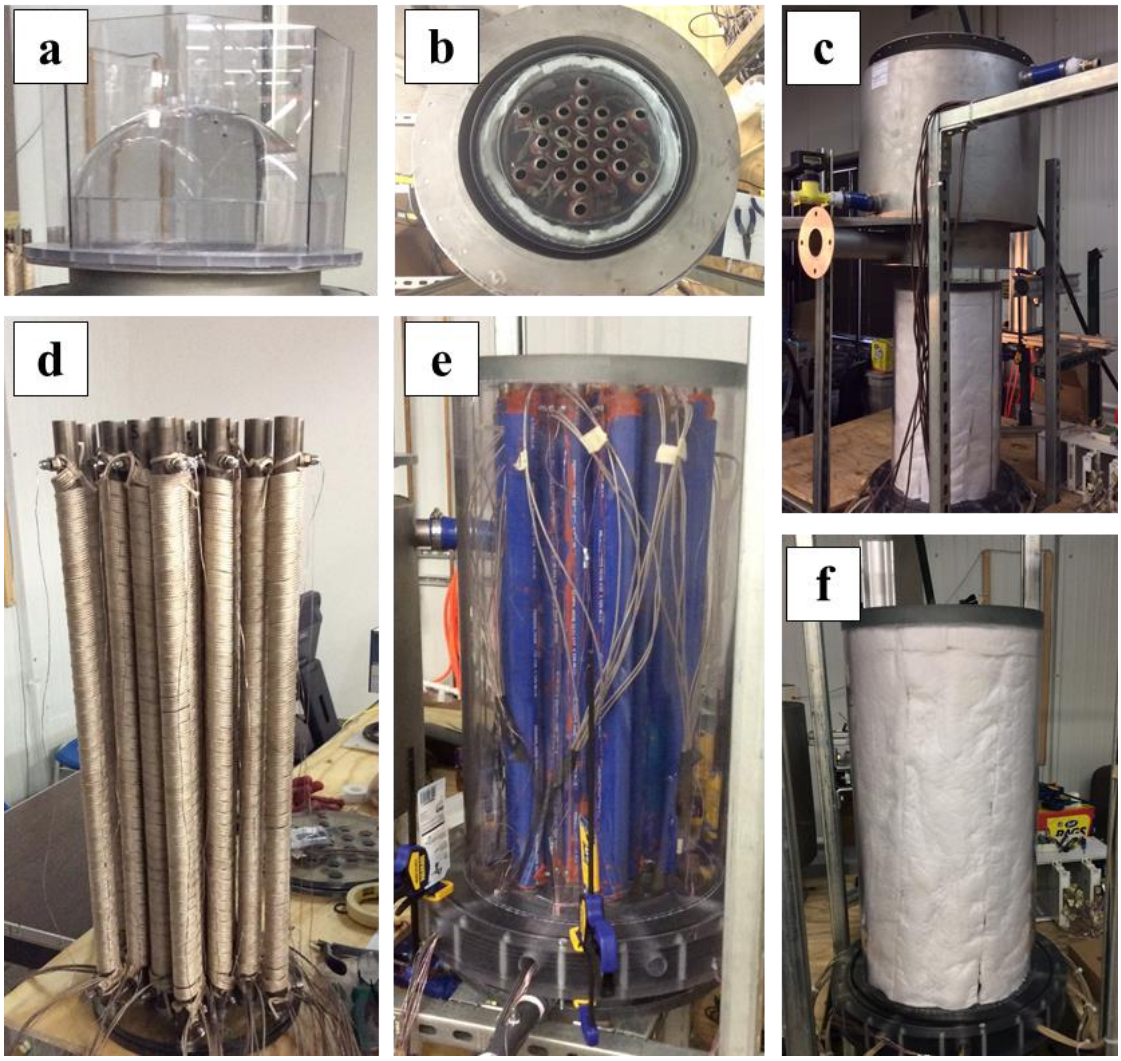

Figure 2.10. Assembly procedure of the test facility: (a) upper plenum with the correction box, (b) internal core top view, (c) outer containment being lowered by a forklift, (d) 25 coolant channel pipes with heating tapes and thermocouples, (e) silicon tubings and core assembly, and (f) core insulation.

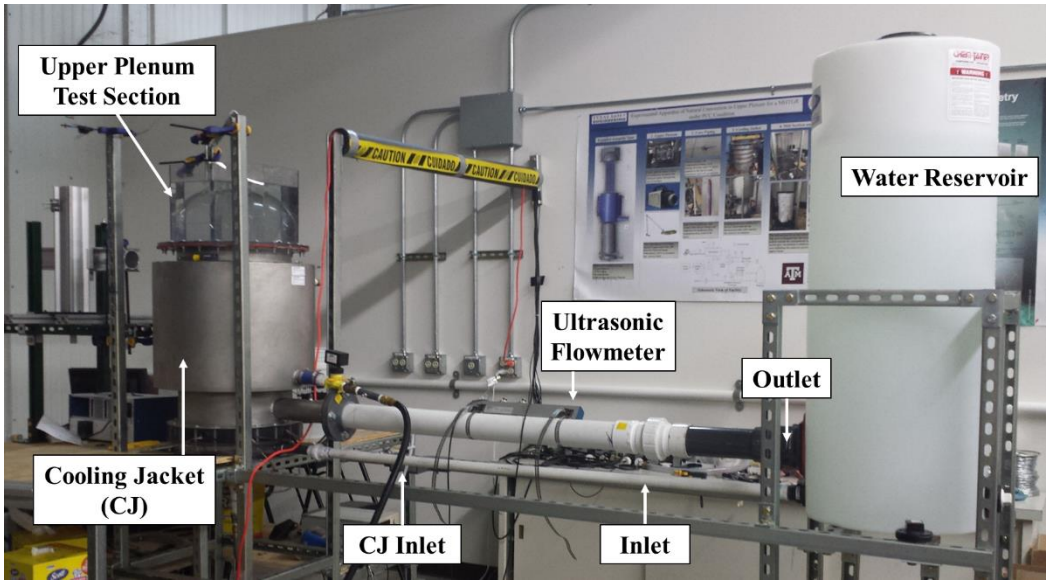

Figure 2.11. Completed test facility

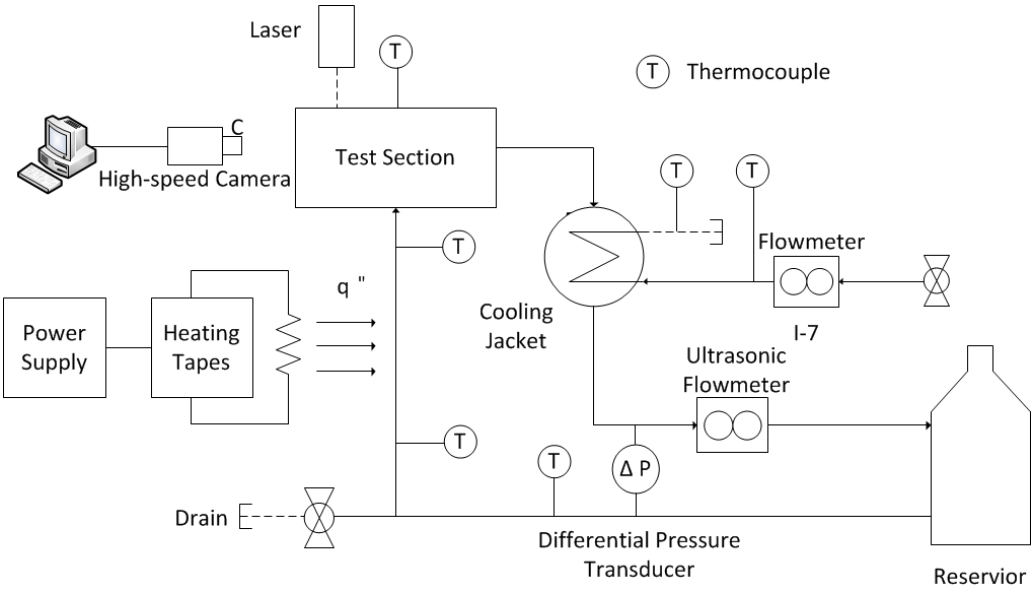

Figure 2.12. Schematic view of facility

3. PRELIMINARY TEST

A set of three preliminary tests has been performed in order to obtain the validity of the PIV data analysis. At the time when the test was being conducted the heated pipes were not fully functioned and only five T-group pipes were operated for the tests. The work on this section was published in a journal paper [11] and the contents of the manuscript has been modified and rearranged*.

3.1 Experimental Method

The system was run at partial core power to test the validity of the PIV process and capabilities of the test facility. Power was supplied only to the five pipes in T-group from Figure 2.4, and the other pipes were sealed off. A total of 1.44 kW power was evenly distributed between the five heating tapes for this preliminary test to run the maximum capability of the current test facility. The camera was positioned to capture a 16 × 13 cm window above the outlets of three adjacent natural convection jets, shown in Figure 3.1 and 3.2. The laser sheet is aligned with marked locations on the test facility, and adjusted for the optimal power output. The laser used was a Vlite-200 from Beamtech Optronics Co. It has an average beam thickness of 1 mm, and can provide up to 200 mJ per pulse; we used 60 mJ. The test heaters were left on, and the cooling jacket was turned on to approximately 41.5 L/min, the maximum flowrate of the local water supply. The test vessel and reservoir were filled with room-temperature water, and then the heaters and

*Reprinted with full citation from "Preliminary tests of particle image velocimetry for the upper plenum of a scaled model of a very high temperature gas cooled reactor" McVay, K.L. et al, 2015, Progress in Nuclear Energy, **83**: p 305-317, Copyright [2016] by Elsevier.

cooling jacket were activated. Steady state was determined when the outlet temperature rise across the core was 25−45 ºC, and the temperature rise of the test vessel remained near 25 ºC and constant for five minutes. Next the particles were injected into the test vessel inlet pipe, and allowed to circulate into the upper plenum. At steady state the coolant outlet temperature of the vessel after passing through the cooling jacket was within 0.5 ºC of the reservoir temperature ensuring there would be no significant temperature rise in reservoir that would impede the system reaching steady state. Additionally the low flow rates and large piping resulted in a very low pressure drop to and from the reservoir so flow was not impeded. Once steady state was achieved the particles were injected at the inlet of the test facility, and particle images were collected. The test length was limited by the camera memory, which could hold up to 2,300 images. Because the fluid velocity was low, the camera and laser were synchronized to record images at 10 Hz, which means that time interval of successive images (Δt) was 0.1 s; the test was run for approximately 4 minutes. The temperature of the system was constant within ±0.5 ºC once the system achieved steady state, and recorded with thermocouples at 1 Hz.

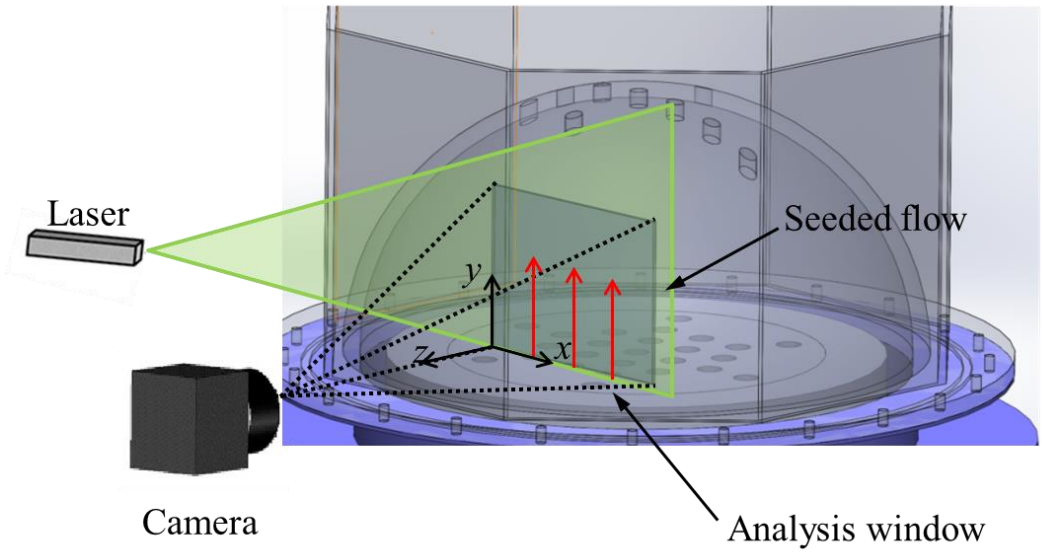

Figure 3.1. PIV schematic.

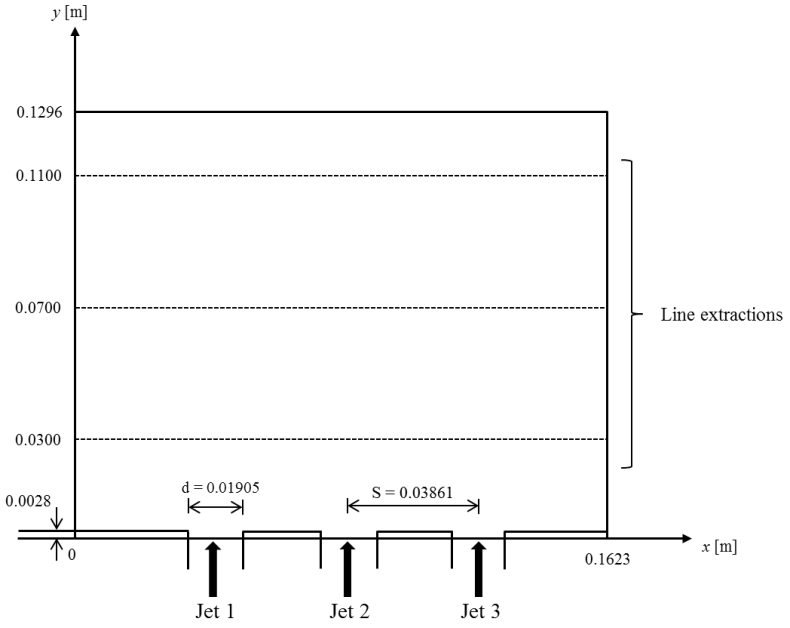

Figure 3.2. Analysis window geometry.

While the test was running the Krohne Optisonic 6400 ultrasonic flowmeter was measuring the total flow rate of the main coolant loop. The flowmeter had a 1% reading value accuracy for larger flow rates, but had no in-situ calibrations at the low operating flow rate of the system. A Krohne Optiflux 1000 electromagnetic flowmeter was installed on a nearby system and validated with an accuracy of ±3% reading value at the operating low flow rate. A electromagnetic flowmeter is more accurate than an ultrasonic flowmeter due to the different measuring principle it employs. Because the flowmeter was in use, and could not operate on the 3" diameter pipe, the electromagnetic flowmeter was used to calibrate the ultrasonic flowmeter. The ultrasonic recorded flow for seven minutes and averaged the values, the average was then compared to the flow rate of the Optiflux reading. This was performed at six different low flow rates. The calibration formed a linear trendline shown in Figure 3.3, and the trendline equation was used to correct all test measurements.

The images were processed using PIVlab (version 1.32). PIVlab is an open source MATLAB-based package developed by Thielicke and Stamhuis [22] and has been verified by several investigators [23-27]. The 2,300 images were imported in a first-second, third-fourth image pair manner so approximately 1,150 image pairs or frames were available.

The analysis window was 16 × 13 cm with a 1280 × 1024 high resolution, and a 0.125 x 0.127 mm/pixel size. Including the time between images, 1 px/frame corresponds to 1.26 mm/s. When the particles are illuminated by the laser they occupy 4 × 4 pixels. When running PIV three interrogation windows were evalutated: 64 × 64, 32 × 32, and 16 × 16, and a step width of 32, 16, and 8 pixels respectively. The average particle shifted 65

pixels in one image pair. The calculated Stokes number of the seeding particles was calculated to be 0.0014 at the worst, confirming the seeding particles followed the fluid flow accurately [28]. After calculating the velocity vectors for each image pair, PIVlab runs an algorithm with that located erroneous vectors with a user input standard deviation threshold value (7) and replaced them with the mean value of the neighboring vectors, the details may be found in the cited document [22].

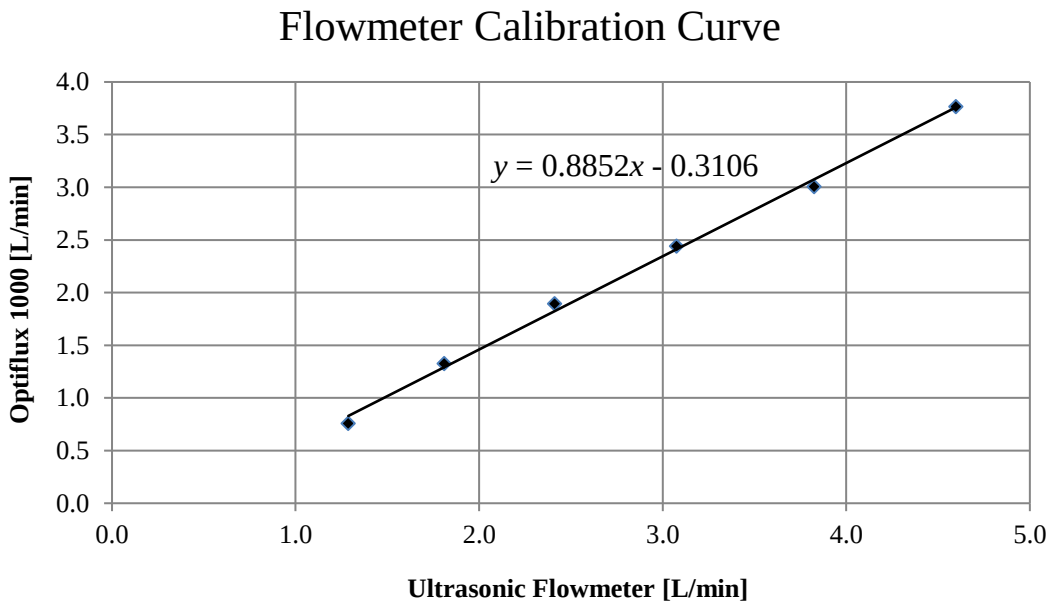

Figure 3.3. Flowmeter calibration line.

3.2 Sensitivity Analysis

The turbulent velocity field is unsteady, but statistically steady state may be measured by averaging the velocity for a batch of frames. This is shown in Equation (3.1),

$$\boldsymbol{v}(r,t) = \overline{\boldsymbol{v}(r)} + \boldsymbol{v}'(r,t), \tag{3.1}$$

where the instantaneous velocity *v* is represented as the averaged velocity $\overline{\boldsymbol{v}}$ and the velocity fluctuation *v'*. In order to validate the results multiple tests need to be run. A total of three tests were run for statistically steady state (Test 1, Test 2, and Test 3). One thousand frames were averaged to achieve the representative averaged velocity field over a duration of 200 seconds. The averaged velocity magnitude contour and streamlines are shown in Figure 3.4 and 3.5. There is a distortion of 7 centimeters from the pipe outlets, this is due to the glued section between the curved dome and the cylinder in the upper plenum which slightly blurs the image and makes the particles harder to track. At 1 cm downstream from the pipe outlet the contour is representative of the experimental flow. There is a slight recirculation between the jets very close to the pipe out let. The jets begin to merge approximately 3 cm downstream from the pipe outlet, but diverge as the flow approaches the top of the test geometry which is exhibited by the streamlines. The x and y-velocity contours are shown in Figure 3.6 and 3.7 respectfully. Figure 3.6 shows that far from the pipe outlet the flow begins moving horizontally towards the downcomer. Figure 3.7 shows that the flow is predominantly vertical as the y-velocity contour nearly matches the velocity magnitude contour. Figure 3.8 shows the averaged vorticity contour, calculated from Equation (3.2).

$$\omega = \frac{\partial v}{\partial x} - \frac{\partial u}{\partial y}. \tag{3.2}$$

A single frame produces an instantaneous flow with eddies, but once averaged the results show good anti-symmetry. Directly between the jets the vorticity fluctuates such that the averaged value is approximately zero.

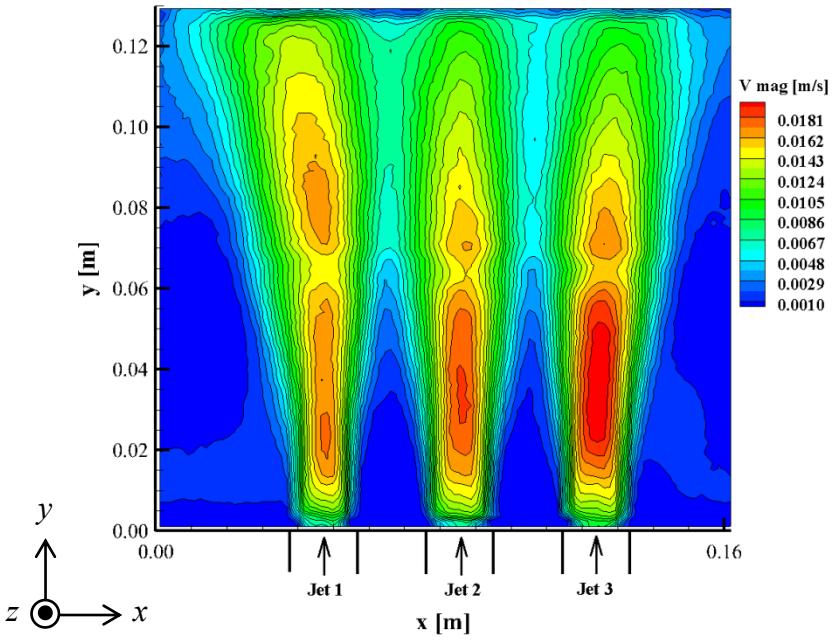

Figure 3.4. Velocity magnitude contour of 1,000 frames.

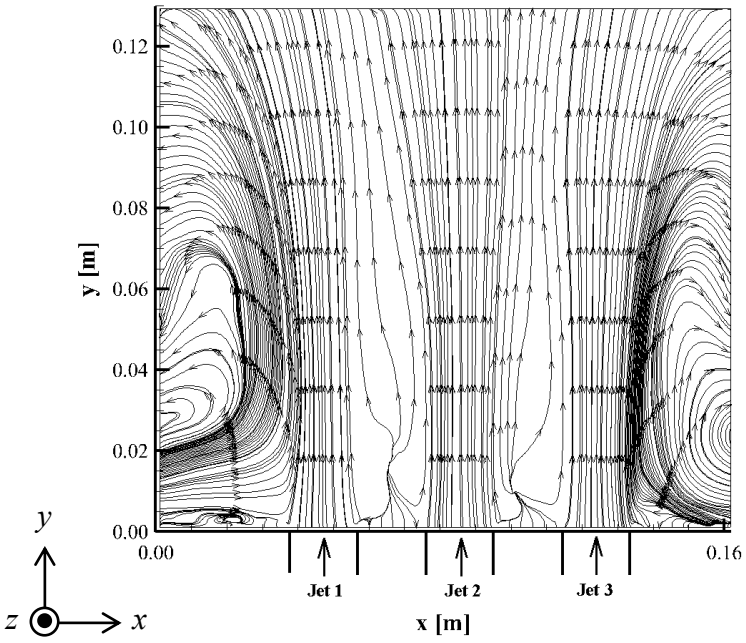

Figure 3.5. Streamline of 1,000 frames.

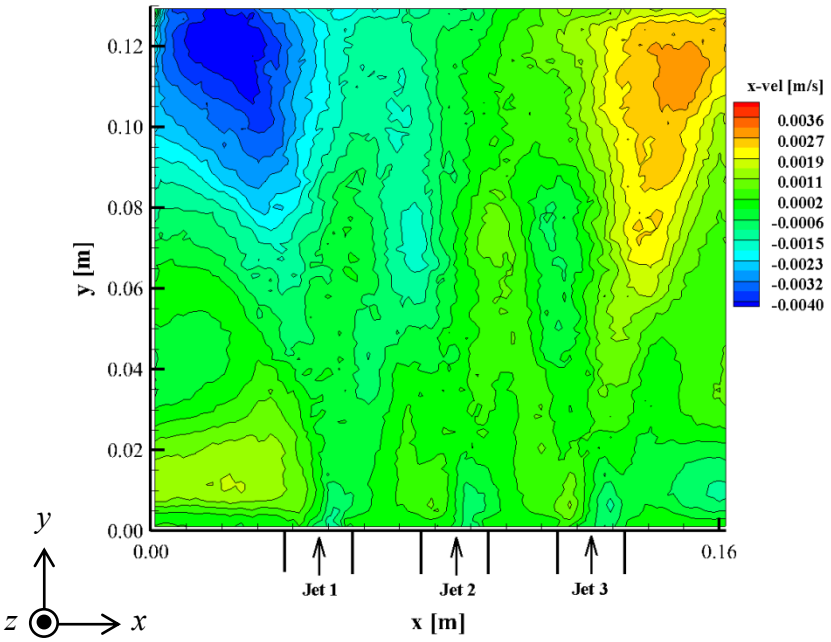

Figure 3.6. x-velocity contour of 1,000 frames.

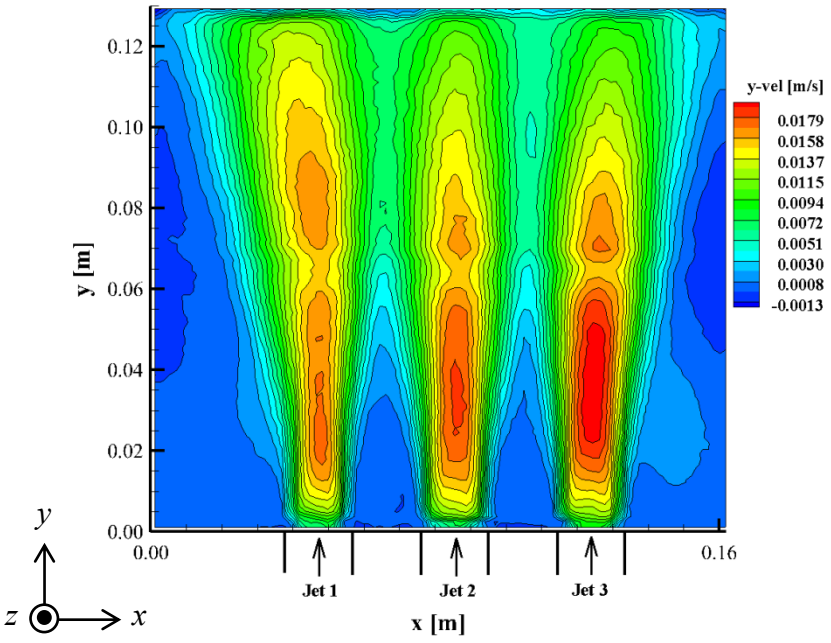

Figure 3.7. y-velocity contour of 1,000 frames.

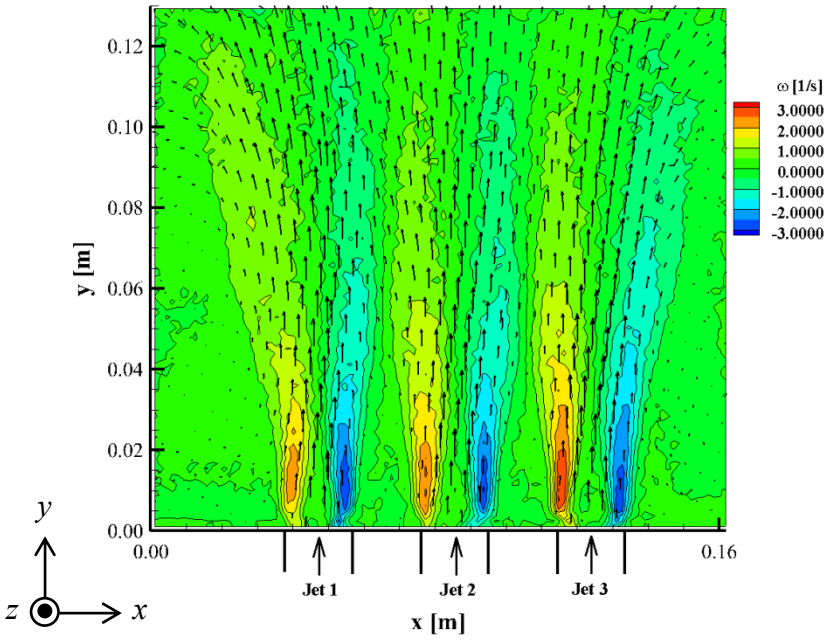

Figure 3.8. Vorticity contour and average velocity vector of 1,000 frames.

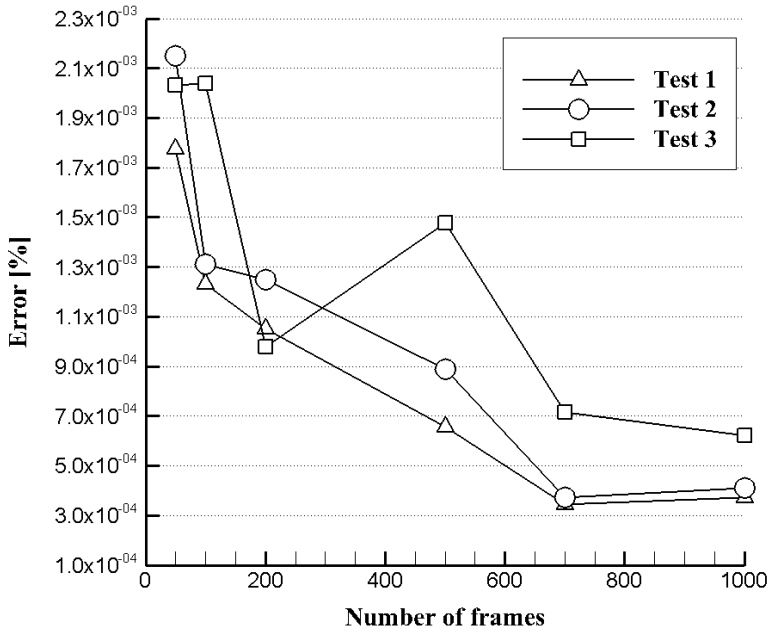

Figure 3.9. Percent error of y-velocity for different batch sizes of frames.

First a sensitivity analysis must be performed to confirm a sufficient number of frames were used to correctly model statistically steady state; a similar analysis was performed by Amini and Hassan [29]. To do this, different batch sizes of frames were used to calculate the averaged velocity field and this was compared to the previous averaged velocity field; as the batch sizes increase the flow profiles should began to match. The root-mean-square (RMS) deviation was calculated using Equation (3.3),

$$Error = \sqrt{\frac{\sum_{i,j=1}^{n}\left(v_{i,j}^{k} - v_{i,j}^{k-1}\right)^{2}}{N}}, \tag{3.3}$$

where $v_{i,j}^{k}$ represents the averaged y-velocity field (i, j) at current frame count (k), $v_{i,j}^{k-1}$ represents the averaged y-velocity field (i, j) at previous frame count (k-1), and N is the current number of frames (k). This was run for all 159 × 127 vectors from PIVlab using the Fast Fourier Transform (FFT) option, the results are shown in Figure 3.9. As the batch sizes increase errors continue to decrease constantly and reach less than 5.0×10^{-4} after the 700 frames average, confirming that 1,000 frames are sufficient to measure statistically steady state. Tests 1 and 2 converge as expected, but Test 3 converges abnormally implying that the results may be misrepresentative of the flow and will not be shown in this study. It is hypothesized that this occurred because insufficient time was allowed to let the particles circulate through the system for Test 3. Figure 2.8 shows the particle density difference between the tests.

Additionally the y-velocity was extracted at 3, 7 and 11 cm downstream of the pipe outlet for different batch sizes. Note that each symbols represents following numbers of frames: 50 frames (○), 200 frames (▼), 500 frames (●) and 700 frames (▽). The solid line is the velocity for 1000 frames and is used as reference. At 3 cm Figure 3.10 and 3.11 show the majority of the batch sizes match the reference. At 7 cm Figure 3.12 and 3.13 show that the 50 and 200 batch sizes begin to differ significantly from the reference. Additionally the jets began merging. At 11 cm Figure 3.14 and 3.15, 500 and 700 frames begin to differ slightly, primarily in Test 1. This suggests when modeling significantly far from the pipe outlet to correctly represent the flow field more images need to be processed. Also the jets continue to merge, but stays within the merging region. The analysis window for this study is too small for the jets to fully merge and reach the combined point.

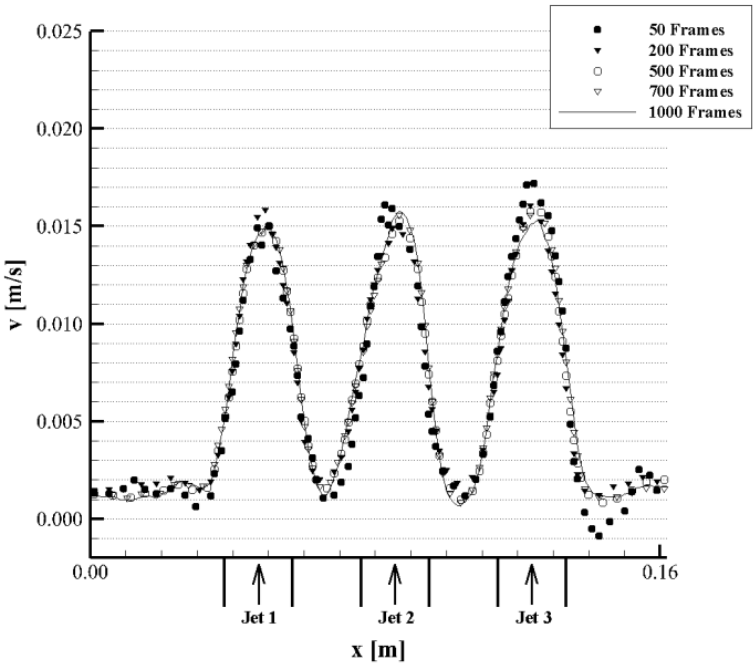

Figure 3.10. Test 1 sensitivity analysis at 3 cm downstream of the pipe outlet.

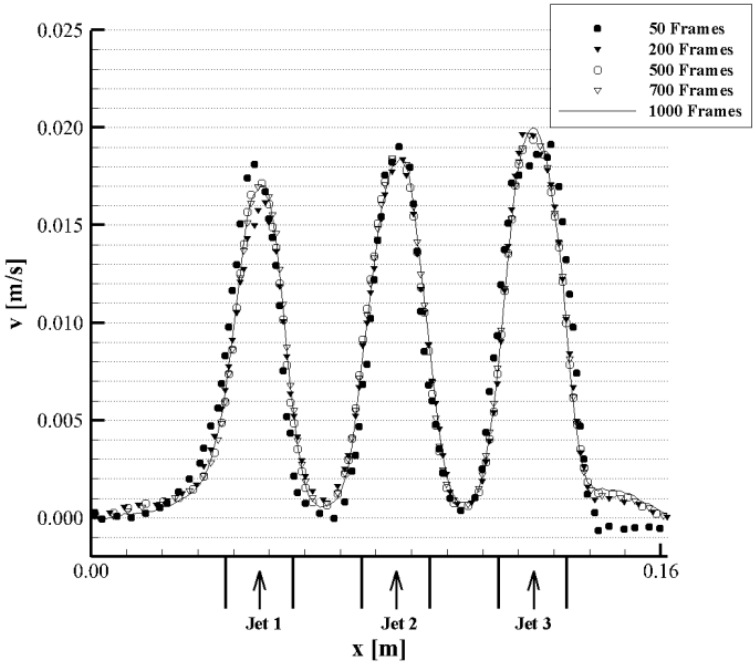

Figure 3.11. Test 2 sensitivity analysis at 3 cm downstream of the pipe outlet.

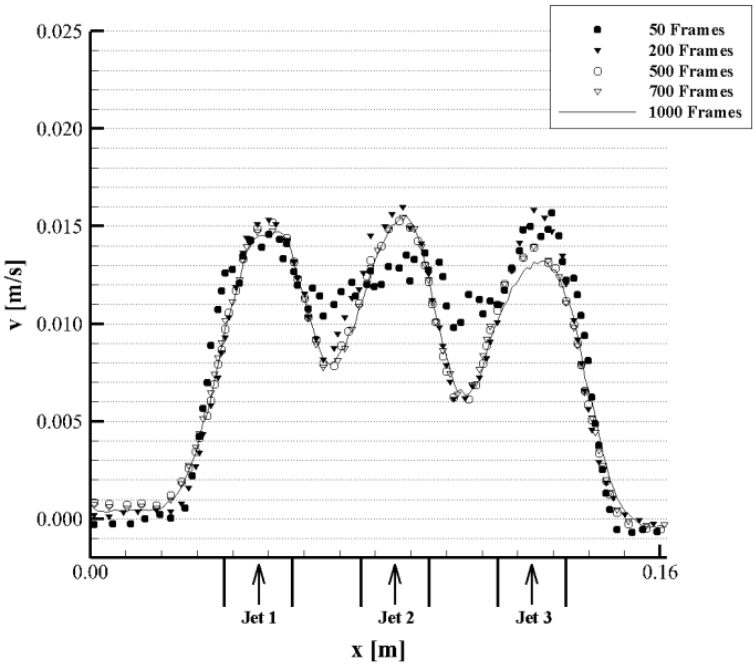

Figure 3.12. Test 1 sensitivity analysis at 7 cm downstream of the pipe outlet.

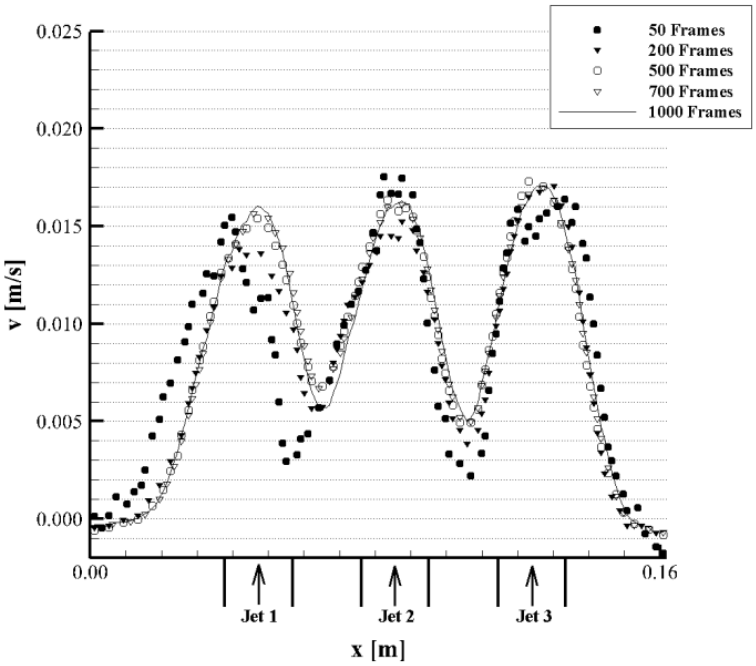

Figure 3.13. Test 2 sensitivity analysis at 7 cm downstream of the pipe outlet.

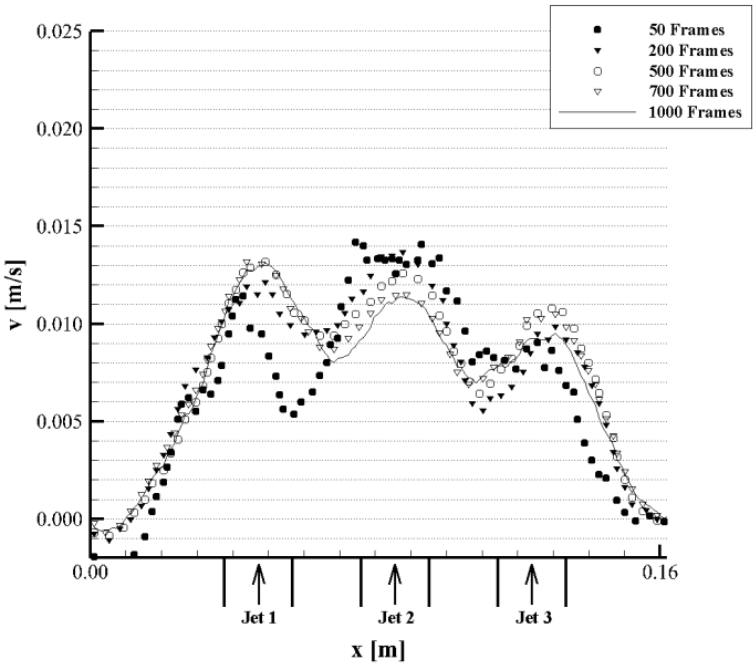

Figure 3.14. Test 1 sensitivity analysis at 11 cm downstream of the pipe outlet.

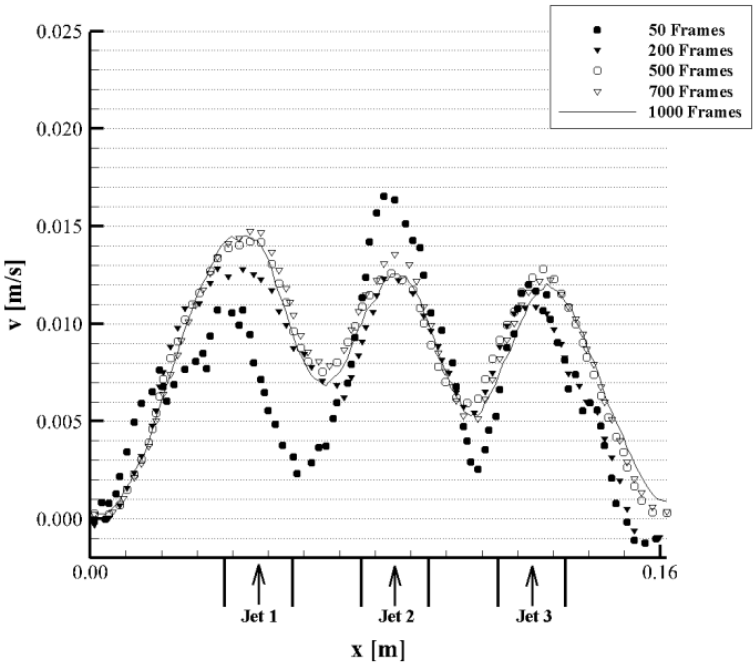

Figure 3.15. Test 2 sensitivity analysis at 11 cm downstream of the pipe outlet.

3.3 Experimental Result

Equation (3.4) was used to average the velocity profile for the 1,000 frames (N) for each test, and average the velocity profile between the tests (M = 2). The uncertainty was generated by standard deviation between the tests. Figure 3.16 shows that there is uncertainty between the tests; to more accurately assess the repeatability, more tests need to be run.

$$v_{ave} = \frac{1}{M}\sum_{m=1}^{M}\left(\frac{1}{N}\sum_{k=1}^{N} v_m^k\right). \tag{3.4}$$

Once the jets enter the upper plenum mixing occurs which causes the flow to become turbulent. The turbulence strength can be calculated by taking the root mean square (rms) of the velocity over a period of time, shown in Equation (3.5).

$$v_{rms} = \frac{1}{M}\sum_{m=1}^{M}\sqrt{\frac{\sum_{k=1}^{N}\left(v_m^k - \overline{v}_m^N\right)^2}{N}}. \tag{3.5}$$

The turbulent intensity (TI) can be calculated by dividing the averaged velocity (v_{ave}) from the turbulence strength (v_{rms}). Figure 3.17 shows the turbulence strength averaged between Test 1 and 2. The turbulent strength is largest inside the jets where the mixing occurs, and the resulting TI is approximately 41% of the peak velocity, meaning TI = 0.4 in the jets. This shows that the flow goes turbulent in the upper plenum where the mixing occurs, but less so between the jets. TI increases to 45% at the jet velocity peak 11 cm from the pipe outlet.

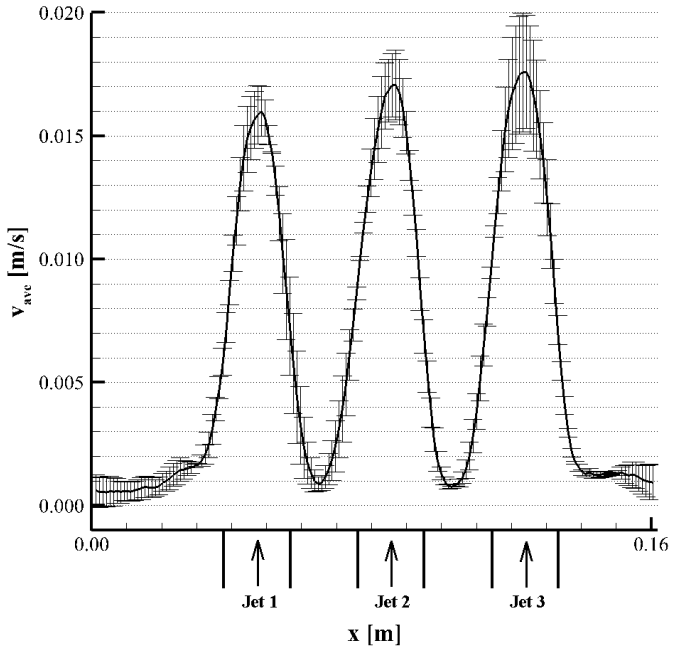

Figure 3.16. Average y-velocity at 3 cm downstream of the pipe outlet with standard deviation between the tests.

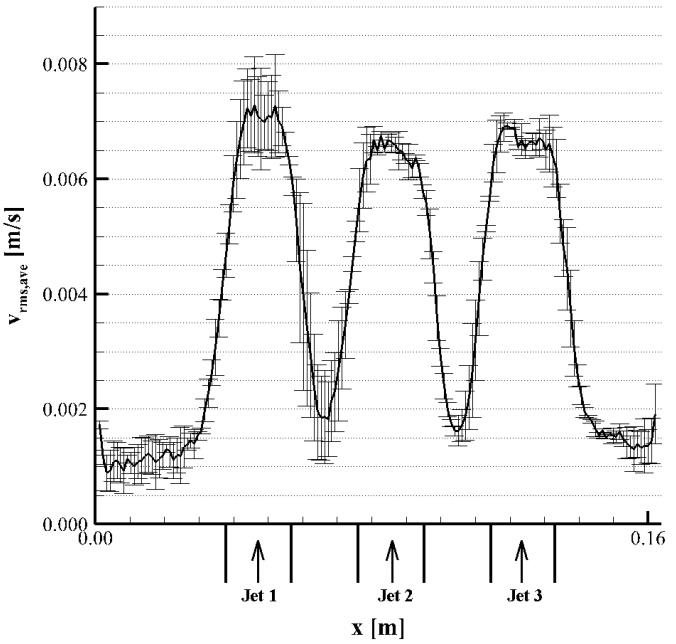

Figure 3.17. Averaged turbulence strength at 3 cm downstream of the pipe outlet with standard deviation between the tests.

Next to validate the PIV results, the averaged flow rate for a single pipe is measured using the statistically steady state velocity vector field, and compared to an analytic flow rate and the ultrasonic flowmeter data. The flow rate of a single pipe may be calculated analytically using the heat balance equation as shown in Equation (3.6),

$$\dot{m} = \frac{Q}{c_p \Delta T}, \tag{3.6}$$

where Q is the heat input (W) from the heating tape, $\dot{m}$ is the mass flow rate (kg/s), c_p is the specific heat capacity for water (J/kg·K), and ΔT is the temperature rise in the core piping (K). Q is controlled with the variable voltage transformer and the pre-measured resistance of the heating tape, and the temperature rise in the core is measured with thermocouples. At the steady state temperatures (approximately 25ºC and 45ºC) the specific heat matches, and there is minimal heat loss due to the insulating tubing. While the tests are running the ultrasonic flowmeter records the total flow rate of the system. The flow rates for all three methods are plotted in Figure 3.18. The analytic flow rate uncertainty is due to the error of the T-type thermocouples. From Equation (3.6), the error propagates to Equation (3.7). It was determined that the uncertainty from using centerline temperature rise over mean temperature rise is negligible compared to the RMS deviation of the thermocouples.

$$\begin{aligned} \xi_{\dot{m}} &= \sqrt{\left(\frac{d\dot{m}}{dT_i}\right)^2 {\sigma_{Ti}}^2 + \left(\frac{d\dot{m}}{dT_o}\right)^2 {\sigma_{To}}^2} \\ &= \sqrt{\left(\frac{Q}{c_p}\frac{1}{(T_o - T_i)^2}\right)^2 0.58^2 + \left(\frac{Q}{c_p}\frac{1}{(T_o - T_i)^2}\right)^2 0.58^2}. \end{aligned} \tag{3.7}$$

The ultrasonic flowmeter uncertainty was set to 3%, the error of the Optiflux electromagnetic flowmeter it was calibrated with. The three jets evaluated in the preliminary test have identical geometry and heating, meaning the flow rate for each jet should be equal. When the test facility is under full operation, the jet flow rates vary depending on the location of the pipe due to mixing and other phenomena, however under partial operation there is insufficient mixing to inhibit flow. To evaluate the accuracy of the jets having matching flow rates, the velocity vectors at a jet outlet generated by PIV analysis were averaged and then multiplied with area and density to calculate flow rate; this was performed for all three jets. The uncertainty for the flow rates calculated from the PIV data is the standard deviation of these three jet flow rates. This assumes axisymmetric behavior for the jet; the accuracy of this assumption is a limitation for the present study. The uncertainty of the PIV system will be calculated with a different method. All uncertainties are shown in Table 3.1. The flow rates for all three methods (Analytic flow rate using Equation (3.6), Ultrasonic flowmeter, and PIV) match closely for Tests 1 and 2. The uncertainties for Test 3 do not overlap, which was shown to be irregular from the sensitivity test and thus cannot be validated to be representative of the flow.

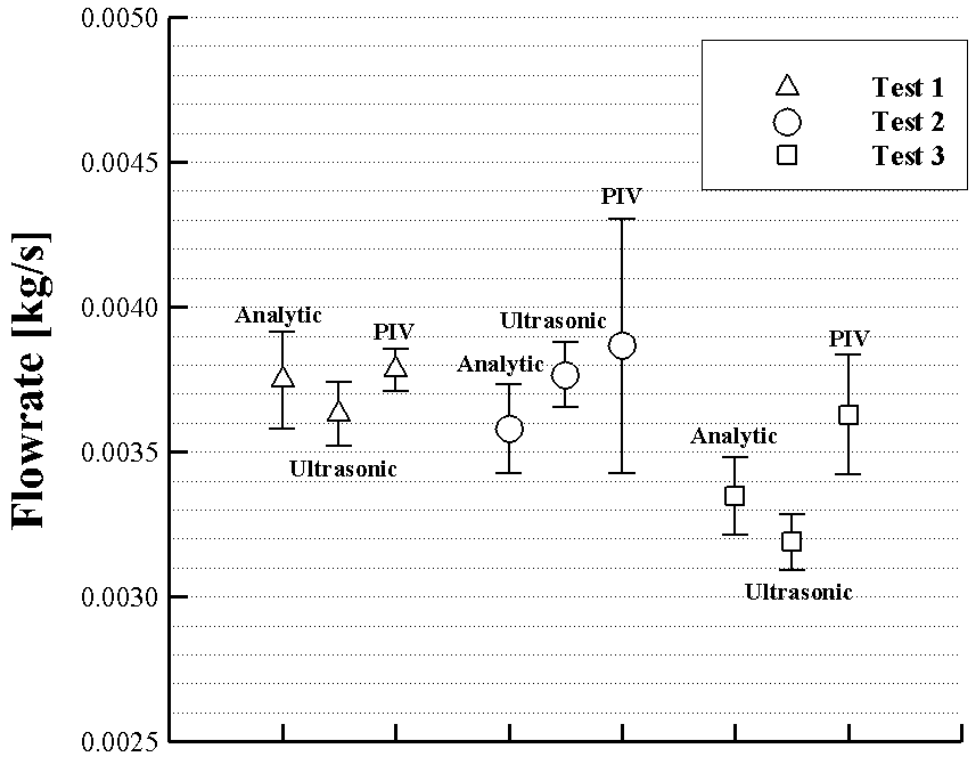

Figure 3.18. Flow rate for a single pipe with different methods.

Table 3.1. Flow rate uncertainties.

	Analytic	Ultrasonic	PIV
Test 1	1.679E-04	1.089E-04	7.166E-05
Test 2	1.534E-04	1.130E-04	4.383E-04
Test 3	1.340E-04	9.565E-05	2.060E-04

The Visualization Society of Japan (VSJ) proposed a guideline for performing an uncertainty analysis for a PIV system. The present uncertainty analysis was developed based on the VSJ recommendation [24]. Similar approach was performed in the works of Domiguez-Ontiveros and Hassan [25]. Four sources of uncertainty parameters were considered; the magnification factor (α), the displacement of particle image (ΔX), the time interval of successive images (Δt), and the experiment uncertainty factor (δu). The summary of PIV uncertainties are shown in Table 3.2, and the combined uncertainty was calculated using the Root-sum-square of the product of standard uncertainty and sensitivity coefficient. The largest uncertainty source in the present study is the mis-matching error between pair particle images and this can be significantly reduced by the improvement of PIV data processing.

Table 3.2. Summary of PIV system uncertainties from VSJ method.

Category	Error sources	Standard uncertainty	Sensitivity coefficient	Combined uncertainty
Calibration α (mm/px)	Reference image	7.00E-01 px	1.87E-04 mm/px^2	6.92E-04 mm/px
	Physical distance	2.00E-02 mm	1.44E-03 1/px	
	Image distortion by lens	3.48E+00 px	1.87E-04 mm/px^2	
	Image distortion by CCD	5.60E-03 px	1.44E-03 mm/px^2	
	Reference position	5.00E-01 mm	2.28E-04 1/px	
	Parallel board	3.50E-02 rad	4.55E-03 mm/px	
Acquisition ΔX (px)	Laser power fluctuation	7.10E-03 mm	7.69E+00 px/mm	2.10E-01 px
	Image distortion by CCD	5.60E-03 px	1.00E+00	
	Normal view angle	3.50E-02 rad	4.55E-03 mm/px	
Reduction ΔX (px)	Mis-matching error	2.00E-01 px	1.00E+00	
	Sub-pixel analysis	3.00E-02 px	1.00E+00	
Acquisition Δt (s)	Delay generator	1.00E-08 s	1.00E+00	1.41E-08 s
	Pulse time	1.00E-08 s	1.00E+00	
Experiment δu (mm/s)	Particle trajectory	5.00E-02 mm/s	1.00E+00	5.44E-02 mm/s
	3-D effects	2.15E-02 mm/s	1.00E+00	

3.4 CFD Validation

For CFD validation, Star-CCM+ 9.02 version was used to compare the PIV experiment results. Two different Reynolds-averaged Navier-Stokes (RANS) equation turbulent models were used as follows: k-ε model and Reynolds stress model. Segregated and coupled solvers were tested for the purpose of convergence efficiency. Tetrahedral and polyhedral meshes were used for mesh generation. Physical properties applied to the model were steady state condition, three dimensional, gravity, two-layer all y+ wall treatment, and constant density. Initial and boundary conditions such as temperature and velocity properties were imposed based on PIV experiment results. Water properties were referenced by NIST Chemistry WebBook [30]. Two cases are compared with the PIV results. The first and second case are k-ε model and Reynolds stress model. Two cases are set to identify the necessity of more complex turbulent models for this particular physical problem.

Results from Figure 3.19 show that at 3 cm from the pipe outlet, the most plausible turbulent model is Reynolds Stress model. The result indicates that the k-ε model is not suitable for the significant mean streamline curvature, flows with strong swirl or secondary flows [31]. Therefore the Reynolds Stress model would be better suited for calculating this type of flows. However, neither of those result show superior outcomes, unsteady calculations or Large-eddy simulation would be needed to fully validate the experiment result.

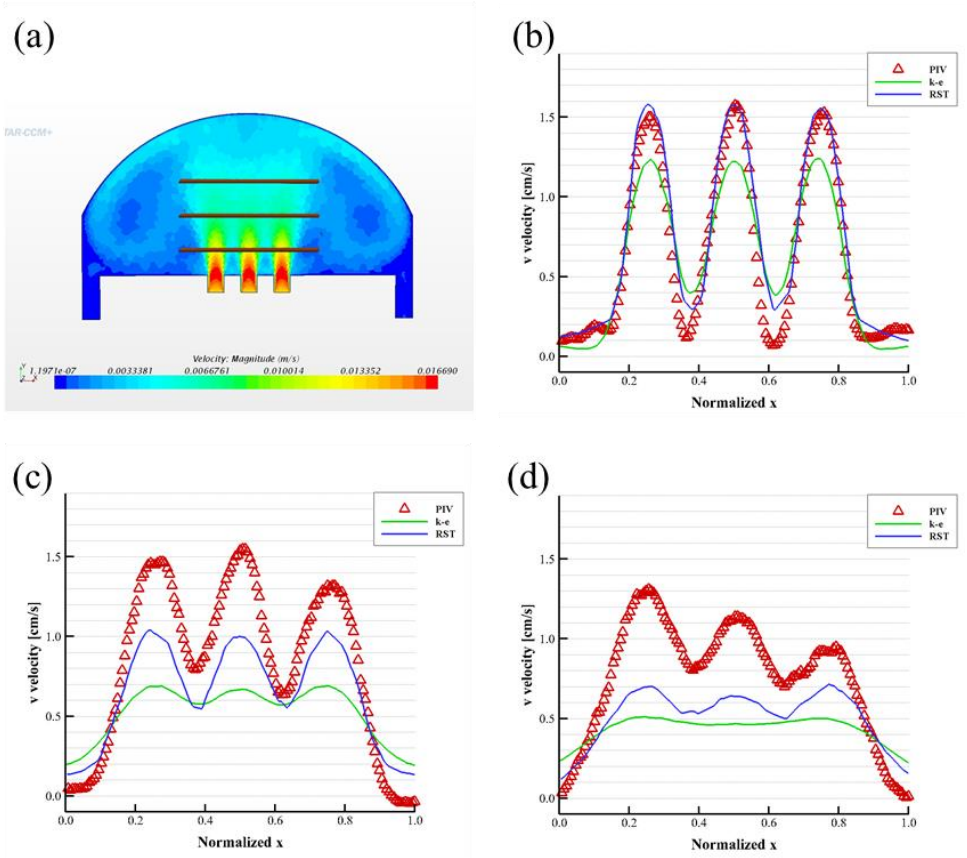

Figure 3.19. PIV and CFD comparison at different vertical location (a) each vertical location for the line extraction from the pipe outlet at, (b) 3 cm, (c) 7 cm, and (d) 11 cm for four cases.

3.5 Summary

A 1/16th scaled VHTR experimental model was constructed and the preliminary test was performed in this study. To produce benchmark data for CFD validation, the facility was first run at partial operation with five pipes being heated. PIV was performed to extract the vector velocity field for three adjacent naturally convective jets at statistically steady state. A small recirculation zone was found between the pipes, and the jets entered the merging zone at 3 cm from the pipe outlet but diverged as the flow approached the top of the test geometry. Turbulence analysis shows the turbulence intensity peaked at 41−45% as the jets mixed. A sensitivity analysis confirmed that 1,000 frames were sufficient to measure statistically steady state. The results were then validated by extracting the flow rate from the PIV jet velocity profile, and comparing it with an analytic flow rate and ultrasonic flowmeter; all flow rates lie within the uncertainty of the other two methods for Tests 1 and 2. This test facility can be used for further analysis of naturally convective mixing, and eventually produce benchmark data for CFD validation for the VHTR during a PCC or DCC accident scenario.

In the next section, additional experimental and computational results will be reported. First, experiments from a single plume to multiple plumes will be performed to better understand the turbulent mixing and thermal stresses in the upper plenum. Temperature measurement technique is also accompanied by a simultaneous measurement of the instantaneous velocity profile. Concurrently, different turbulent models with multiple initial conditions will be considered to obtain better results of turbulent

calculations. For example, turbulent viscosity is not obtained from the PIV experiment so a better prediction of these properties should lead to a significant improvement in the CFD results. Comparing the PIV, PLIF, and CFD results will provide a substantial understanding of the natural circulation during PCC and DCC events and will be used for benchmark data for assessment and improvement of codes proposed for NGNP design and safety studies [32].

4. EXPERIMENT MODIFICATION

After the preliminary tests, the experiment facility was shut down and dissembled to repair the water leak and enhance the performance of the PIV experiment. There were several problems encountered during the preliminary tests as follows:

1. Internal water leakage caused the malfunction of other groups of heating tapes.
2. The individual control towers were needed to manipulate the each heated pipes.
3. Light coming from the outside of the test section produced reflections that needed to be blocked completely.
4. The fluorescent orange particles for PIV experiments are expensive and the amount of particles increased as we subsequently incorporated more numbers of heated pipes.

The first issue was solved by installing the waterproof shrink tubing between the connection of the heating tapes and extension wires. Figure 4.1 shows the previous wire burned out and the current connection wires. The orange-colored shrink tubing has a high temperature sustainability. For the second issue, two additional variable transformers and seven of six-outlet on/off surge protectors were installed as shown in Figure 4.2. Therefore, the contemporary test facility is capable of controlling each individual heating pipe line for the purpose of plume/jet experiment tests.

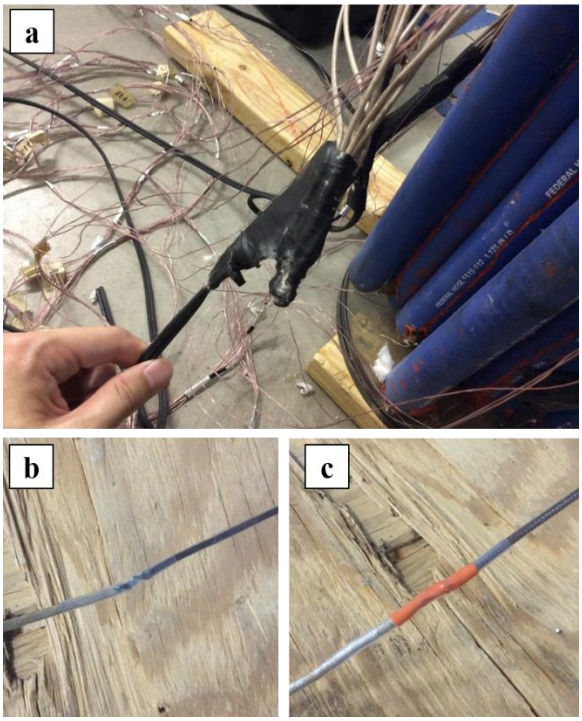

Figure 4.1. The procedure of the experiment modification for heating tapes and extension wires. (a) Damaged wires were burned due to a short circuit; as a result, heating tapes were disconnected. (b) A transparent shrink tubing was installed to protect each individual wire. (c) An orange high temperature shrink tubing was installed to enhance the thermal barrier to wire connections.

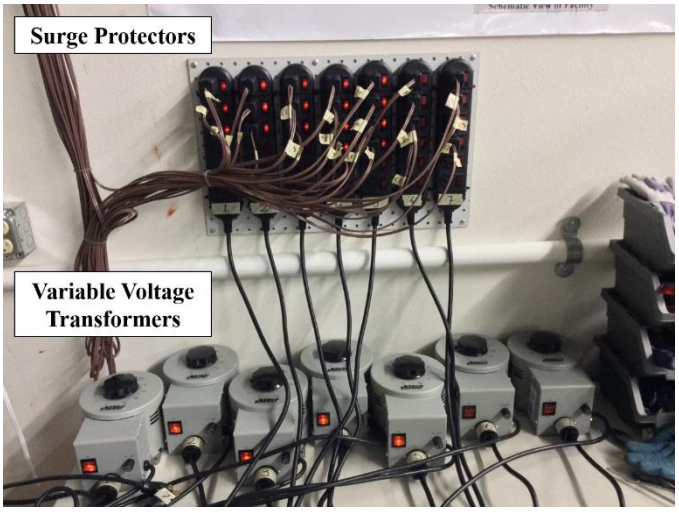

Figure 4.2. Surge protectors and variable voltage transformers.

Furthermore, the Unistrut curtain frames were constructed to effectively remove any lighting source coming from the outside as shown in Figure 4.3. The particle recycle system was constructed and installed next to the test facility. This system connects the facility drain pipeline, the sieve, and the water tank. The stainless steel sieve has an opening size of 44 μm (= 325 Mesh), which is sufficiently small compared to the particle size (53 - 63 μm) used for the PIV experiments. Figure 4.4 shows collected particles on top of the sieve after recycling. It is estimated about 70% of particles can be recycled with this system.

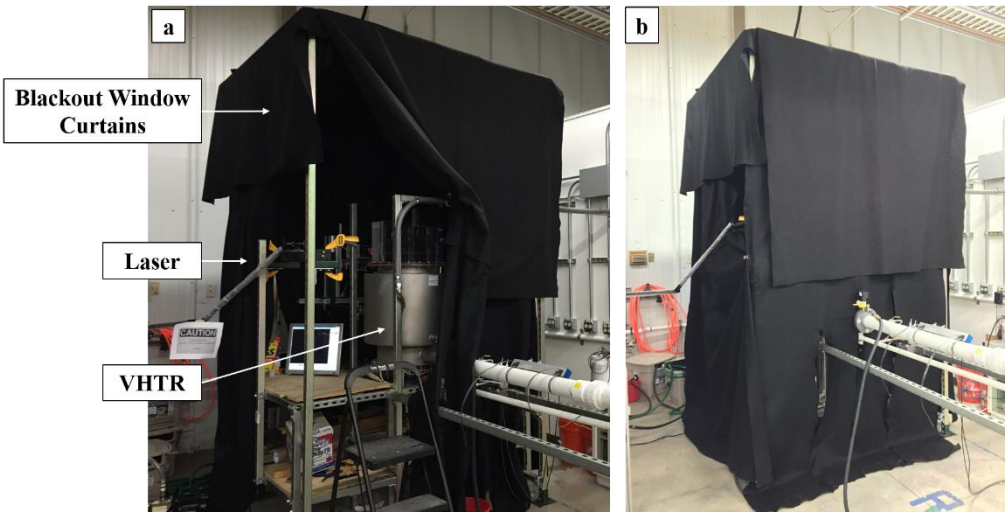

Figure 4.3. The blackout window curtains with the double pulse laser, high speed camera, and scaled VHTR when curtains were opened (a) and closed (b).

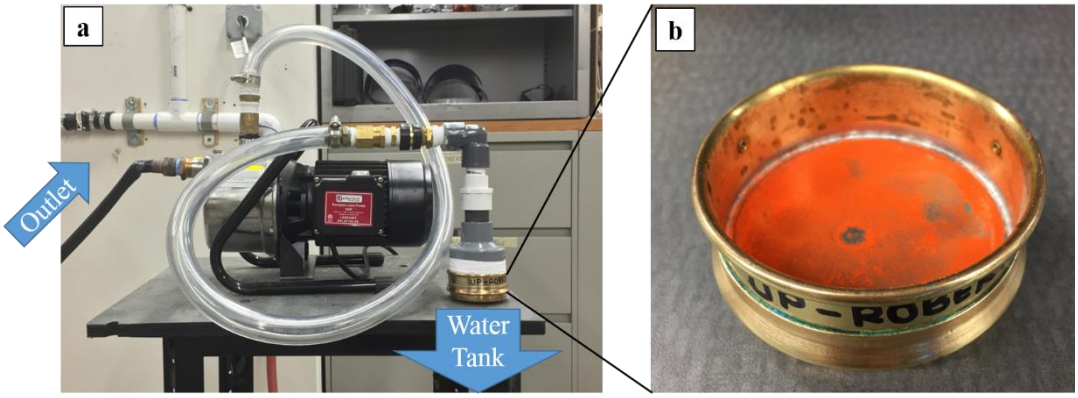

Figure 4.4. Fluorescent orange particle recycle system. (a) A pump was connected with an exit hose from the test facility and stainless steel sieve. (b) A zoom in view of the sieve after collecting particles.

In addition to the issues reported above, the new type of laser system, Nd:YAG laser system made by New Wave Research, including the cooling device, laser power supply, laser head, arm and pulse generator was utilized and is shown in Figure 4.5. It has dual laser-head system and provides a highly stable green light source for PIV application. The output energy has 15-200 mJ at 532 nm and the frequency varies from 1 to 15 Hz or continuous depending on the test purpose. A quantum Composer 9618+ delay pulse generator was used to control the delay period between the camera shutter speed and laser pulse.

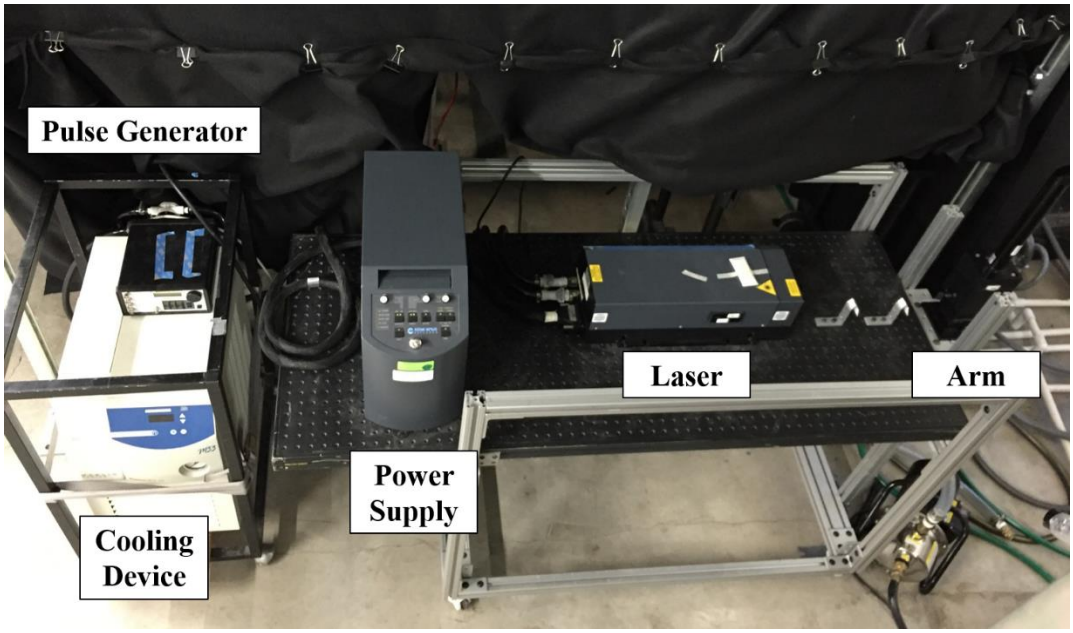

Figure 4.5. Overview of PIV laser system.

The flowmeter calibration data are listed in in Table 4.1 and 4.2 and the calibration curve is shown in Figure 4.6. The same method was used as in Section 3 and at this time two upwards and one downward calibrations were delivered to have hysteresis. A calibration curve fit very well with R^2 value of 0.9992 and this calibration equation was used for the last portion of the analysis for every flowmeter dataset.

Table 4.1. A comparison of flowmeter calibrations between a magnetic (denoted Magnetic) and floating (denoted Floating) flowmeter. They were compared for the initial flowrate calibration.

Targeted										
Magnetic [GPH]	30	60	90	120	150	180	210	240	270	300
Floating [GPM]	0.5	1	1.5	2	2.5	3	3.5	4	4.5	5
Measured										
Magnetic [GPH]	30.4	60	90.1	120	150	180	210	240	270	300
Magnetic [GPM]	0.51	1.00	1.50	2.00	2.50	3.00	3.50	4.00	4.50	5.00
Floating [GPM]	0.51	0.98	1.45	1.92	2.41	2.89	3.42	3.81	4.32	4.79
Error [%]	0.66	2.00	3.44	4.00	3.66	3.61	2.29	4.75	4.00	4.26

Table 4.2. A comparison of flowmeter calibrations between a magnetic and ultrasonic flowmeter. To check hysteresis both upward, i.e., increasing flowrate, and downward, i.e., decreasing flowrate, were performed.

Unit [GPM]	Upward calibration													
Target	0.33	0.50	0.67	0.83	1.00	1.17	1.33	1.50	1.67	1.83	2.00	2.17	2.33	2.50
Magnetic flowmeter	0.34	0.50	0.66	0.83	1.00	1.16	1.33	1.50	1.67	1.84	2.00	2.17	2.34	2.50
Ultrasonic flowmeter	0.41	0.61	0.80	0.98	1.18	1.33	1.50	1.67	1.85	2.03	2.19	2.38	2.55	2.71
Error	22.63%	21.47%	21.21%	17.29%	17.84%	14.26%	13.01%	11.21%	10.75%	10.82%	9.62%	9.98%	9.26%	8.59%
Unit [GPM]	Downward calibration													
Target	0.33	0.50	0.67	0.83	1.00	1.17	1.33	1.50	1.67	1.83	2.00	2.17	2.33	2.50
Magnetic flowmeter	0.34	0.50	0.67	0.84	1.00	1.17	1.33	1.50	1.67	1.84	2.00	2.17	2.33	2.50
Ultrasonic flowmeter	0.41	0.59	0.81	1.02	1.17	1.35	1.51	1.71	1.88	2.04	2.24	2.39	2.58	2.73
Error	21.55%	16.99%	22.50%	22.40%	17.38%	15.32%	13.55%	13.80%	12.84%	11.00%	11.95%	10.07%	10.62%	9.31%
Unit [GPM]	Upward calibration													
Target	0.33	0.50	0.67	0.83	1.00	1.17	1.33	1.50	1.67	1.83	2.00	2.17	2.33	2.50
Magnetic flowmeter	0.33	0.50	0.67	0.83	1.00	1.17	1.34	1.50	1.67	1.83	2.00	2.17	2.33	2.50
Ultrasonic flowmeter	0.45	0.60	0.80	0.97	1.18	1.37	1.52	1.70	1.89	2.04	2.24	2.40	2.58	2.74
Error	34.48%	20.40%	20.89%	17.19%	17.36%	17.05%	13.78%	13.22%	13.48%	11.34%	11.88%	10.63%	10.37%	9.59%

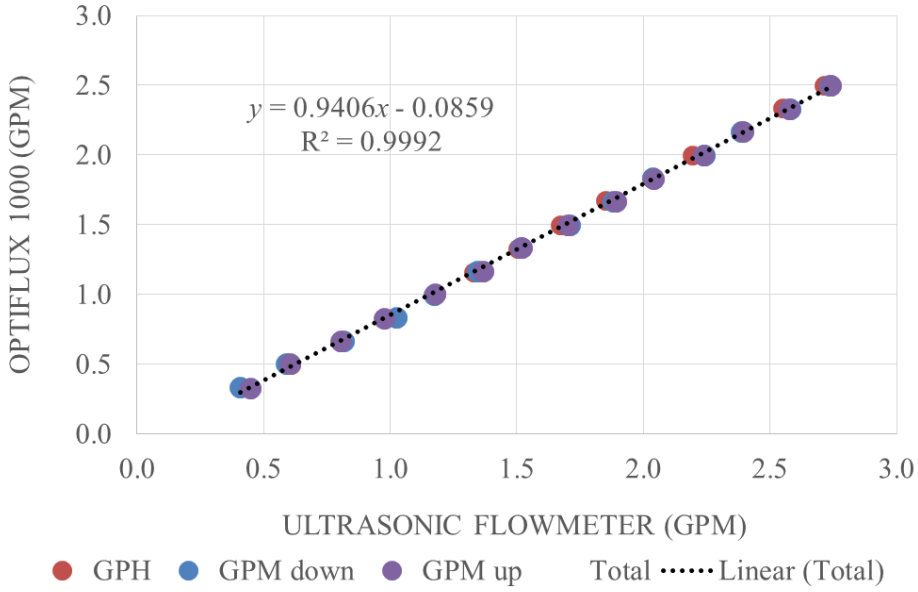

Figure 4.6. A comparison of flowmeter calibrations between a magnetic and ultrasonic flowmeter with corresponding calibration curve.

5. A SINGLE BUOYANT JET STUDY

In this section, the study focuses on a very simple basic geometry, boundary and initial condition: i.e., a single buoyant jet experiment. The results from a single buoyant jet experiment are superior and fundamental to the experiments with multiple jets and are, therefore, employed as a starting point for the subsequent experiments. Also there are literature on numerical and experimental studies that analyze a single buoyant jet, thus it is the best standard for validating the other test conditions for multiple jets. However, the significance of this study differs from the other studies due to the range of test conditions and geometry. In the present experiment, the same setup for the PIV preliminary test with one exception to the laser system mentioned in the previous section is used. The sensitivity analysis provides valid information for the pre-processing work that should be confirmed before analyzing the statistics. In the experiment result section, the statistically steady state results provide the significance of this experiment and the importance of this study.

The present test condition is to simulate the natural circulation phase of the DCC event during a LOFC accident scenario without air ingress. During the DCC event, a rapid depressurization of the primary coolant and scram are initialed with the passive RCCS operational and without air ingress [8]. The decay heat from the core creates the relative high temperature distribution inside the core. When the temperature difference is sufficient to generate buoyancy force, the natural circulation phase begins. During this phase the flow reverses, i.e. flows from the outlet plenum pipe to the core region, enters the upper plenum region, traverses down the channels on the core barrel, and exits through the pipe

[33]. In this section a situation where only one coolant channel is opened and a single buoyant jet is created from the heated pipe channel is investigated. Several analytical tools are used to understand the physics of a single buoyant jet and this analysis will assist in understanding much more complex turbulent jet mixing in the upper plenum of the scaled VHTR.

5.1 Turbulent Vertical Buoyant Jet

Turbulent jets and plumes are classified as free shear flows. Free shear flows are inhomogeneous flow and remote from the solid body**.** The appearance of both jets and plumes are similar and they share similar characteristics in terms of turbulent motion: mixing with the ambient fluid is efficient; kinetic energy is lost to turbulence; momentum is conserved; and velocity and width of the jet/plume are functions of distance from the source. However, their fundamental mechanism is different. A jet is a flow driven by momentum of the source whereas a plume is driven by buoyancy of the source. Also, in the jet, mixing is directly related to the inertia of the turbulent eddies where in the plume, the buoyancy force produced the inertia, which leads to mixing [34]. If the mechanism is a combination of both momentum and buoyancy, it is called a buoyant jet or forced plume.

The present test condition is classified in a round turbulent vertical buoyant jet. The center line pipe is heated by a uniform heat flux and produces vertical natural convection which leads to vertical flow motion inside the pipe. However, the study is limited to the downstream of the pipe outlet because the physical information inside the

heated pipe such as the boundary layer development and velocity or temperature distribution are not accessible due to the limitation of the test material (stainless steel) and geometry.

Turbulent plumes and jets are studied in many field of studies. In civil engineering, the discharge of waste such as the disposal of wastewater via ocean outfalls is the common interest [35-37]. Geological volcanic fissure eruption on Earth [38] generally forms turbulent buoyant plumes and jets. In nuclear engineering, when the reactor is shut down and the natural circulation is the only driving force, the decay heat from the core vessel creates the turbulent plumes and jets in both pressurized and depressurized loss-of-forced circulation accidents .

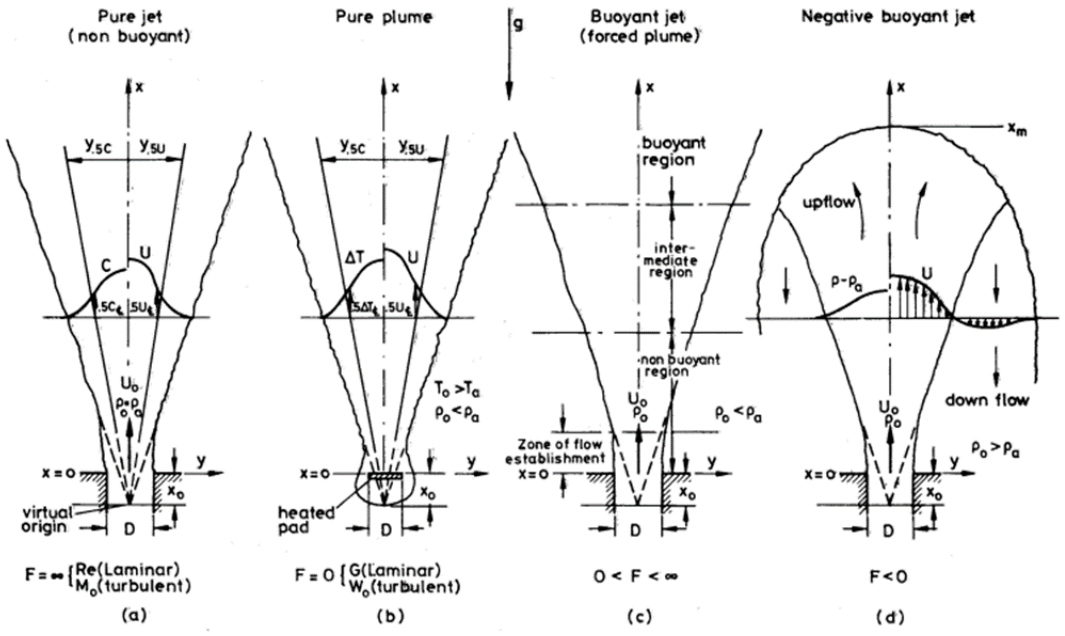

Figure 5.1. Buoyant jets in uniform surroundings [39].

Chen et al. [39], one of the pioneers of turbulent buoyant jet study, classified four types of the buoyant jets in terms of source densimetric Froude number (Fr) as shown in Figure 5.1: pure jet, pure plume, buoyant jet (forced plume) and negative buoyant jet. Here the densimetric Froude number, which represents the ratio of inertial forces to buoyancy forces, is defined as

$$\mathrm{Fr} = \frac{w_0}{\sqrt{\left(\frac{\Delta\rho_0}{\rho_a}\right) gD}}, \tag{5.1}$$

where w_0 is the velocity at the source, $\Delta\rho_0 = |\rho_0 - \rho_a|$ is the density difference between the source fluid and the ambient fluid, ρ_a is the ambient density, and D is the size of the source (note: in his paper $\mathrm{Fr}^2 = \mathrm{F}$). When the density of the discharge is the same as the environment the buoyancy forces are absent, it is a pure jet (a). When no initial momentum is generated and a heat source creates the buoyancy force to drive the flow, it is a pure plume (b). In a buoyant jet (forced plume), relatively lower density of fluid is discharged with the initial momentum (c). When the density of discharging fluid is higher than the environment, it is a negative buoyant jet (d). In the current test condition, the higher temperature fluid which is heated inside the pipe, i.e. lower density fluid, is discharged through a nozzle, and therefore, it is classified as buoyant jets or forced plumes.

The cylindrical coordinate system is chosen for the round buoyant jet as shown in Figure 5.2. The axial direction and axial velocity with the origin at the center of the round nozzle exit are represented by z and w respectively while those with radial directions are denoted by r and u, respectively. The ambient temperature is denoted by T_a. The

fluctuating velocities are denoted by the apostrophe (′); for example, the fluctuating axial velocity is denoted by w'. The averaged velocities are denoted by the angled bracket < > and determined by time averaging. Therefore, the instantaneous velocities (~) are composed of mean and fluctuating components by using Reynolds decomposition

$$\tilde{v}_i = v_i + v_i', \tag{5.2}$$

where v is the tensor notation (i = 1, 2, 3). Therefore each of the cylindrical component can be written as follows:

$$\begin{aligned}
&\text{Radial Component}\left(r\right) && : \ \tilde{u} = u + u' \\
&\text{Axial Component}\left(z\right) && : \ \tilde{w} = w + w' \\
&\text{Azimuthal Component}\left(\theta\right) && : \ \tilde{v}_\theta = v_\theta + v_\theta' \\
&\text{Temperature} && : \ \tilde{T} = T + T' \\
&\text{Concentration} && : \ \tilde{c} = c + c' \\
&\text{Reduced gravity} && : \ \tilde{g}' = g' + g''
\end{aligned} \tag{5.3}$$

where the reduced gravity, the buoyancy force per unit mass of the jet/plume fluid $g'\left(r,z\right) = g\left(\rho_0 - \rho_a\right)/\rho_a$, has the same profile as the concentration of any tracer [39].

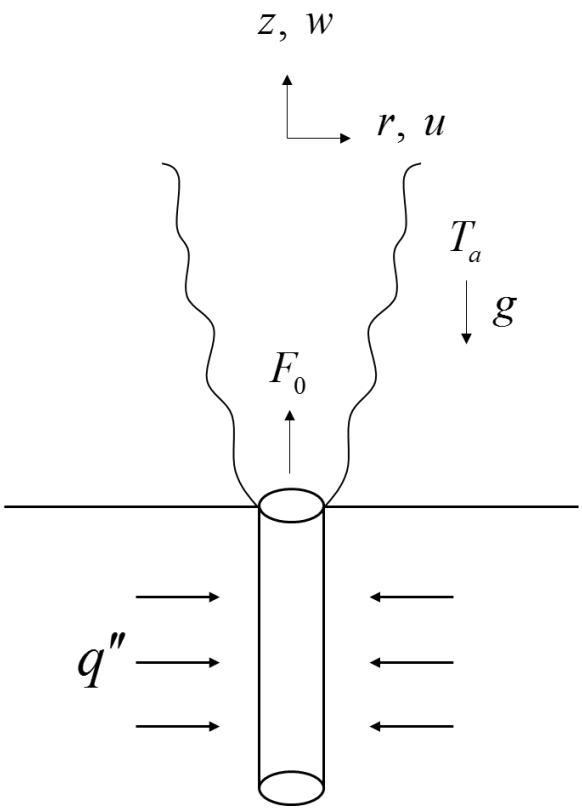

Figure 5.2. A cylindrical coordinate system and nomenclature.

The governing equations for mass, momentum and buoyancy with the Boussinesq approximation and negligible viscous effects are given by

$$\frac{1}{r}\frac{\partial(ru)}{\partial r}+\frac{\partial w}{\partial z}=0, \tag{5.4}$$

$$u\frac{\partial w}{\partial r}+w\frac{\partial w}{\partial z}=-\frac{1}{r}\frac{\partial}{\partial r}\left(r\left\langle u'w'\right\rangle\right)-\frac{\partial}{\partial z}\left(\left\langle w'^{2}\right\rangle-\left\langle u'^{2}\right\rangle\right)+g\beta\Delta T, \tag{5.5}$$

$$u\frac{\partial g'}{\partial r}+w\frac{\partial g'}{\partial z}=-\frac{1}{r}\frac{\partial}{\partial r}\left(r\left\langle u'g'\right\rangle\right)-\frac{\partial}{\partial z}\left(\left\langle w'g'\right\rangle\right), \tag{5.6}$$

where β is the thermal expansion coefficient, ΔT is the temperature difference between ambient temperature $\Delta T = T - T_a$ and g is the gravitational acceleration. The concentration

c can be replaced by the reduced gravity g' in Equation (5.6) that yields the advection-diffusion equation. Note that assumptions are made according to the analysis done by Hussein et al. [40] where the term $\partial\langle u'^2\rangle/\partial z$ in Equation (5.5) is obtained from the axial pressure gradient $(-1/\rho)(\partial P/\partial z)$ by integrating the radial momentum equation.

Studies on the vertical axisymmetric jet/plume show that the profiles of axial velocity and reduced gravity can be well described by Gaussian functions at distances $z/D > 5$ where D is the nozzle diameter [41] as follows:

$$w(r,z) = w_c(z)\exp\left\{\frac{-r^2}{b^2(z)}\right\}, \tag{5.7}$$

$$g'(r,z) = g'_c(z)\exp\left\{\frac{-r^2}{\lambda^2 b^2(z)}\right\}, \tag{5.8}$$

where the subscript c represents the mean vertical centerline location so that $w_c(r,z) = w(0,z)$, b is the jet width where the velocity is equal to $1/e$ of the centerline value and λ is the ratio between the diffusion of mass and momentum. Note that the jet width b is a function of z-direction.

One pioneering analysis for turbulent buoyant plumes and jets was reported by Morton et al. [42] where they introduced mean fluxes of volume Q, specific momentum M and specific buoyancy B defined as

$$\begin{aligned} Q(z) &= 2\pi\int_0^\infty w(r,z)\,r\,dr, \\ M(z) &= 2\pi\int_0^\infty w^2(r,z)\,r\,dr, \\ B(z) &= 2\pi\int_0^\infty w(r,z)\,g'(r,z)\,r\,dr. \end{aligned} \tag{5.9}$$

A Morton length scale is defined as Equation (5.10).

$$l_M = \frac{(M_0)^{\frac{3}{4}}}{(B_0)^{\frac{1}{2}}}. \tag{5.10}$$

The Morton length scale (l_M) provides the criteria of the contribution of jets and plumes. The research done by Papanicolaou and List [43] showed that when $z/l_s < 1$ the buoyant jet behaves like a jet due to the initial momentum while when $z/l_s > 5$ it behaves like a plume due to the loss of momentum.

Previously, most research is limited to unbounded jets and flat surface impingement [44-46]. In addition the Morton length scale is limited to free shear flows and the assumption of Gaussian distribution is only made by far field region. Therefore, the objectives of the present section is to study the behavior of bounded buoyant jet and the impingement of the dome surface to investigate whether the flow is preserved as self-similar. Additionally, the current investigation will help in understanding the turbulent eddy structures in a single buoyant jet and identify the mechanism of these vortical interactions.

5.2 Scaling of Mixing of Jet Flows entering the Upper Plenum

The objective of the current study is to understand the flow behavior of the upper plenum during DCC event. The flow into the upper plenum is more complicated than a single buoyant jet and involves multiple intersecting jets and the interactions of the jets with surrounding components. According to Peterson [47], the divergence angle of a single buoyant jet is 20° and is independent of Reynolds number. Therefore, scaling of jet intersection and jet co-mixing solely depend on geometry. Through the geometric scaling analysis performed in Section 2, the pitch to diameter ratio (P/D_{Hole}) for both full-scale and model was estimated 2.03 so the geometry, i.e. the turbulent jet mixing phenomena, for full-scale jets and model jets are well scaled (Figure 5.3). The one significant trade-off of this approach is that the ratio of jet diameter (D_{Hole}) divided by upper plenum radius ($D_{CID}/2$) is larger than the prototypical value, which will reduce the amount of mixing in the fluid that reaches the upper plenum boundary.

Jet Reynolds number should be sufficiently large that a turbulent buoyant jet is ensured. According to Tritton [48], the critical Reynolds number based on the jet diameter (Re_D) should be larger than a few 10's. In general, jets that are laminar within the confined channel, in our case heated pipes, are turbulent when they become free. The Coanda effect, the tendency of a fluid jet to stay attached to a convex surface, will increase the divergence angle between closely spaced jets and draw jets to nearby walls. The Coanda effect is caused by fluid entrainment into the jet lowering the local pressure in the volume from

which the fluid is entrained. If jet entrainment is well scaled, then jet divergence angles should also be well scaled.

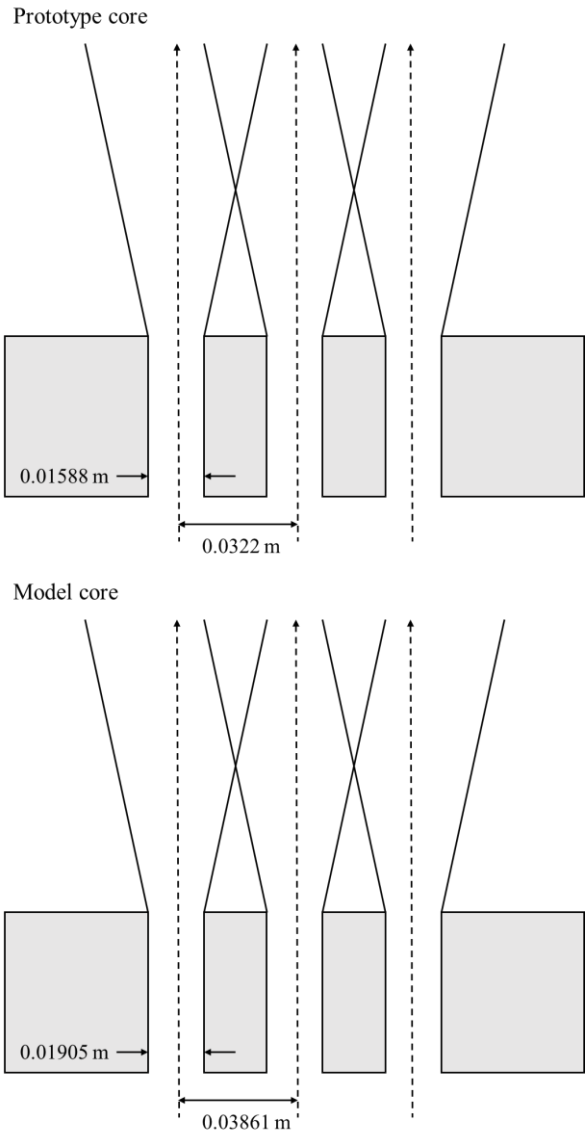

Figure 5.3. Turbulent buoyant jet mixing.

5.3 Experiment Method

A 1/16th scaled VHTR test facility is developed for the turbulent buoyant jet experiment. The test facility with instruments are shown in Figure 5.4 to 5.6 and the schematics of the field of view (FOV) and the region of interest (ROI) are shown in Figure 5.7. Two thermocouples are located at 1 inch below/above the heating pipe's inlet/outlet, which are named in c1t (center group-1-top) and c1b (center group-1-bottom) respectively. Also four thermocouples are located at the system inlet/outlet, i.e. the inflow/outflow pipe line from the water reservoir, and cooling jacket inlet/outlet to monitor the steady state temperature for the system and estimate the rate of heat transfer on the heat sink.

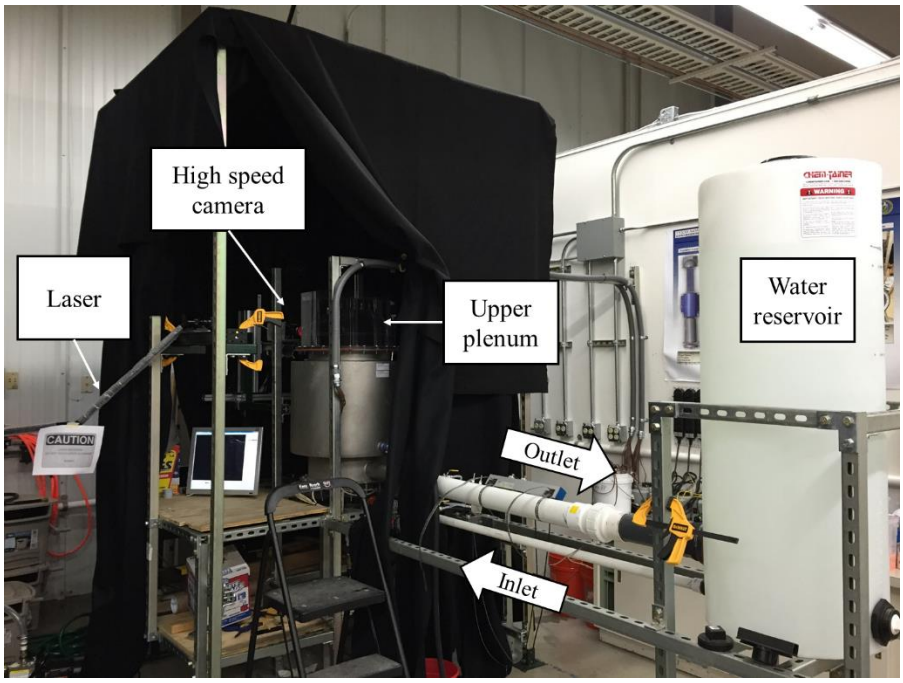

Figure 5.4. Components of the experiment test facility: 1/16th scaled VHTR with the upper plenum, the PIV laser system with the high speed camera, the system inlet/outlet pipe lines and the water reservoir.

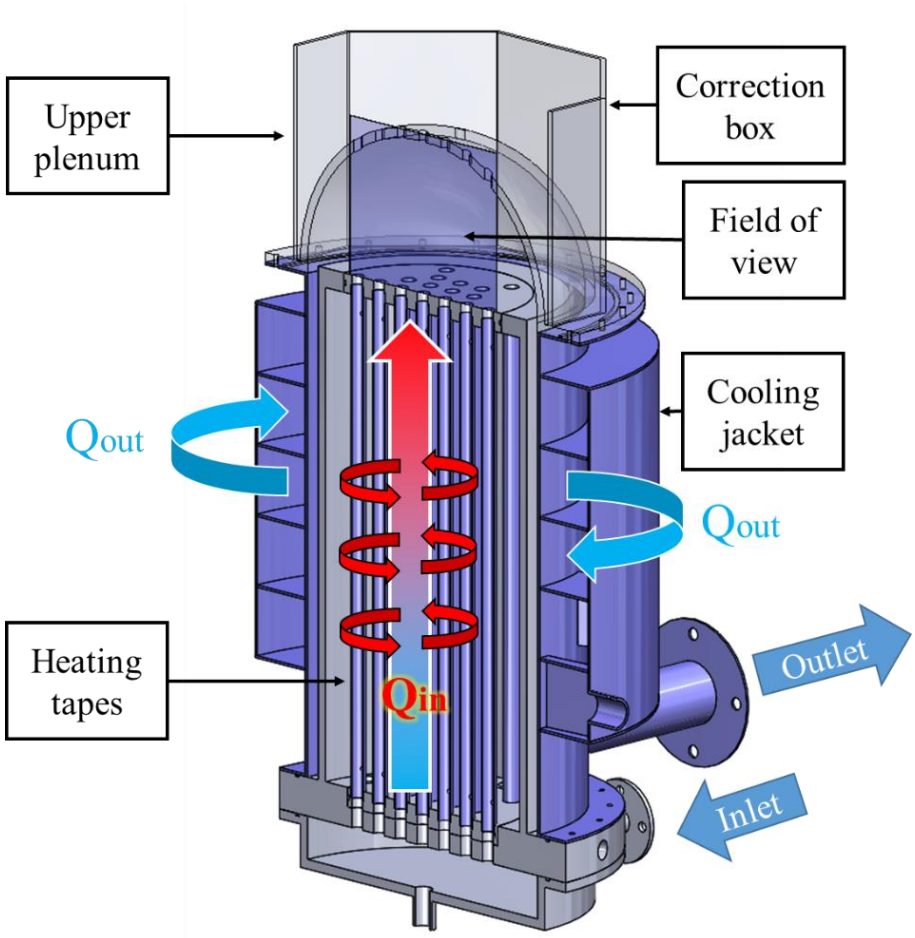

Figure 5.5. VHTR test cross section view.

Two optical filters, a polarizer and orange bandpass filter, are used in the PIV laser/camera system as shown in Figure 5.6. A polarizer is placed in a plane perpendicular to the camera and FOV to remove reflections, i.e. undefined or mixed polarization into a beam. An orange bandpass filter is used to remove the background image from the FOV to ease post-processing as shown in Figure 5.8.

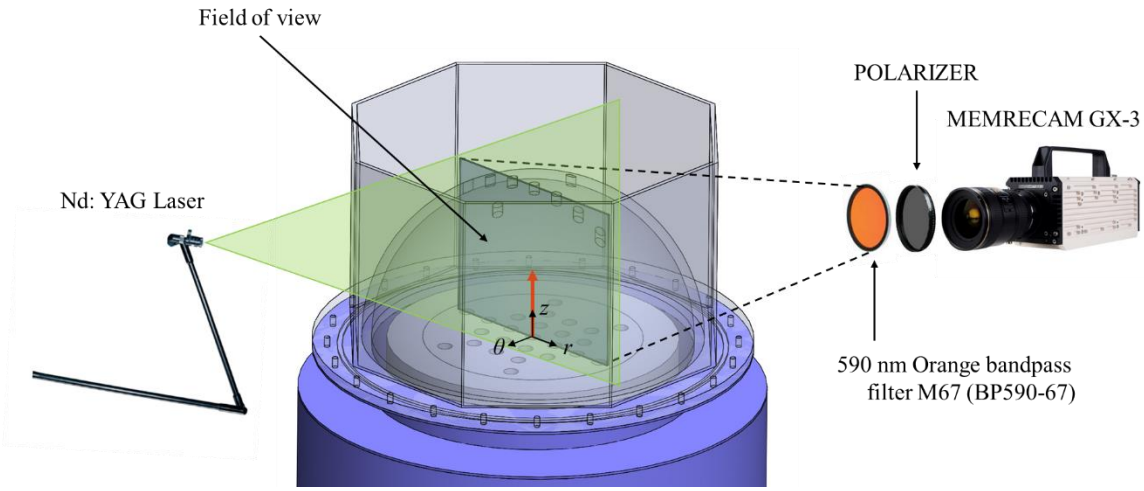

Figure 5.6. Schematic of PIV laser and camera system. The origin of a cylindrical coordinate system is located at the center of the pipe outlet.

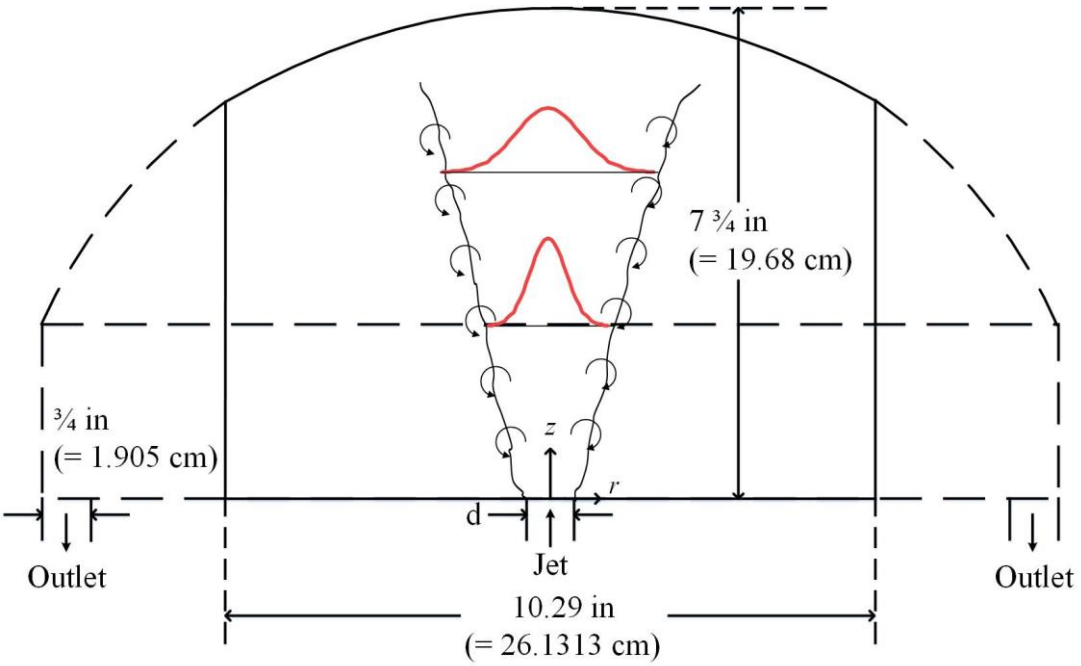

Figure 5.7. Schematics of the test section (solid and dotted line) and region of interest (solid line).

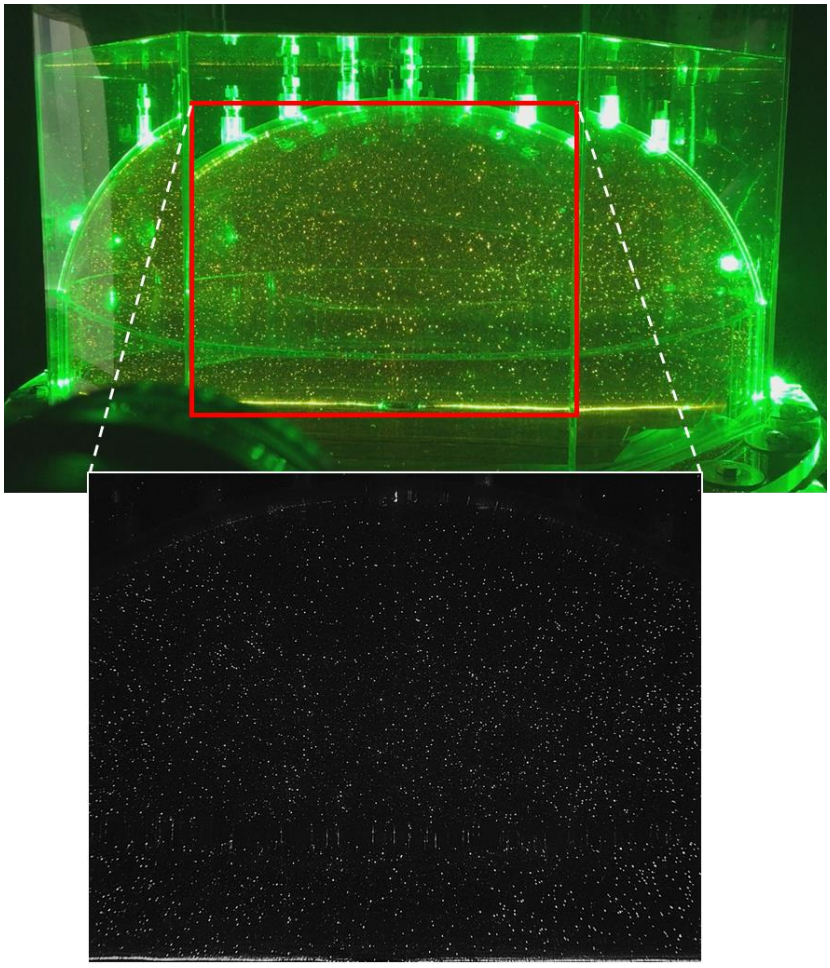

Figure 5.8. Real time experiment image (top) with the green laser sheet and orange fluorescent particles and filtered image (bottom) after the polarizer and orange bandpass filter in the field of view (red box). The color of orange fluorescent particles is orange (top) and white (bottom).

A size of ROI is close to FOV since the only difference is the dome shape on the top edge of the FOV, which is removed during post-processing. The FOV, shown in Figure 5.9 red line, is chosen to capture up the outlet flow behavior of up to five pipes for further study. The restriction is made due to the curvature of the correction box, which do not allow for an extended the view to the maximum number of jets.

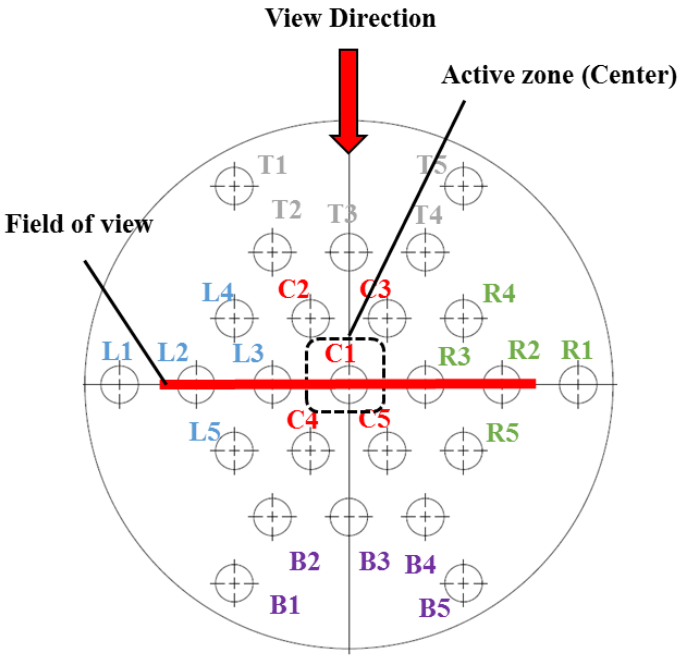

Figure 5.9. Pipe layout, test section and a center pipe (C1) plan view.

A flow visualization method for the experiment is the same as the preliminary experiment: the PIV method. The only difference is the laser system; a Nd:YAG laser system made by New Wave Research. Table 5.1 shows the list of the experiment setup used for the single buoyant jet study and Table 5.2 shows its PIV settings for the analysis. Similar to the preliminary test, PIVlab, the MATLAB software, version 1.41 is used for PIV analysis.

Table 5.1. PIV camera and laser test conditions.

Application	Turbulent buoyant jet
Flow geometry	Parallel to light sheet
Field of view	264.3 × 211.5 mm^2
Region of interest	261.3 × 196.8 (curved) mm^2
Observation Distance	y_0 = 0.645 m
Recording method	Single frame / double exposure (Δt = 100 ms)
Recording lens	f = 50 mm, $f_\#$ = 2
Recording medium	Carl Zeiss Makro-Planar T* 2/50 ZF.2
Ambiguity removal	Polarizer / 590 nm orange bandpass filter M67 (BP590-67)
Illumination	Nd:YAG laser 15 mJ/pulse at 532 nm
Pulse delay	Continuous
Seeding material	Polyethylene microsphere (d_p = 53 - 63 μm, ρ_P = 1002 kg/m^3)
Seeding type	Fluorescent orange
Camera resolution	1280 x 1024 pixel

Table 5.2. PIV computation settings.

Evaluation method	Fully digital evolution, cross correlation
Peak finding	2x3 point Gaussian fit
Size of interrogation area	64 x 64, 32 x 32, 16 x 16 pixel
Size of FFT	64 x 64, 32 x 32, 16 x 16 pixel
Grid distance	32 x 32, 16 x 16, 8 x 8 pixel
Overlap of interrogation area	50%

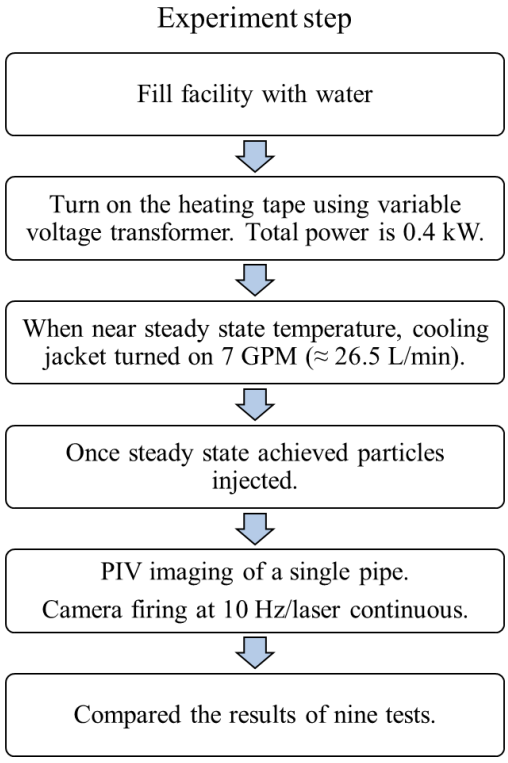

Figure 5.10. Experiment test procedure for PIV.

Nine tests are performed and compared for a single buoyant jet study; they follow the same experiment steps as shown in Figure 5.10. The maximum power of 0.4 kW is applied for the variable voltage transformer. The power is sufficient for flow to become turbulent when it exits from the pipe outlet. The cooling jacket is turned on to 7 GPM when the system is close to the steady state temperature to cool down the reactor vessel. The steady state temperature is achieved when the difference of the system inlet/outlet temperature reaches ± 0.5 °C, which is the accuracy of the thermocouple.

A number of dimensionless numbers have been used to comprehend the physical interpretation of the present test condition which is shown in Table 5.3. The definition of each dimensionless number is in Equation (5.11) to (5.14),

$$\mathrm{Re} = \frac{w_0 D}{\nu_0}, \tag{5.11}$$

$$\mathrm{Gr} = \frac{g\beta\left(T_0 - T_\infty\right)D^3}{\nu_0^2}, \tag{5.12}$$

$$\mathrm{Ri} = \frac{g\beta\left(T_0 - T_\infty\right)D}{w_0^2} = \frac{\mathrm{Gr}}{\mathrm{Re}^2}, \tag{5.13}$$

$$\mathrm{Ra} = \frac{g\beta\left(T_0 - T_\infty\right)D^3}{\nu_0 \alpha} = \mathrm{Gr} \cdot \mathrm{Pr}, \tag{5.14}$$

where w_0 is the nozzle top-hat velocity (i.e. assuming constant velocity distribution across the jet), D is the nozzle diameter, ν_0 is the viscosity at the nozzle, T_0 is the temperature at the nozzle, T_∞ is the ambient temperature, β is the thermal expansion coefficient at the nozzle temperature and α is the thermal diffusivity at the nozzle.

The Re is sufficiently large to generate turbulent jets. The Grashof number (Gr) measures the ratio of the buoyancy to viscous forcing acting on a fluid. The Gr is not enough to induce the transition to turbulent flow for natural convection from the coolant pipe. However, when the flow exits from the nozzle, high entrainment of the fluid from the ambient flow enhances the turbulence in the flow. The Richardson number (Ri) measures the ratio of buoyant to inertial forces. The Ri is the criteria to determine whether the flow is governed by either natural or forced convection. Typically when Ri < 0.1 the natural convection is negligible and when Ri > 10 forced convection is negligible. However, like the present test condition where 0.1 < Ri < 10, neither of them is negligible. Both mechanisms are important in the present study and corresponds to the range of Fr. The Rayleigh number (Ra) is a product of Gr and Pr. The Ra measures the heat transfer

mechanism, either conduction or convection, associated with buoyancy driven flow. When the Ra is less than 10^8 the flow is laminar and when the Ra is high than 10^{10}, the flow is fully turbulent. Again the Ra is not sufficient for the beginning of turbulence in natural convection in the vertical channel flow; nevertheless the Re ensures the jet becomes turbulent.

Table 5.3. Dimensionless numbers of the present test condition

Dimensionless number	Acronym	Value (Average)
Reynolds number	Re	227 - 450 (351)
Grashof number	Gr	$1.3 – 2.73 (2.04) \times 10^5$
Richardson number	Ri	1.35 – 2.52 (1.66)
Rayleigh number	Ra	$0.79 - 1.55 (1.19) \times 10^6$
Densimetric Froude number	Fr	0.57-1.01 (0.81)

5.4 PIV Data Validation

PIV data is obtained through the cross-correlation of successive images from interrogation windows. A PIV method is a very effective optical technique of flow visualization and has a broad range of application due to its ease of use. Unlike laser Doppler velocimetry and hot-wire anemometry, the PIV method is both a non-intrusive and field measurement technique so it is suitable for the present natural circulation study. The typical experimental setup for a PIV system is composed of a laser, a high-speed camera, seeding particles and a synchronizer. The specification of these setup is listed in Table 5.1 and 5.2. However, the validity of PIV results cannot be guaranteed unless thorough understanding of the PIV method is guaranteed. Therefore, the test results were validated with multiple steps as follows: 1. Physical and technical examination; 2. Image pre-processing; 3. Image evaluation; 4. Post-processing; and 5. Sensitivity analysis. Each step is sequentially time order. Physical and technical examination should be delivered in advance to experimental tests. Image pre-processing is a prerequisite just before the analysis. Image evaluation is sole methodology of the PIV cross-correlation. Post-processing removes the erroneous vectors from data sets. A sensitivity analysis uses a statistical approach to evaluate the mathematical method for the PIV system.

Physical and technical examination which involves predetermination quantities for the PIV settings include the selection of tracer particles, laser setup and camera setup. First of all, a primary source of error is the gravitational force due to the density difference between the fluid ρ_f and the tracer particles ρ_p. Raffel et al. [49] introduced the velocity

lag of a particle in analogy to Stokes' drag law to estimate the particle's behavior as follows:

$$U_s = U_p - U = d_p^2 \frac{\left(\rho_p - \rho_f\right)}{18\mu} a = \tau_s a, \tag{5.15}$$

where U_p is the particle velocity U is the fluid velocity, a is the acceleration of the particle, μ is the dynamic viscosity of the fluid, d_p is the diameter of the particle and τ_s is the relaxation time constant. Since the density difference between the fluid (water) and the particle is minimal the time constant is estimated 0.86 μs based on the average temperature of the pipe inlet and outlet (22.48 °C). Note that this should be pre-estimated in advance to the test so that the rough estimation is made from the beginning. In addition, the Stokes number (St) provides the effect of inertia on the motion of particles in a fluid flow, for example, if St << 1 the tracer particles faithfully follow the fluid motion. It is defined as

$$\mathrm{St} = \frac{\tau_v}{\tau_\eta} = \frac{1}{18}\left(\frac{\rho_p}{\rho_f}\right)\left(\frac{d_p}{\eta}\right)^2, \tag{5.16}$$

where τ_v is the particle viscous relaxation time, $\tau_\eta = \left(\nu/\varepsilon\right)^{1/2}$ is the Kolmogorov time scale and $\eta = \left(\nu^3/\varepsilon\right)^{1/4}$ is the Kolmogorov length scale [28]. When the integral length scale L is estimated the by the diameter of the nozzle (0.01905 m) and the standard deviation of velocity v_{std} (0.01239 m/s) is obtained from the test result, St is estimated 2.04×10^{-3}, which is substantially small so the errors due to tracer particles can be negligible (Table 5.4). Additionally, the exposure time of the measurement is 100 ms and is close to the Kolmogorov time scale so most of velocities were measured instantaneously.

Table 5.4. Experiment parameters.

v_{rms} (mm/s)	L (mm)	ε (m^2/s^3)	η (μm)	τ_η (ms)	Δx (μm/px)
12.39	19.05	0.0001	303	97	206

Laser and camera setups have another important components that cause high influence on the accuracy of the PIV system. As they are listed in Table 5.1 and 5.2, a continuous Nd:YAG laser and high speed camera are used for the setup. When tracer particles are first detected by the camera lens, the size of the particles can be distorted and altered due to many reasons. The two main reasons are light scattering behavior due to the laser and distortion of images due to a circular camera lens [49]. The characteristics of light scattered by tracer particles is in fact beneficial to the PIV analysis since the detection of the location of tracer particles becomes easier (see Figure 5.11). According to the Mie's theory, the normalized diameter, q, can be defied by:

$$q = \frac{\pi d_p}{\lambda}, \tag{5.17}$$

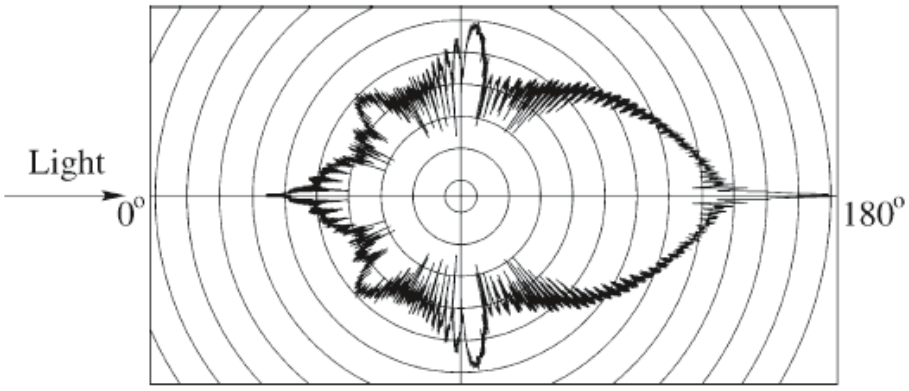

Figure 5.11. Light scattering by a 30 μm glass particle in water at λ = 532 nm [49].

where λ is a wavelength of the incident light (532nm). The present test condition has q = 3.43×10^2 indicating that approximately 343 local maxima q appear over the range from 0° to 180°. Hence, this condition is advantageous to record tracer particles. To check the image distortion caused by the camera lens, a convectional dotted plate which is spaced each 1 inch location is inserted to the upper plenum test section filled with water. Images were taken from the camera setup that is exactly the same as the test condition and test the alignment of straight lines by connecting the dotted points (see Figure 5.12). The duplicated image location can be removed as it shows in red lines (top). As a result, no distortion is observed and every line was achieved as a straight line.

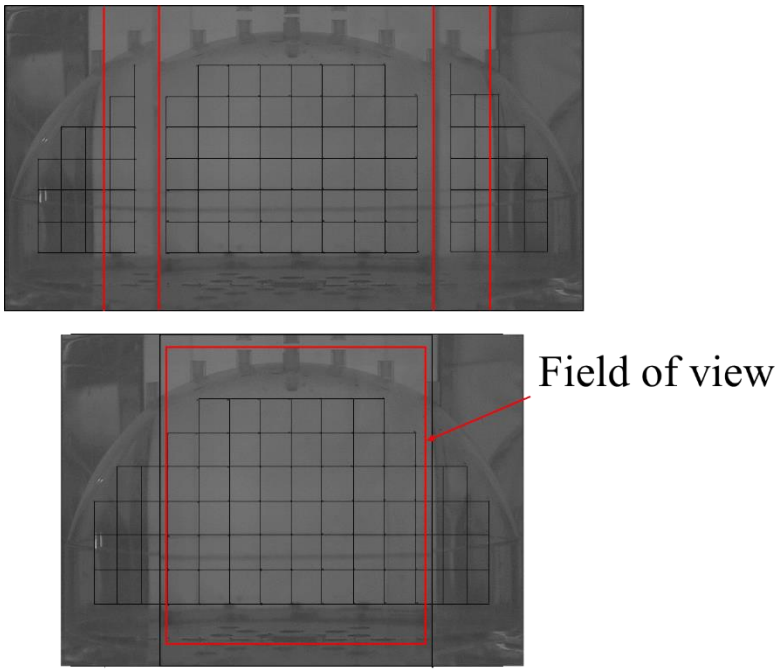

Figure 5.12. PIV image and camera calibration. Dotted points were connected to draw the lines to check the distortion. Red borders (top) represent duplicated images due to the shape of the correction box which were removed and corrected with post-processing (bottom).

The size of FOV is determined based on the purpose of the study and the size of interrogation window. Essentially, the study focuses on the behavior of a single buoyant jet, the size of FOV should cover the most of jet physics from the start of the jet (inlet) to the impingement on the top surface (dome). The size of interrogation window is chosen to have 16 × 16 px as it is recommended from many authors [49-51] so the target size of FOV is listed in Table 5.5. The estimated value is not deviated from the actual test results that the maximum velocity magnitude was obtained 0.0157 m/s so the size of FOV is allocated for the test.

Table 5.5. FOV setup based on the high speed camera.

#	Variable	Value (approx.)	Value (real)	Unit	Equation
	Size of interrogation window	16		px	
	Maximum particle displacement	8		px	
	Scattered light from each particle	2 - 4		px	
a	Assumed maximum velocity	0.016	0.0156	m/s	
b	Target pixel displacement	8		px	
c	High speed camera shutter speed	10		Hz	
d	Assumed maximum velocity in px	80		px/s	b*c
e	Maximum velocity distance	0.0016		m	a/c
f	Real distance in pixel size	0.0002		m/px	e/b
g	Target horizontal distance	0.2560	0.2643	m	f*1280
h	Target vertical distance	0.2048	0.2115	m	f*1024

Next, image pre-processing is performed to enhance the image quality. There are several options to enhance the PIV images in PIVlab. Contrast limited adaptive histogram equalization (CLAHE) is one of them and is first introduced in medical imaging by Pizer et al. [52]. CLAHE increases the possibility of detecting particles in the images by 4.7 ± 3.2 %. CHAHE is used for averaging PIV data and ensemble-averaged experiments data and is set 20 pixels for the window size as an optimized value. The other two methods are high-pass and intensity capping techniques. These techniques are used to enhance detecting the valid velocity vectors in the transient particle motions, i.e. to capture unsteady phenomena (see Figure 5.13). Enabling 15 pixel filter size for high-pass is employed as it produces higher particle detection rates and intensity capping was turned on. Detail explanations of these image pre-processing is well explained in Thielicke's dissertation [53].

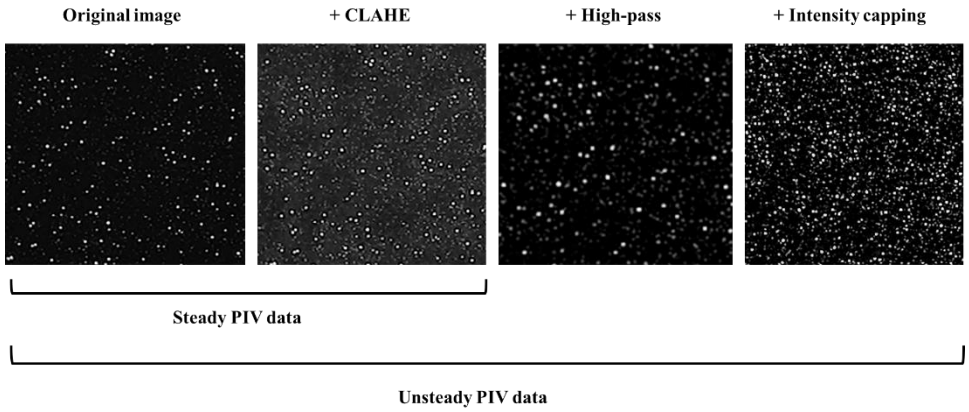

Figure 5.13. The effect of image pre-processing functions in PIVlab.

Afterward, image evaluation is followed. At this point the actual PIV analysis with the cross-correlation is performed. The cross-correlation determines the possible particle displacements within the interrogation windows by using statistical approaches. To implant into a computer algorism, the equation should be discretized. The discrete cross-correlation function *c* is evaluated [54]:

$$c(m,n) = \sum_{i,j} A(i,j)B(i-m, j-n), \tag{5.18}$$

where A and B are corresponding interrogation windows from image A and B. *m* and *n* are the shift locations in horizontal and vertical directions. Two common approaches to solve this equation are direct cross-correlation (DCC) [55] and discrete Fourier transform (DFT) [56]. In essence, the difference of two methods is the size of the interrogation windows from image B. DCC uses two different interrogation windows to yield the correlation matrix in the spatial domain whereas DFT uses identical interrogation window size [22] in the frequency domain. The drawback of DCC is the computational cost. The present study selects to use DFT approach since number of images are large (3,000) so it

needs fast calculations. The drawback of DFT is when the displacement of particles is larger than half the size of the interrogation window, the correlation peak appears on the opposite side [49]. Therefore the displacement of the particles should be smaller than the half the size of the interrogation window [53] as calculated in Table 5.5.

Post-processing includes calibration and vector validation technique. In order to calibrate the pixels to physical domain, the calibration images must be taken in prior to each test as shown in Figure 5.14. The RMS error for calibrating horizontally and vertically is minimal so all calibrations are done by this vertical line calibration methods. For validating vectors, three methods are used: standard deviation filter, median filter and data interpolation. Standard deviation filter removes any erroneous vectors in eight neighborhood within the threshold limits (n) and is defined as

$$t_{upper,lower} = \overline{v} \pm n \times \sigma_V , \tag{5.19}$$

where $t_{upper,lower}$ is the lower and upper thresholds, $\overline{v}$ is mean velocity and σ_V is standard deviation of $\overline{v}$. It is noted that n is set to be 5 for all tests since it gives the most reliable vector limits in our system. In addition the local median filter is used to improve the quality of the velocity validation by evaluating the median in a neighborhood around the center vector [53]. The optimum threshold and epsilon (ε) for the median test are found 4 and 0.1, respectively as Westerweel et al. recommend [57]. The PIV data is further tested with a sensitivity analysis to insure the averaged quantities are statistically converged.

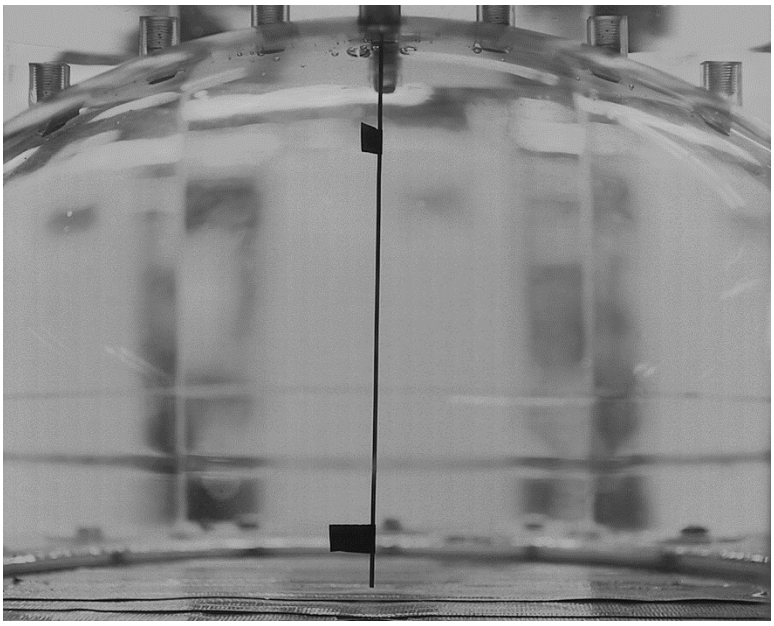

Figure 5.14. Calibration image for Test 1. The distance between two black flags were measured 5 inches (= 127 mm).

5.5 Sensitivity Analysis

The objective of performing the sensitivity analysis is following; first of all, to confirm the validity (robustness) of the PIV steady state result. In other words, in order to obtain a time-independent result, certain number of images have to be averaged but depending on the order of the statistics (e.g. mean velocity, mean vorticity, second-order statistics, third-order moments) this may be changed. Therefore, the adequate amount of temporal PIV data should be estimated in terms of the order of the statistics. Secondly, residual analysis is performed in a various type of residual definitions. Throughout this residual analysis the most suitable residual definition is identified and used for the later study.

Four different residual definitions are proposed. Recall the residual definition in Equation (3.3) and re-define this as the root-mean-square deviation (RMSD). Three residual definitions are derived from Equation (5.20)

$$\mathrm{RMSD} = \sqrt{\frac{\sum_{i,j=1}^{n}\left(v_{i,j}^{k} - v_{i,j}^{k-1}\right)^{2}}{N}}, \tag{3.3}$$

$$\mathrm{NRMSD} = \frac{\mathrm{RMSD}}{\mathrm{norm}(i)}, \tag{5.20}$$

where $i = \{1,\ 2,\ 3\}$. The value norm (1) is representing RMSD residual without normalization, norm (2) is normalized by the maximum value of v denoted by $\mathrm{NRMSD}_{\max}$ (normalized root-mean-square deviation) residual and norm (3) is normalized by the mean

value of v also denoted by $NRMSD_{mean}$. The fourth definition is a relative residual and is defined as following:

$$\text{Relative residual} = \left| \frac{mean\left(v_{i,j}^{k} - v_{i,j}^{k-1}\right)}{mean\left(v_{i,j}^{k-1}\right)} \right|. \tag{5.21}$$

Note that v in here can be either radial velocity (u), axial velocity (w) or vorticity (ω). Every residual definition shows an exponentially decreasing trend for every test results (see Figure 5.15). To test individual definitions, the result from Test 8 is plotted in Figure 5.16. The most robust residual definition is obtained in $NRMSD_{max}$ as axial velocity residual is the highest at all frames. This is to observe where the axial velocity (w) converges at last to have the strictest criteria for the turbulent buoyant jet. It is reasonable that radial velocity (u) and vorticity (ω) converge faster due to geometrical symmetry along the axis $r = 0$. The $NRMSD_{mean}$ residual does not show good definition criteria in our study because in the range of ROI, approximately 2/3 of velocity values were almost stationary (zeros) so when averaged it minimizes the residual values inhibiting to check the real system convergence. RMSD also shows good agreement with $NRMSD_{max}$ however it is better to have normalized quantities to facilitate the comparison between different datasets.

On the other hand, the relative residuals show the difference between current and previous approximate values. The differences peak at certain number of frames and exponentially decrease as a number of frames increases. Both relative u and ω residuals show irregular peaks before achieving averaged 2,000 frames while relative w residual is smoothly converged. Contrary to the conclusion in Section 3, 1,000 frames are not

sufficient to get statistically averaged data for a single jet due to lots of stationary vectors in ROI but at least 2,000 frames must be averaged. $NRMSD_{max}$ residual definition shows the best acceptable for our case and the convergence criteria value can be measured as 0.003 as shown in Figure 5.16 (b).

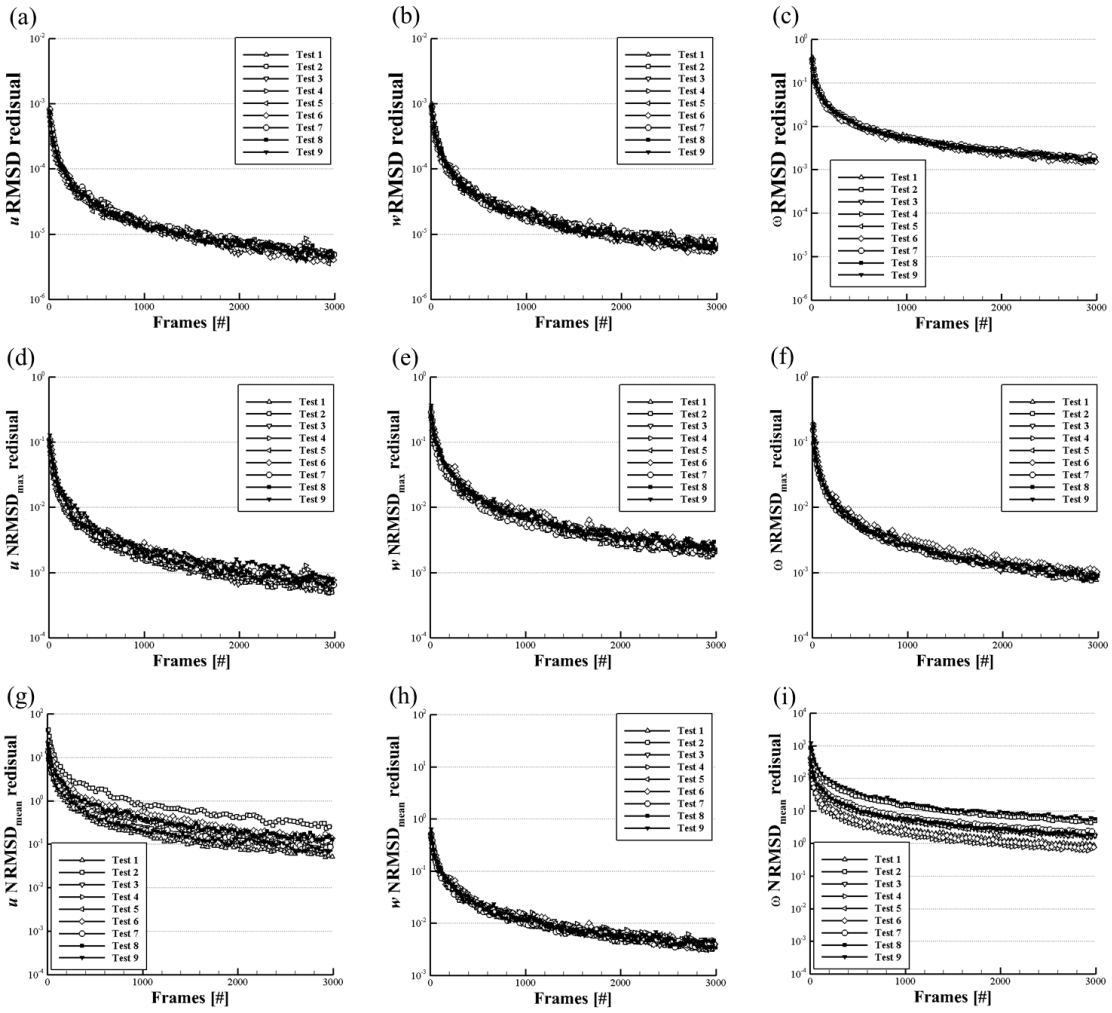

Figure 5.15. Results from different Residual definitions for nine tests with increasing number of frames. (a) to (c) are RMSD residual; (c) to (e) are $NRMSD_{max}$; and (g) to (i) are $NRMSD_{mean}$.

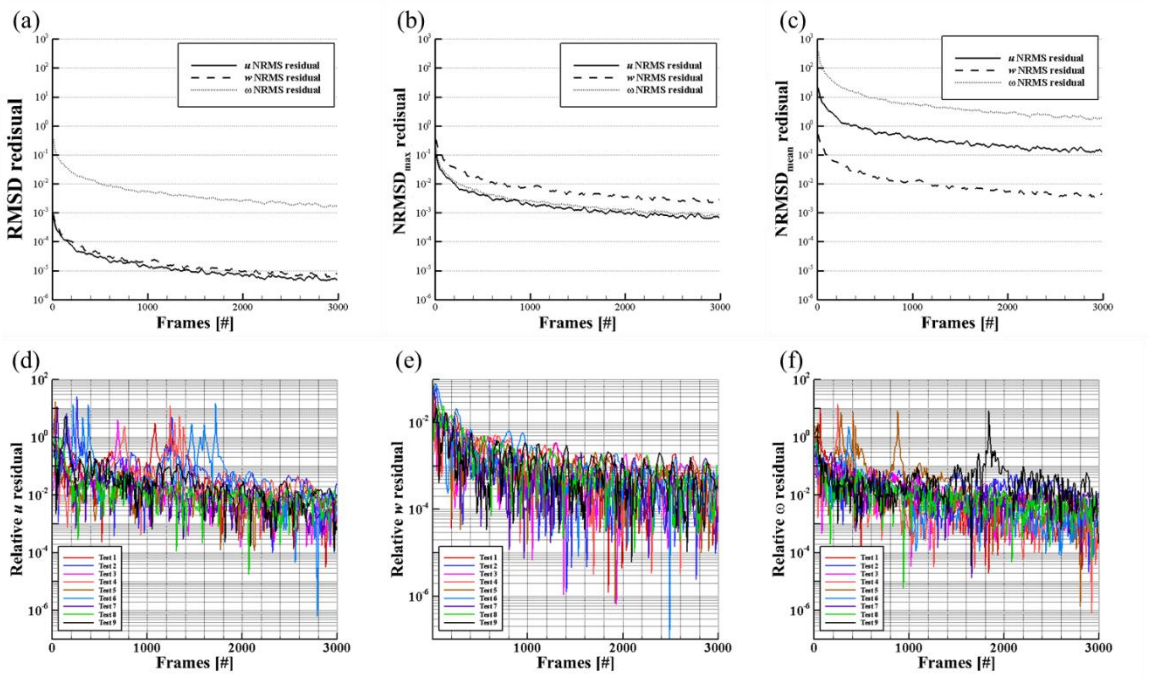

Figure 5.16. Residuals from three different definitions for Test 8 and relative residuals for nine tests results.

5.6 Experimental Results

Time-averaged profiles are achieved by averaging 3,000 PIV frames with 1-2, 2-3, 3-4 ⋯ image sequencing style. Since images are recorded by 10 Hz (= 100 ms), the total time for the steady state profiles are determined by Reynolds-averaging for 300 seconds (= 5 minutes). After obtaining time-averaged profiles, ensemble-averaged profiles are evaluated by averaging nine experiment test results. Figure 5.17 to 5.21 show ensemble-averaged profiles of Reynolds-averaged first-order, second-order, third-order, fourth-order statistics as well as turbulent kinetic energy (k) and turbulent intensity (TI). In addition, Figure 5.22 to 5.26 show their corresponding radial profiles and Figure 5.27 show the centerline axial velocity profile.

The radial velocity u shows that the maximum (-0.68 cm/s) and minimum (0.69 cm/s) values are obtained close to the dome surface at r = -6.06 cm and 6.10 cm, respectively and in time it is immediately after impinging to the highest point. Close to the jet inlet a symmetrical right-hand and left-hand side radial velocity are formed due to the Rayleigh-Taylor (RT) instability which occurs when relatively lighter fluid pushes the heavier fluid. At the beginning, the lighter fluid accumulates adjacent fluids until it reaches a sufficiently large volume to burst out of the fluid upward creating RT instability [58-61]. This instability of two different density fluids creates vorticity along the interface and entrains the heavier fluid toward the lighter fluid. This vorticity form a large toroidal vortex with a diameter approximately equal to the jet inlet narrowing the jet fluid and accelerates the flow below. The accumulation of these fluid and acceleration can be

observed from the temperature measured at the location 1 inch below the jet inlet as shown in Figure 5.28. The steep gradients of the *u* velocity indicates the existence of the jet boundary and entrainment of the ambient fluid. The entrainment of the fluid gradually weakens as the jet flows upward; however due to the vortex created by the dome shape additional counter directional fields are formed below the impingement region where *z* = 13 cm. The axial velocity *w* shows almost symmetrical distribution across the ROI where the maximum velocity (1.57 cm/s) was obtained at z_m = 12.51 cm as shown in Figure 5.27. The axial velocity is 2.28 times higher than the radial velocity. The mean velocity magnitude *V* is estimated by the square-root of the axial and radial velocity. Two big counter-rotating vortices are observed from the streamline plot. These vortical structures are important for the study of a single jet so a detail description of the turbulent structures will be discussed in the later section. The maximum and minimum vorticity were obtained near the wall at the location where (*r*, *z*) = (-6, 19) and (6.79, 18.95) (*r*/*D* = 3.15 ~ 3.56), respectively.

In order to calculate the turbulent kinetic energy budget, the triple correlation should be estimated. Thus in a single jet study, the second, third and fourth moments are calculated and results are shown in Figure 5.18 to 5.20 and Figure 5.23 to 5.25. It is noted that the axial and radial direction Reynolds stresses have a ratio of 2:1.

The standard deviations of the radial and axial velocity are maximized near the jet inlet because the high volume of fluid are entrained and the toroidal vortex increases the velocity magnitude. Assuming axisymmetric condition $\langle u'^2 \rangle = \langle v_\theta'^2 \rangle$, turbulent kinetic energy, turbulent viscosity and turbulent intensities are defined as follows:

$$k = \frac{1}{2}\left(\left\langle u'^2 \right\rangle + \left\langle w'^2 \right\rangle + \left\langle v_\theta'^2 \right\rangle\right) = \frac{1}{2}\left(2 \times \left\langle u'^2 \right\rangle + \left\langle w'^2 \right\rangle\right), \tag{5.22}$$

$$\nu_t = \frac{\left\langle u'w' \right\rangle}{-\frac{\partial \left\langle w \right\rangle}{\partial r}}, \tag{5.23}$$

$$TI_u = \frac{u_{std}}{u},\ TI_w = \frac{w_{std}}{w}, \tag{5.24}$$

where u_{std} and w_{std} are the root-mean-square (RMS) or standard deviation of the turbulent velocity fluctuations (u' and u'). *TI* goes extremely high values toward the jet boundaries although the Reynolds stresses <$u'u'$> and <$w'w'$> decay along the vertical direction. The turbulent viscosity near the jet boundary is always positive and independent of the radial direction since $\partial \left\langle w \right\rangle / \partial r$ is negative where the Reynolds stress <$u'w'$> is positive and vice versa.

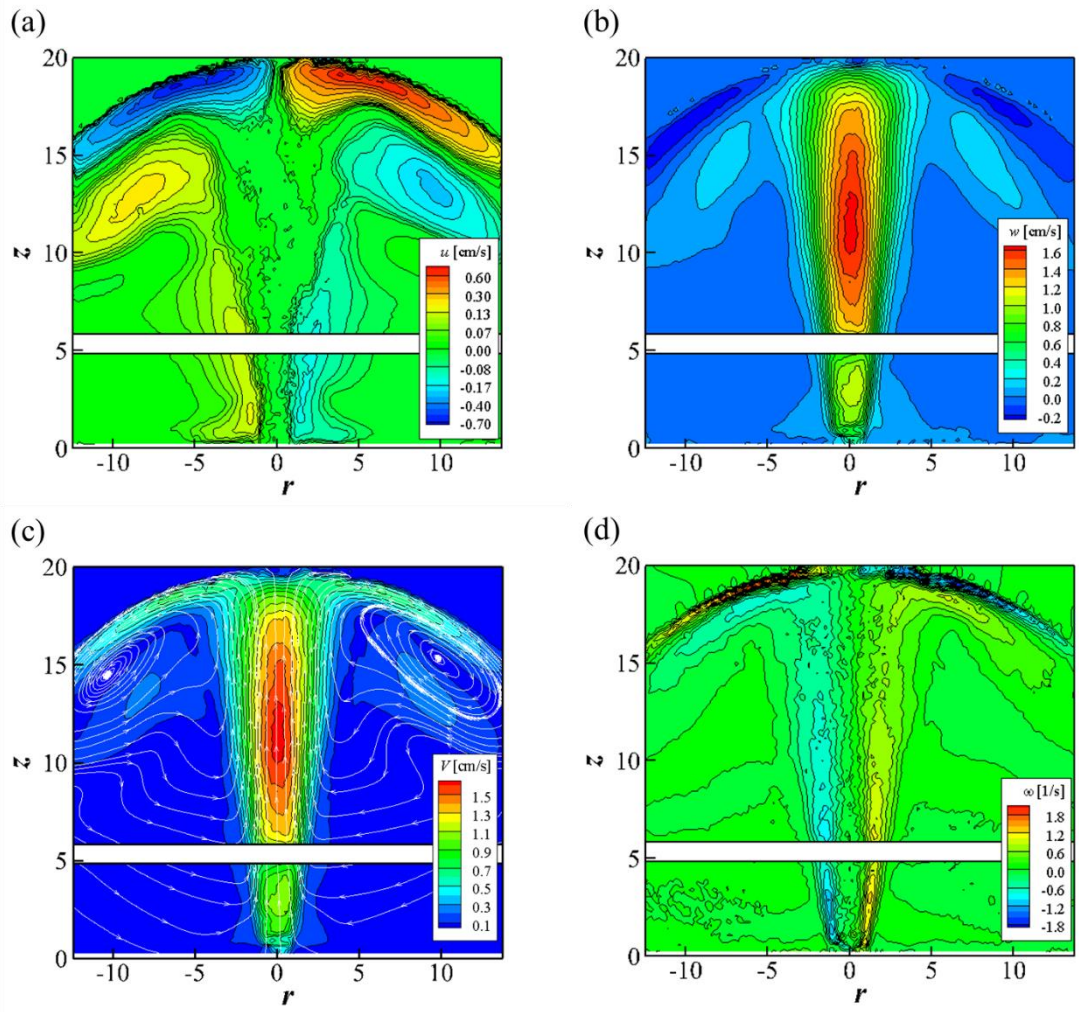

Figure 5.17. Contours of averaged single buoyant jet; (a) mean radial velocity; (b) mean axial velocity; (c) mean velocity magnitude with streamlines; and (d) vorticity (ω).

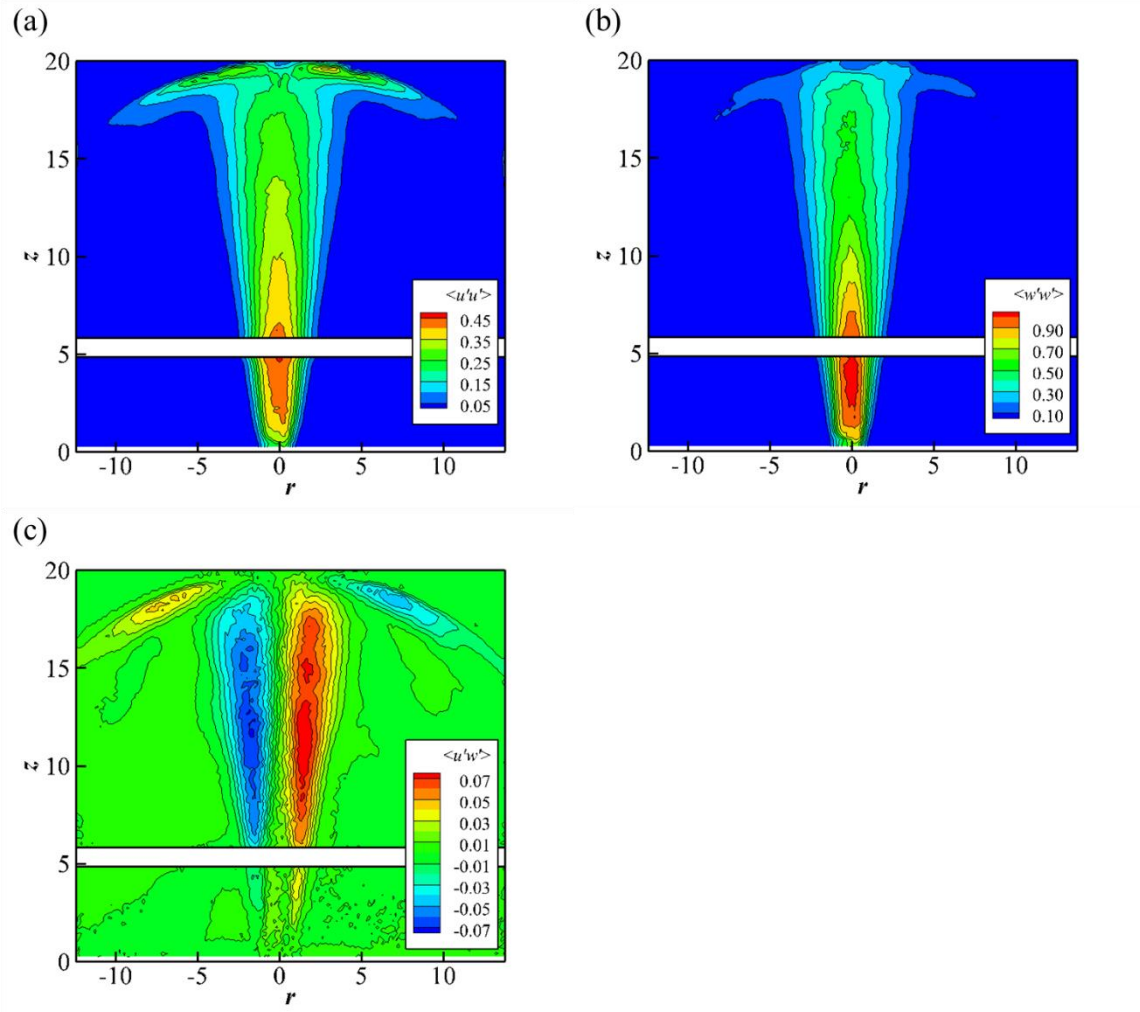

Figure 5.18. Contours of averaged single buoyant jet; (a) Reynolds stress <*u'u'*>; (b) Reynolds stress <*w'w'*>; and (c) Reynolds stress <*u'w'*>.

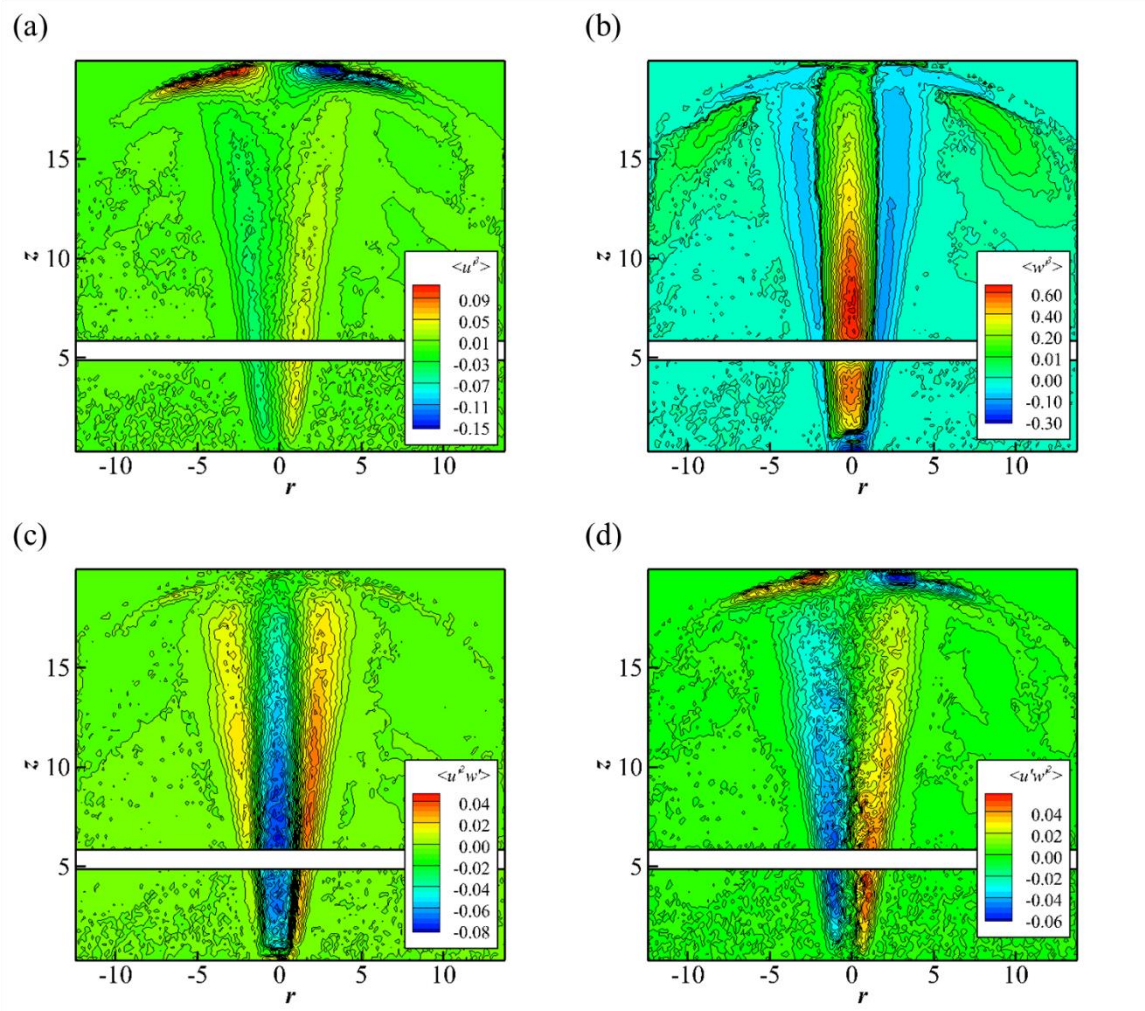

Figure 5.19. Contours of averaged single buoyant jet; (a) third moments $\langle u'^3 \rangle$; (b) third moments $\langle w'^3 \rangle$; (c) third moments $\langle u'^2 w' \rangle$; and (d) third moments $\langle u' w'^2 \rangle$.

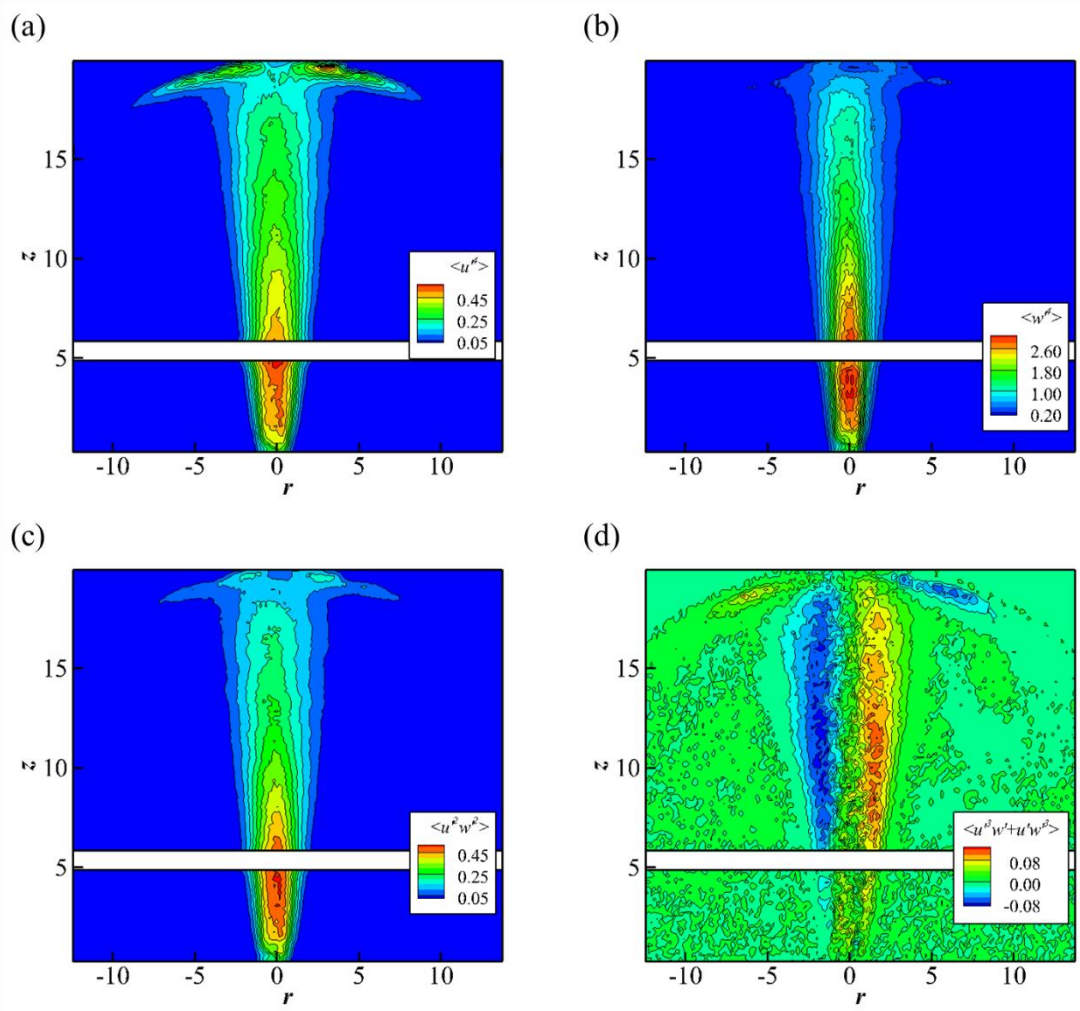

Figure 5.20. Contours of averaged single buoyant jet; (a) fourth moments $\langle u'^4 \rangle$; (b) fourth moments $\langle w'^4 \rangle$; (c) third moments $\langle u'^2 w'^2 \rangle$; and (d) fourth moments $\langle u'^3 w' + u' w'^3 \rangle$.

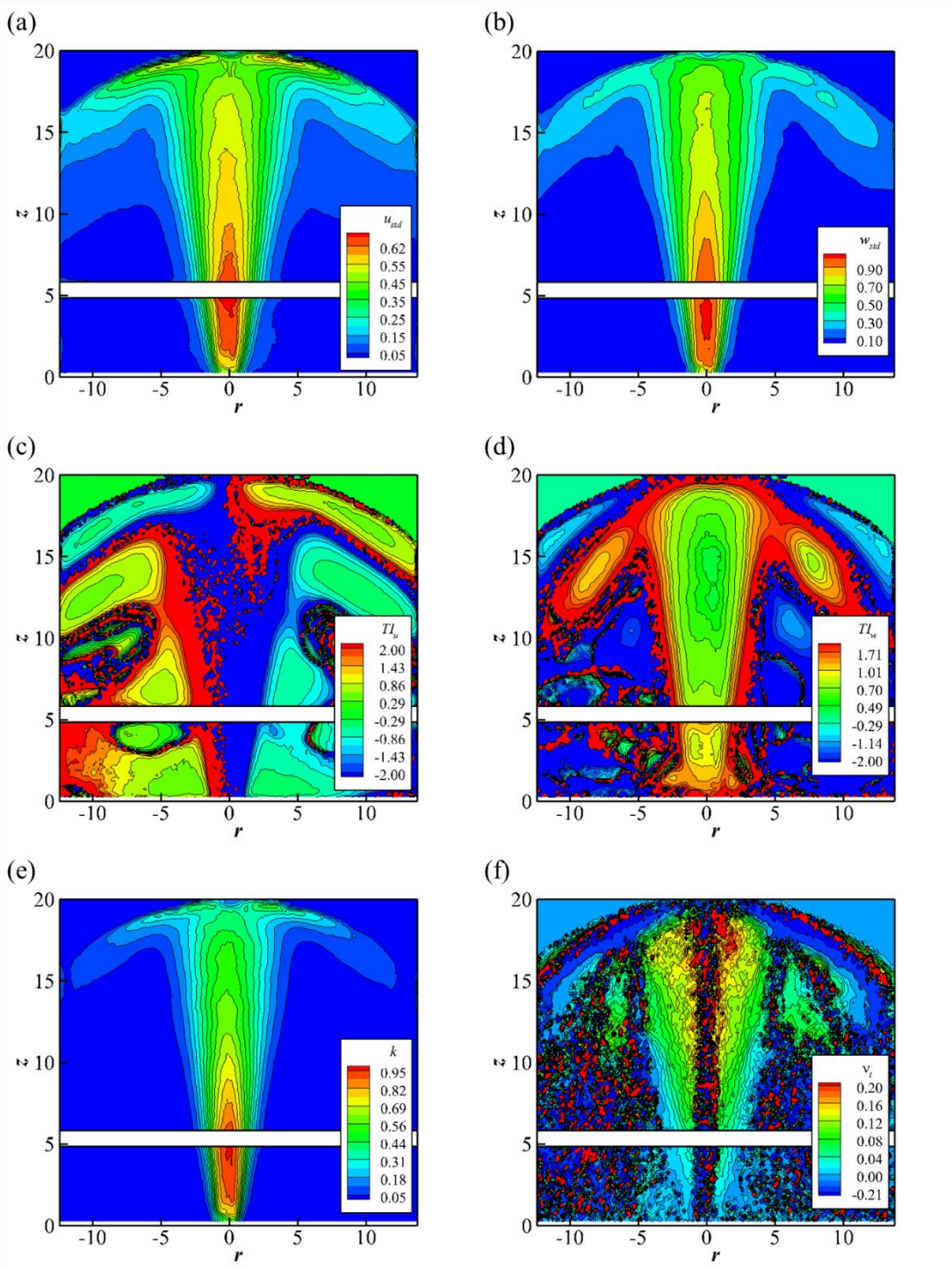

Figure 5.21. Contours of averaged single buoyant jet; (a) standard deviation of radial velocity; (b) standard deviation of axial velocity; (c) turbulent intensity in radial direction; (d) turbulent intensity in axial direction; (e) Turbulent kinetic energy (*k*); and (f) turbulent viscosity (ν_t).

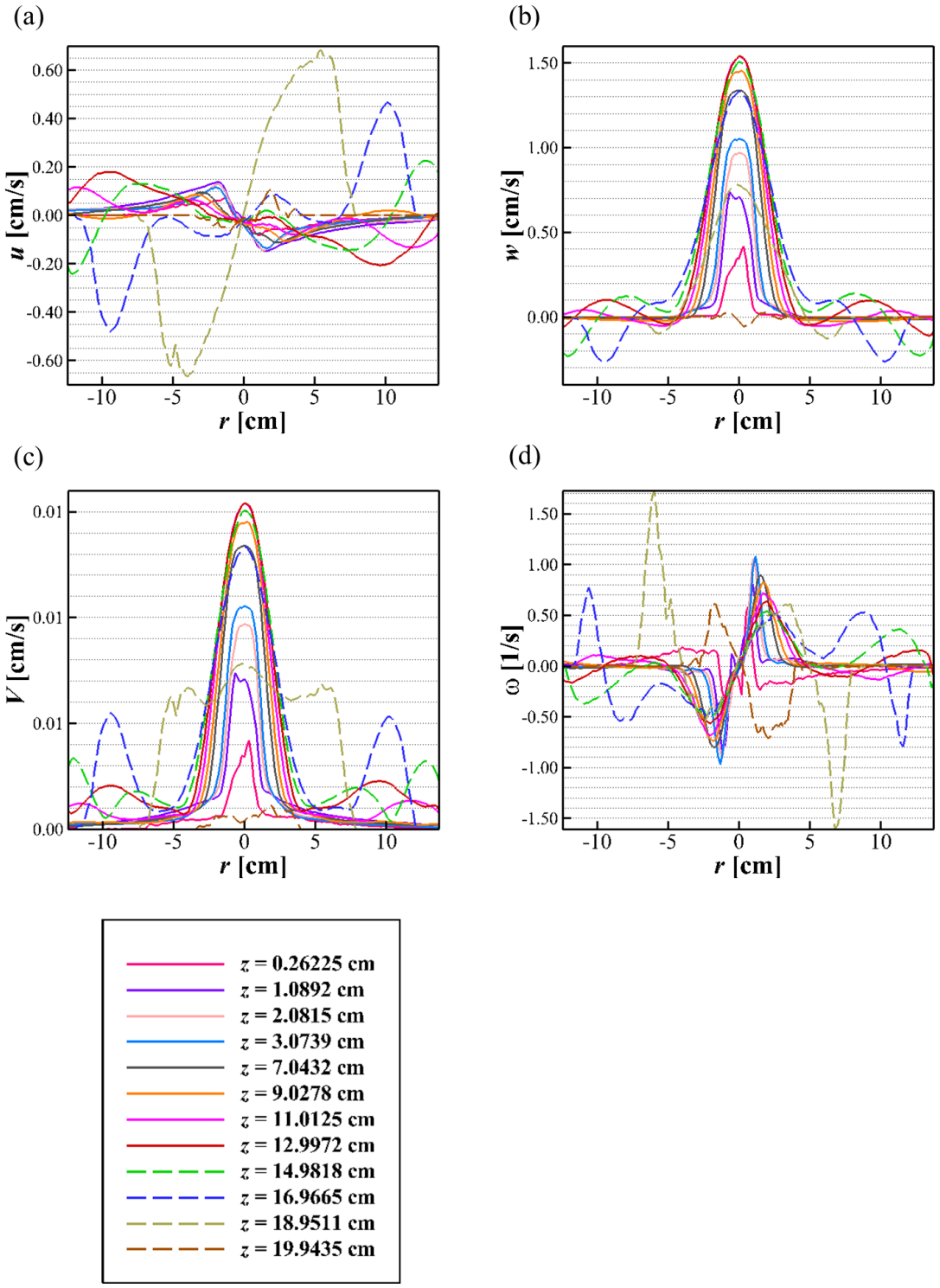

Figure 5.22. Radial profiles of (a) radial velocity, (b) axial velocity, (c) velocity magnitude and (d) vorticity for a single buoyant jet.

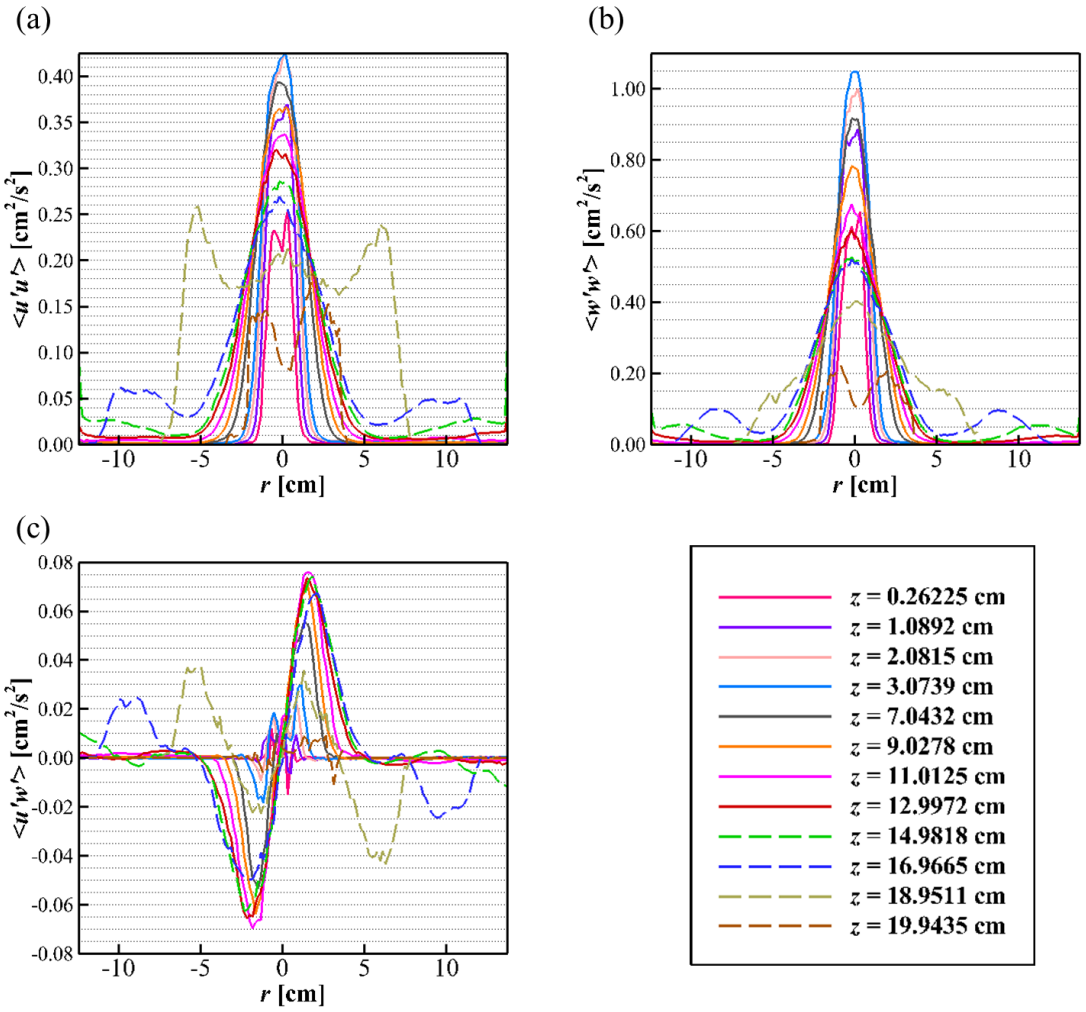

Figure 5.23. Radial profiles of Reynolds stresses ((a) - (c)) for a single buoyant jet.

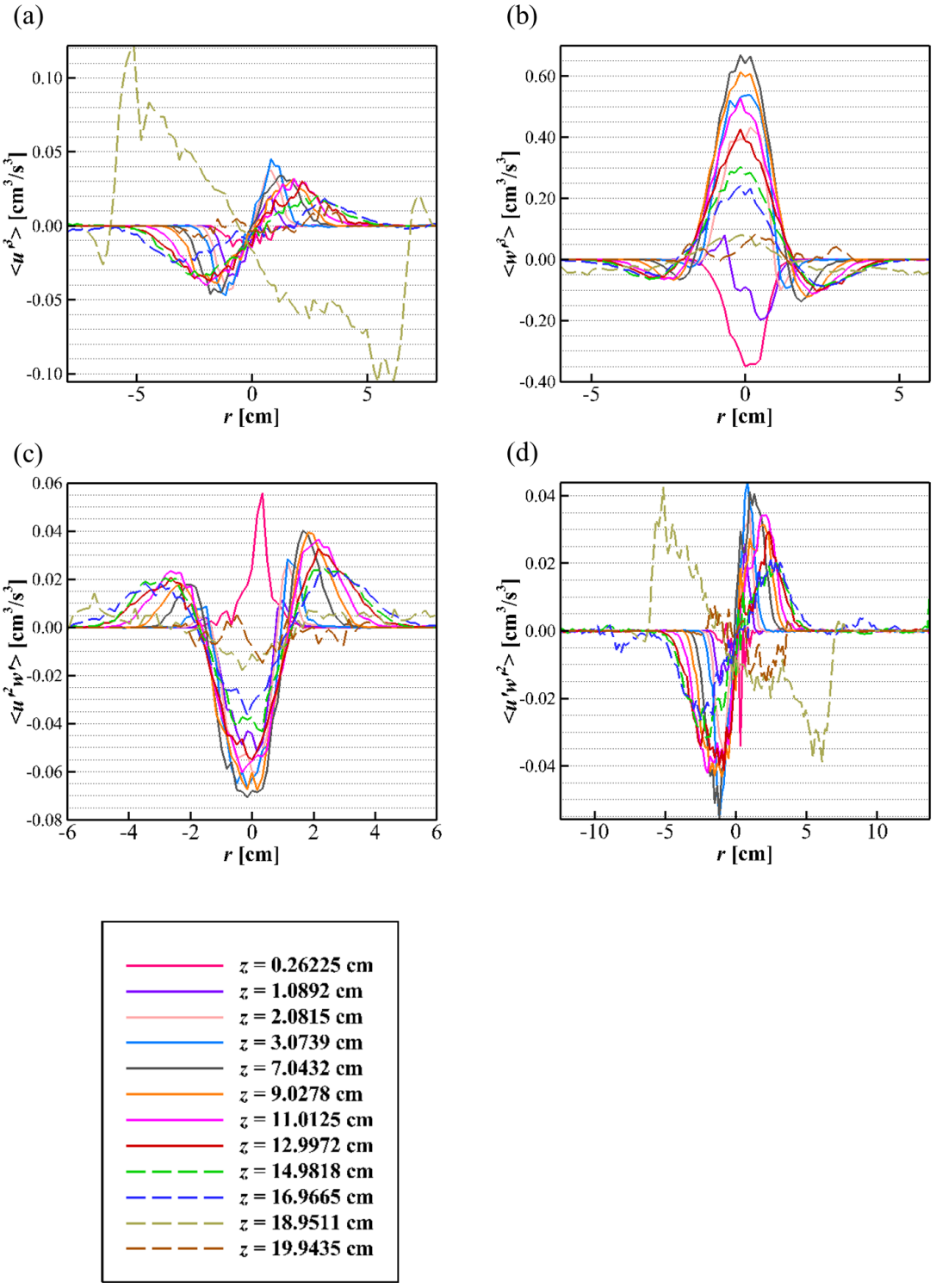

Figure 5.24. Radial profiles of third moments ((a)-(d)) for a single buoyant jet.

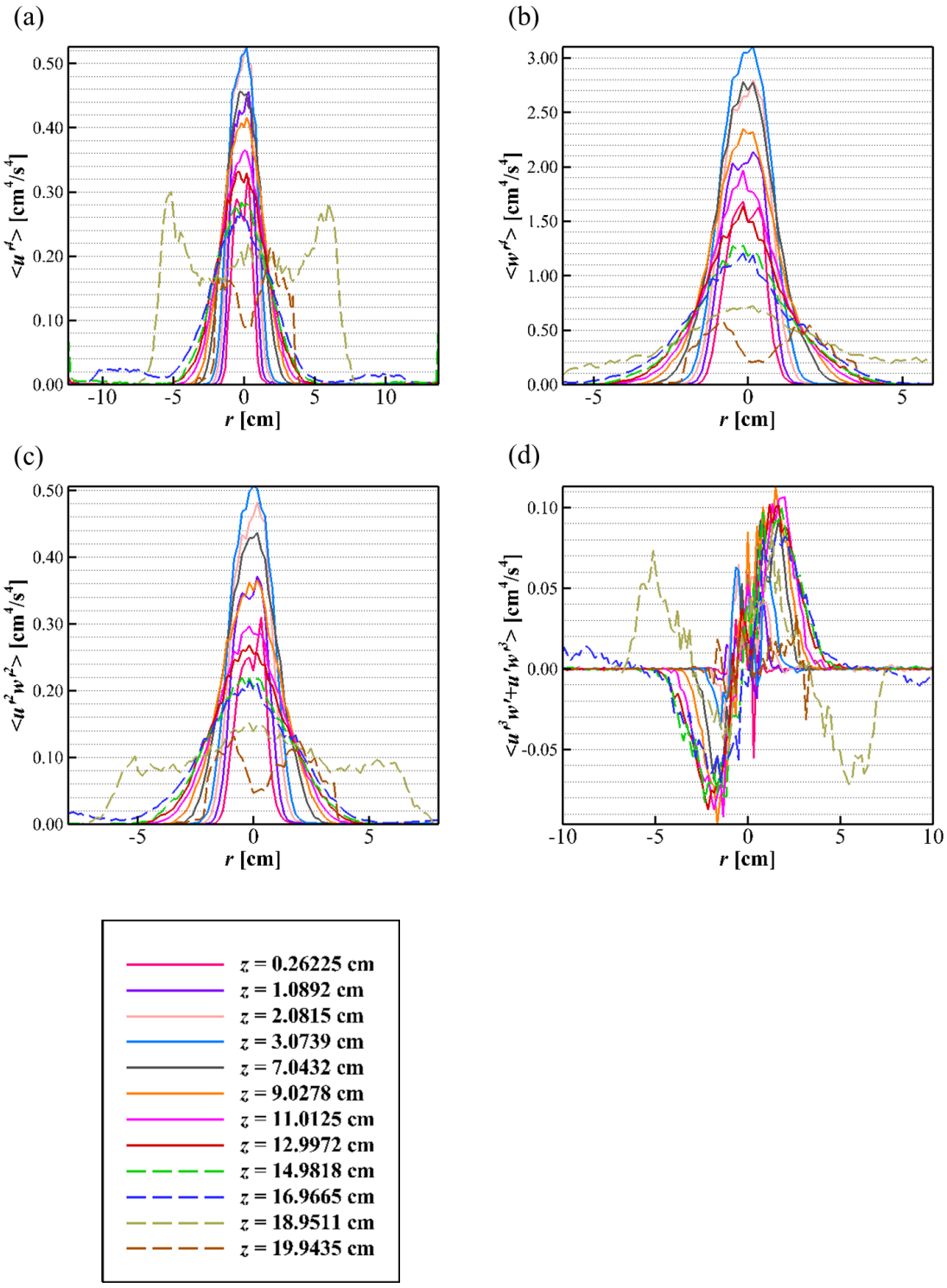

Figure 5.25. Radial profiles of fourth moments ((a)-(d)) for a single buoyant jet.

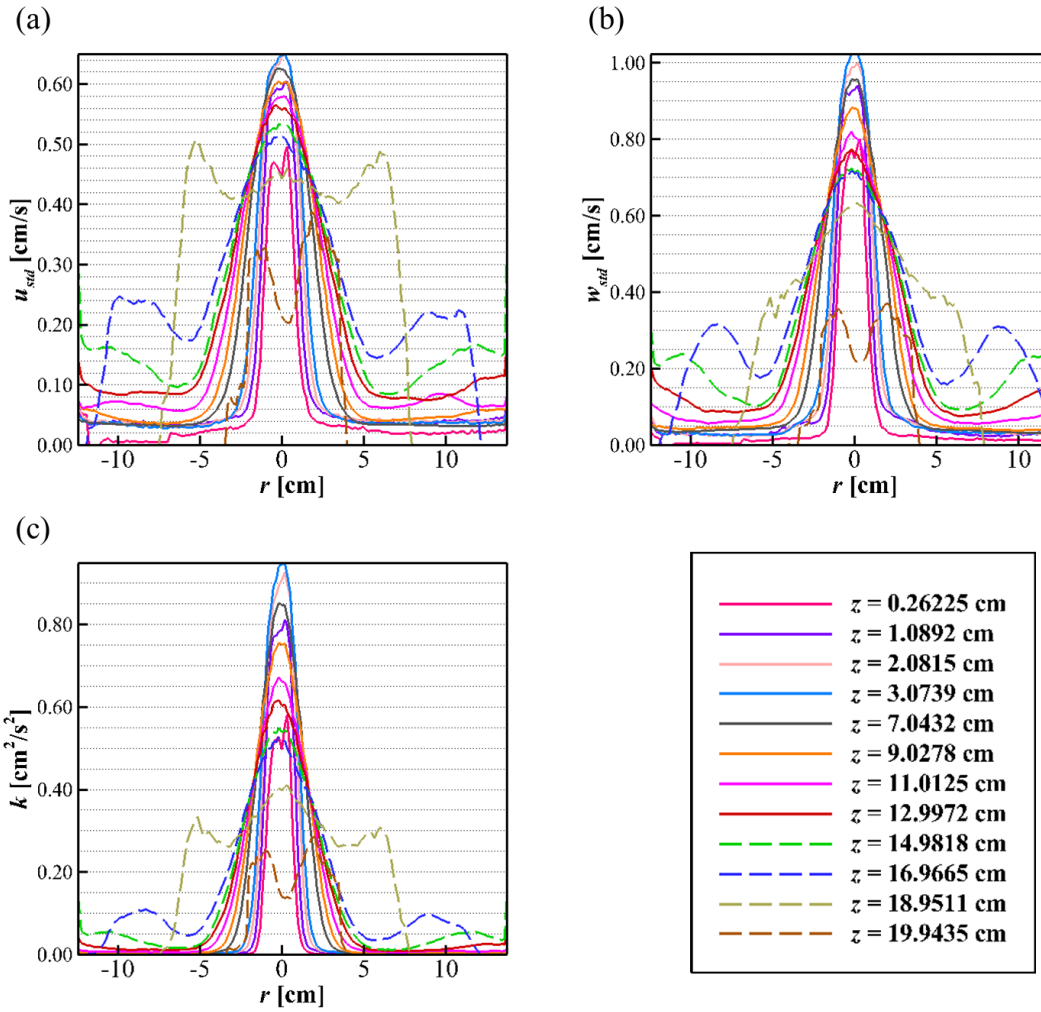

Figure 5.26. Radial profiles of the standard deviations of (a) radial velocity and (b) axial velocity; and (c) kinetic energy distribution for a single buoyant jet.

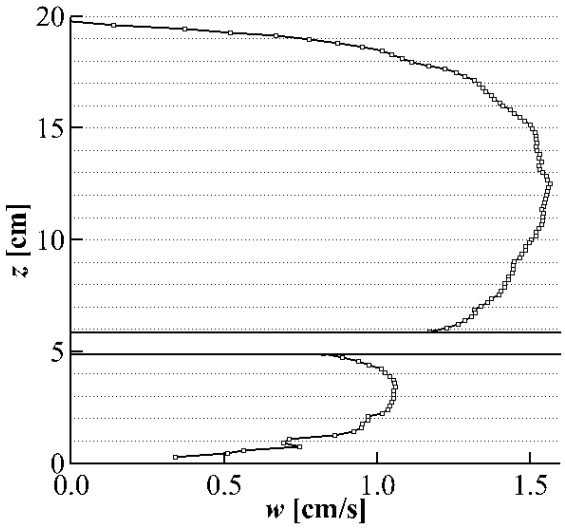

Figure 5.27. The axial velocity distribution along the *z*-direction at $r = 0$ cm. The maximum velocity is obtained at $z = 12.51$ cm.

The temperature distributions at each location are shown in Figure 5.28 and the summarized temperature and flowrate data are listed in Figure 5.29 and 5.30. The average c1b and c1t temperatures for nine tests are 18.23 °C and 26.74 °C, respectively. The c1t temperature is maximized about 20% of its average temperature when it fluctuates. The temperature difference of c1b and c1t is 8.51 °C. The flowrate data is well justified with the PIV velocity data by calculating the mean velocity from the volume flux. A discrete Fourier transform (DFT) of the inlet pipe temperature (c1t) estimates the dominant frequency (f), or in other words a characteristic puffing frequency, as 0.03 Hz for all tests so the characteristic puffing period (T) is determined to be 33.33 s. This is a frequency of the largest vortex emerged at the pipe inlet. The second largest frequency is obtained at 0.063 Hz (15.87 s). Therefore every two times when the largest vortex is created the second largest vortex is formed. These structures are observed in transient contour Figures.

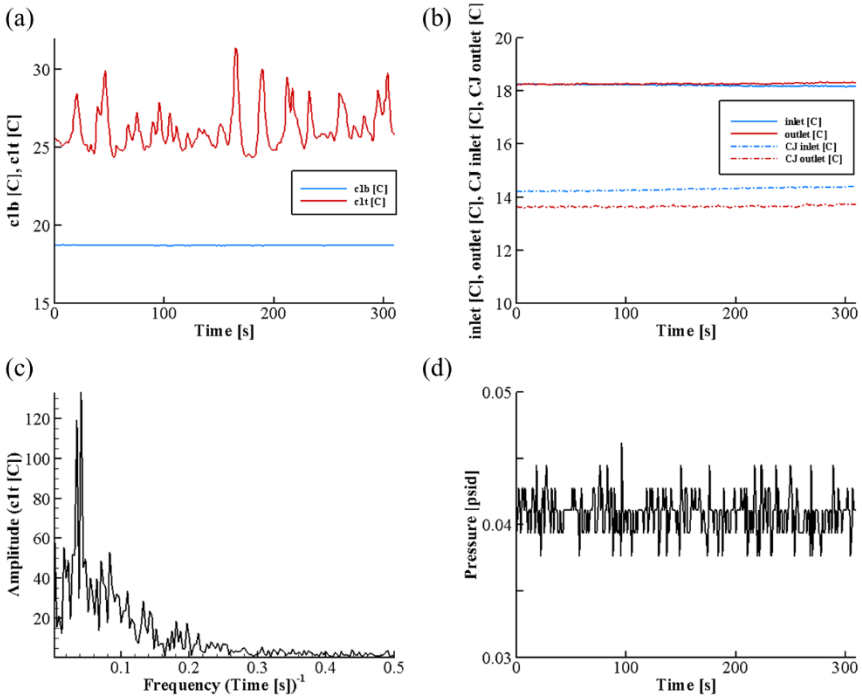

Figure 5.28. Time series of temperature at location r = 0 and z = - 2.54 cm in Test 3. Temperature time history of (a) an inlet and outlet and (b) system inlet/outlet and CJ inlet/outlet. (c) DFT of the temperature time series on the inlet. (d) Pressure time history (psid).

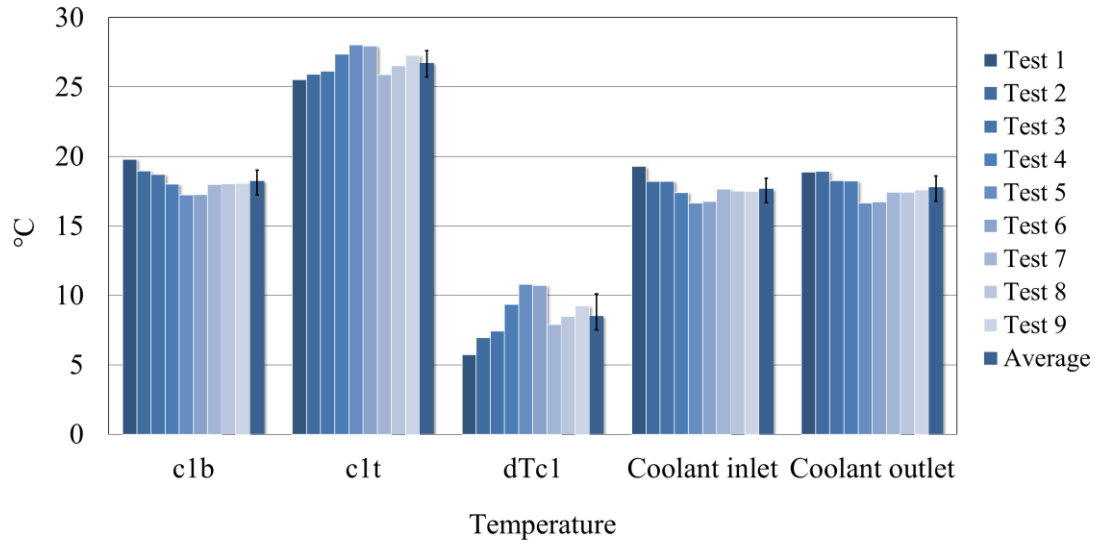

Figure 5.29. Temperature data for a single jet at each location for nine test results and averaged temperature data.

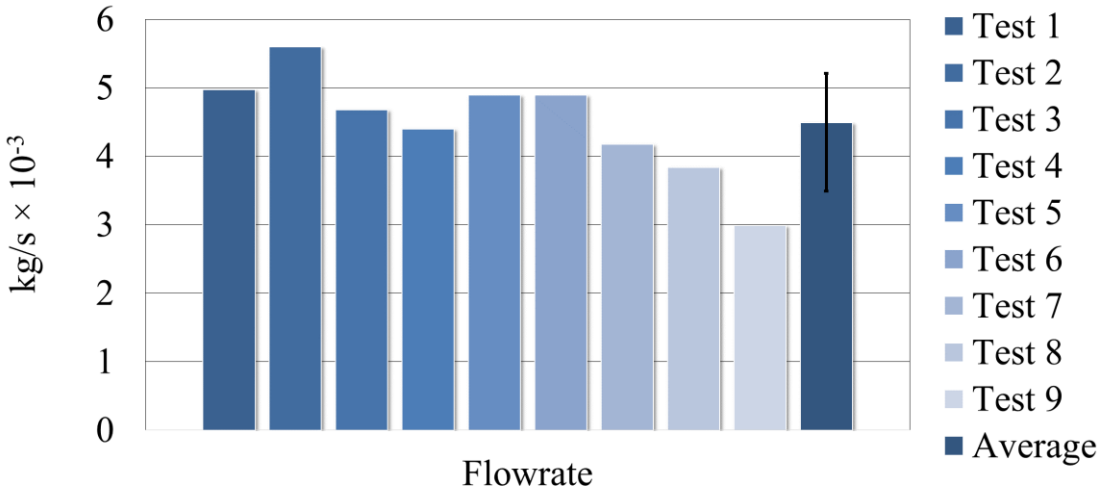

Figure 5.30. Flowrate data for a single jet at each location for nine test results and averaged flowrate data.

Self-similarity is an important concept in jet and plume studies because it provides the general behavior of buoyant jets. Soon after the flow is developed from the jet inlet time-averaged profiles show a Gaussian distribution. When these profiles collapse into a single Gaussian profile, the turbulent structure reaches self-preserving region. Many authors from different studies define the transition of this self-similarity with slightly different parameters. Two very common parameters are $(z-z_0)/D$ (or z/D) and $(z-z_0)/l_M$ where z_0 is a virtual origin where two jet boundaries are met, D is a diameter of the jet inlet and l_M is a Morton length scale defined in Equation (5.10). However, these studies were limited to free jets where jets develop without bound [43, 62, 63]. The present results show when and where these self-similarity patterns are observed in the dome shaped geometry. The velocity and radial distribution profiles are normalized by the centerline axial velocity w_c and $(z-z_0)$ or b, respectively. A virtual origin is obtained by estimating the width of the jet and extending these lines to find the point where they intersect as shown in Figure 5.31.

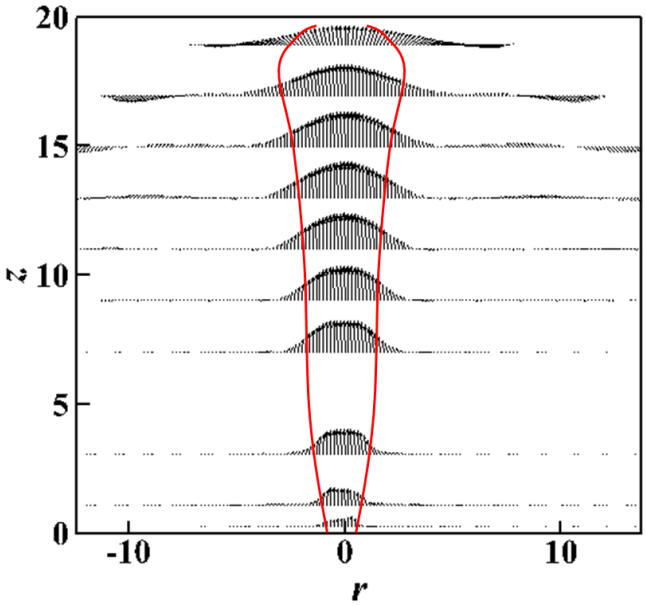

Figure 5.31. Turbulent jet boundary of a single jet.

The radial profiles of each non-dimensional property are shown from Figure 5.32 to 5.35. Self-similarity profiles are obtained in the axial velocity and velocity magnitude profile where the radial velocity did not show any similarity pattern. This is due to the large counter rotating vortices located near the dome surface. To examine self-similarity, each test results in the range $0.57 < z/d < 9.43$ are plotted and compared with a Gaussian curve. As shown in Figure 5.36 and 5.37, the non-dimensional axial velocity profiles for all tests tightly collapse on to the Gaussian curve with $R^2 > 0.95$ and RMSE < 0.066, which corresponds to the results of Ezzamel et al [64]. Note that Figure 5.37 has a converged point in the right side at $r/b = 1$ since the data is normalized by the right side of the jet width. The normal components of Reynolds stresses have self-similarity within the range of $z/D > 5.78$. The profiles of non-dimensional Reynolds stress $\langle u'w' \rangle$ are shown in

Figure 5.38 and 5.39 fitted with a negative second derivative of a sigmoid function as follows:

$$f(\eta) = \frac{c_0 e^{c_1 \eta}\left(e^{c_2 \eta} - c_3\right)}{\left(e^{c_4 \eta} + 1\right)^3}, \tag{5.25}$$

where η is a similarity variable and can be either $r/(z - z_0)$ or r/b. The self-similarity of the Reynolds stress is obtained with $R^2 > 0.6$ and RMSE < 0.0034. Contrary to other self-similarity free jet studies [31, 41, 65], it is not highly correlated as the axial velocity profiles. It is because the profiles behave more like a plume and this results corresponds to the results from Ezzamel et al [64] where the profiles of the Reynolds stresses for a jet collapse into a single profile while ones for a plume does not.

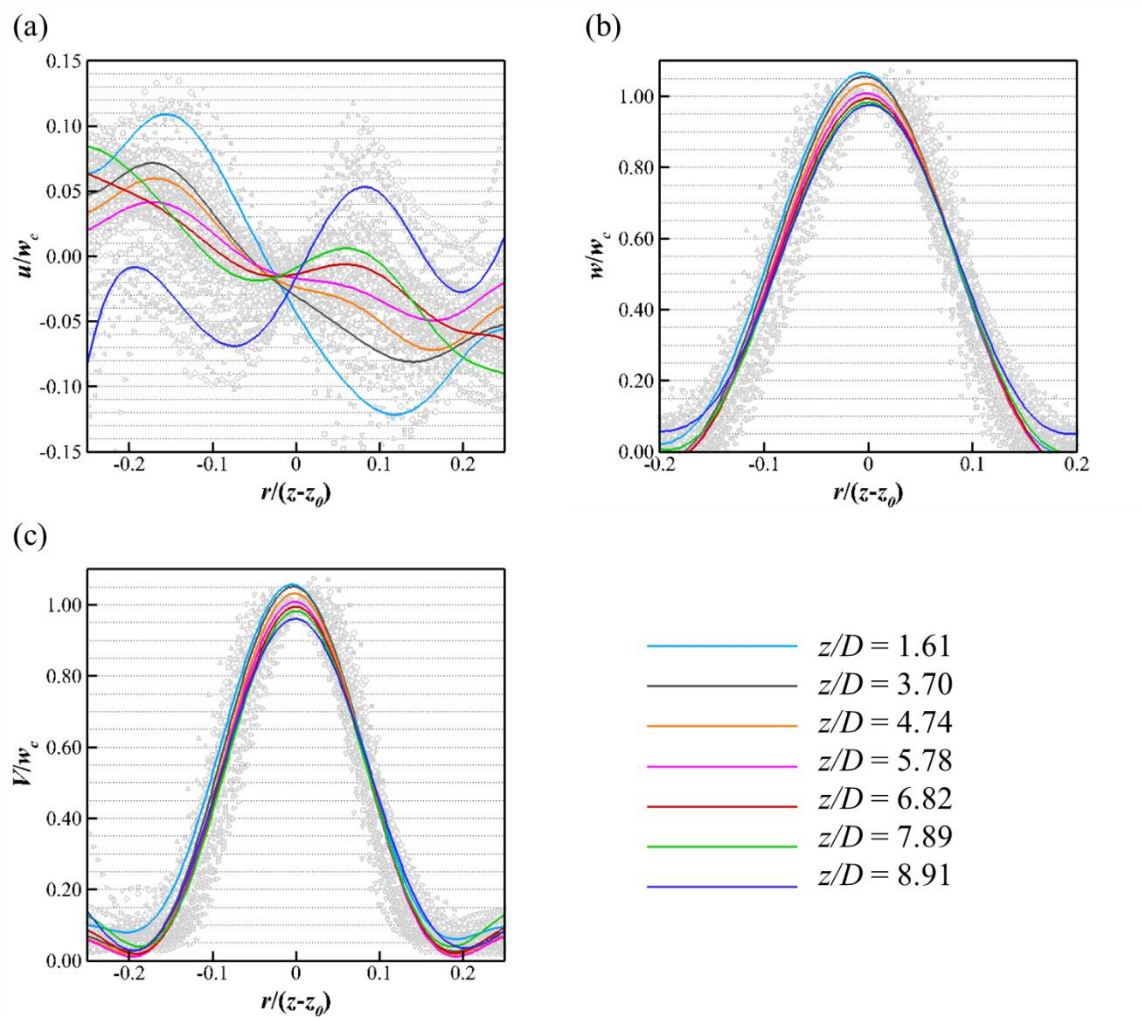

Figure 5.32. Radial profiles of non-dimensional (a) radial velocity, (b) axial velocity and (c) velocity magnitude for a single buoyant jet.

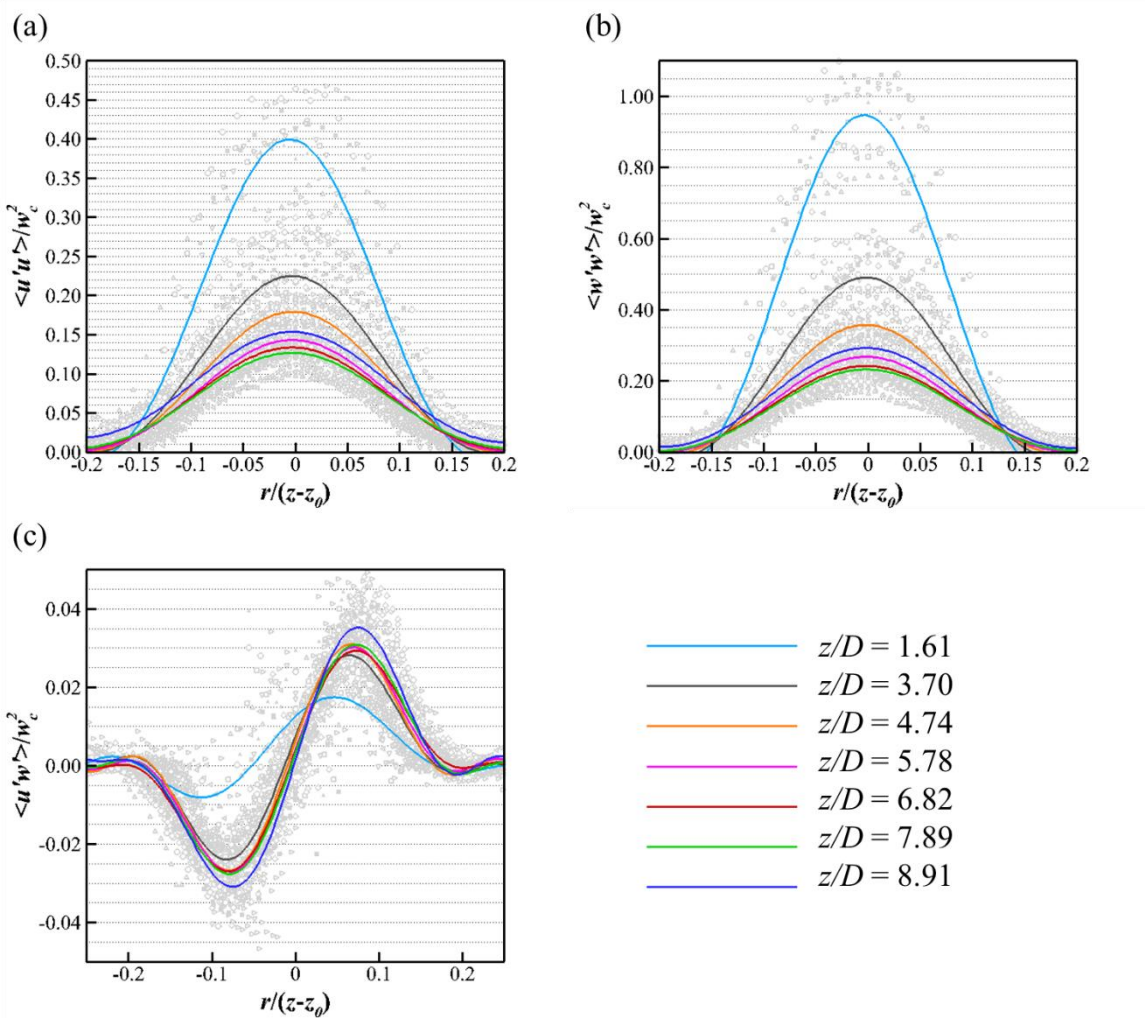

Figure 5.33. Radial profiles of non-dimensional Reynolds stresses ((a) - (c)) for a single buoyant jet.

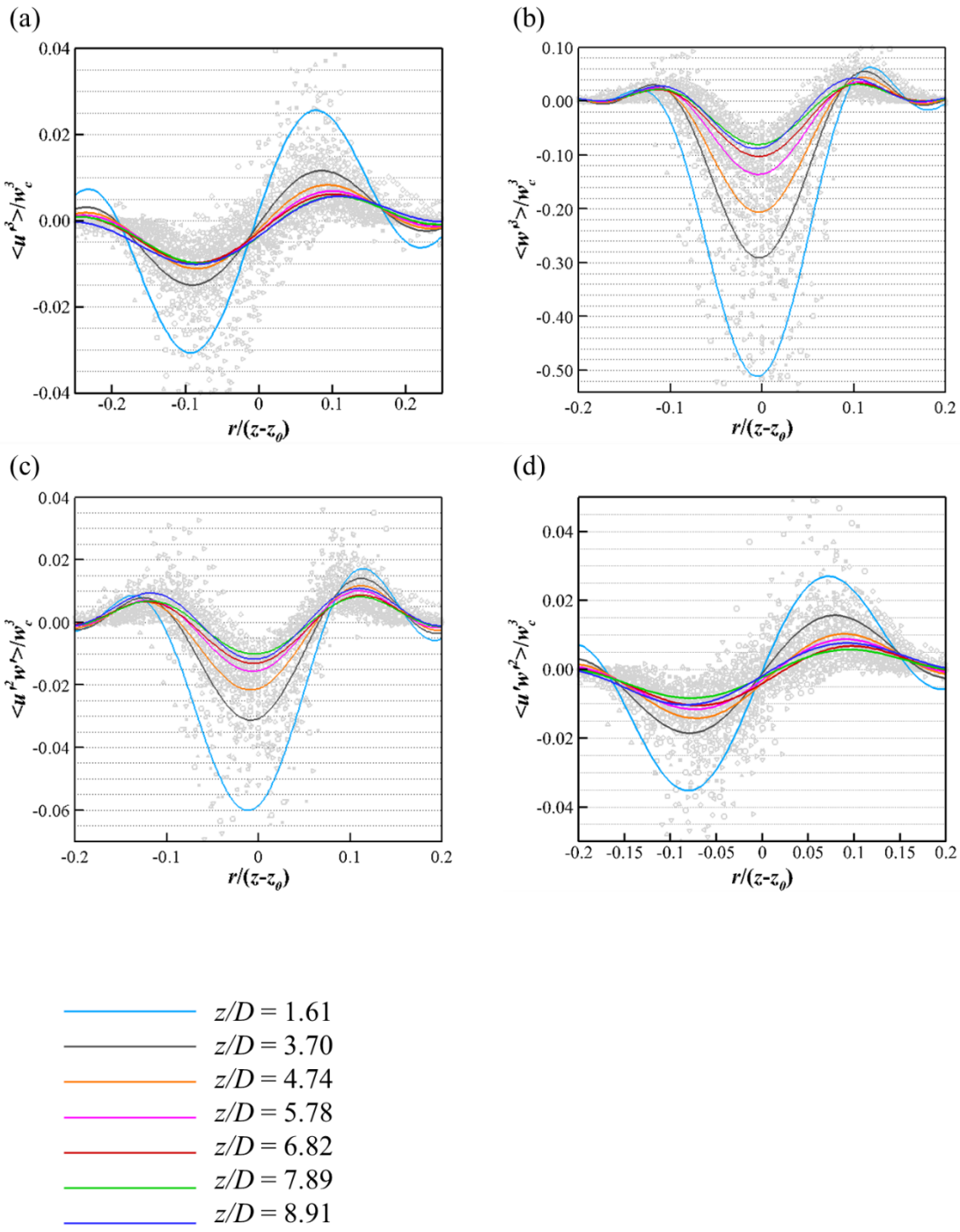

Figure 5.34. Radial profiles of non-dimensional third moments ((a) - (d)) for a single buoyant jet.

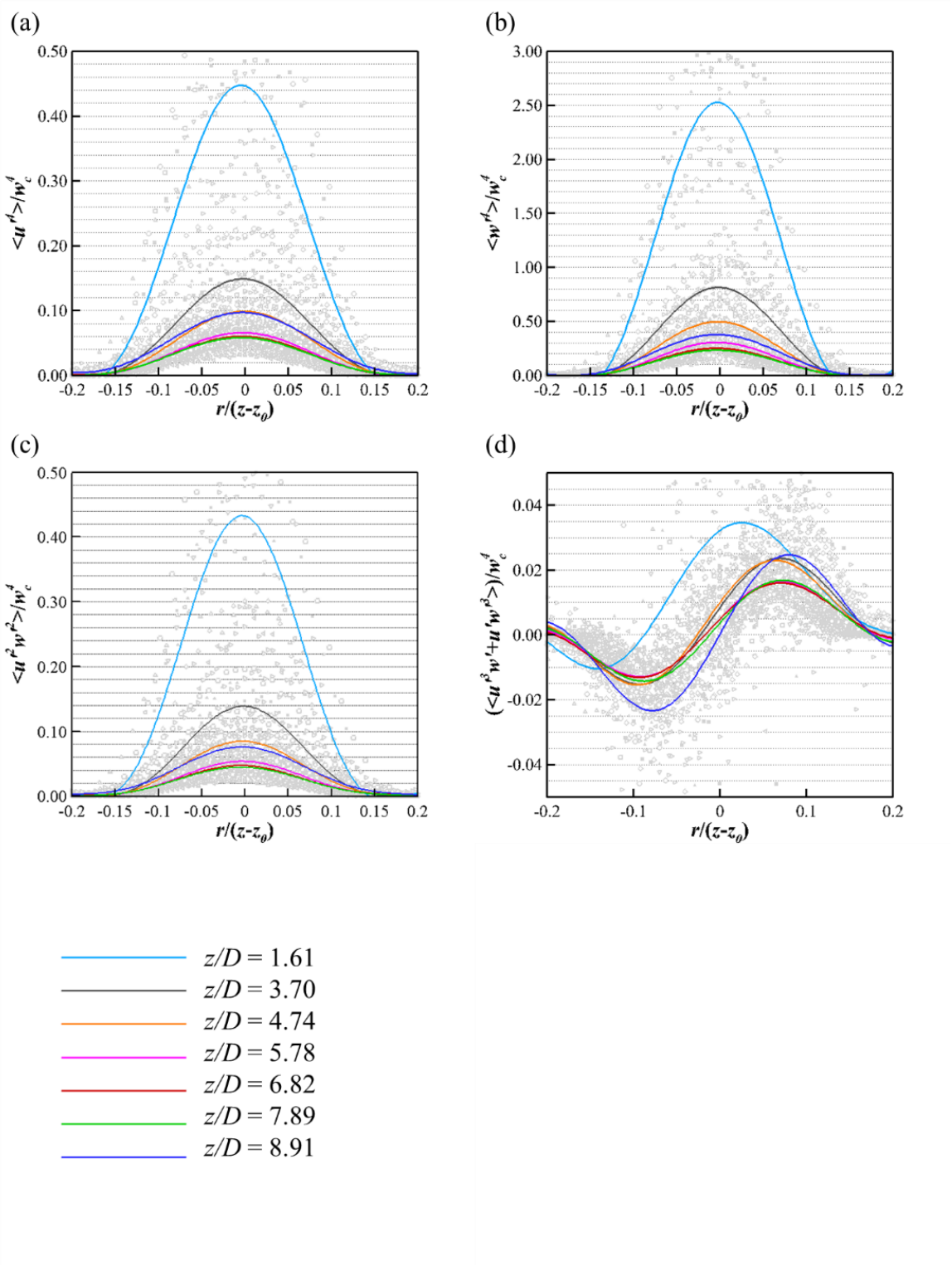

Figure 5.35. Radial profiles of non-dimensional fourth moments ((a) - (d)) for a single buoyant jet.

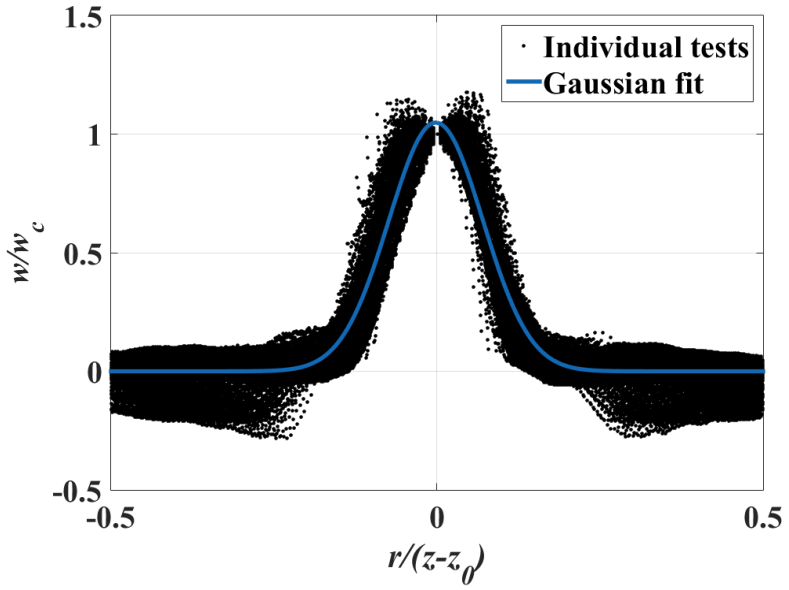

Figure 5.36. The Gaussian profile fit for non-dimensional (z-z_0) radial profiles of the vertical velocity for nine experiments results. Self-similarity is obtained in the range $0.57 < z/d < 9.43$. $R^2 = 0.955$ and RSME = 0.06535.

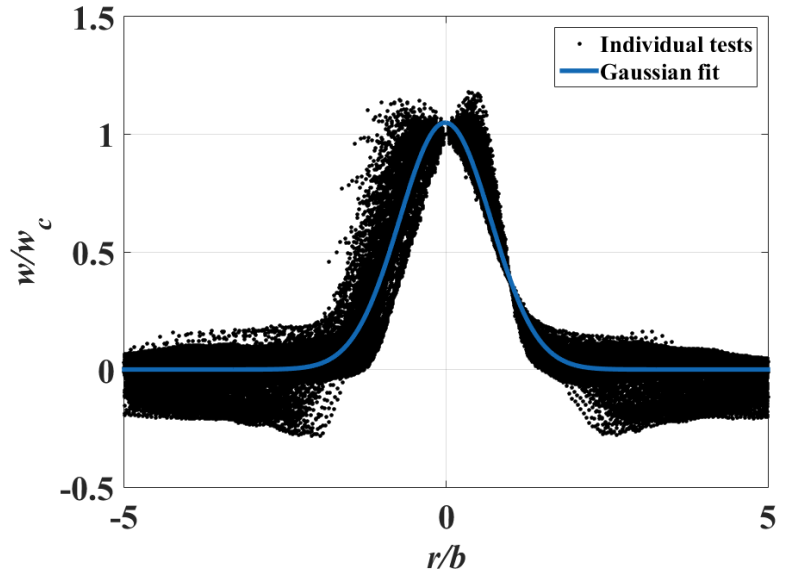

Figure 5.37. The Gaussian profile fit for non-dimensional r/b radial profiles of the vertical velocity for nine experiments results. Self-similarity is obtained in the range $0.57 < z/d < 9.43$. $R^2 = 0.9562$ and RSME = 0.06452.

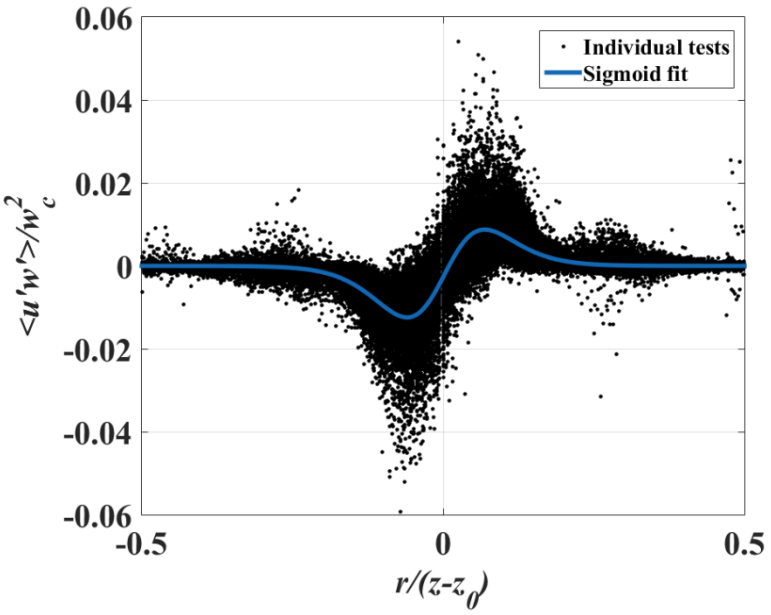

Figure 5.38. The negative second derivative of a sigmoid fit for non-dimensional (z-z_0) radial profiles of the Reynolds stress for nine experiments results in the range 3.18 < z/d < 9.43. R^2 = 0.5997 and RSME = 0.003397.

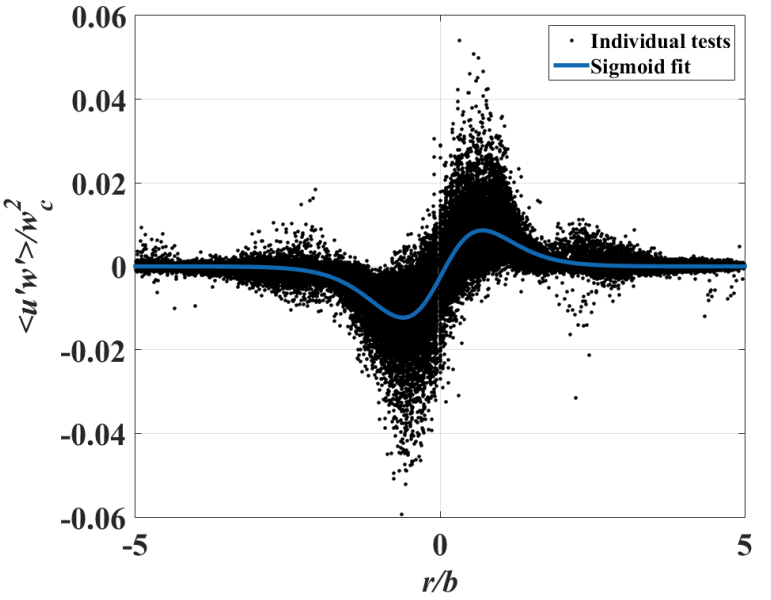

Figure 5.39. The negative second derivative of a sigmoid fit for non-dimensional r/b radial profiles of the Reynolds stress for nine experiments results in the range 3.18 < z/d < 9.43. R^2 = 0.6074 and RSME = 0.003365.

Morton length scale (l_M) is measured based on Equation (5.10) and has an average value of 0.0119 m in single buoyant jet tests. Therefore, a buoyant jet behaves like a jet for z < 1.19 cm ($z / l_M < 1$) and a jet for z > 5.97 cm ($z / l_M > 5$). So the present buoyant jet will have a transition region between 1.19 < z < 5.97 (0.63 < z/d < 3.13). Unfortunately, the transition part is not fully observed due to the portion that is glued. This phenomena can be confirmed from a log-log plot of the vertical velocity profile at r = 0. Figure 5.40 shows the transition from a jet-like behavior to a plume-like behavior. In the range of 0 < z/D < 0.63, $w / w_0 \propto (z / D)^1$ and 3.5 < z/D < 6.5, $w / w_0 \propto (z / D)^{1/2}$ where w_0 is an average vertical velocity at the inlet.

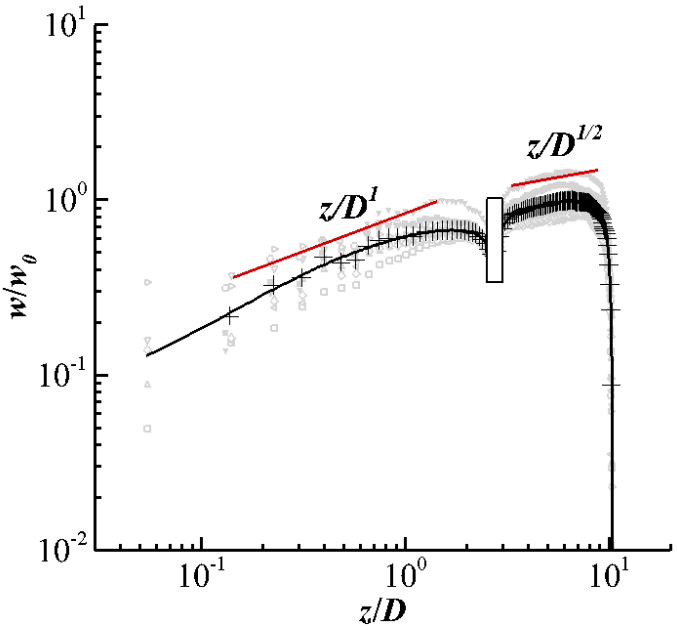

Figure 5.40. Vertical profiles of a single jet in terms of z/D. Gray symbols indicate each test result and error bars indicate the standard deviates of locations and vertical velocities.

A jet boundary is defined as a jet width *b* as shown in Figure 5.41. The width starts to decrease approximately at *z* = 17.56 cm (z/*D* = 9.22) near the wall since its vertical velocity asymptotically decreases to become zero at the stagnation point. The entrainment coefficient α_G and spreading rate β_s are defined as follows:

$$\alpha_G(z) = \frac{u_e(z)}{w_c(z)}, \tag{5.26}$$

$$\beta_S(z) = \frac{b(z)}{z}, \tag{5.27}$$

where $u_e(z) = |u|_{r=\pm b} =$ entrainment velocity. The entrainment velocity u_e is proportional to the jet centerline velocity w_c. The jet boundary is symmetrical along the centerline. Recall the continuity equation and rewrite,

$$\frac{\partial(ru)}{\partial r} + \frac{\partial(rw)}{\partial z} = 0. \tag{5.28}$$

Integrate over *r* from 0 to ∞, then we get

$$\frac{d}{dz}\int_0^\infty rwdr = -[ru]_0^\infty. \tag{5.29}$$

Assume the entrainment hypothesis proposed by Morton et al. [42] where

$$-[ru]_0^\infty = bu_e. \tag{5.30}$$

Resulting in

$$\frac{d}{dz}\int_0^\infty rwdr = bu_e. \tag{5.31}$$

Applying the Gaussian self-similar velocity profile, we derive the volume flux conservation equation from Equation (5.32):

$$\frac{dQ}{dz} = 2\pi \frac{d}{dz}\int_0^\infty rwdr = 2\pi b u_e = 2\pi b \alpha_e w_c. \qquad (5.32)$$

Therefore the entrainment coefficient is closely related to the volume flux conservation equation [64]. The entrainment is unstable at $0 \le z \le 6$ cm ($0 \le z/D \le 3.15$) and steadily deceases until $z \le 14.75$ cm ($0 \le z/D \le 7.74$). The large entrainments are obtained as expected where the buoyancy forces are developed (RT instability). The magnitude of the entrainment coefficient is almost constant but becomes opposite sign and goes to large values since the axial velocity gradually is converted into the radial velocity to conserve the continuity equation. The average α_G is obtained 0.1711 ± 0.038 at z = 6 cm (z/D = 3.15) and goes zero at z = 14.75 cm (z/D = 7.74) thus the average entrainment coefficient is estimated $\alpha_G = 0.0767 \pm 0.0189$ in the range of $6 \le z \le 14.7$ cm ($3.15 \le z/D \le 7.74$). For Gaussian profiles, the entrainment coefficient of pure jets is in the range of $0.045 < \alpha_G < 0.056$ and pure plumes is in the range of $0.07 < \alpha_G < 0.11$ [66]. In general the entrainment coefficient for plumes is doubled than that for jets. As we discussed in Morton length scale, this also justifies that the single buoyant jet behaves like a plume. A value of the spreading rate β_S is almost constant 0.292 ± 0.0114 at z = 6 cm (z/D = 3.15) and becomes 0.1731 ± 0.0016 at z = 17.56 cm (z/D = 9.22). An average spreading rate is 0.2073 ± 0.0041. The average rate of change in the jet width, also known as a constant spreading rate, is $db/dz = 0.111 \pm 0.0084$ which corresponds to values in the range of $0.102 < db/dz < 0.112$ confirming a constant spreading rate hypothesis proposed by Morton [42].

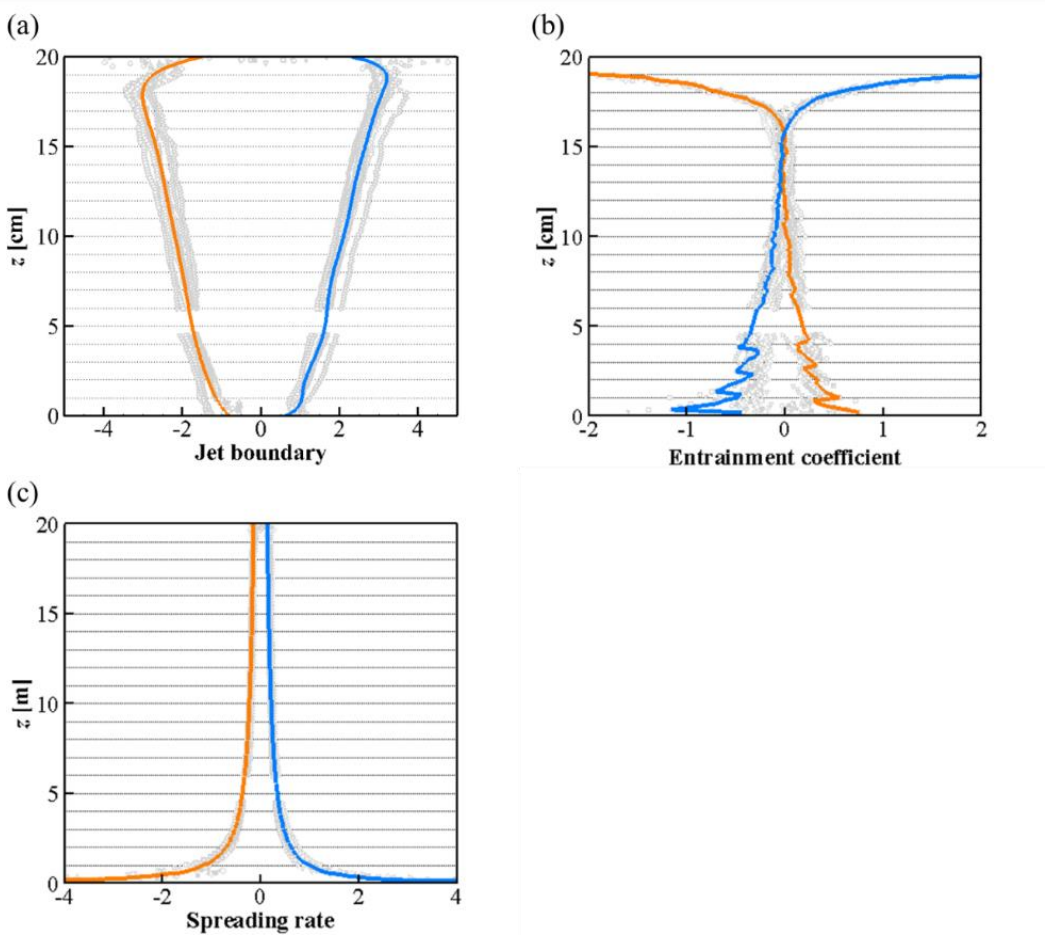

Figure 5.41. The characteristics of a single buoyant jet. (a) jet boundary, (b) entrainment coefficient and (c) speeding rate. The orange line indicates the left-hand side value while the blue line represents the right-hand side value.

The turbulent kinetic energy equation in cylindrical coordinate can be derived from the Reynolds stress equation where the average fluctuating kinetic energy per unit mass is defined as:

$$k \equiv \frac{1}{2}\left\langle q^2 \right\rangle = \frac{1}{2}\left[\left\langle u'^2 \right\rangle + \left\langle w'^2 \right\rangle + \left\langle v_\theta'^2 \right\rangle\right]. \tag{5.33}$$

Neglecting the viscous diffusion the turbulence kinetic energy equation can be written as:

$$\begin{aligned}
&u\frac{\partial k}{\partial x} + w\frac{\partial k}{\partial r} + \frac{v_\theta}{r}\frac{\partial k}{\partial \theta} - v_\theta \frac{\left\langle w'v_\theta' \right\rangle}{r} + w\frac{\left\langle v_\theta'^2 \right\rangle}{r} = \\
&-\frac{1}{\rho}\left[\frac{\partial \left\langle pu' \right\rangle}{\partial x} + \frac{1}{r}\frac{\partial \left(r\left\langle pw' \right\rangle\right)}{\partial r} + \frac{1}{r}\frac{\partial \left\langle pv_\theta' \right\rangle}{\partial \theta}\right] \\
&-\frac{1}{2}\left[\frac{\partial \left\langle u'q^2 \right\rangle}{\partial x} + \frac{1}{r}\frac{\partial \left(r\left\langle w'q^2 \right\rangle\right)}{\partial r} + \frac{1}{r}\frac{\partial \left\langle v_\theta' q^2 \right\rangle}{\partial \theta}\right] - \varepsilon \\
&-\left[\left\langle u'^2 \right\rangle \frac{\partial u}{\partial x} + \left\langle u'w' \right\rangle \frac{\partial u}{\partial r} + \frac{\left\langle u'v_\theta' \right\rangle}{r}\frac{\partial u}{\partial \theta} + \left\langle u'w' \right\rangle \frac{\partial w}{\partial x} + \left\langle w'^2 \right\rangle \frac{\partial w}{\partial r} + \frac{\left\langle w'v_\theta' \right\rangle}{r}\frac{\partial w}{\partial \theta}\right. \\
&\left.+\left\langle u'v_\theta' \right\rangle \frac{\partial v_\theta}{\partial x} + \left\langle w'v_\theta' \right\rangle \frac{\partial v_\theta}{\partial r} + \frac{\left\langle v_\theta'^2 \right\rangle}{r}\frac{\partial v_\theta}{\partial \theta}\right].
\end{aligned} \tag{5.34}$$

For an axisymmetric jet, $\partial / \partial \theta$ terms are vanished and the correlations $\left\langle w'v_\theta' \right\rangle$ and $\left\langle u'v_\theta' \right\rangle$ are neglected [67] so the equation becomes

$$\underbrace{-\left[u\frac{\partial k}{\partial x}+w\frac{\partial k}{\partial r}\right]}_{\text{Convection}}$$
$$\underbrace{-\frac{1}{\rho}\left[\frac{\partial\langle pu'\rangle}{\partial x}+\frac{1}{r}\frac{\partial\left(r\langle pw'\rangle\right)}{\partial r}\right]}_{\text{Pressure Transport}}$$
$$\underbrace{-\frac{1}{2}\left[\frac{\partial\langle u'q^2\rangle}{\partial x}+\frac{1}{r}\frac{\partial\left(r\langle w'q^2\rangle\right)}{\partial r}\right]}_{\text{Diffusion}}-\underbrace{\varepsilon}_{\text{Dissipation}} \tag{5.35}$$
$$\underbrace{-\left[\langle u'^2\rangle\frac{\partial u}{\partial x}+\langle u'w'\rangle\frac{\partial u}{\partial r}+\langle u'w'\rangle\frac{\partial w}{\partial x}+\langle w'^2\rangle\frac{\partial w}{\partial r}+\langle w'v'_\theta\rangle\frac{\partial v_\theta}{\partial r}+w\frac{\langle v'^2_\theta\rangle}{r}\right]}_{\text{Production}}=0.$$

The dissipation term is estimated by subtracting the other terms of the kinetic energy equation. The pressure diffusion term is not measured from the experiment so the Lumley's estimate is used such that $\langle pv_i\rangle=-\frac{1}{10}\langle q^2v_i\rangle$ [68]. The errors due to this assumption is well justified since the dissipation rate includes the errors due to Lumley's assumption and the present measurement errors [63]. Again the axisymmetric condition assumes $\langle w'^2\rangle=\langle v'^2_\theta\rangle$. Unlike other literature [40, 63, 67, 69, 70], the present study calculates the triple correlation terms in the diffusion term and thus more accurate kinetic energy budget is estimated. When calculating the triple correlation terms, it is assumed that $\langle w'v'^2_\theta\rangle=\langle w'^3\rangle$ while the errors introduced by this assumption is less than 10% [40]. In addition each term is scaled by u_c^3/b. Figure 5.42 shows the kinetic energy budget at z/D = 5.26 where each line is fitted with polynomial regression. We note that advection term is a major portion of the budget until the boundary of the jet, i.e. r/b = 1, where the

production term has the maximum value. Most of the turbulent energy is gained by the advection term at the centerline of the jet and is balanced by dissipation and diffusion terms. Close to the boundary of the jet, the turbulent stress generated by mean strain creates free shear flows so the maximum value of the production term is obtained in the kinetic energy budget. The pressure transport term is almost zero and negligible in the process. A half distance away from the jet boundary (r/b = 1.5) the diffusion process is maximized toward the outside of the jet. The dissipation is the lowest at the centerline of the jet and monotonically decreases across the turbulent jet. The flow is not local equilibrium (production ≠ dissipation) within the jet boundary (r/b = 1) but becomes in local equilibrium outside of the jet boundary.

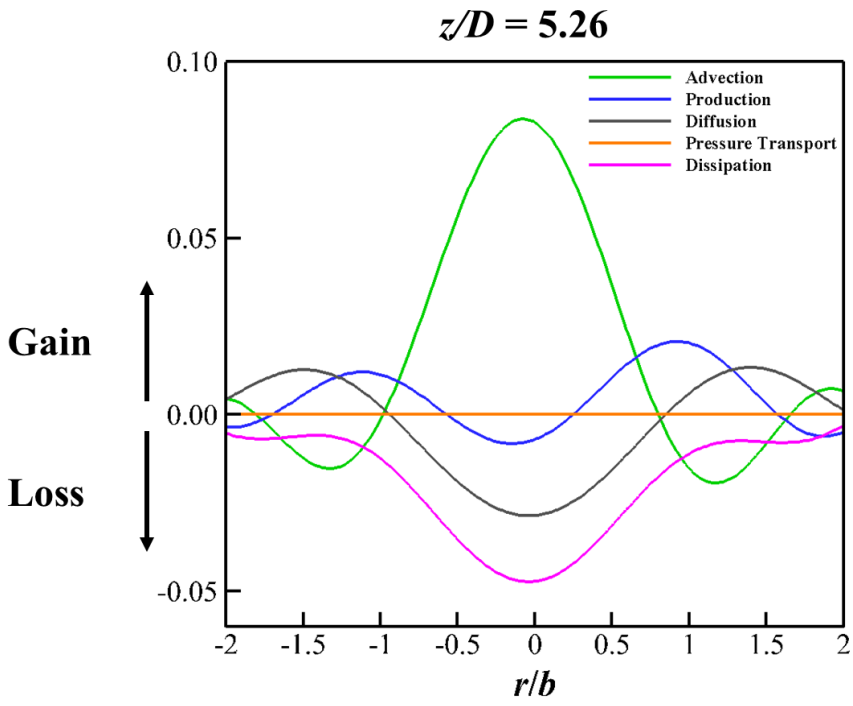

Figure 5.42. Kinetic energy budget for a single buoyant jet for Test 8.

To identify the structure of the vortex three most popular Galilean-invariant definitions are proposed: Q criterion, Δ criterion and λ_2 criterion. Defining the velocity gradient tensor $v_{i,j} = \frac{\partial v_i}{\partial x_j}$ then this second order tensor can be decomposed into the rate of strain tensor $S_{ij} = \frac{1}{2}\left(v_{i,j} + v_{j,i}\right)$ and vorticity tensor $\Omega_{ij} = \frac{1}{2}\left(v_{i,j} - v_{j,i}\right)$. Now, the characteristic equation for $v_{i,j}$ can be derived as

$$\lambda^3 + P\lambda^2 + Q\lambda + R = 0, \tag{5.36}$$

$$P \equiv -tr\left[v_{i,j}\right] = -v_{i,i}, \tag{5.37}$$

$$Q \equiv \frac{1}{2}\left(v_{i,i}^2 - v_{i,\mathrm{j}}v_{j,i}\right) = -\frac{1}{2}v_{i,j}v_{j,i} = \frac{1}{2}\left(\Omega_{ij}\Omega_{ij} - S_{ij}S_{ij}\right), \tag{5.38}$$

$$R \equiv -\det\left[v_{i.j}\right], \tag{5.39}$$

where *P*, *Q* and *R* are the three invariants of the velocity gradient tensor $v_{i.j}$.

The Q criterion searches the fluid region with positive second invariant, i.e. Q > 0. Therefore, it identifies the vortices region where the rate of vorticity is greater than the rate of strain, i.e. $\|\Omega\|^2 > \|S\|^2$ [71, 72]. The Δ criterion identifies a vortex core located at the region where the complex eigenvalues of $v_{i.j}$ exists [73]. If complex eigenvalues occur, these streamlines are closed or spiraling in a moving reference frame. The Δ criterion can be determined by the discriminant of the characteristic equation

$$\Delta = \left(\frac{Q}{3}\right)^3 + \left(\frac{R}{2}\right)^2 > 0. \tag{5.40}$$

From Equation (5.40), we see that the Q criterion (Q > 0) is more sensitive definition than the Δ criterion (Δ > 0) [71]. The λ_2 criterion searches for a pressure minimum discarding the contributions of unsteady irrational straining and viscous terms in the Navier-Stokes equations [71]. The gradient of the Navier-Stokes equations gives

$$a_{i,j} = -\frac{1}{\rho} p_{,ij} + \nu v_{i,jkk}, \tag{5.41}$$

where $a_{i,j}$ is the acceleration gradient and $p_{,ij}$ is symmetric pressure Hessian. Then the equation is decomposed into symmetric and antisymmetric parts

$$a_{i,j} = \underbrace{\left[\frac{DS_{ij}}{Dt} + \Omega_{ik}\Omega_{kj} + S_{ik}S_{kj}\right]}_{\text{Symmetric}} \underbrace{\left[\frac{D\Omega_{ij}}{Dt} + \Omega_{ik}S_{kj} + S_{ik}\Omega_{kj}\right]}_{\text{Antisymmetric}}. \tag{5.42}$$

The symmetric part is the vorticity transport equation and it can be written as

$$\frac{DS_{ij}}{Dt} - \nu S_{ij,kk} + \Omega_{ik}\Omega_{kj} + S_{ik}S_{kj} = -\frac{1}{\rho} p_{,ij}. \tag{5.43}$$

Neglect the contributions of unsteady irrational straining (the first term) and viscous effect (the second term), we obtain $S^2 + \Omega^2$ to determine the local pressure minimum due to a vortical motion. The λ_2 criterion defines 'a vortex core as a connected region with two negative eigenvalues of $S^2 + \Omega^2$ [71].' Let λ_1, λ_2 and λ_3 be the eigenvalues and $\lambda_1 \geq \lambda_2 \geq \lambda_3$, then the λ_2 criterion can be found where $\lambda_2 < 0$.

For the flows in two dimensional, $v_3 = 0$ then the velocity gradient tensor $v_{i,j}$ becomes

$$v_{i,j} = \begin{bmatrix} v_{1,1} & v_{1,2} & 0 \\ v_{2,1} & v_{2,2} & 0 \\ 0 & 0 & 0 \end{bmatrix}. \tag{5.44}$$

Since the determinant of the velocity gradient tensor R vanishes, roots of the cubic characteristic equation becomes

$$\lambda_{2D} = 0, \ \frac{P_{2D} \pm \sqrt{P_{2D}^2 - 4Q_{2D}}}{2}, \tag{5.45}$$

where

$$P_{2D} = v_{1,1} + v_{2,2} = 0 \ \text{(for incompressible flow)}, \tag{5.46}$$

$$Q_{2D} = v_{1,1}v_{2,2} - u_{1,2}u_{2,1}, \tag{5.47}$$

$$R_{2D} = 0. \tag{5.48}$$

Now we obtain

$$\lambda_{2D} = \pm\sqrt{-Q_{2D}}. \tag{5.49}$$

To satisfy Q criterion, i.e. $Q_{2D} > 0$, the eigenvalues should be imaginary. Therefore, in incompressible two dimensional flows the three criterions are identical.

The Q criterion is applied to the averaged velocity profile and significantly important vortical structures are extracted as shown in Figure 5.43. Toroidal vortices are located near the inlet at (r, z) = (-2.12, 1.15) and (2, 1.47) and they contributes to the development of the axial velocity profile. Turbulent shear layer vortices are created due to the Kelvin-Helmholtz (KH) vortices where velocity differences stimulate the instability across the jet boundary. Secondary vortices are created due to the impingement on the surface at the distance 0.5 cm from the wall. They occupy very large portion of the top

surface and their size is about 11 cm. In these areas, vortices are formed by vortex-pairing of primary KH vortices from the downstream with secondary wall separated ring vortices detached from the surface. There are also recirculation zones located between KH and secondary vortices but their magnitude is small and stationary. Secondary vortices have the highest energy contained within the eddy structure followed by KH, toroidal and recirculated vortices.

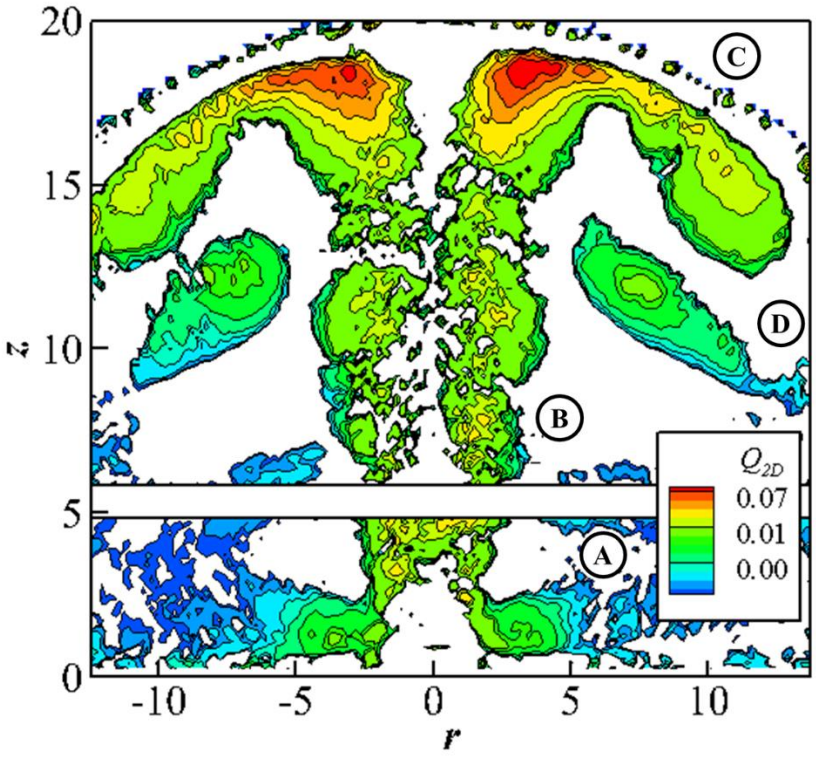

Figure 5.43. Vortical structure of the turbulent buoyant jet applied with the Q criterion. A: toroidal vortices due to RT instability; B: KH vortices due to turbulent shear layers; C: Secondary vortices due to the jet impingement and D: recirculation zone.

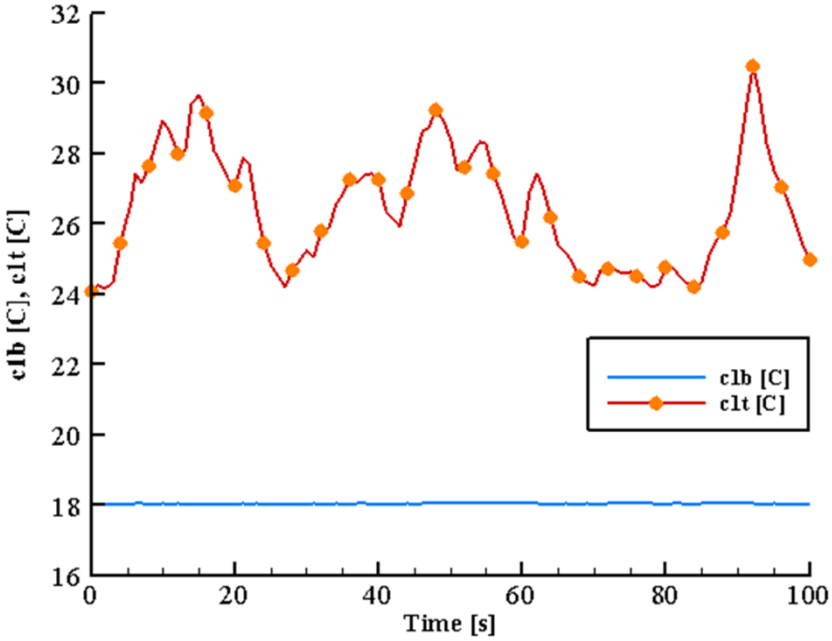

Figure 5.44. Temperature history in the range of 0 to 100 where dots represent each four seconds.

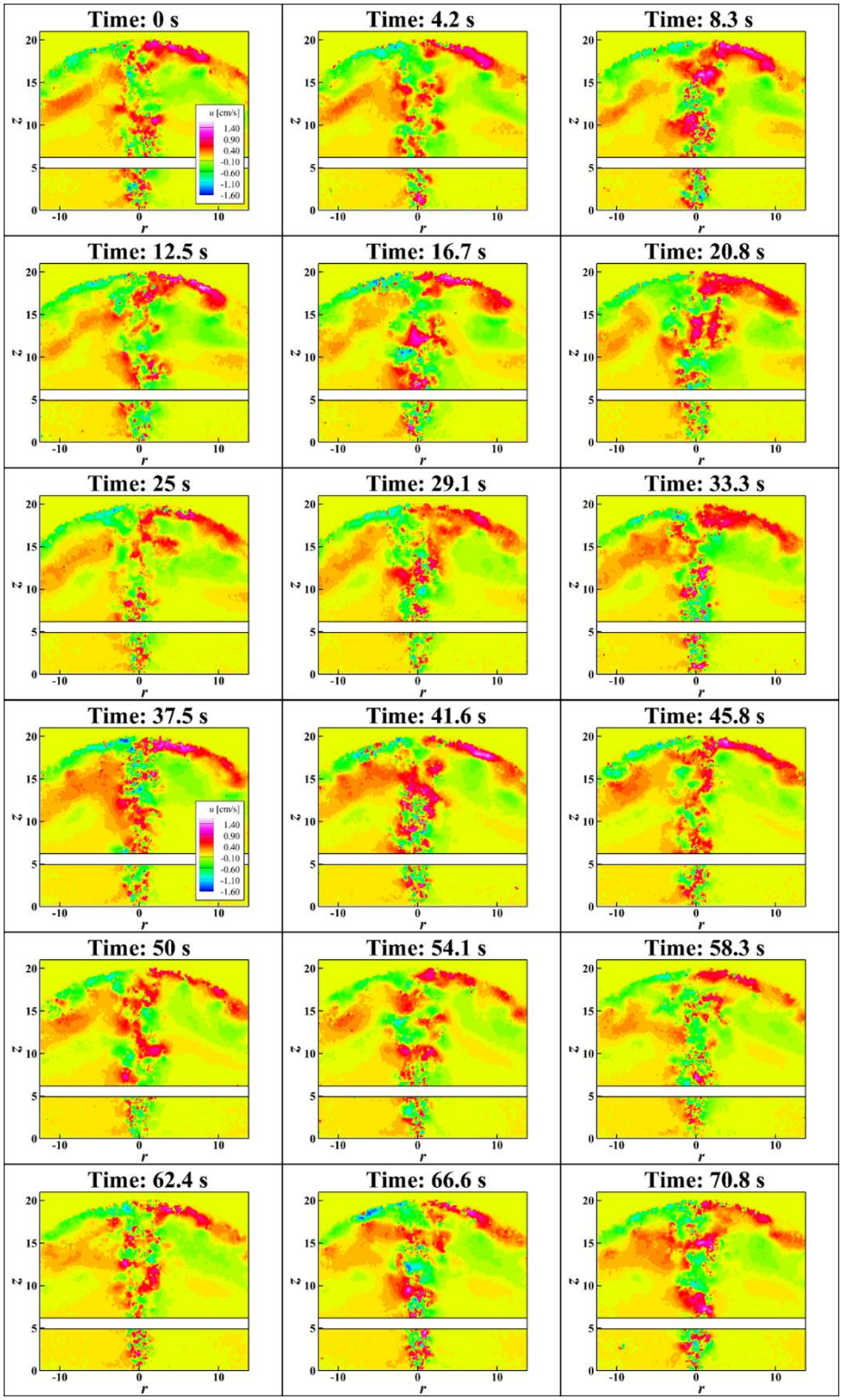

Figure 5.45. Transient contours of the radial velocity for a single jet.

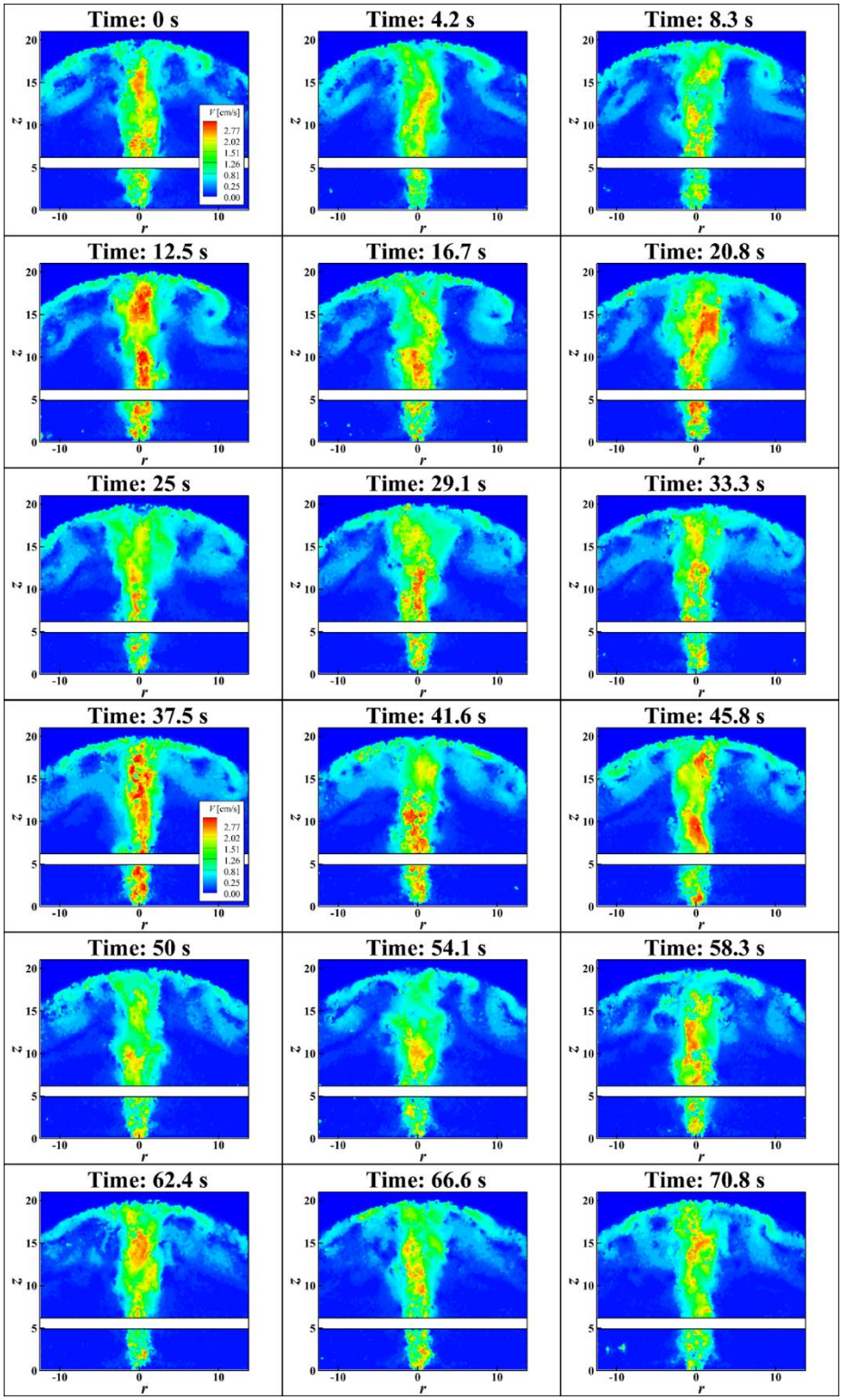

Figure 5.46. Transient contours of the velocity magnitude for a single jet.

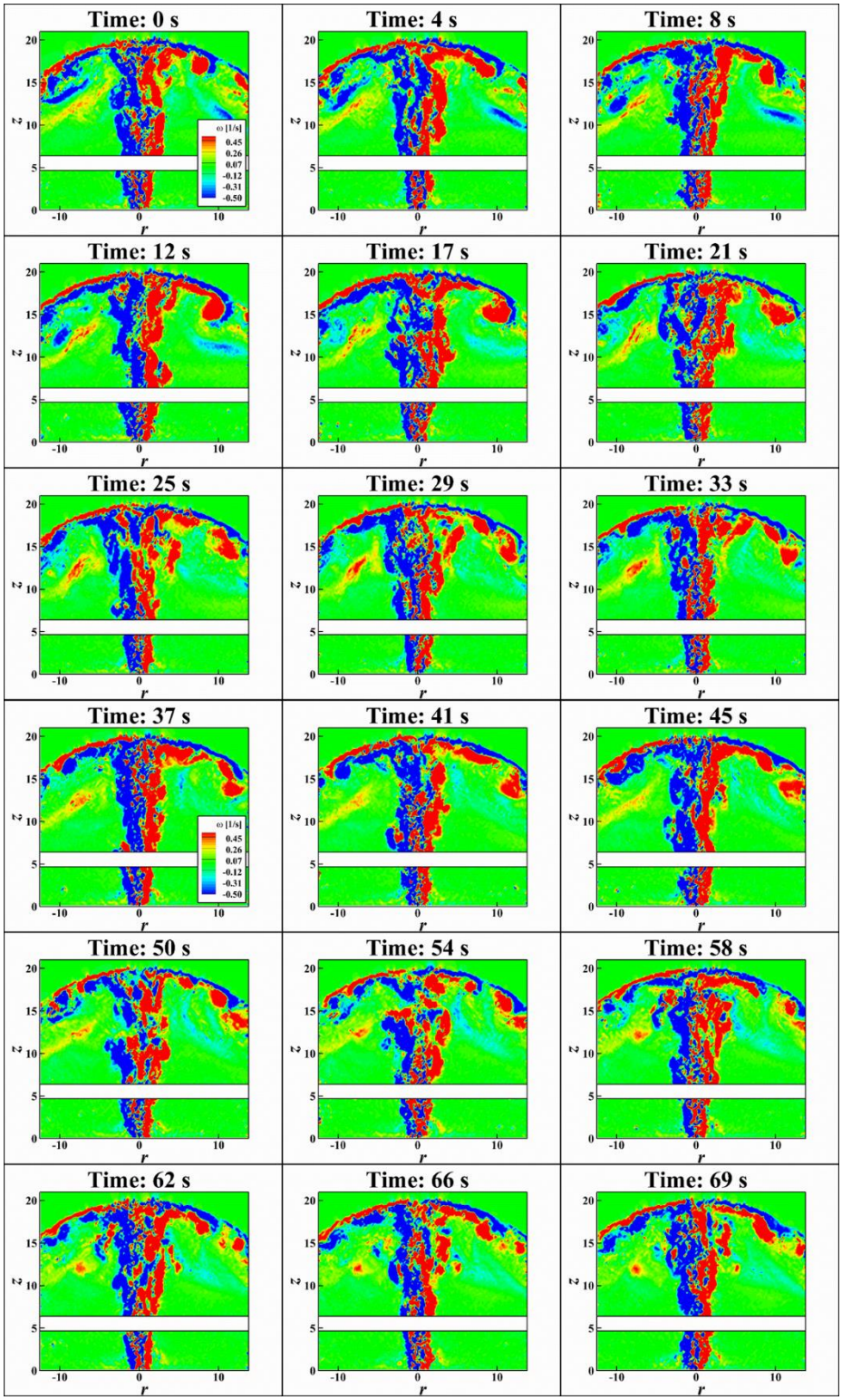

Figure 5.47. Transient contours of the vorticity for a single jet.

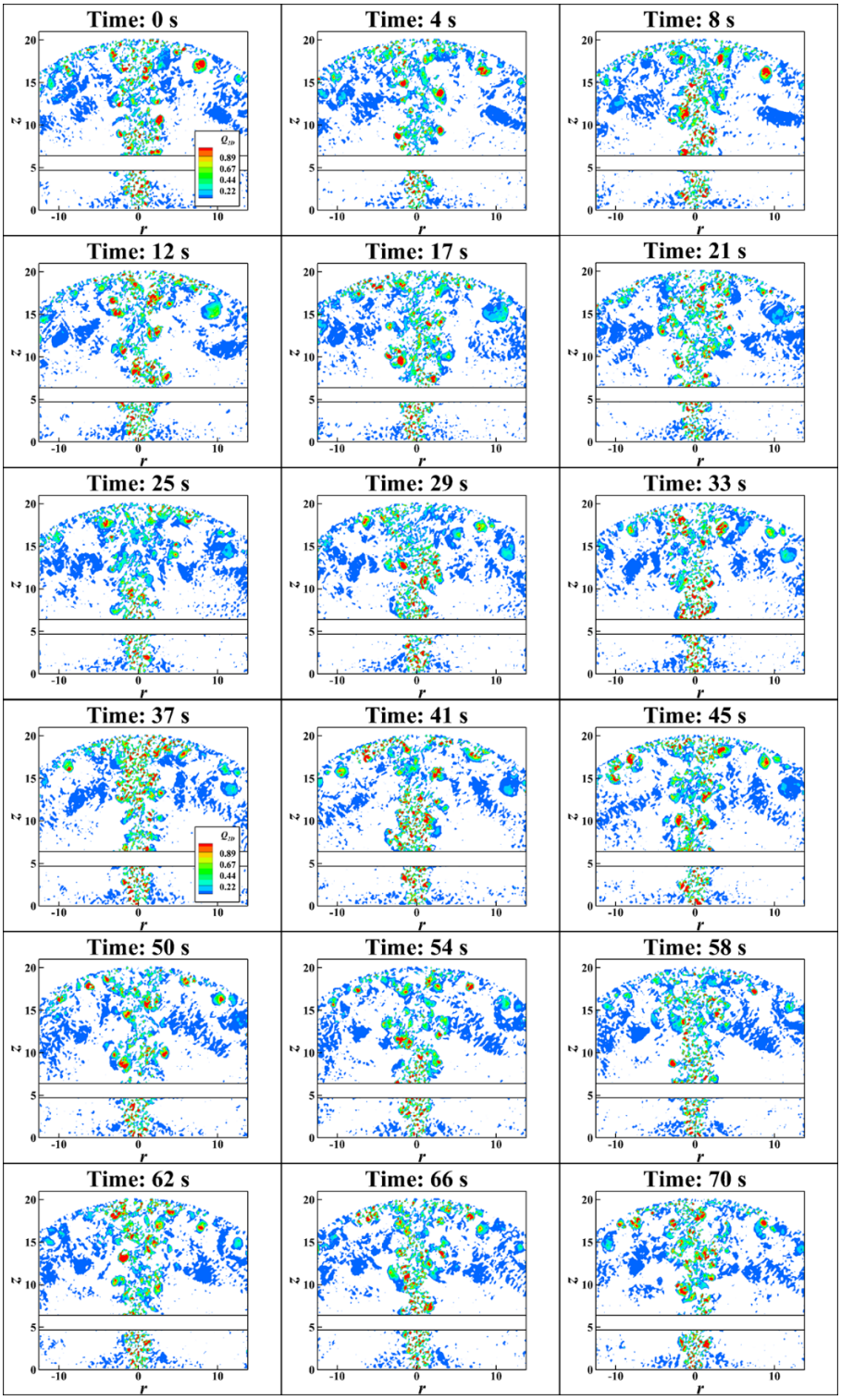

Figure 5.48. Moving averaged transient contours of the Q criterion for a single jet.

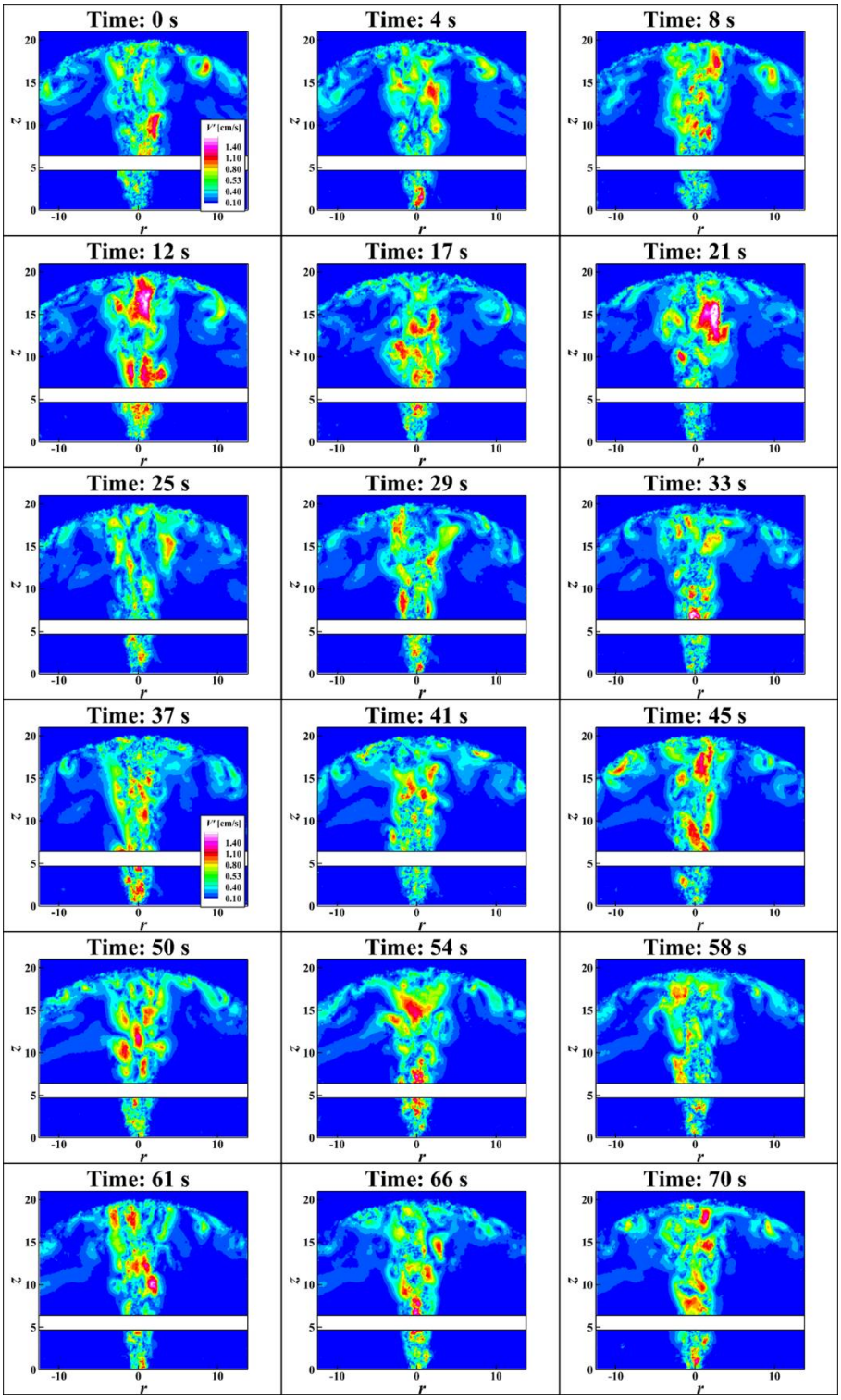

Figure 5.49. Moving averaged transient contours of the resolved fluctuating velocity magnitude for a single jet.

Next the vortical structures, i.e. eddies, of the flow in time frames are investigated. Instantaneous PIV velocity data is used to identify the structure of eddies. Time evolution of the temperature profiles are plotted in Figure 5.44, the velocity profiles are plotted in Figure 5.45 to 5.47 and the moving averaged velocity profiles are plotted in Figure 5.48 and 5.49. Instantaneous velocity and vorticity profiles show the trend of the evolution of the buoyant jet on the top surface but do not provide relevant eddy structures inside the jet. Therefore the moving average and Q criterion to our instantaneous PIV velocity data is applied. An *N*-moving average (denoted MA) is defined as follows:

$$v_{MA} = \frac{1}{N_{MA}} \sum_{n=i}^{i+N_{MA}-1} v_n, \tag{5.50}$$

where v_{MA} is velocities in x and y directions at every x and y location, N_{MA} is the number of frames to be moving-averaged (here N_{MA} = 10) from i to $i + N_{MA} - 1$. Then the instantaneous velocity $\tilde{v}$ can be decomposed into the time-averaged velocity v_{MA}, a resolved fluctuation v'' and fluctuation velocity v'. Therefore the Equation (5.2) becomes,

$$\begin{aligned} \tilde{v} &= v + v' \\ &= v_{MA} + v'' + v'. \end{aligned} \tag{5.51}$$

Time steps are set to have two cycles of the period 33 s since the characteristic puffing frequency is obtained 0.03 Hz. Note that the flow is fully turbulent so the eddy structure is not periodic for a corresponding periodic temperature profiles in time. The moving average velocity profiles are used to show the detailed turbulent eddy structures since this method will smooth out the structures of eddies and show better in visualization. However, the determination of N_{MA} should be carefully made because when N_{MA} is too

large the moving average fields neither capture the eddy structures nor represent the real physical behavior. Ten time steps are averaged so each snapshot have 1 s time distance instead of 0.1 s. The Q criterion is again applied to the moving averaged velocity profiles. As shown in Figure 5.48, the behavior of the turbulent buoyant jet is not straight forward in streamwise direction and continuous in time but have meandering discontinuous behavior. In time the motion of the buoyant jet is undulated and meandered along the center axis. These motions are very unstable and vary in time and surprisingly when they are averaged their behaviors statistically converge into Gaussian distributions. Along the boundary of the jet four counter-rotating vortices are created alternately as it shown in 4 s. The intensity of the rotation is stronger within the jet while after impinging to the surface its magnitude decreases. Several counter-rotating RT vortices are observed at $z < 5$ cm ($z/D < 2.62$) and these eddies are magnified as they travels in streamwise direction becoming KH vortices at $z > 6$ cm ($z/D > 3.15$). These eddy paths perfectly correspond to the location of the jet width and the average KH vortices. Therefore it is concluded that these KH eddies contribute to the entrainment mechanism by absorbing ambient fluid at the boundary as Landel et al. expected [74]. Recirculated vortices are always located between KH and secondary vortices. They are neither intensified nor disappeared. In addition, KH eddies inside of the jet move faster than that of outside of the jet. So the average vertical velocity at the center core is maximized due to core eddies. The KH vortices become larger and stay to accumulate until they impinge to the surface. Most of eddies from core to peripheral are decelerated and combined near the surface at $r = \pm 3$ cm and $z = 18.5$ cm ($r/D = 1.57$, $z/D = 9.71$) creating larger vortex pairs on the top. The

mechanism of these vortex pairs is following [75]: 1. Primary KH vortices are detached from the jet width line and attached to the surface. 2. At the surface these primary vortices generate counter-rotating secondary vortices in the presence. 3. Primary KH vortices and secondary vortices induced by primary vortices are paired and detached from the surface: a formation of vortex-dipole. 4. Primary KH vortices and wall separated vortices (vortex-dipole) leave the wall. These vortex-pairs become slower than KH vortices as they flow across the dome surface but bigger in size. At r = ± 11 cm and z = 15 cm (r/D = 5.77 and z/D = 7.87), vortex-pairs become stationary for 25 ~ 50 s, accumulating more eddies to become larger and larger to dissipate to heat. Usually they absorb two or three eddies until they are dissipated. Essentially, two cycles are needed to completely observe the temporal behavior of vortex-pairing.

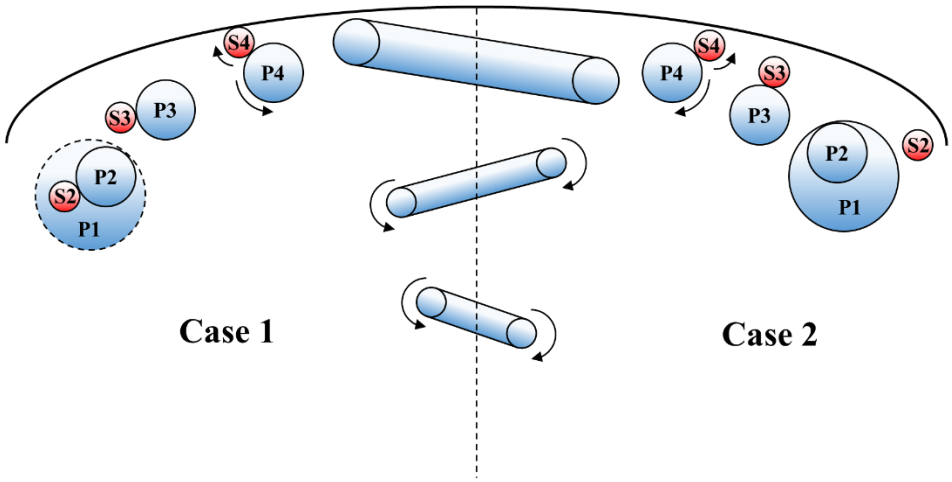

Figure 5.50. Two cases of vortex dynamics for the jet impingement on the concave surface.

Dynamics of vortex-dipole is similar to vortex dynamics associated with the flat surface [76]. However the concave surface in the present study has very distinct two cases as shown in Figure 5.50. The first case is called 'unfavorable interactions.' When undulated KH ring vortices (primary vortex: P4) impinge on the surface they stretch to left and right side of the domain. They induced secondary vortices (S4) on the surface and paired each other. Then the secondary vortices (S3) are detached from the surface and become wall separated vortices. Until here the dynamics are the same as the flat surface. However, the concave or dome surface generate centripetal forces and rotates the vortex-pairs. Depending on the locations of the primary vortices (P3) and wall separated vortices (S3) the previous existed vortices (P2) can be either attenuated or amplified. When wall separated vortices (S3) encounter primary vortices (P2) first, the magnitude of the previous existed primary vortices (P1) are attenuated and dissipated to heat (case 1). On the other hands, the second case, i.e. 'favorable interactions,' can happen when primary vortices (P3) meet primary vortices (P2) first they merge each other and becomes bigger (P1) (case 2). Favorable interactions can be continuously recurring until unfavorable interactions happens. These evolution of vortex-pair interactions cannot be predicted and no cyclic period can be obtained since the interactions are random and eddy structures are turbulent.

The moving average resolved velocity magnitude contours (see Figure 5.49) represent the fluctuation velocities of the unsteady Reynolds averaged Navier Stokes (URANS) equation with the time step of 1 s. It is defined as

$$V' = \sqrt{\left(v_i'' + v_i'\right)^2} = \sqrt{\left(u'' + u'\right)^2 + \left(w'' + w'\right)^2}. \qquad (5.52)$$

This shows that typically three vortices are created within the jet: the left, right and core vortices providing Reynolds decomposed fluctuation. These three eddies are important since they represent the core and KH vortices. Reynolds decomposition is very useful to identify the turbulent eddy structures other than Q criterion and Galilean decomposition [77].

6. TRIPLE BUOYANT JETS STUDY

In this section, the results of triple buoyant jet experiments will be discussed. First, the same analytical approach is considered to obtain the essence of this triple jets' physical phenomena. Second, the comparison between a single jet and triple jets is considered to comprehend the different velocity distributions and vortical structures. Lastly, the shear stress distributions between the single jet and triple jet studies are analyzed to understand the potential fatigue and thermal stresses on the surface of the dome which could lead to additional severe accidents scenarios.

6.1 Experiment Result

Triple buoyant jet experiment is performed with the operation of l3, c1 and r3 heated pipes as shown in Figure 5.9. The test procedures are the same as single buoyant jet experiments. The steady state average contour plots are shown from Figure 6.1 to 6.3 and their radial profiles are shown from Figure 6.4 to 6.8. The locations of the maximum (0.71 cm/s) and minimum (-0.69 cm/s) radial velocity are (r, z) = (-7.3, 18.09) and (6.45, 18.58) cm, respectively. The magnitude is very similar to the single jet experiment but the location is 0.8 ± 0.445 cm (13%) wider than that of the single jet. It is attributed by two additional jets located to the side of the center jet. The locations of recirculation zones for radial velocities are also widened and lowered from (9.4 ± 0.135, 13.11 ± 0.145) for a single buoyant jet to (11.77 ± 0.5, 9.68 ± 0.175) for triple buoyant jets which is 25 % wider

and 26 % lower. The maximum axial velocity is obtained at the center jet (1.69 cm/s) which is 8% higher than that of a single jet whereas the entrainment of the ambient fluid is observed by the left and right side of the jet as well as two sides of a center jet. As shown in Figure 6.9, multiple jets have two important point in general: Merging point (MP) and combining point (CP). A MP is defined by the coincidence of the dividing streamlines where the mean axial velocities between jets become zero. A CP is defined by the coincidence of the jet centerline where the mean axial velocities become a single jet profile. Average MP is obtained 0.8 cm and no CP is obtained for the present case. Therefore most of the region is a merging region. In addition the locations of two counter-rotating vortices are also lowered and widened. The location of vortices are moved toward the outlet compared with the result from a single jet. Only the vorticity outside of the jet width can reach to the top surface (see Figure 6.1 (d)). The axial and vertical Reynolds stress is maximized where the jet develops and merge which is similar to single jet tests.

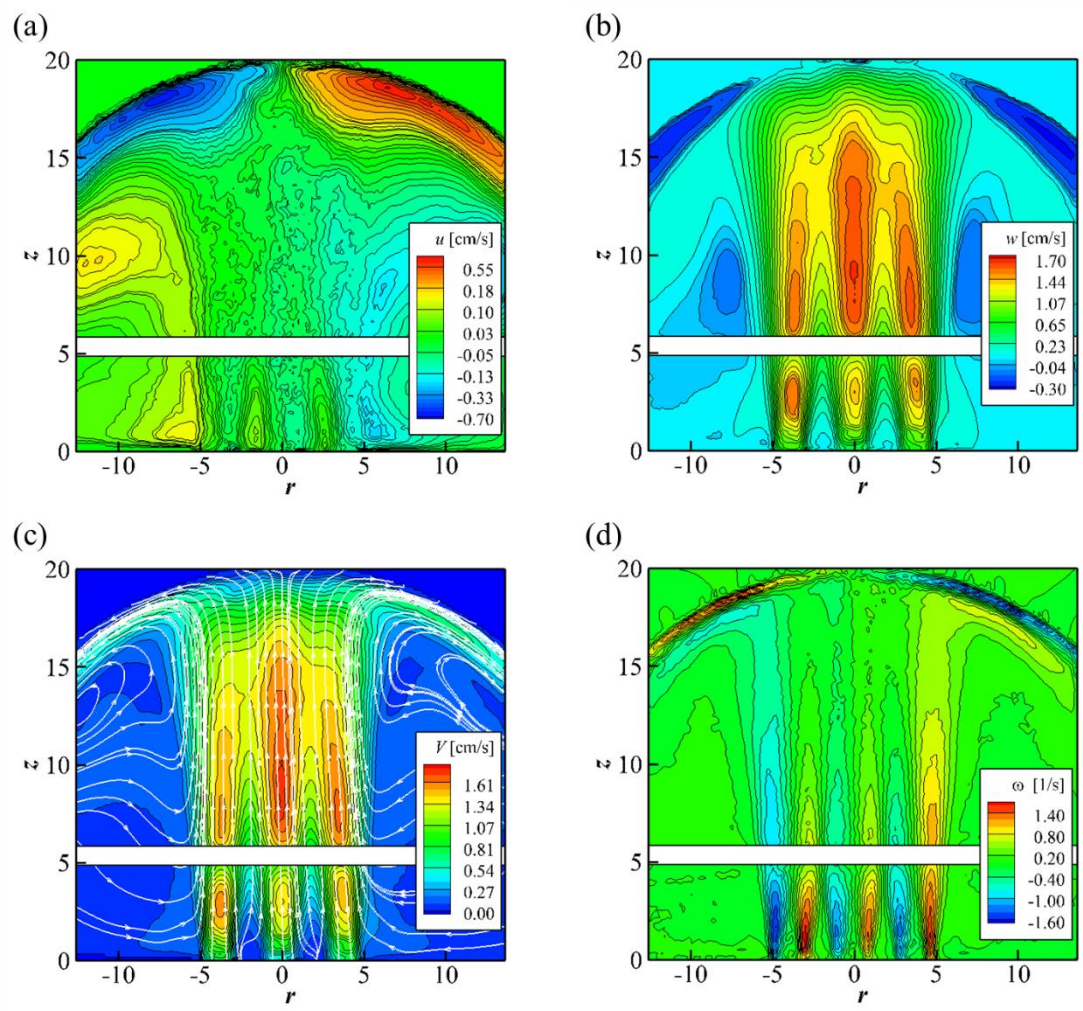

Figure 6.1. Contours of averaged triple buoyant jets; (a) mean radial velocity; (b) mean axial velocity; (c) mean velocity magnitude with streamlines; and (d) vorticity (ω).

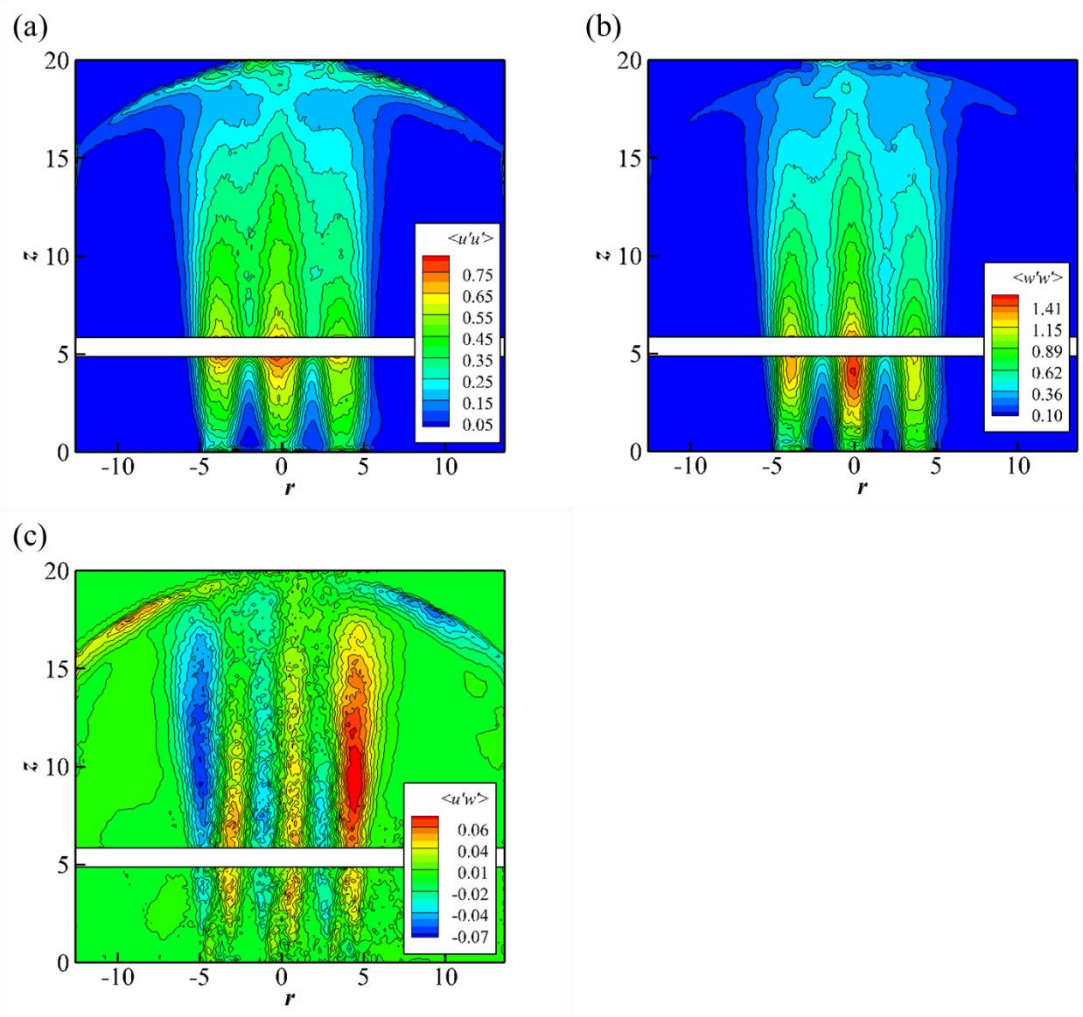

Figure 6.2. Contours of averaged triple buoyant jets; (a) Reynolds stress <*u'u'*>; (b) Reynolds stress <*w'w'*>; and (c) Reynolds stress <*u'w'*>.

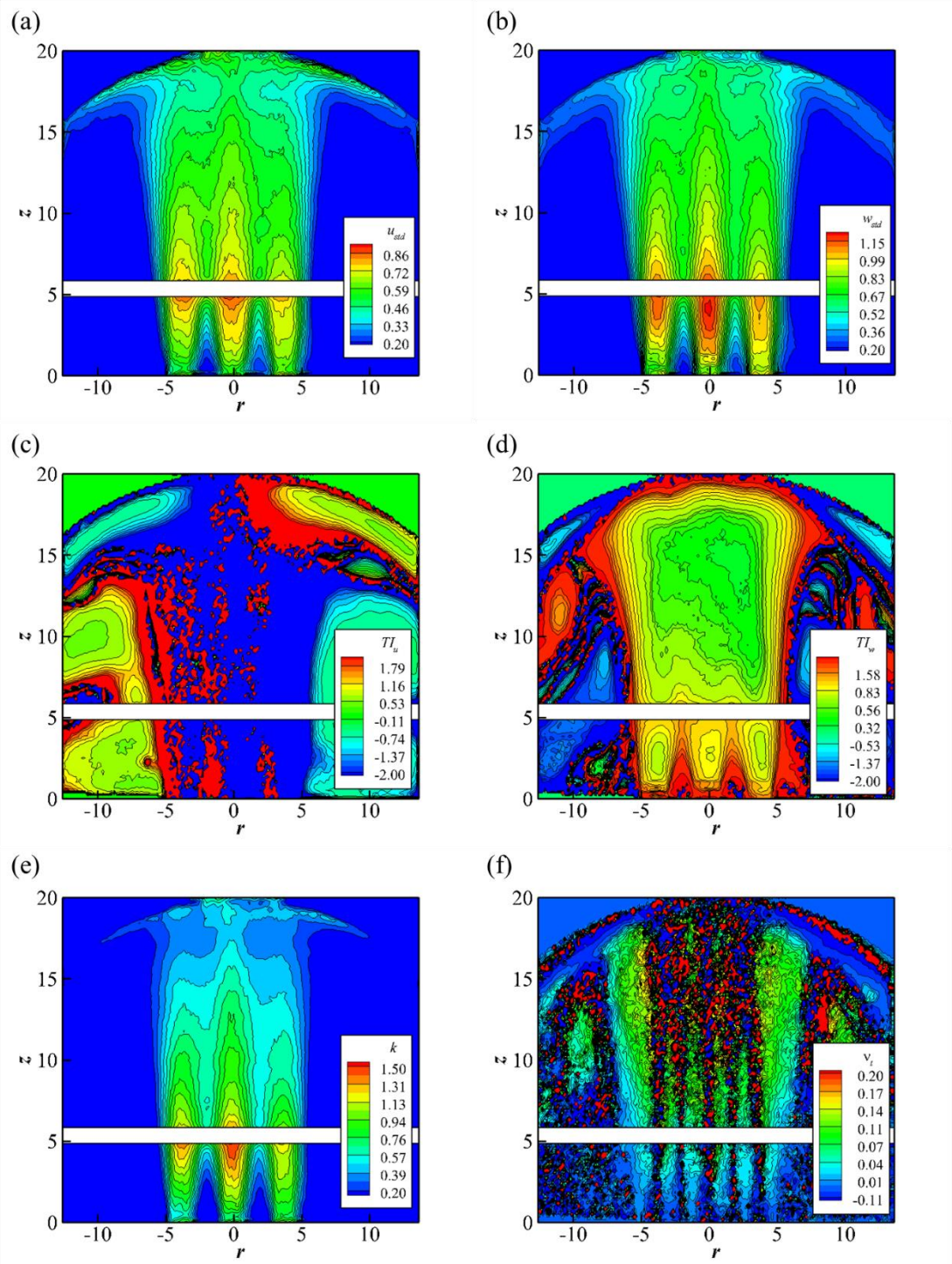

Figure 6.3. Contours of averaged triple buoyant jets; (a) standard deviation of radial velocity; (b) standard deviation of axial velocity; (c) turbulent intensity in radial direction; (d) turbulent intensity in axial direction; (e) Turbulent kinetic energy (k); and (f) turbulent viscosity (ν_t).

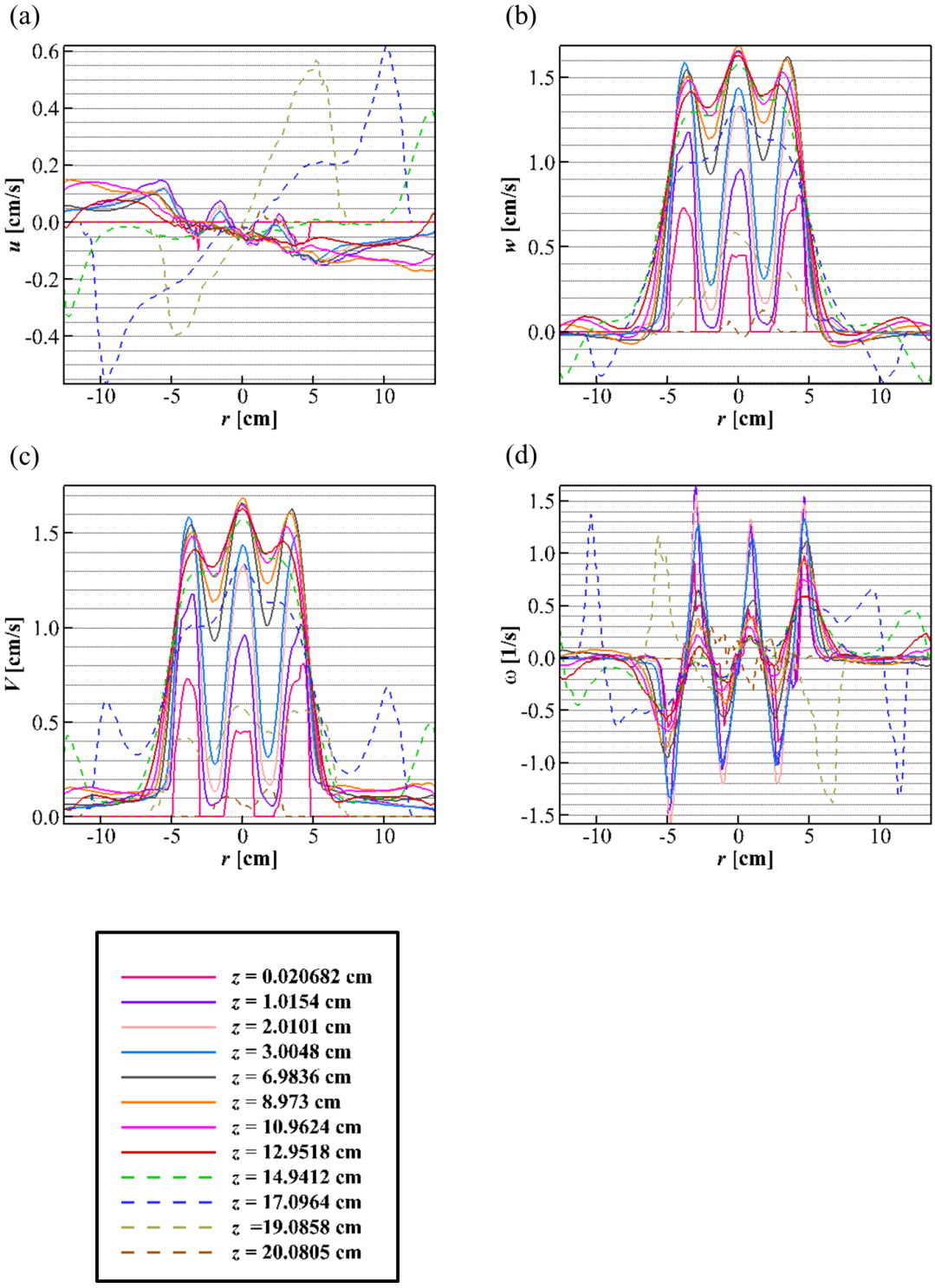

Figure 6.4. Radial profiles of (a) radial velocity, (b) axial velocity, (c) velocity magnitude and (d) vorticity for triple buoyant jets.

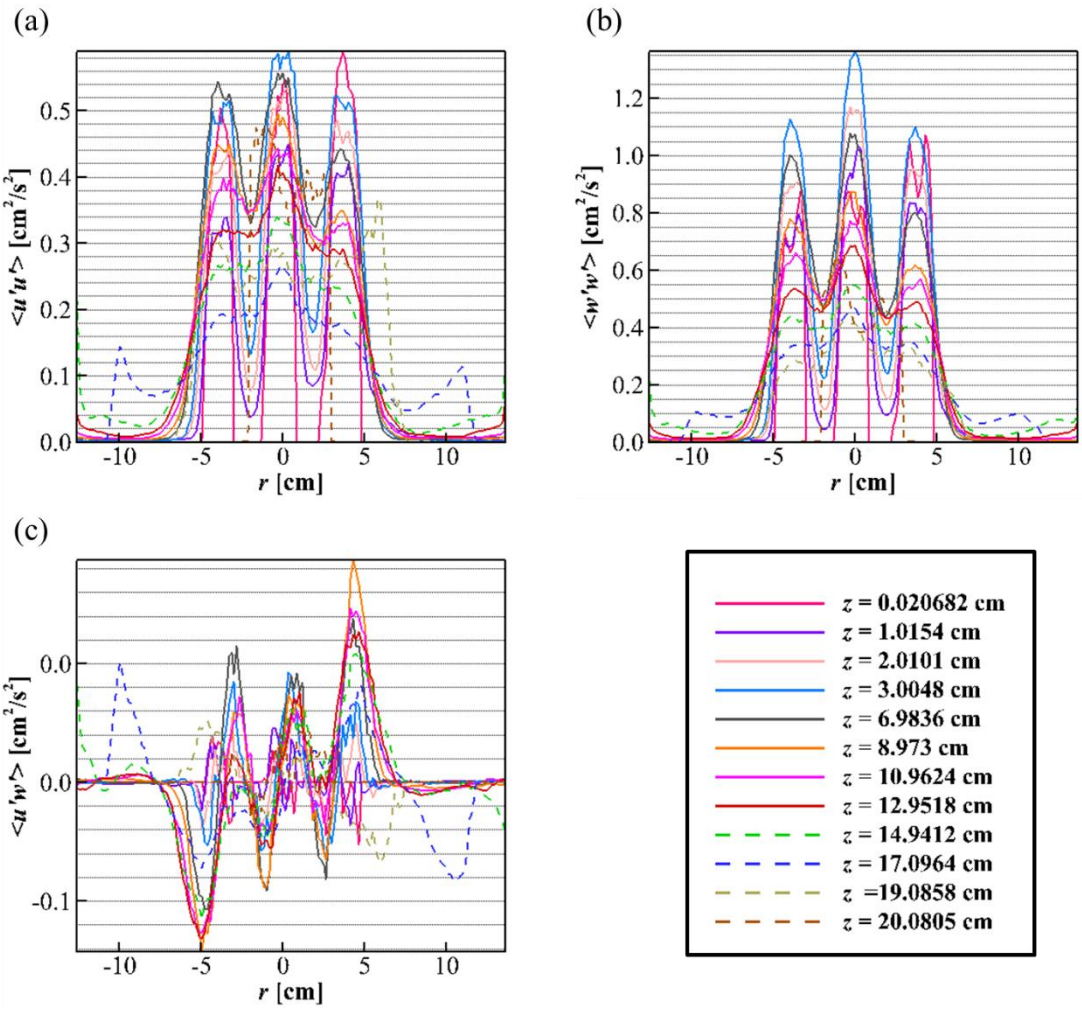

Figure 6.5. Radial profiles of Reynolds stresses ((a) - (c)) for triple buoyant jets.

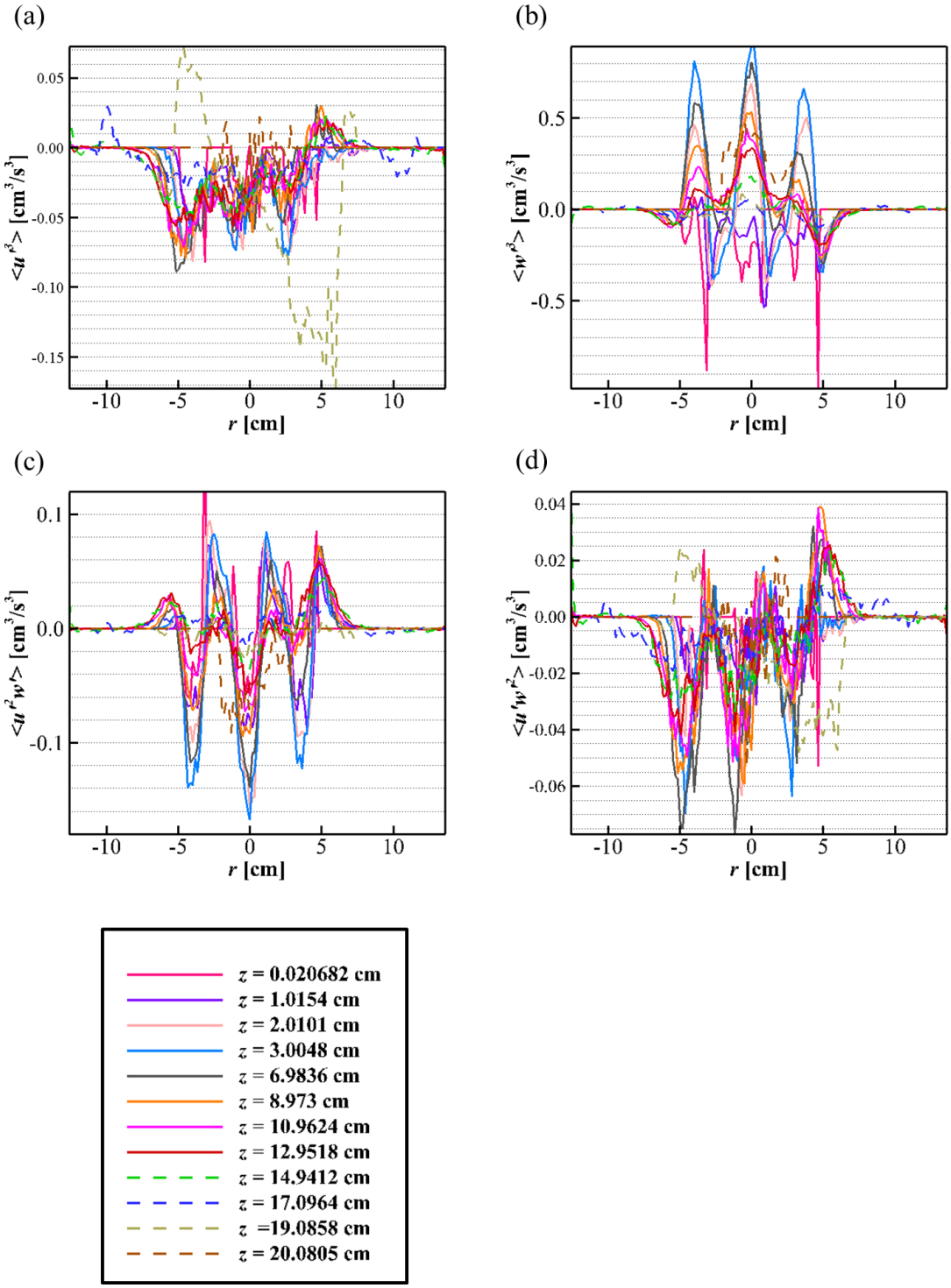

Figure 6.6. Radial profiles of non-dimensional third moments ((a)-(d)) for triple buoyant jets.

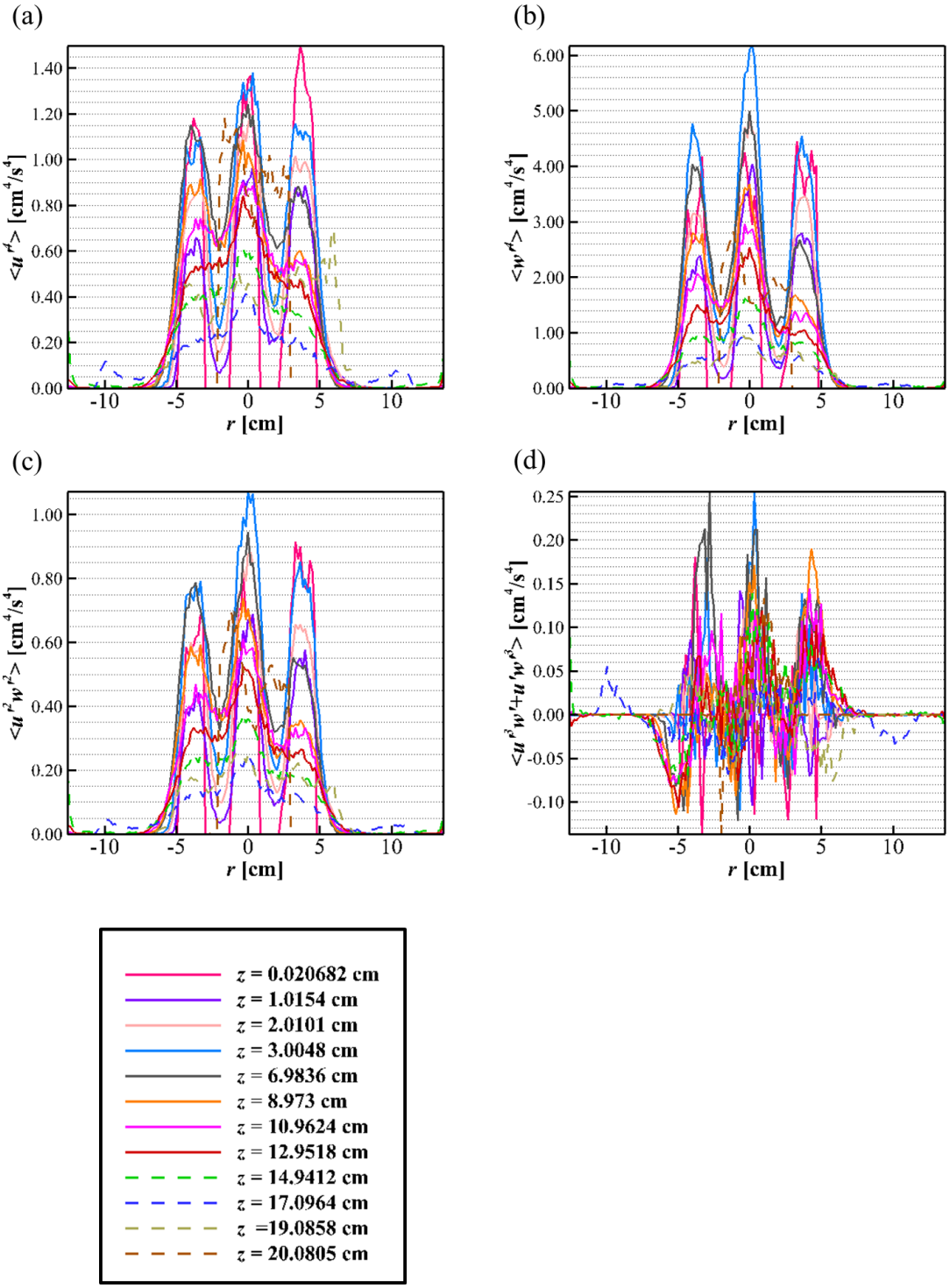

Figure 6.7. Radial profiles of fourth moments ((a)-(d)) for triple buoyant jets.

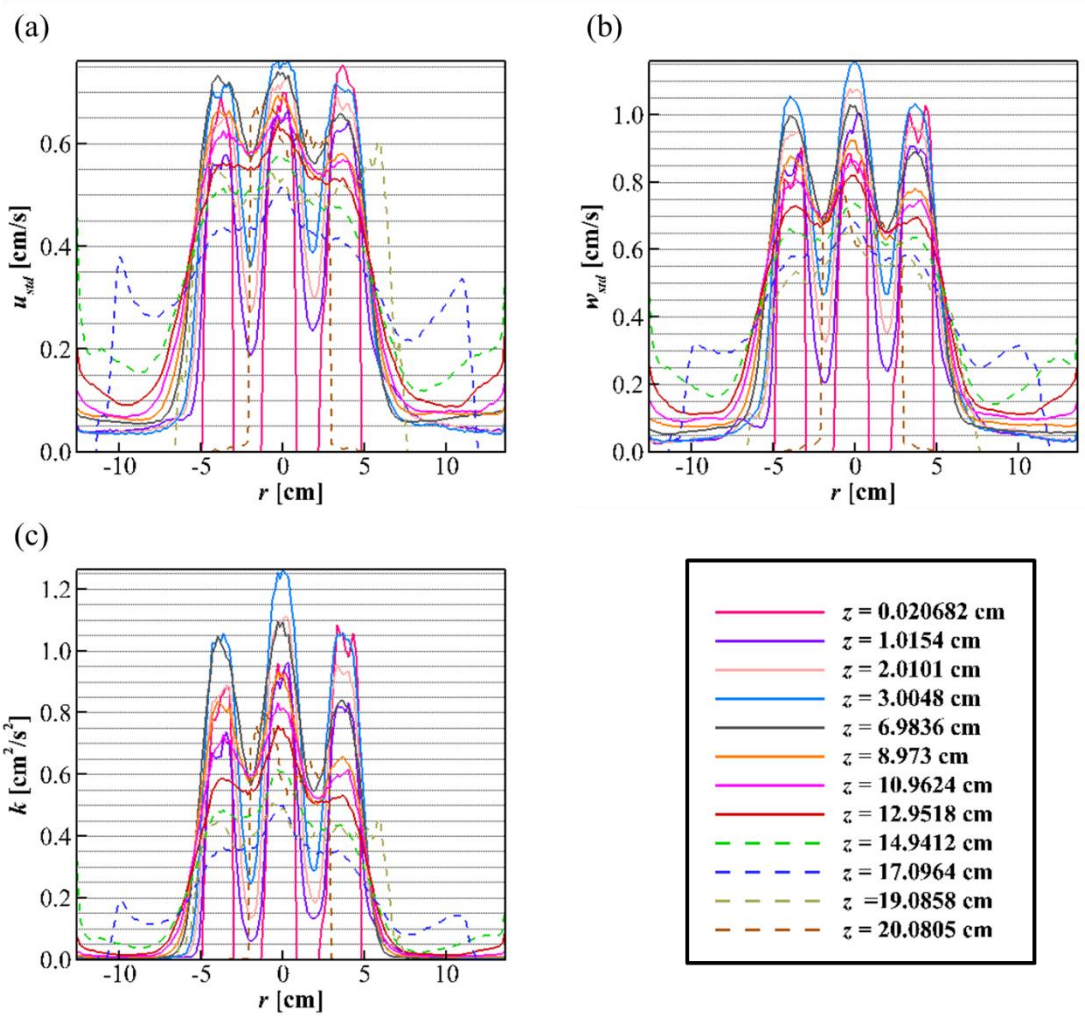

Figure 6.8. Radial profiles of the standard deviations of (a) radial velocity and (b) axial velocity; and (c) kinetic energy distribution for triple buoyant jets.

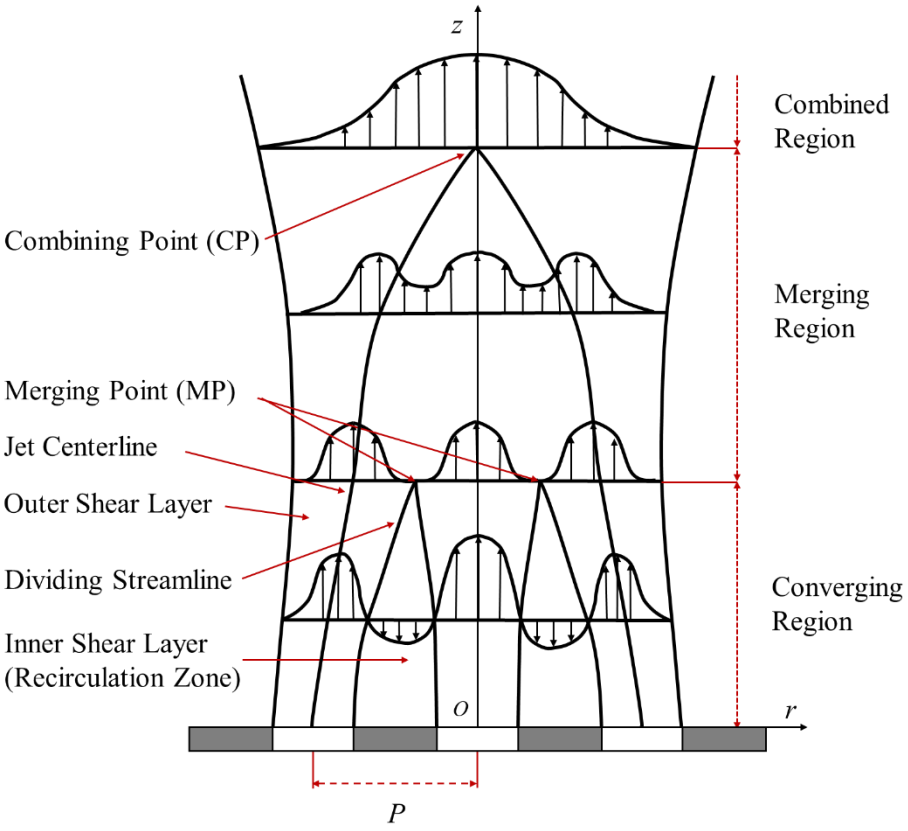

Figure 6.9. A schematics of triple buoyant jet.

Time evolution of temperature profiles for three inlets, inlet/outlet of the system, CJ inlet/outlet, DFT of three inlets and pressure are shown in Figure 6.10 and the summarized temperature and flowrate data are listed in Figure 6.11 and 6.12. The average bottom temperature (l3b, c1b, r3b) is 22.33 °C and the average top temperature (l3t, c1t, r3t) is 41.03 °C. The average temperature difference of bottom and top temperatures is 18.71 °C which is 120% higher than that of single jet tests. The bottom temperatures are 23 % higher than single jet tests due to the restriction of the temperature condition (initial temperatures). The top temperature reached 54% higher temperature than single jet tests. The flowrate is 2.8 times larger than that of single jet tests. A DFT plot shows the dominant characteristic puffing frequencies of three inlet pipes (l2t, c1t, r3t) and are obtained as 0.04, 0.043 and 0.031 Hz, respectively. Therefore the mean characteristic puffing period is obtained 25 s and is applied to one period cycle for the transient time period.

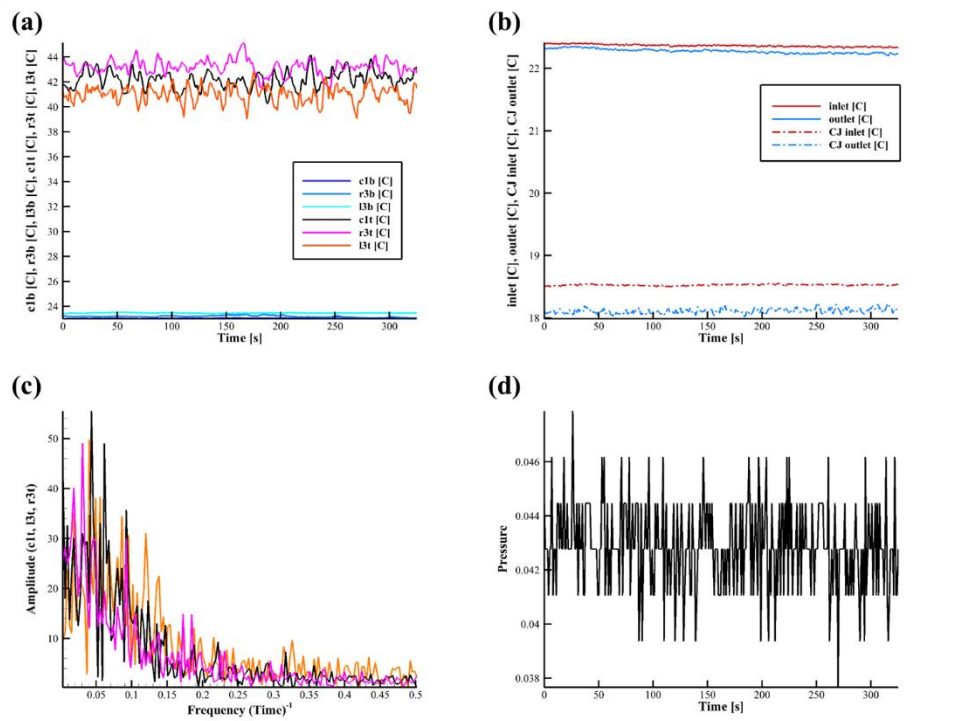

Figure 6.10. Time series of temperature at location r = 0 and z = - 2.54 cm in Test 6. Temperature time history of (a) 3 inlets and outlets and (b) system inlet/outlet and CJ inlet/outlet. (c) DFT of the temperature time series on three inlets. (d) Pressure time history (psid).

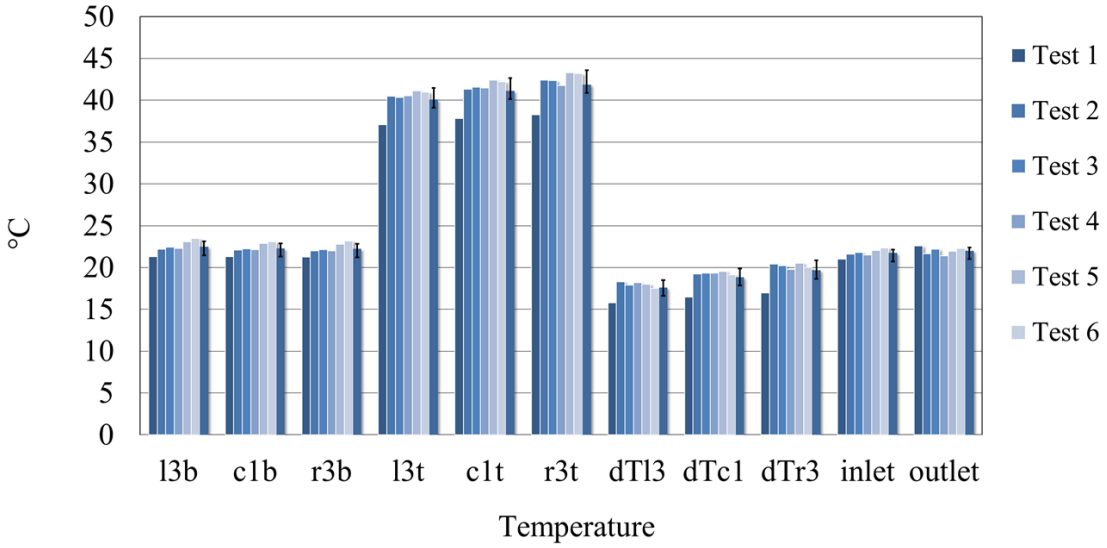

Figure 6.11. Temperature data for triple jets at each location for six test results and averaged temperature data.

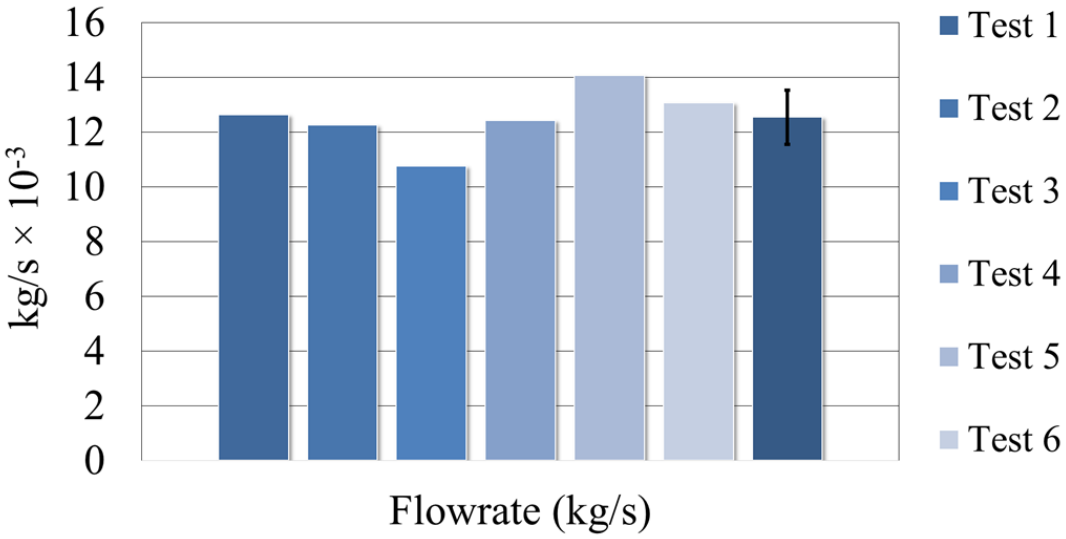

Figure 6.12. Flowrate data for triple jets at each location for six test results and averaged temperature data.

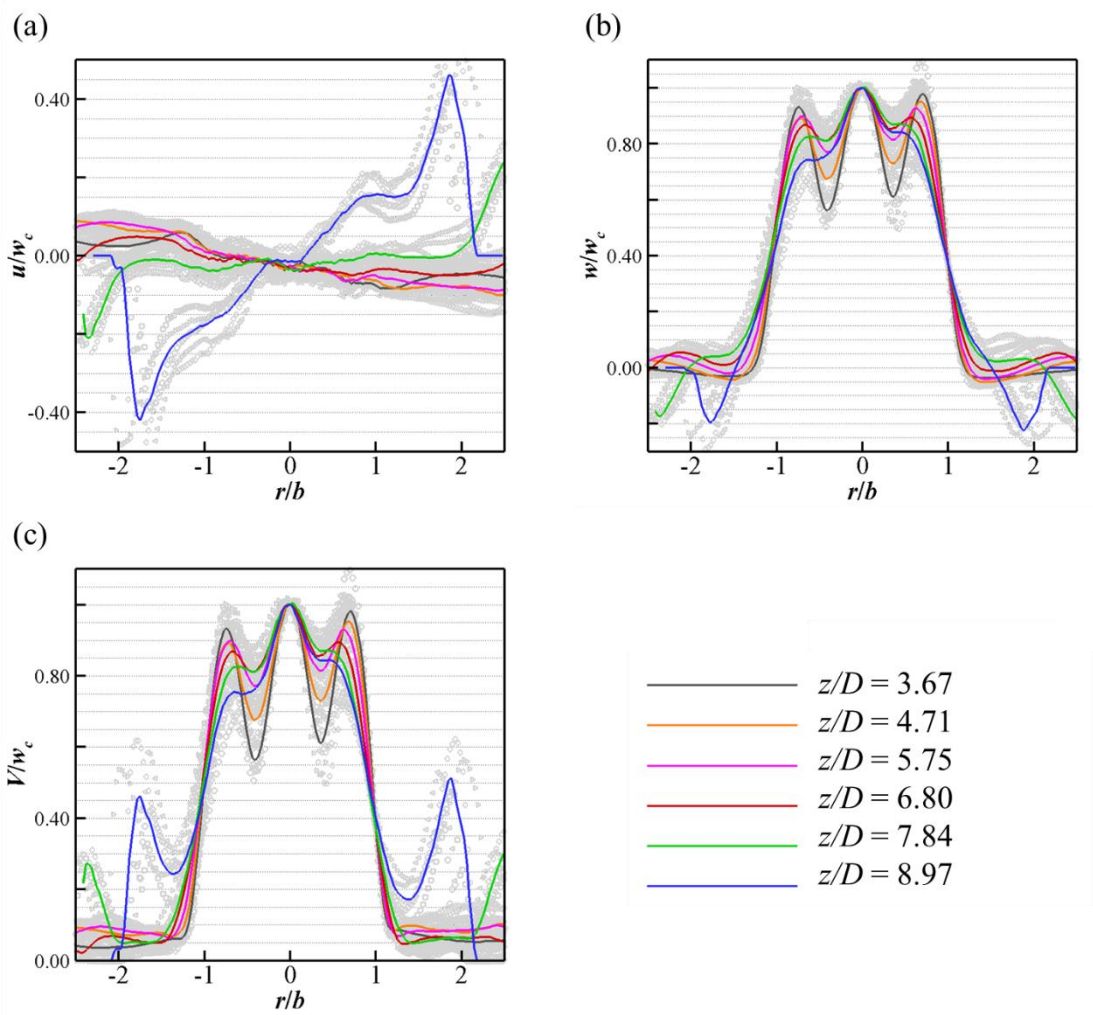

Figure 6.13. Radial profiles of non-dimensional (a) radial velocity, (b) axial velocity and (c) velocity magnitude for triple buoyant jets.

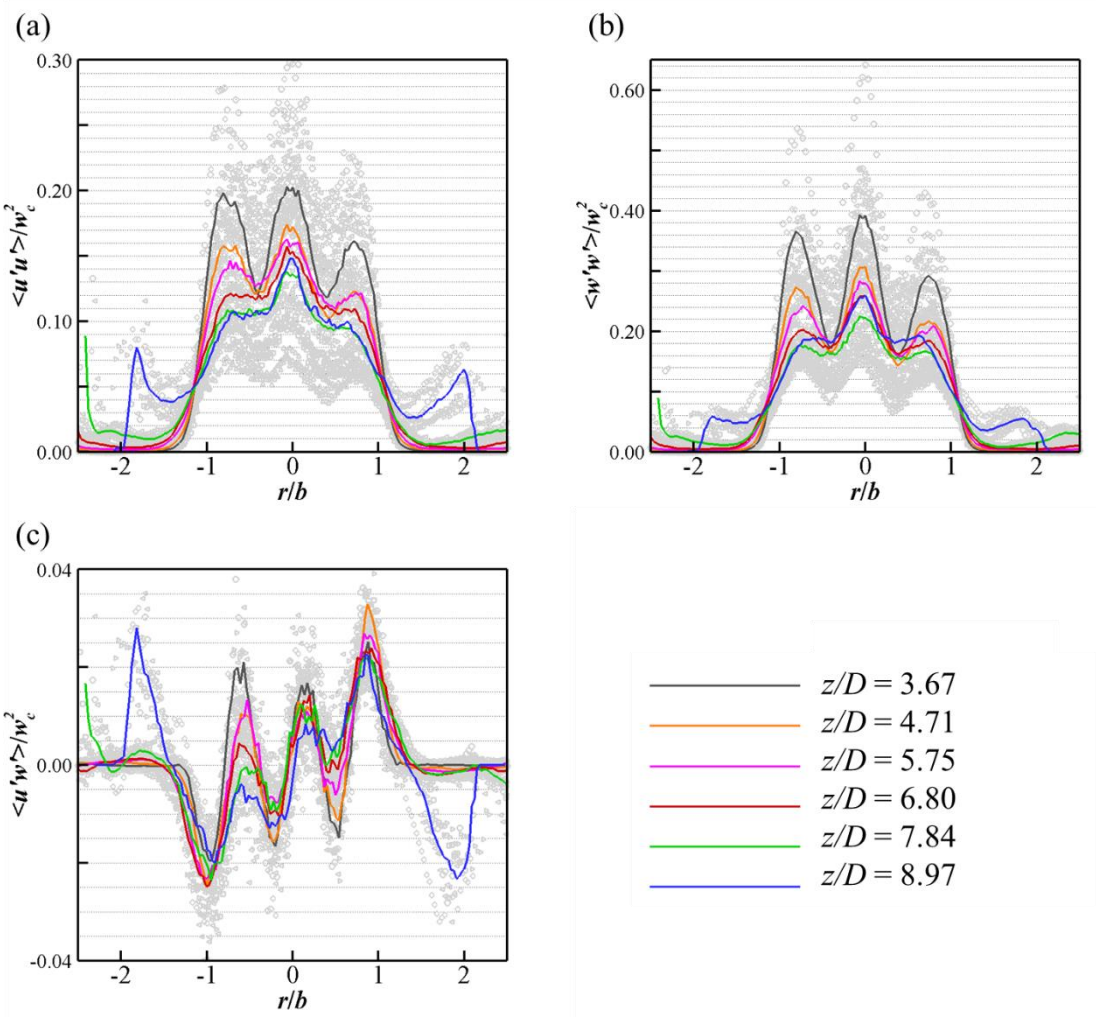

Figure 6.14. Radial profiles of non-dimensional Reynolds stresses ((a) - (c)) for triple buoyant jets.

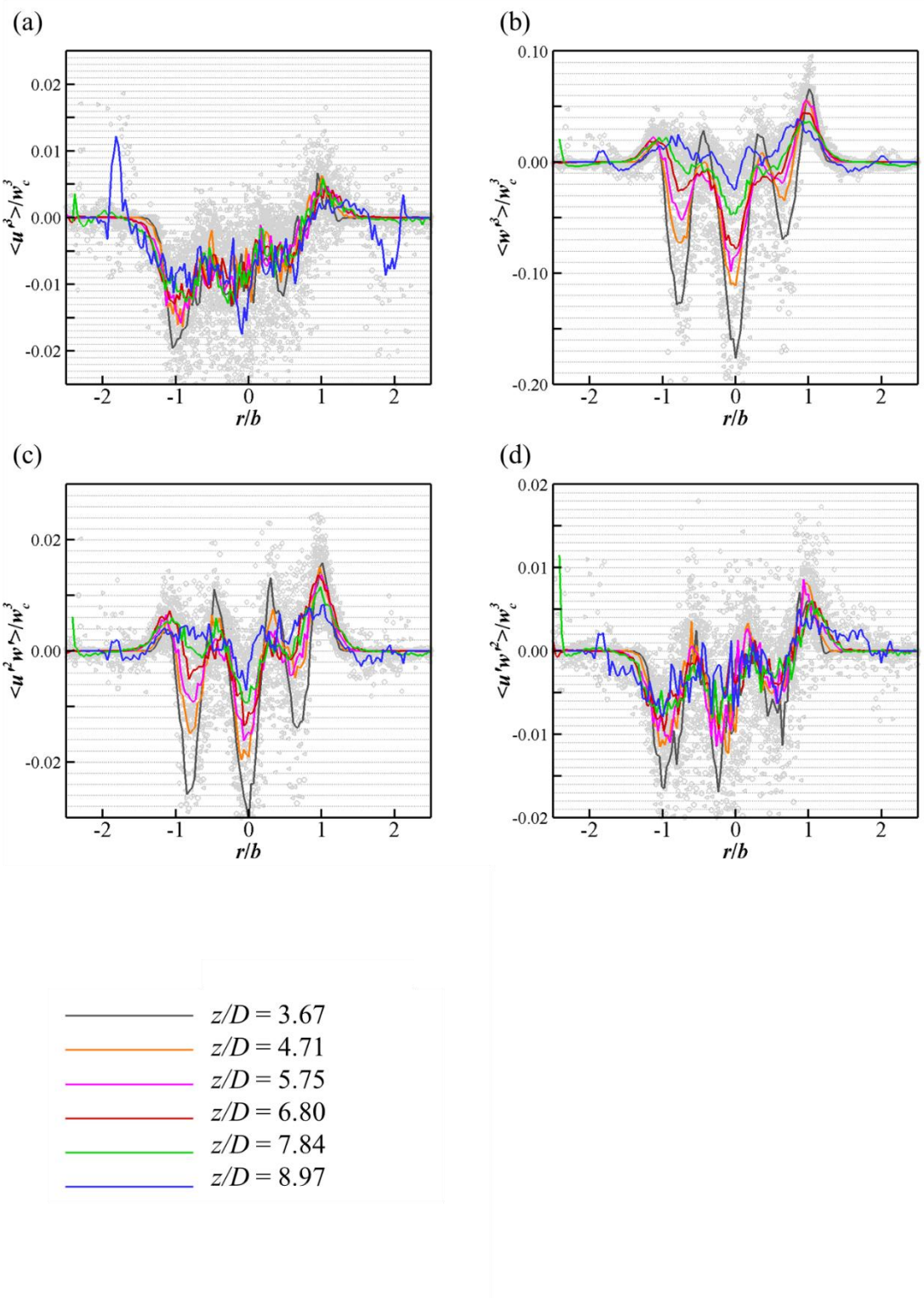

Figure 6.15. Radial profiles of non-dimensional third moments ((a)-(d)) for triple buoyant jets.

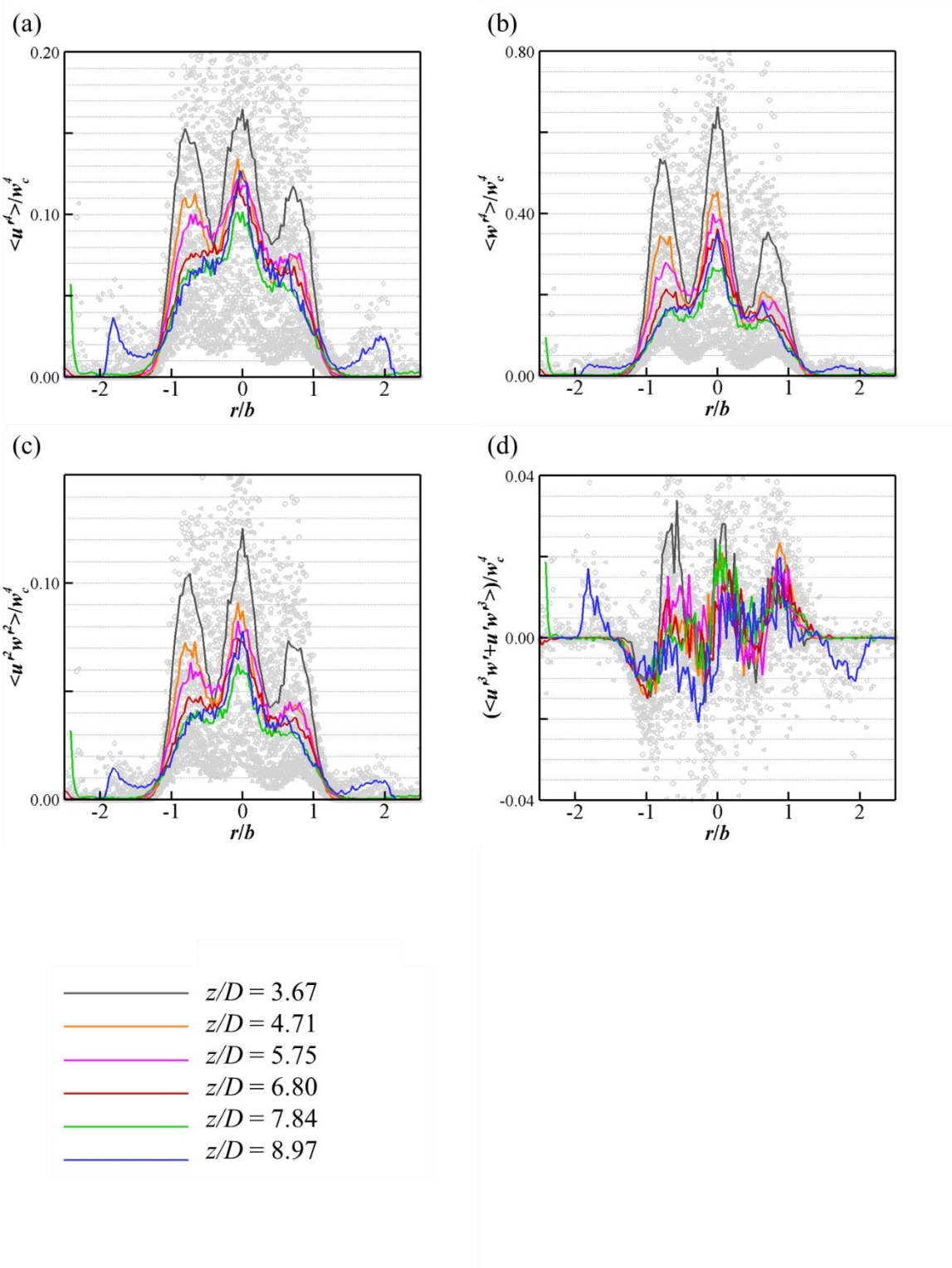

Figure 6.16. Radial profiles of non-dimensional fourth moments ((a)-(d)) for triple buoyant jets.

Non-dimensional radial profiles of every property are shown in Figure 6.13 to 6.16. Note that self-similarity is not obtained in triple jet experiments. Since it is still in the merging region there can be no self-similar profiles observed. It is further noted that Reynolds stress $\langle u'w' \rangle$ shows a plume like behavior.

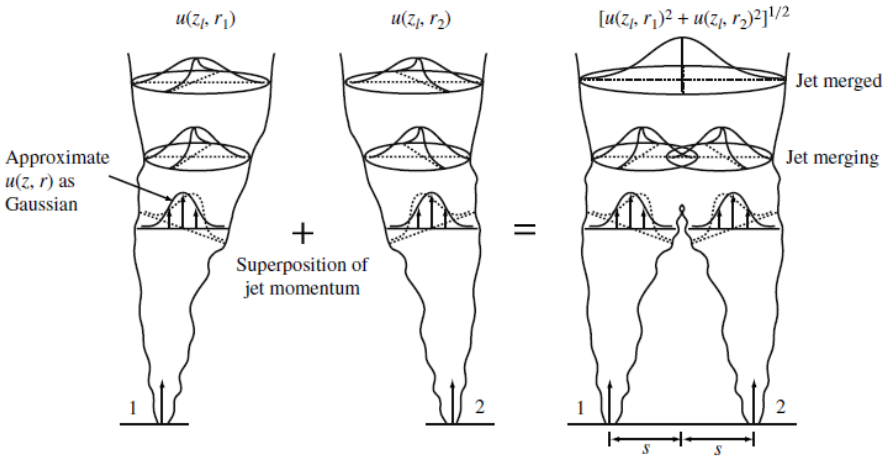

Figure 6.17. Momentum superposition for two interacting jets [78].

Dynamics of triple buoyant jets after merging can be interpreted as momentum superposition for the velocity field of three interacting jets (see Figure 6.17) as Lai et al described [78]. To estimate the velocity distributions for multiple N_J number of jets the mean square velocity (momentum) of each Gaussian distributed velocity profiles of each jet at every location is superimposed as follows:

$$v_{N_J} = \left(\sum_{i=}^{N_J} v_i^2 \right)^{1/2} . \qquad (6.1)$$

The model is only valid for pure jets. For pure plume the model can be extended to the superposition of the kinetic energy of each plume as follows:

$$v_{N_J} \approx \left(\sum_{i=}^{N_J} v_i^3 \right)^{1/3} . \tag{6.2}$$

Figure 6.18 shows the velocity vectors at each elevation and jet width for triple jets. It is clear that as they are merged the Gaussian distributed velocity profiles are superimposed. It is observed that as they are combined the width of the buoyant jet increases linearly until the impingement. As they impinge to the surface the boundary is abstruptly decreased and sharpened as axial momentum spreads to radial directions.

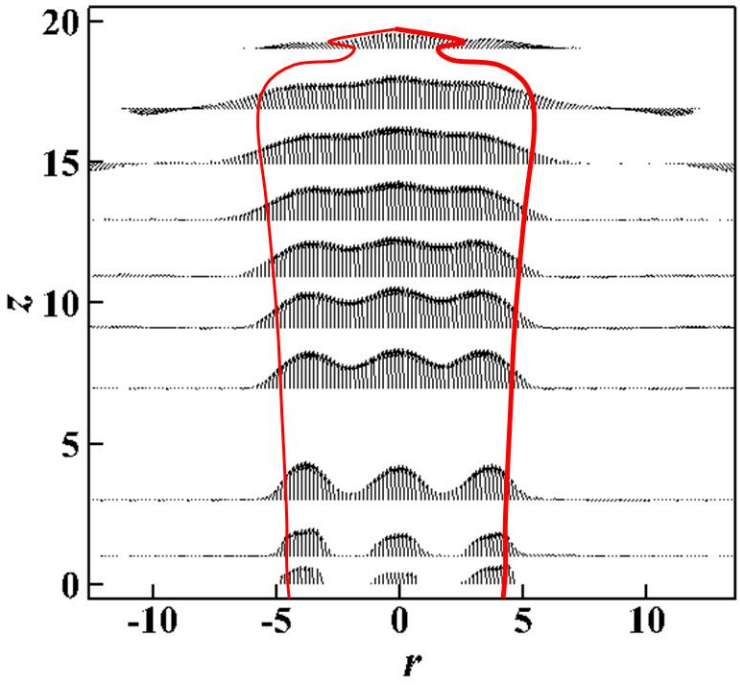

Figure 6.18. Turbulent jet boundary of triple jets.

The evolution of vertical velocity profiles behaves differently than that of single jet experiments as shown in Figure 6.19. The vertical velocity increases as a function of $(z/D)^1$ up to z/D = 0.9 and gradually changes as a function of $(z/D)^{1/2}$. The vertical velocity decreases as a function of $(z/D)^{-1/3}$ because at this point the three jets are mixed and exchange their momentum so the location of the maximum vertical velocity is obtained lower than that of single jet tests.

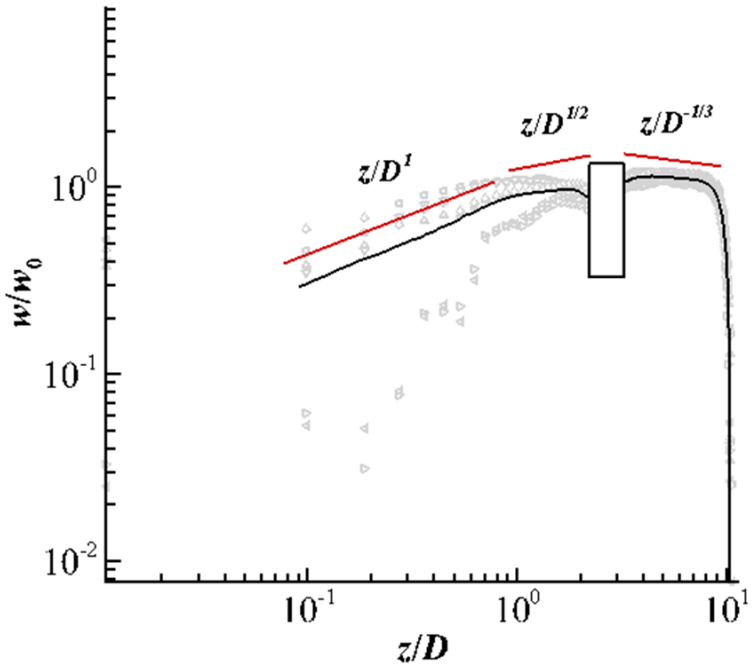

Figure 6.19. Vertical profiles of triple jets in terms of *z*/*D*. Gray symbols indicate each test result.

A Q criterion result from average velocity profiles for triple jet experiments is shows in Figure 6.20. The result shows that the size of RT vortices become smaller than

single jet results and two additional RT vortices are observed jets inbetween. The KH vortices and secondary vortices are combined in the triple jet result. The locations of maximum Q valued secondary vortices are similarity obtained near the wall. The distances from the wall is almost the same (~ 3%) as single jet test but become two times far apart due to the presence of two additional jets. Recirculated vortices are still present although the locations are 27% lowered and 33% widened than the single jet results.

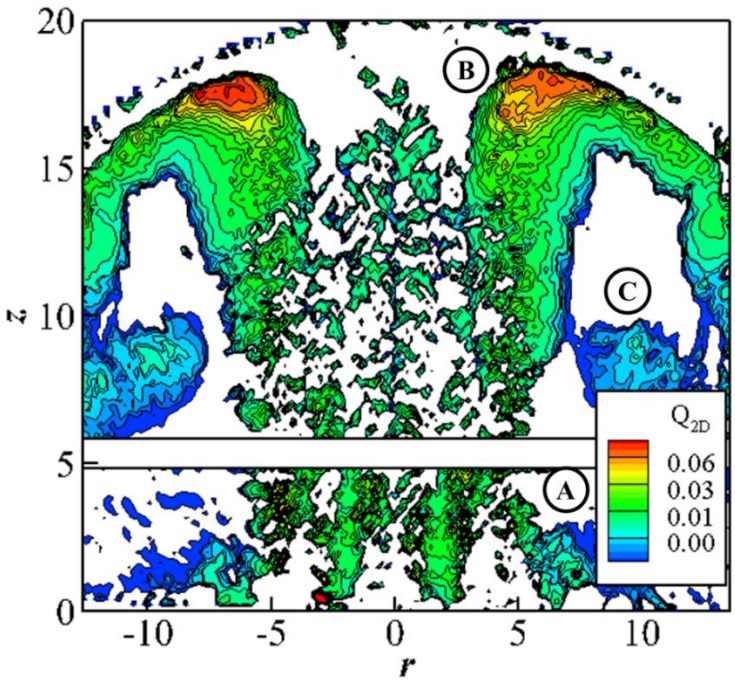

Figure 6.20. Vortical structure of the triple buoyant jets applied with the Q criterion. A: toroidal vortices due to RT instability; B: KH vortices due to turbulent shear layer and secondary vortices due to jet impingement; and C: recirculation zone.

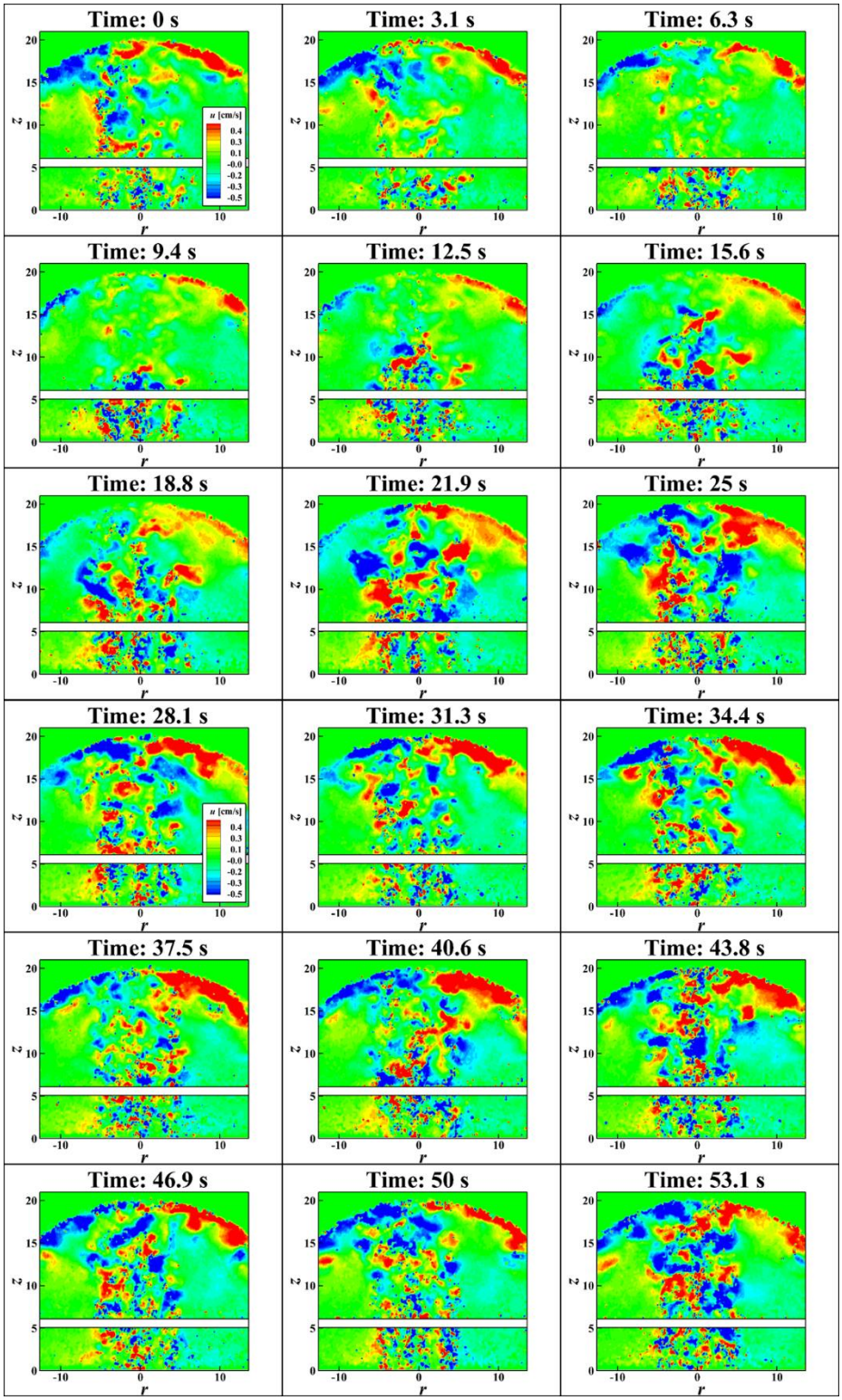

Figure 6.21. Transient contours of the axial velocity for triple jets.

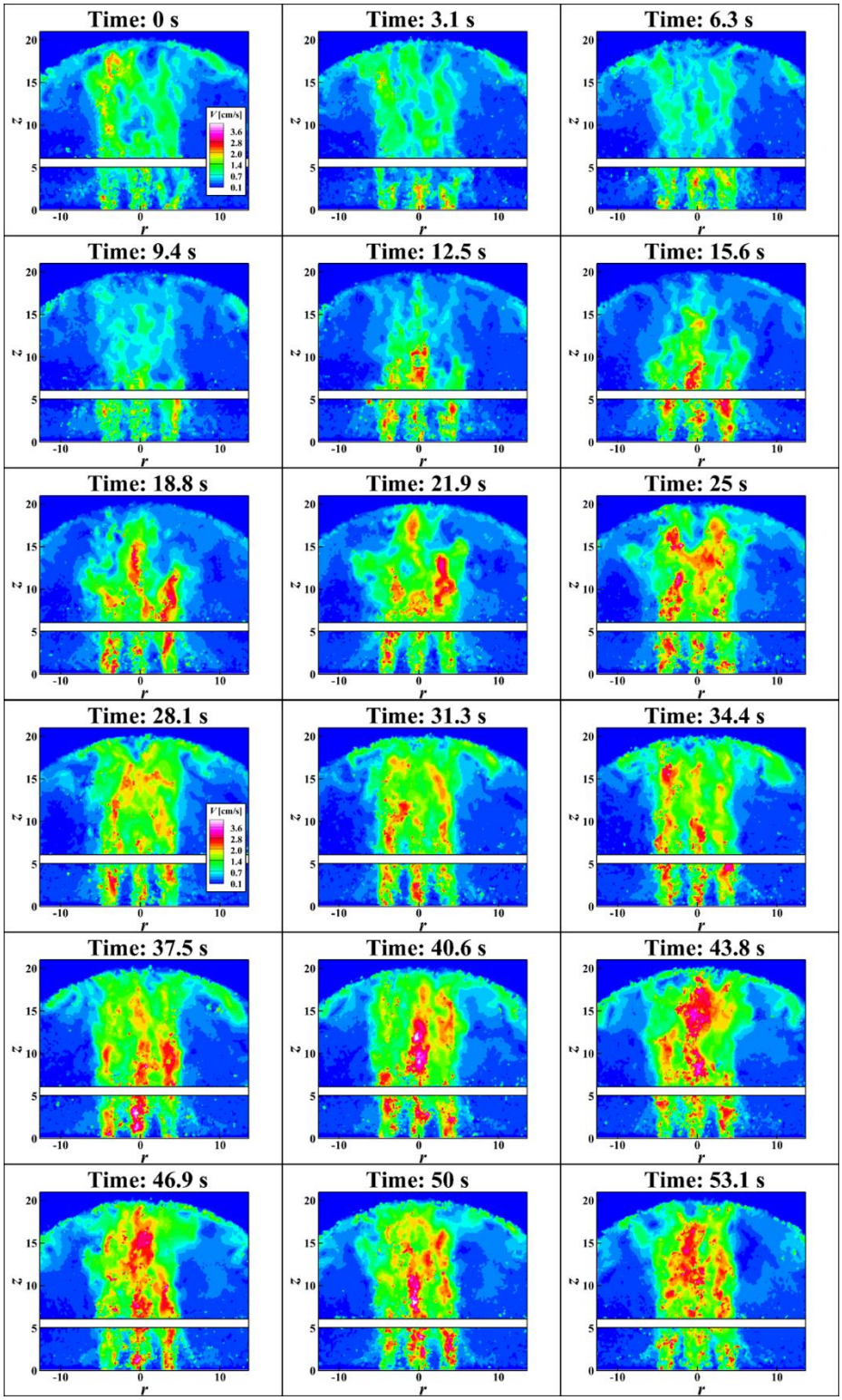

Figure 6.22. Transient contours of the velocity magnitude for triple jets.

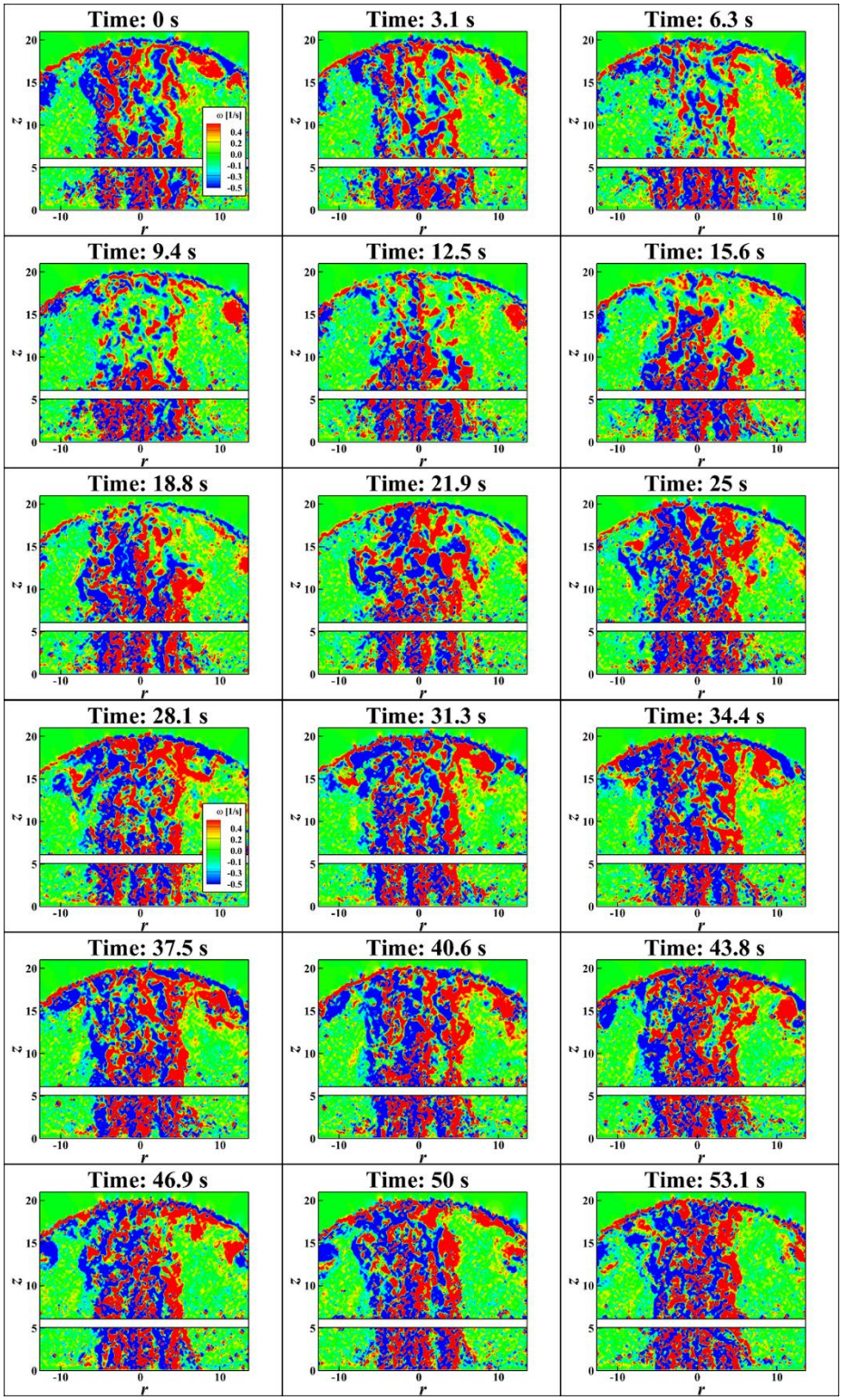

Figure 6.23. Transient contours of the vorticity for triple jets.

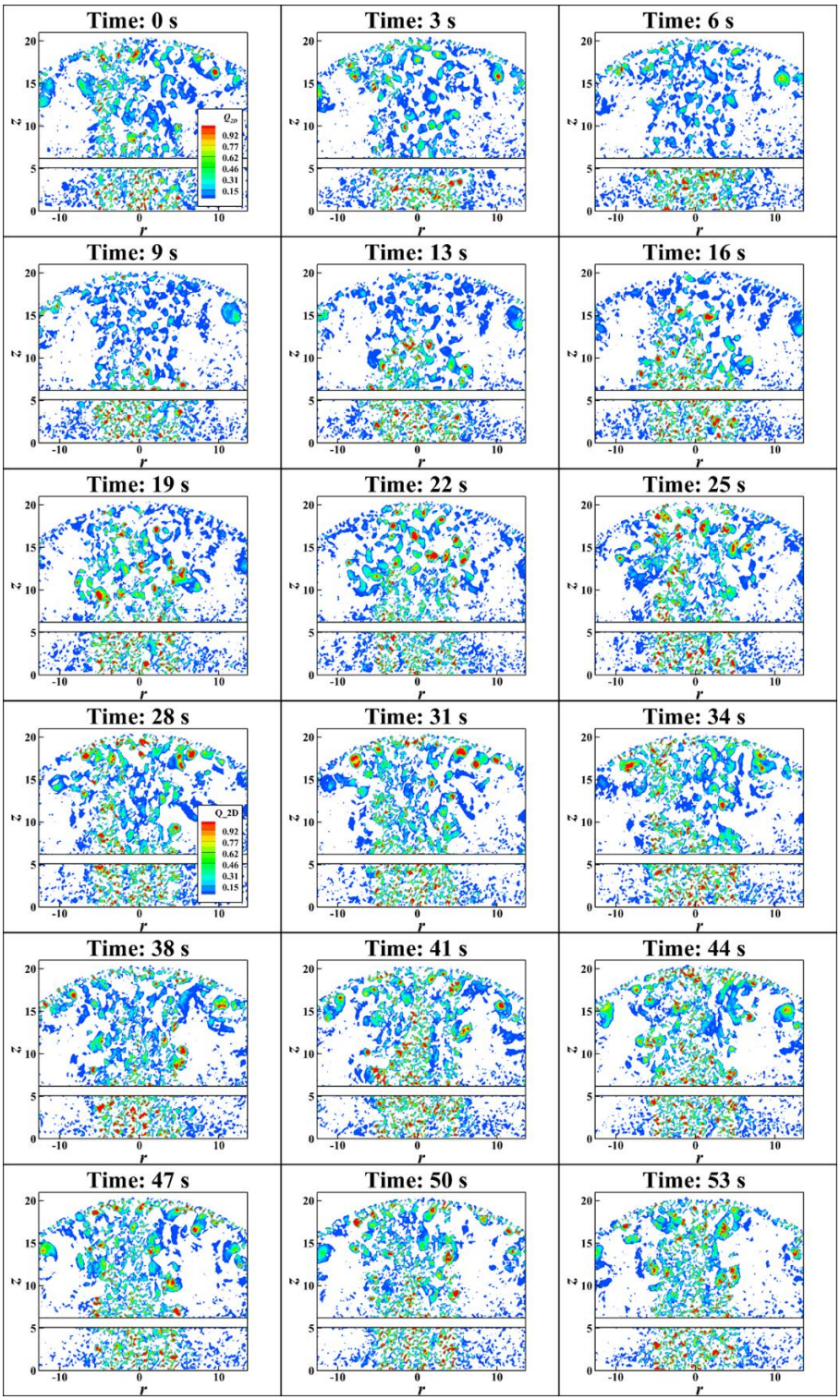

Figure 6.24. Moving averaged transient contours of the Q criterion for triple jets.

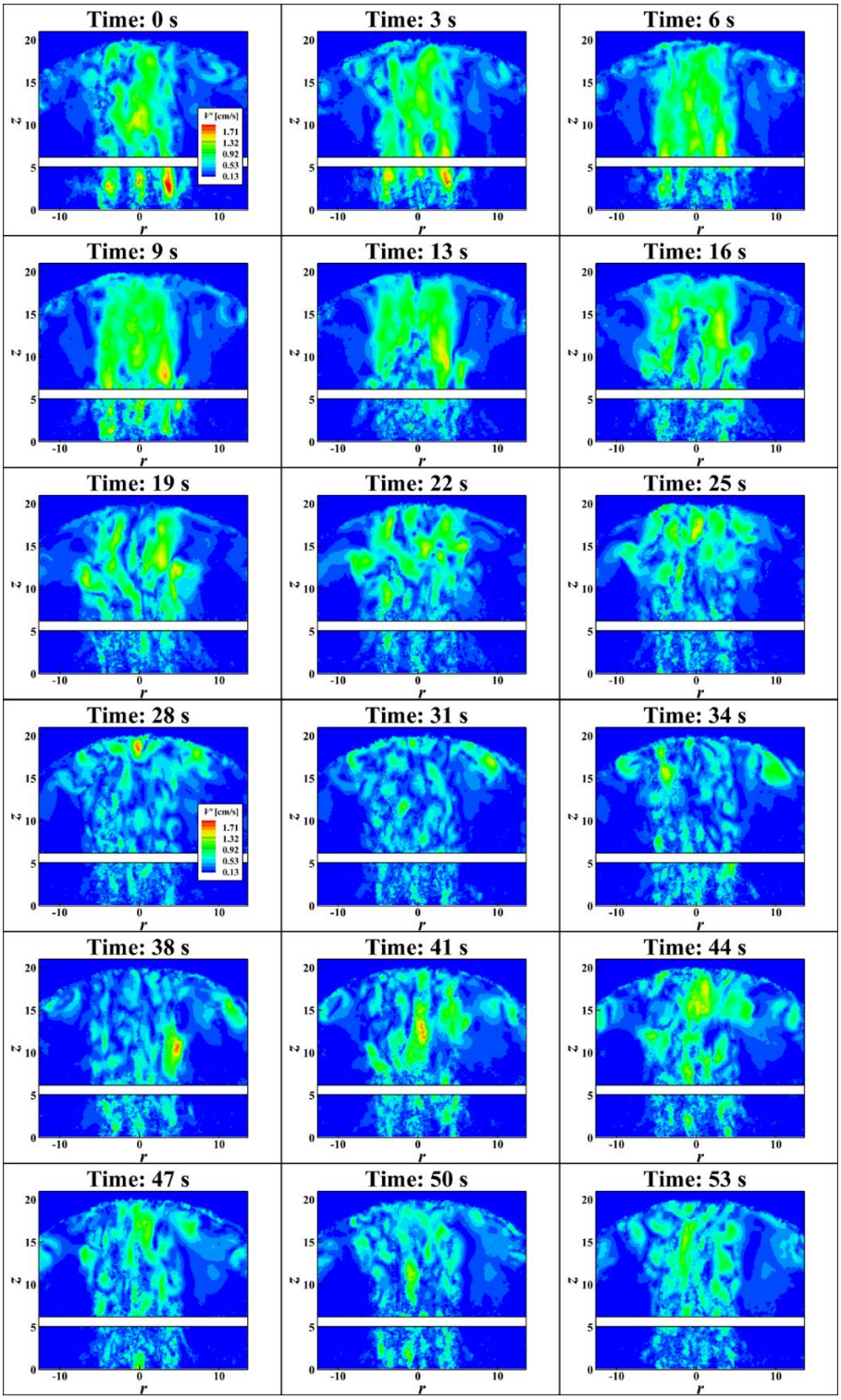

Figure 6.25. Moving averaged transient contours of the resolved fluctuating velocity magnitude for triple jets.

The evolution of turbulent eddy structures for triple buoyant jets are shown from Figure 6.21 to 6.25. The basic eddy interactions are similar to Figure 5.50 however in triple jets, more eddies are preserved between the three jets so many random interactions can happen. The larger eddies are observed along the jet boundaries contributing large secondary vortices in presence. Within the jet boundaries these eddy structures can easily destroyed due to limited space. The resolved fluctuating velocity magnitude shows that more number of eddies are observed to describe the turbulent motion of triple jets.

6.2 Proper Orthogonal Decomposition

The proper orthogonal decomposition (POD) is a method to identify the structure of the flow pattern and statistically characterize the coherent structure of the turbulent flows. POD decomposes a set of time and space data into a set of eigenfunctions and orthonormal coefficients with respect to higher kinetic energy. POD first introduced by Sirovich [79] and has been applied wide variety of physical processes. In essence, the object of the POD analysis for the application of fluid dynamics is to obtain low-dimensional approximate descriptions of a high-dimensional turbulent coherent structures [80]. For POD analysis two methods are proposed: a direct method and a snapshot method. We use the second technique since the difference is minimal but the computational time and memory consumption are advantageous for the second method.

Consider decomposing a velocity field $v(x,t)$ into a sum of temporal POD coefficients $a_m(t)$ and individual POD eigenfunctions ϕ_m:

$$v(x,t) = \sum_{m=1}^{\infty} a_m(t)\phi_m(x). \tag{6.3}$$

Each mode is required to satisfy the orthonormality,

$$\int \phi_m(x)\phi_n^*(x)dx = \delta_{mn}, \tag{6.4}$$

where δ_{mn} is the Kronecker delta. Then the POD coefficients can be found by using the property of orthonormality. Then Equation (6.3) becomes

$$a_m(t) = \int v(x,t)\phi_m^*(x)dx. \tag{6.5}$$

Now, in order to satisfy the condition to minimize the mean square error of the orthonormal functions, a Fredholm integral equation of the second kind with kernel $R(x,x')$ is derived [50]. The expression is

$$\int R(x,x')\phi_m(x')dx' = \lambda_m \phi_m(x), \tag{6.6}$$

where the eigenfunctions of the two point spatial correlation functions $R(x,x')$ are given by

$$R(x,x') = \frac{1}{T}\int v(x,t)\cdot v(x',t)dt. \tag{6.7}$$

Note that the notation $(\cdot)$ represents the classical scalar product of two vectors. The solutions of the Equation (6.6) give us to find both an eigenvalues λ_m and corresponding eigenfunctions ϕ_m for each mode *m* [50, 81].

For the application for PIV vector field, the snapshot method is very powerful. Consider the fluctuating part of velocity components for *N* snapshots as follows:

$$\mathbf{V} = \left[\mathbf{v}_1\ \mathbf{v}_2\ \mathbf{v}_3\ \cdots\ \mathbf{v}_N\right] = \begin{bmatrix} u_1^1 & u_2^1 & \ldots & u_N^1 \\ \vdots & \vdots & \vdots & \vdots \\ u_1^M & u_2^M & \ldots & u_N^M \\ v_1^1 & v_2^1 & \ldots & v_N^1 \\ \vdots & \vdots & \vdots & \vdots \\ v_1^M & v_2^M & \ldots & v_N^M \end{bmatrix}. \tag{6.8}$$

Then calculate the data to form the correlation matrix C_{ij} defined as

$$C_{ij} = \frac{1}{N}\int v(x,t_i)\cdot v(x',t_j)dx = \frac{1}{N}\mathbf{V}^T\mathbf{V}. \tag{6.9}$$

Now solve the eigenvalue problem

$$\mathbf{CA} = \boldsymbol{\lambda}\mathbf{A}, \tag{6.10}$$

where **A** is the complete set of eigenvectors such that

$$\begin{aligned} \mathbf{A}^1 &= \left[a^1(t_1),\ a^1(t_2),\ \cdots,\ a^1(t_N) \right]^T, \\ &\vdots \\ \mathbf{A}^N &= \left[a^N(t_1),\ a^N(t_2),\ \cdots,\ a^N(t_N) \right]^T. \end{aligned} \tag{6.11}$$

Then rearrange solutions by eigenvalues as

$$\lambda_1 > \lambda > \cdots > \lambda_N = 0 \quad \text{with} \quad \boldsymbol{\Psi} = \left[\phi^1\ \phi^2\ \cdots\ \phi^N \right], \tag{6.12}$$

where the highest eigenvalues represent the modes contained the highest kinetic energy. Next the eigenfunctions are normalized so that

$$\frac{1}{N}\sqrt{\left(\mathbf{A}^n, \mathbf{A}^m\right)} = \lambda_n \delta_{mn}, \tag{6.13}$$

where the inner product $(f, g) = \int f(x) \cdot g(x)\, dx$ then eigenfunctions, i.e. POD modes, can be found

$$\phi^n(x) = \frac{\sum_{k=1}^{N} a_n^k \mathbf{v}_k}{\left\| \sum_{k=1}^{N} a_n^k \mathbf{v}_k \right\|} = \frac{1}{N\lambda_n} \sum_{k=1}^{N} a_n(t_k)\, \mathbf{v}(x, t_k). \tag{6.14}$$

Now, the POD coefficient a_n can be found for the snapshot n

$$a_n = \left(\phi^n, v^i\right) \qquad \text{or} \qquad \mathbf{a}^n = \boldsymbol{\Psi}^T \mathbf{v}^n \quad \text{(matrix)}. \tag{6.15}$$

Therefore, a snapshot at time j can be found as

$$v_j(x, t_k) = \sum_{n=1}^{N} a_n(t_k)\, \phi_j^n(x), \tag{6.16}$$

which comes to the original Equation (6.3).

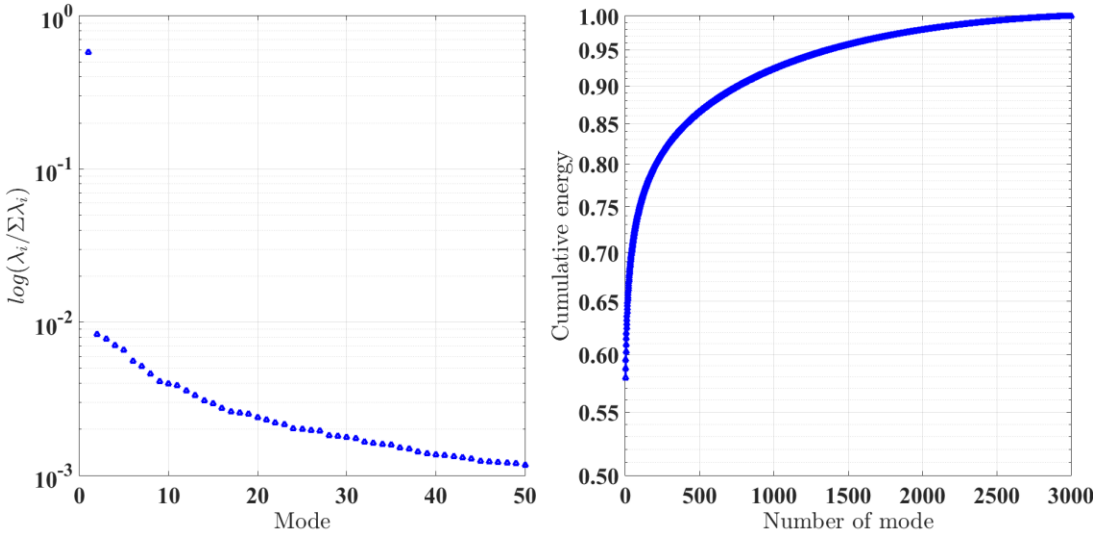

Figure 6.26. The energy distribution of the POD mode for a single buoyant jet. Eigenvalue contributions for the relative energy associated with mode (left) and the convergence of cumulative energy of eigenvalue sum (right).

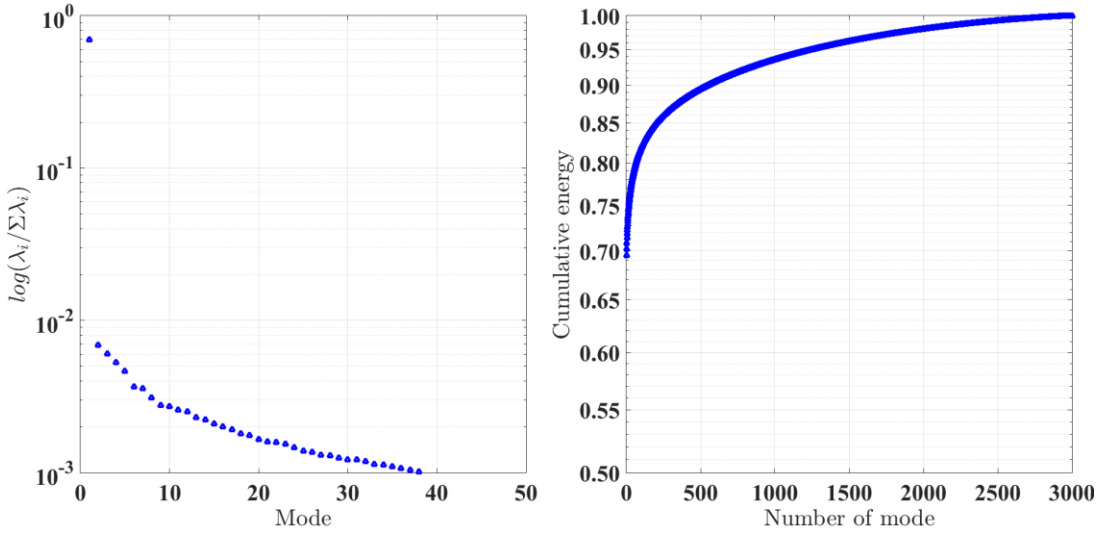

Figure 6.27. The energy distribution of the POD mode for triple buoyant jets. Eigenvalue contributions for the relative energy associated with mode (left) and the convergence of cumulative energy of eigenvalue sum (right).

The energy distributions of single and triple buoyant jets for each mode are shown in Figure 6.26 and 6.27. For a single jet, 58% of the total kinetic energy is contained in the first mode while for triple jets, 70% of the total kinetic energy is contained in the first mode. Triple jets have higher kinetic energy in the field so more energy is computed in the first mode. As a number of modes increase both of the cumulative energy grow logarithmically. The number of modes to reach a time constant ($1-1/e \approx 63.2\%$) is obtained only 10 mode for single jet tests. In other words when the velocity profiles are reconstructed with 10 modes, the system represents 63.2 % of the total kinetic energy. Whereas the first mode of triple jets already represents the system response.

Contours for single and triple buoyant jets of each mode were shown in Figure 6.28 to 6.35. The first mode represents the mean velocity profile. It is noted that unlike transient contours of velocities, vorticity and Q criterion, contours from POD of those do not show any difference in identifying turbulent eddy structures of the flow. Therefore POD is a powerful technique to reconstruct the turbulent eddies and provides low-pass filters of inhomogeneous flows [77]. When those eddy structures are added together, we can reconstruct the time evolution of the velocity field which represents the instantaneous velocity field and identify the structure of turbulent eddies. As the number of modes increases the reconstructed velocity field becomes more similar to each instantaneous velocity field. Therefore detailed smaller eddies are identified to the system and the unsteady nature of turbulent fluctuations are observed that are close to the real phenomena while filtering small scale turbulence [82].

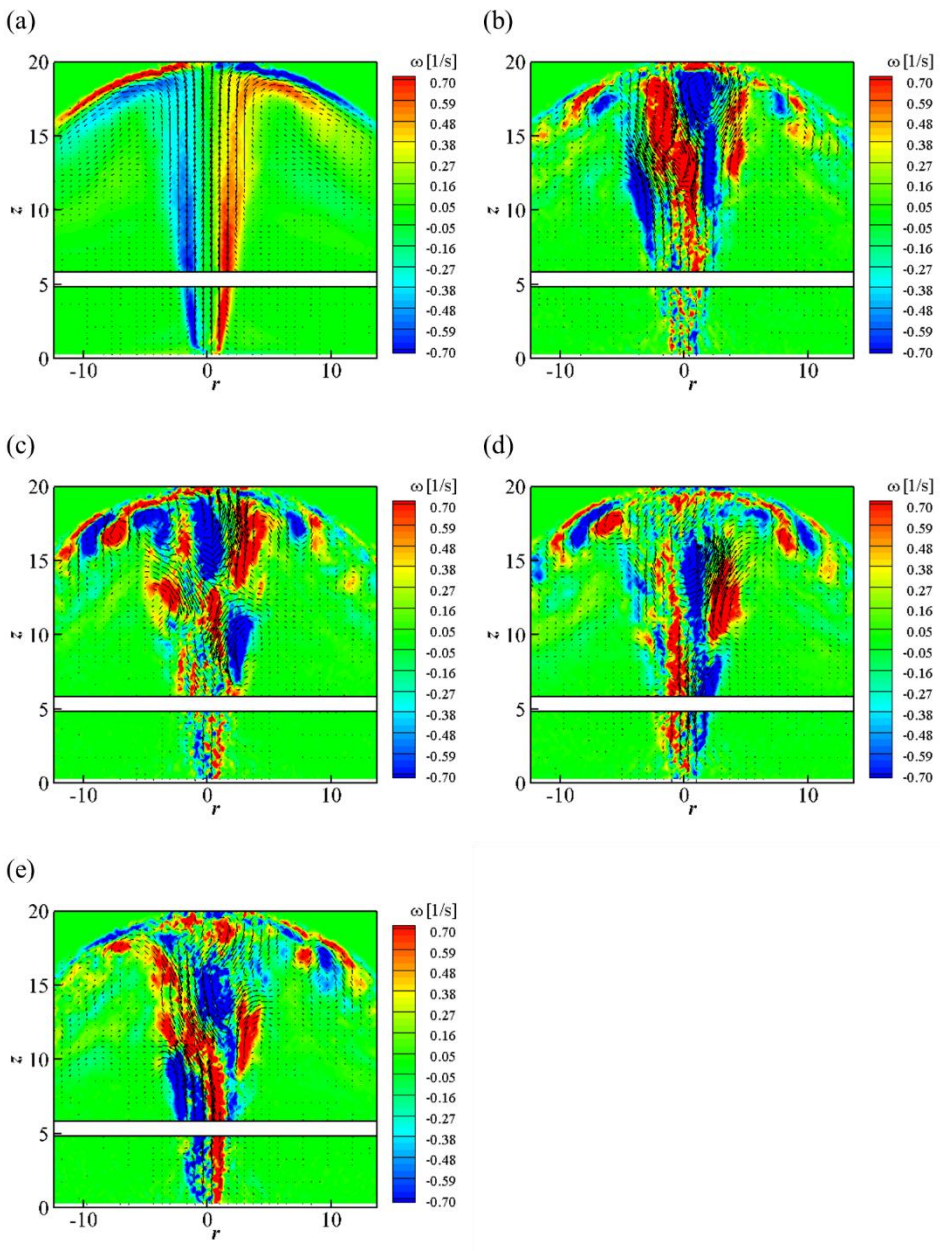

Figure 6.28. The POD analysis of mode 1 (a) to 5 (e) for a single buoyant jet with the vorticity contour and velocity vectors.

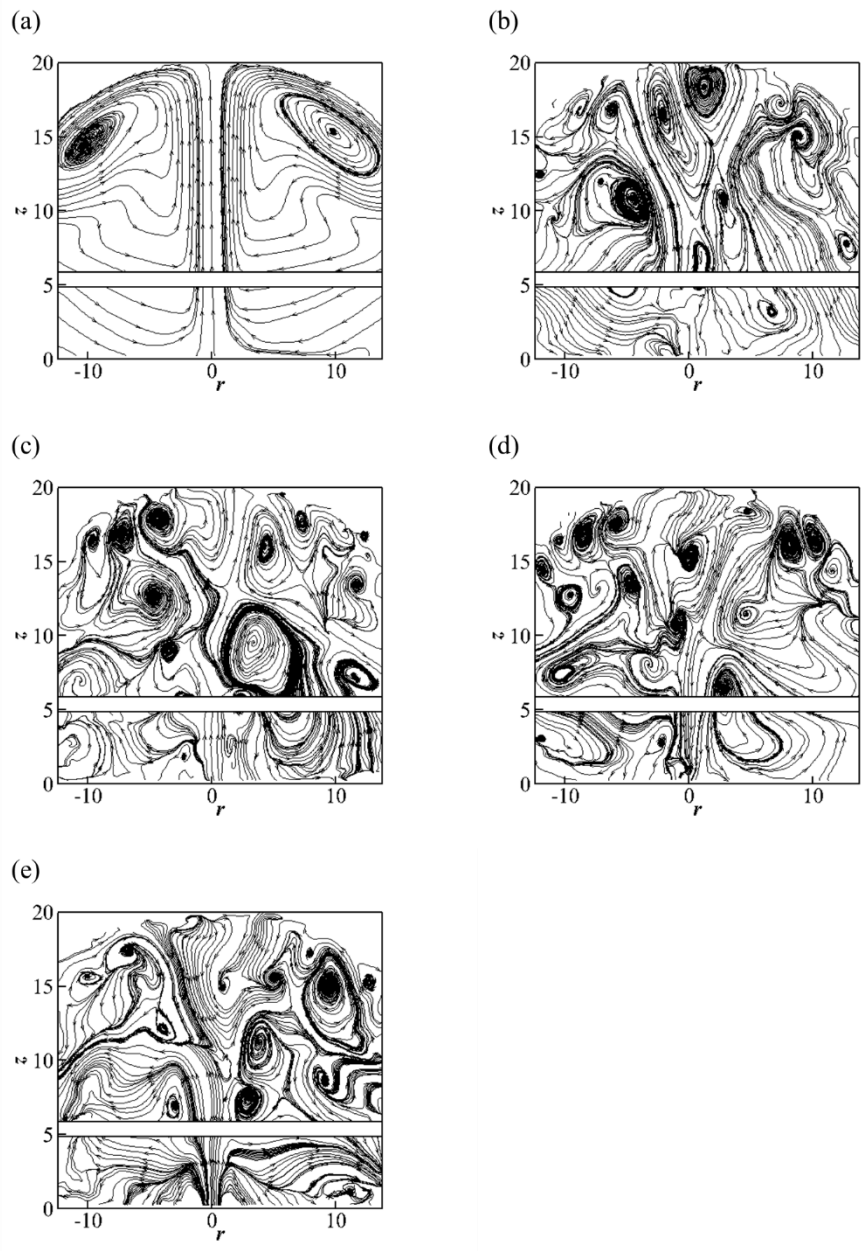

Figure 6.29. The POD analysis of mode 1 (a) to 5 (e) for a single buoyant jet with streamlines.

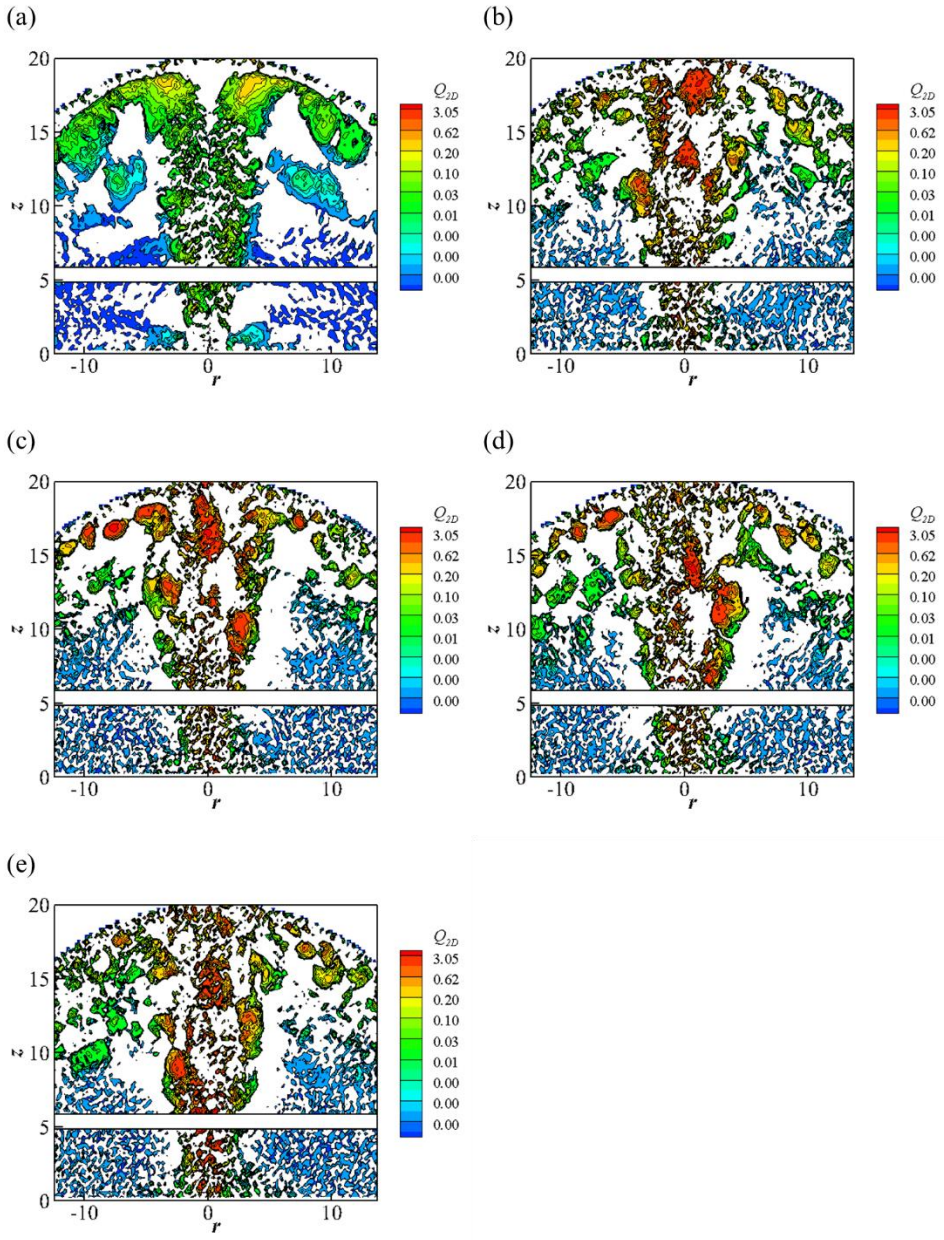

Figure 6.30. The POD analysis of mode 1 (a) to 5 (e) with the Q criterion for a single buoyant jets.

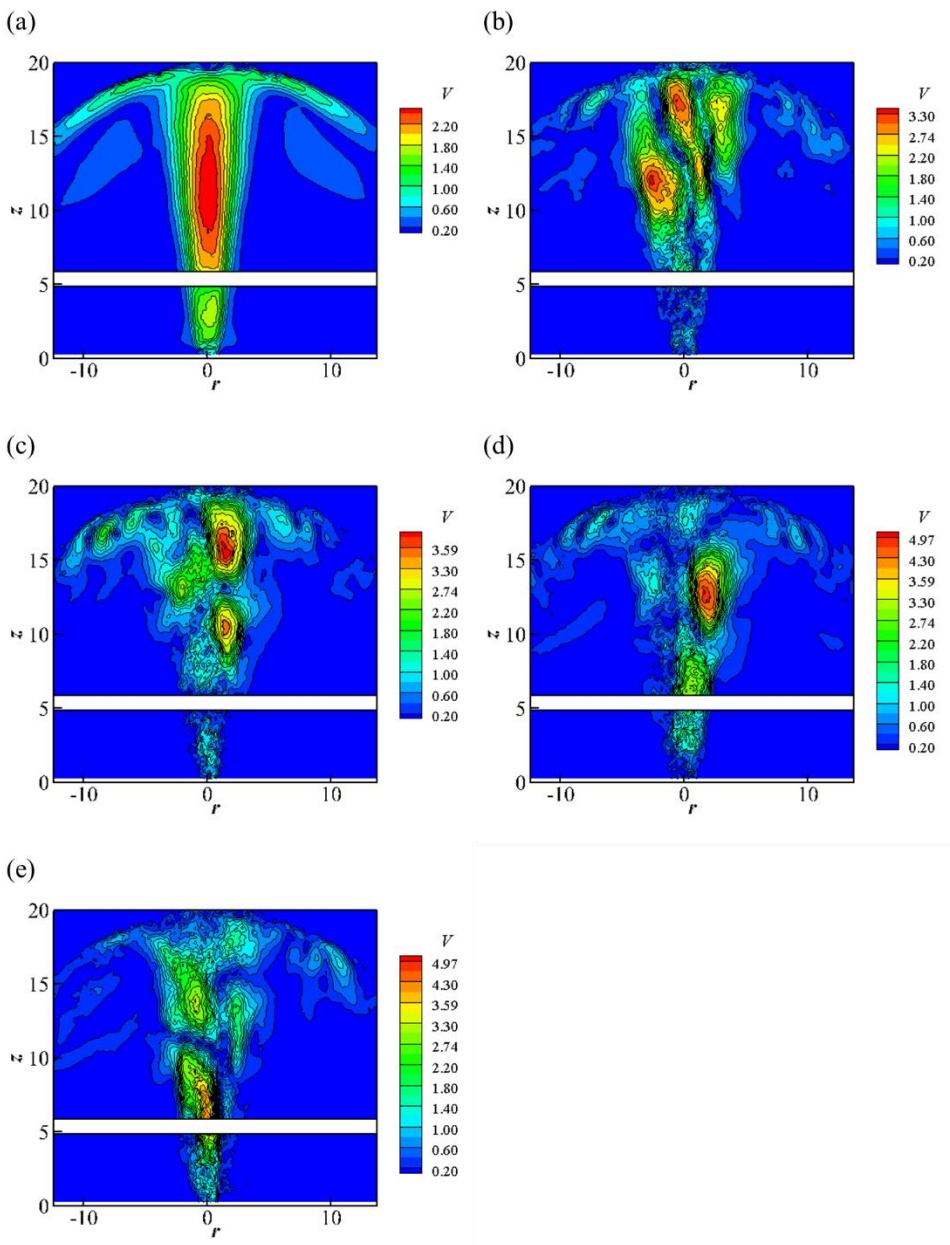

Figure 6.31. The POD analysis of mode 1 (a) to 5 (e) with the velocity magnitude for a single buoyant jet.

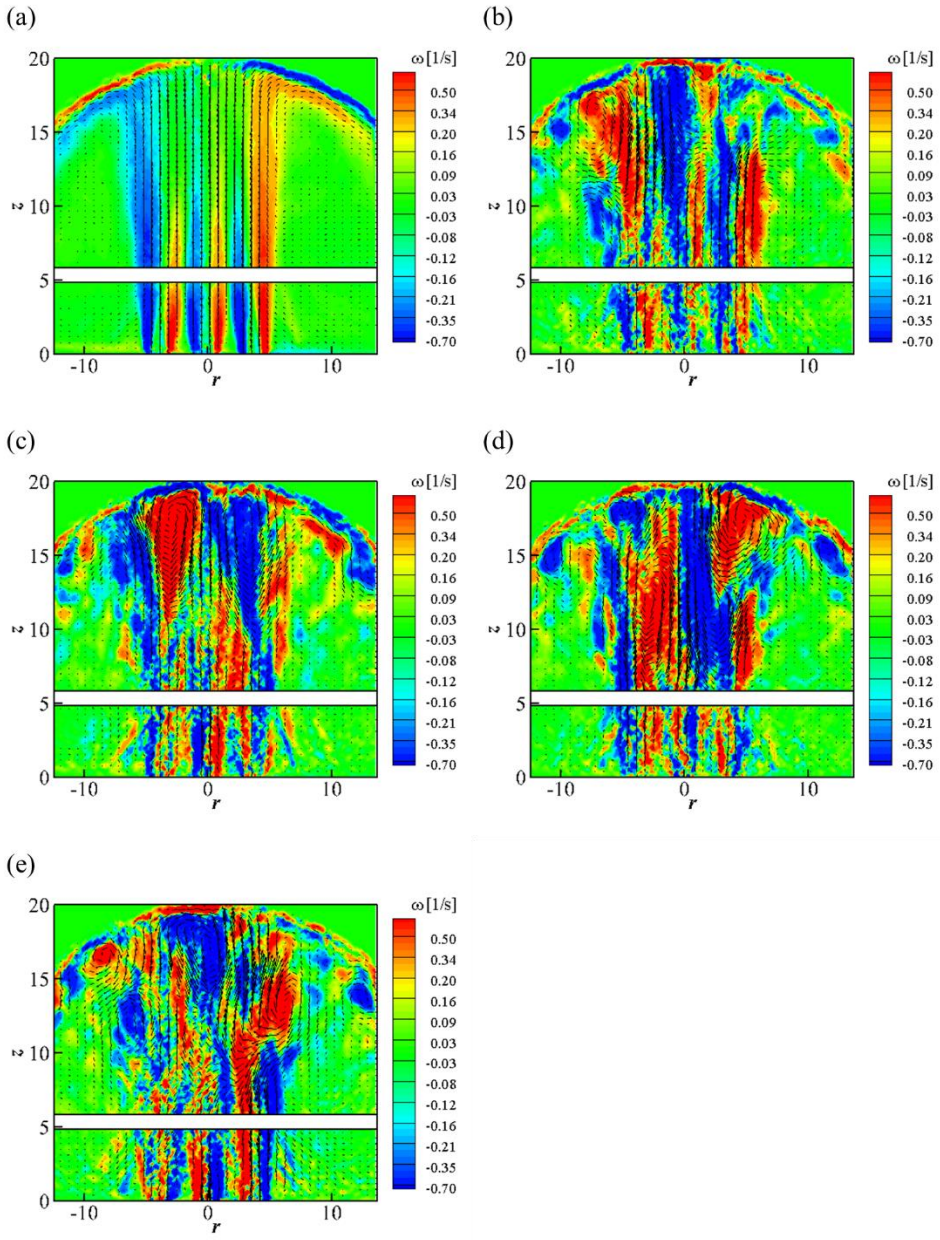

Figure 6.32. The POD analysis of mode 1 (a) to 5 (e) for triple buoyant jets with the vorticity contour and velocity vectors.

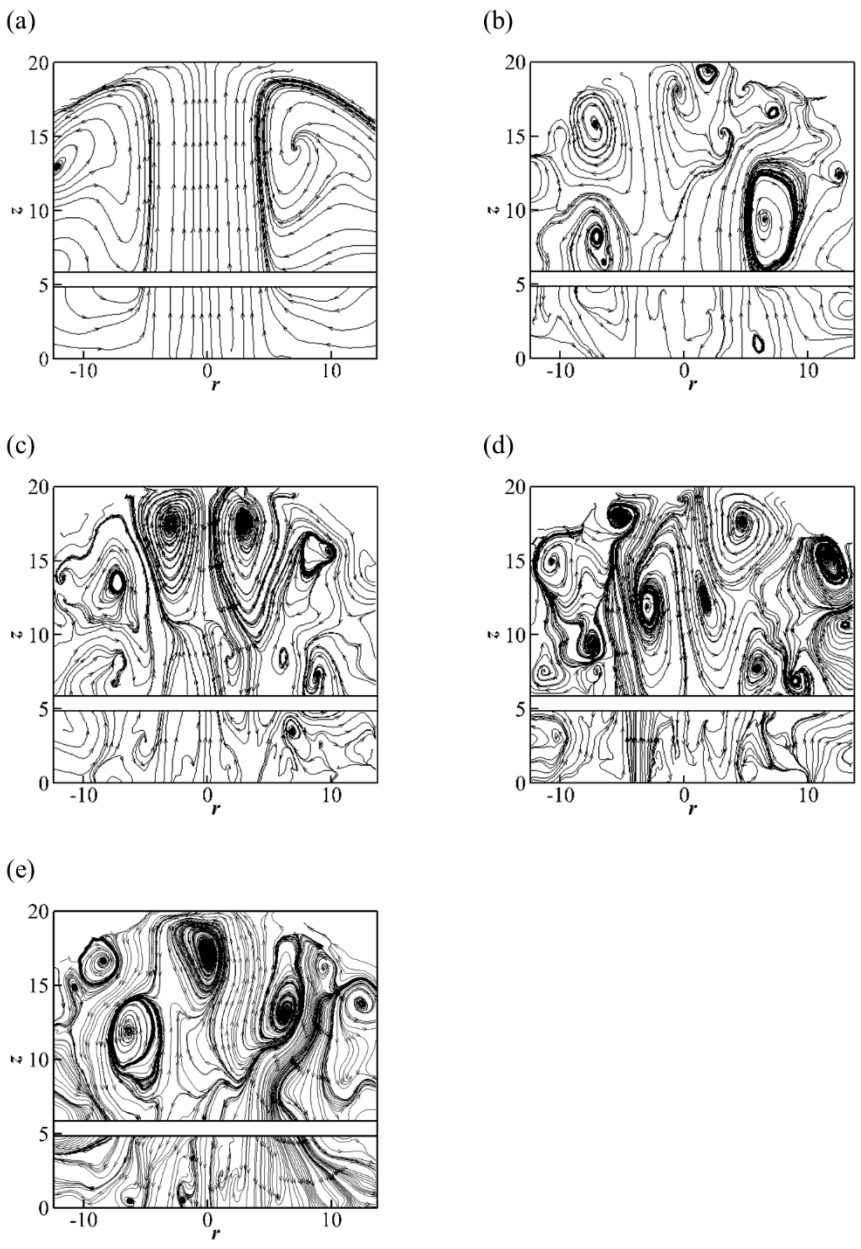

Figure 6.33. The POD analysis of mode 1 (a) to 5 (e) for triple buoyant jets with streamlines.

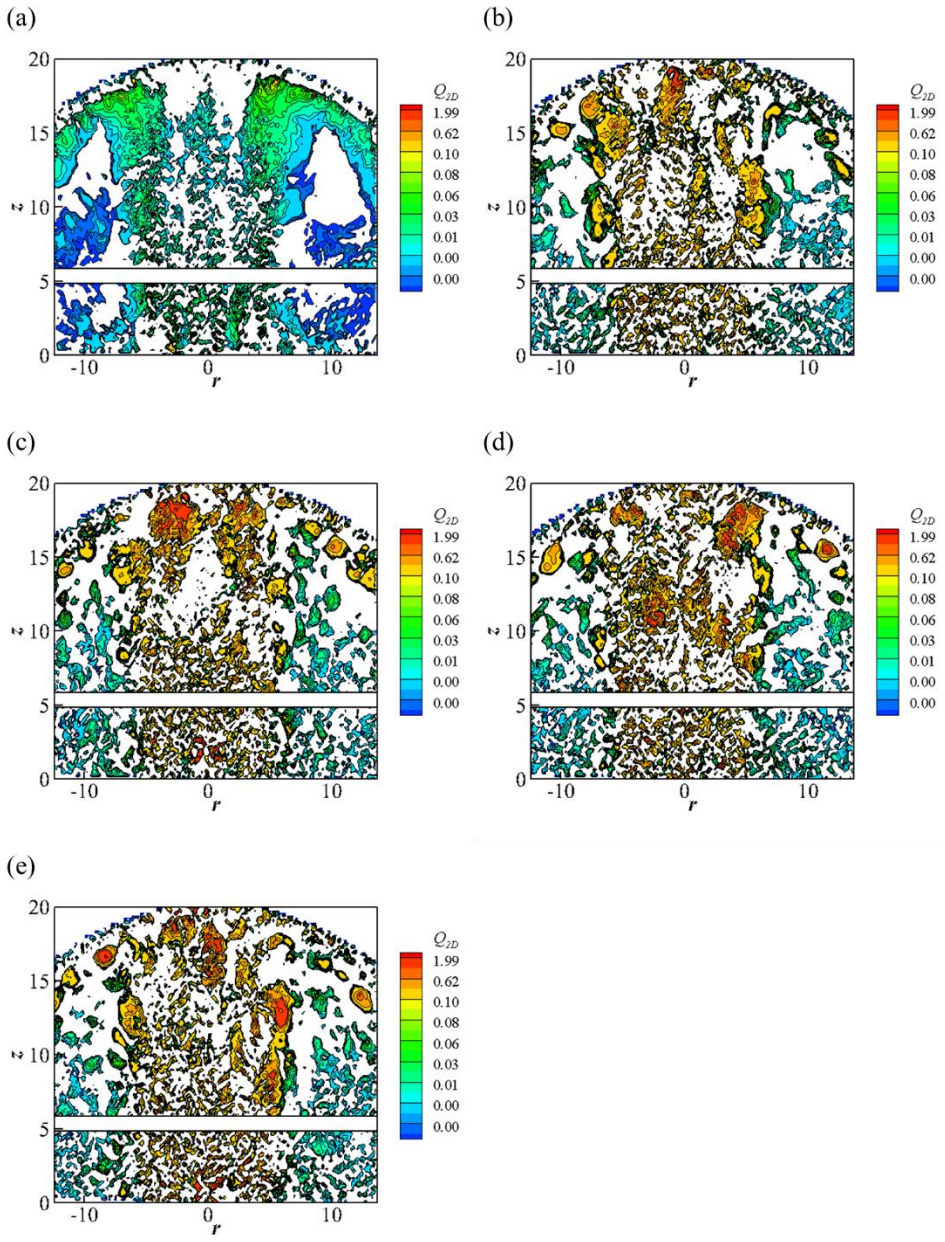

Figure 6.34. The POD analysis of mode 1 (a) to 5 (e) with the Q criterion for triple buoyant jets.

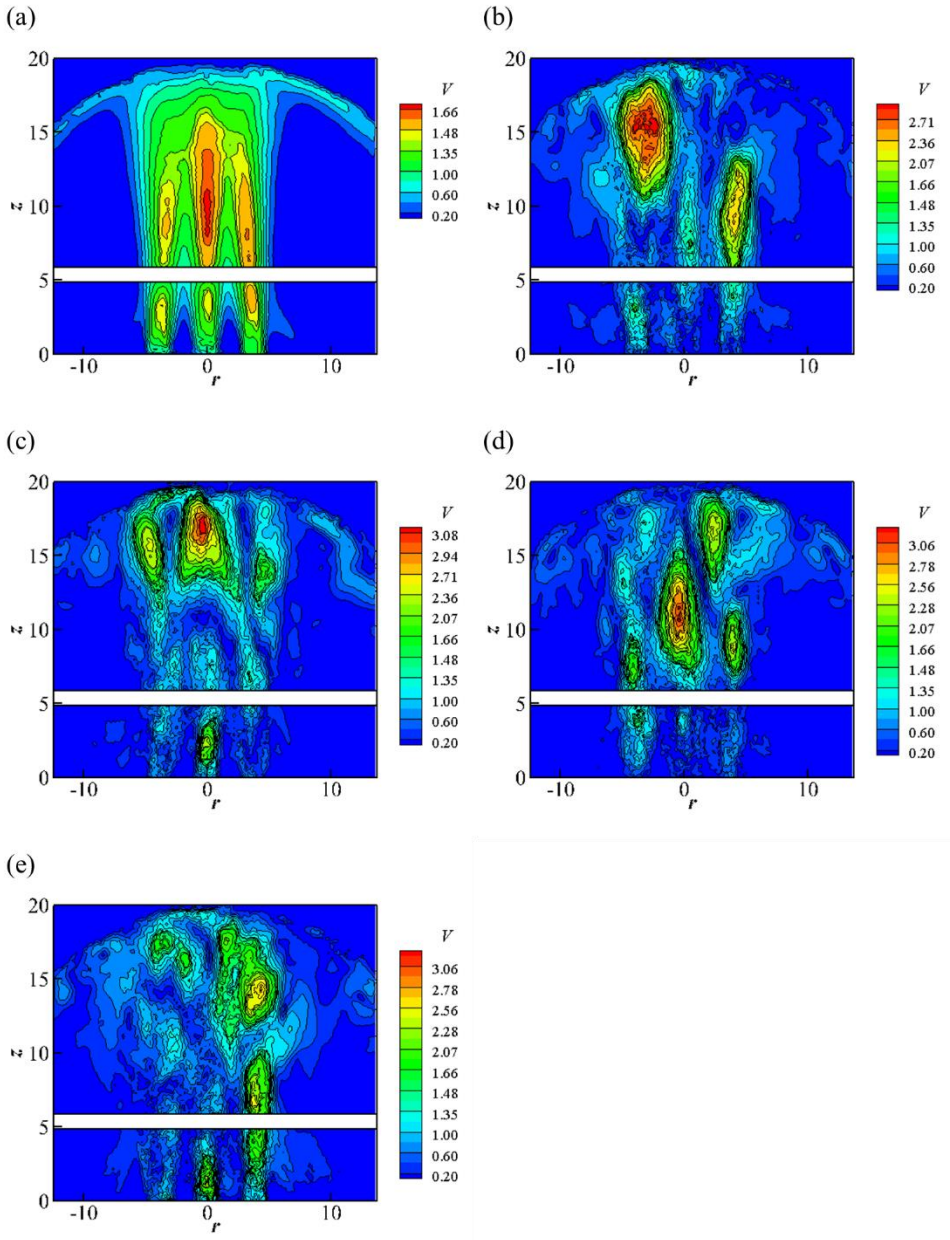

Figure 6.35. The POD analysis of mode 1 (a) to 5 (e) with the velocity magnitude for triple buoyant jets.

6.3 Wall Shear Stress Comparison

This section provides the average velocity profile for a single jet and triple jet along the top surface of the dome in the upper plenum and compares the wall shear stress (τ_w) distributions. Measurements of shear stress is significantly important in the studies of impinging jets with various configuration because it is closely related to heating, cooling and drying of the surface in interest for many industrial applications [83]. The important parameters are Re, TI and *H*/*D*, a ratio between height of the upper plenum (*H*) and the diameter of the nozzle (*D*). In the present study, *H*/*D* is estimated 10.34.

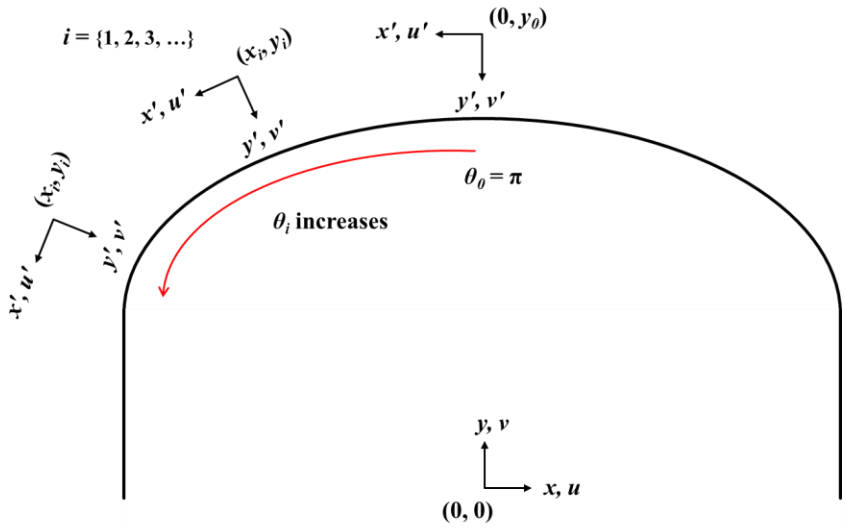

Figure 6.36. A schematic of coordinate transformations along the top surface and each transformed coordinate systems.

To estimate the wall velocity distribution a coordinate transformation was applied so that the location of each velocity position is perpendicular to the each surface location.

Figure 6.36 and 6.37 show how these reference frames change along the surface of the dome shape. It is noted that the dome is not perfectly circular but rather it is an elliptically concaved surface. Suppose two reference frames S and S' where S has the coordinates of (x, y) and S' has the coordinates of (x', y'), then the coordinate transformation is as follows:

$$\begin{bmatrix} x_i' \\ y_i' \end{bmatrix} = \underbrace{\begin{bmatrix} \cos\theta_i & \sin\theta_i \\ -\sin\theta_i & \cos\theta_i \end{bmatrix}}_{\text{Rotation matrix}} \begin{bmatrix} x_i - x_0 \\ y_i - y_0 \end{bmatrix}, \tag{6.17}$$

where i is each location on the surface denoted by integers, θ is a rotation angle with respect to the reference frame and a subscript 0 indicates the location of the reference frame where $r = z = 0$. The vector components can be obtained from vector components transformation as follows:

$$\begin{bmatrix} u' \\ v' \end{bmatrix} = \begin{bmatrix} \cos\theta_i & \sin\theta_i \\ -\sin\theta_i & \cos\theta_i \end{bmatrix} \begin{bmatrix} u \\ v \end{bmatrix}. \tag{6.18}$$

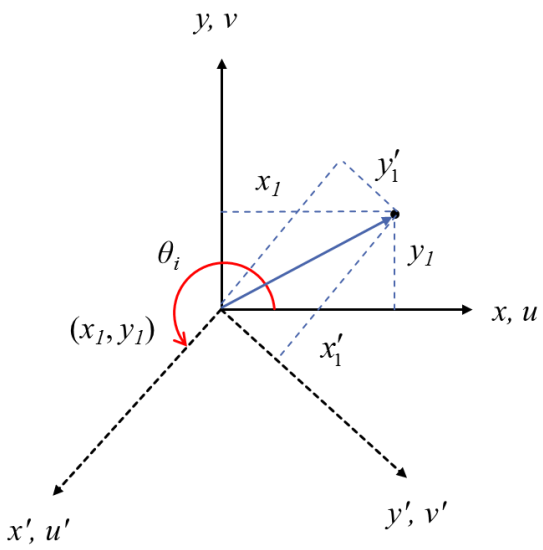

Figure 6.37. Standard configuration for coordinate transformations.

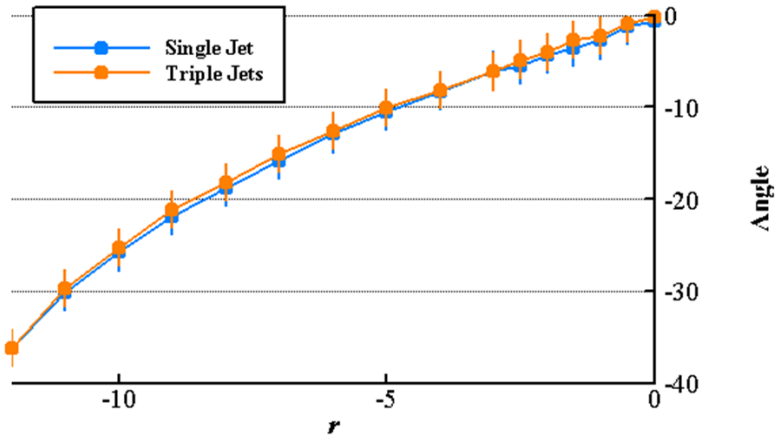

Figure 6.38. Distributions of angles (θ_i - π) in the configuration for both a single jet and triple jets. The bar shows the standard deviation of each angle for the location.

Figure 6.38 shows calculated each angle distribution (θ_i - π) along the surface for both jet studies justifying that the coordinate transformation well estimated the geometry of the concave surface. The typical impinging jet flow can be subdivided into three characteristic regions as shown in Figure 6.39. A free jet region is where the jet axial velocity develops and the jet boundary is widened. When the jet is close to the surface the axial velocity is decelerated and reduces to zero and the radial velocity is accelerated; this region is called a stagnation region. In this region the boundary layer thickness (δ) tends to keep constant and the streamwise velocity is accelerated by the pressure gradient. The wall jet region is formed where the excess pressure on the wall approaches zero and the static pressure and ambient pressure become identical [84, 85].

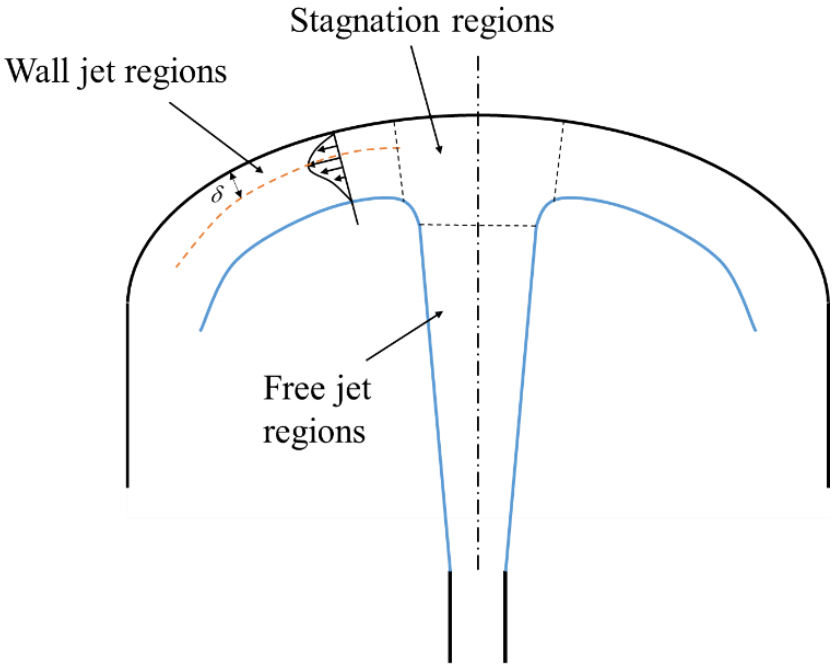

Figure 6.39. Impinging jet shape and three characteristic regions.

The coordinate transformed perpendicular velocity u' profiles for single and triple jet results are shown in Figure 6.40 and 6.41. For single jet experiments, as r increases the maximum u' increases until r = -7 cm then gradually decreases. The inflection point is first observed at r = -4 cm, i.e. weak pressure gradient, and zero shear stress, i.e. a separation point or critical adverse pressure gradient, is obtained at r = -6 cm, however backflow is not observed at the wall. For triple jet experiments, the maximum u' is measured at r = -8 cm. The pressure condition and velocity distribution along the radial direction is much different than single jet experiments. There are backflows at r = -0.5 and 1.5 cm where excessive adverse pressure gradients are observed.

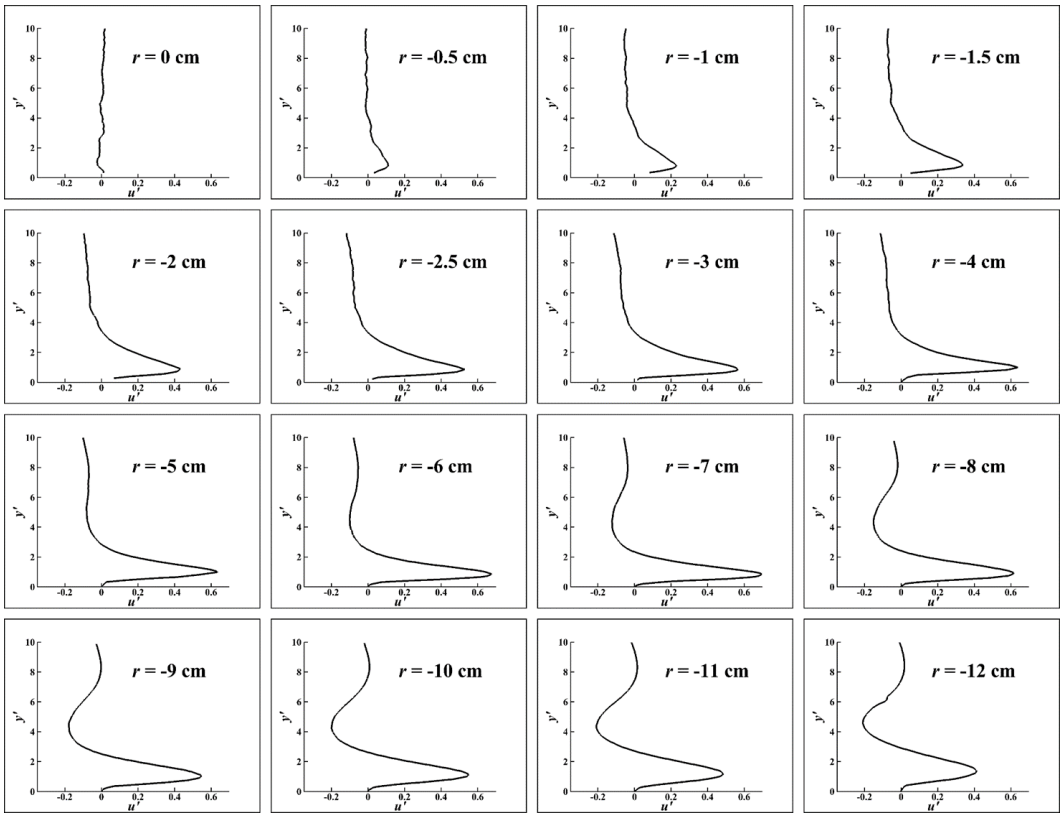

Figure 6.40. Perpendicular velocity distributions along the top surface for a single jet.

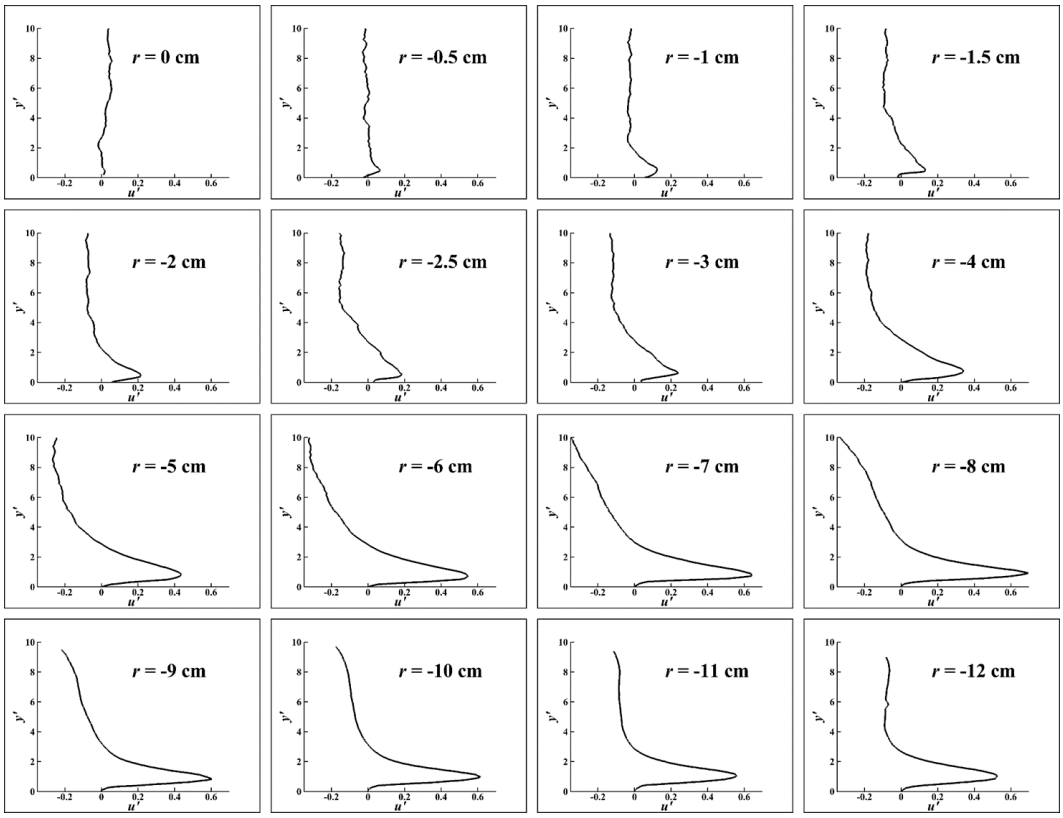

Figure 6.41. Perpendicular velocity distributions along the top surface for triple jets.

To investigate the velocity distribution close to the wall, we examine the law of the wall (see Figure 6.42 and 6.43). The coefficients of the general logarithmic formulations are derived as follows [86]:

$$\begin{aligned} u^+ &= y^+ && \text{for} \quad y^+ \le 5, \\ u^+ &= -3.05 + 5\ln\left(y^+\right) && \text{for} \quad 5 \le y^+ \le 26, \\ u^+ &= 5.0 + 2.44\ln\left(y^+\right) && \text{for} \quad y^+ > 26, \end{aligned} \tag{6.19}$$

where $y^+ = \frac{y' u_\tau}{\nu}$, $u_\tau = \sqrt{\frac{\tau_w}{\rho}}$ and $\mathrm{u}^+ = \frac{u'}{u_\tau}$. In general, the viscous sublayer has linear behavior up to $y^+ = 1$. Due to the presence of the secondary vortices, at the buffer layer and log-law region, the values of u^+ are higher than the analytic solutions. For the flat plate, far away downstream these buffer layer and log-law region are matched with the analytic solution [86] but because of the geometrical effect, i.e. the dome surface, these values still deviated from the analytical behaviors.

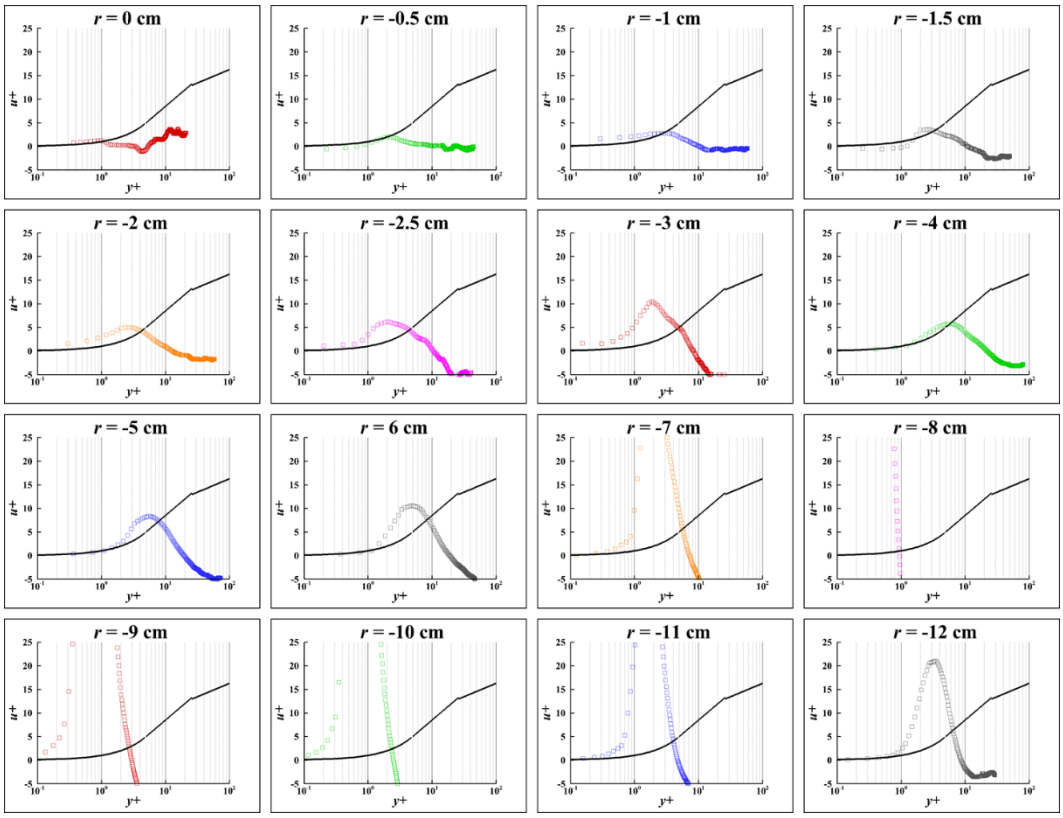

Figure 6.42. Velocity profiles near the wall with the law of the wall for a single jet.

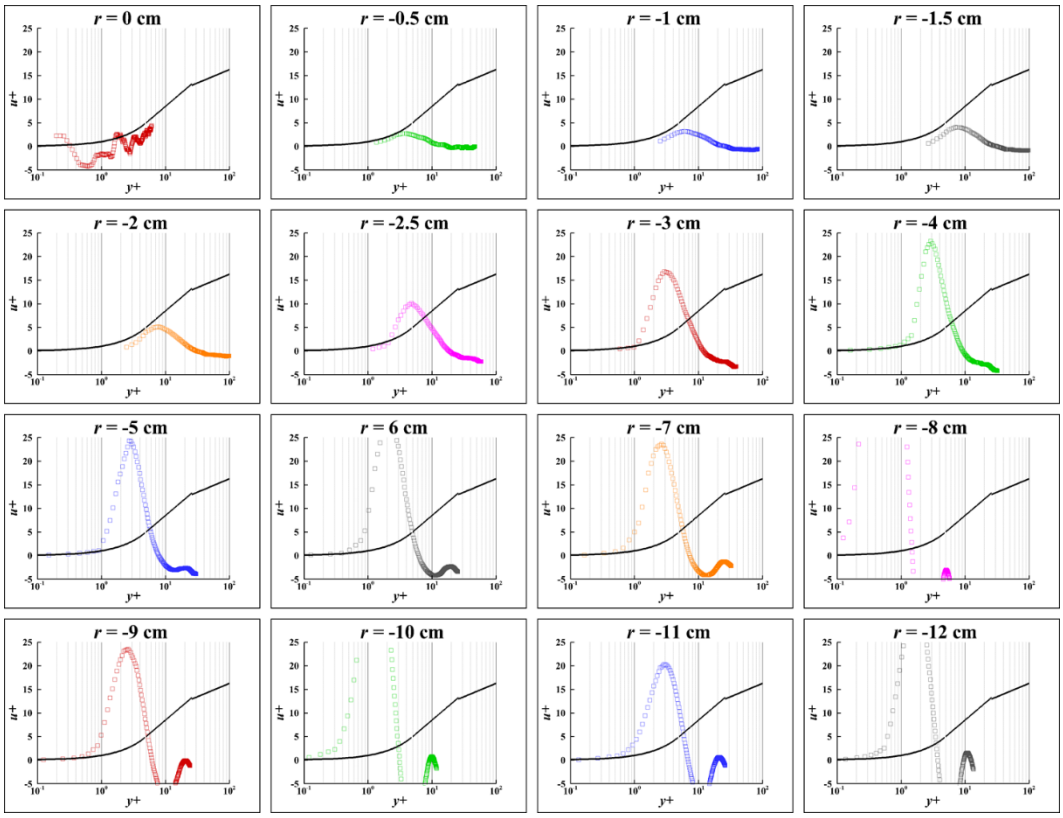

Figure 6.43. Velocity profiles near the wall with the law of the wall for triple jets.

The analytic solutions of the length scale δ and the velocity scale $u'_{\max}$ can be given by [84]

$$\frac{\delta}{H} = 0.095\left(\frac{r}{H}\right)^{0.9}, \tag{6.20}$$

$$\frac{u'_{\max}}{w_0} = \frac{1.03}{r/D}. \tag{6.21}$$

These analytic solutions are compared with the test results for single and triple jet experiments as shown in Figure 6.44. Note that the experiment results are spline fitted. The length scale gradually increases and typically the single jet has wider boundary layer thickness. It is anticipated the higher velocity gradient in triple jet tests contribute to the narrow boundary layer thicknesses. The analytic solution matches well where *r*/*H* is smaller than -0.67. The analytic solution for normalized maximum radial velocity profiles predicts well with single jet tests when *r*/*D* is less than -4 and similar to the results from Ghaneeizad et al. [84]. The normalized maximum radial velocities for triple jets have lower magnitude up to *r*/*D* = -3.67 where the three jets are mixed and combined and exceed those of the single jet values in the downstream starting at the point where the vorticities are maximized. The wall shear stress τ_w is defined as

$$\tau_w = \mu \left.\frac{\partial u'}{\partial y'}\right|_{wall}. \tag{6.22}$$

The shear stress for single jet tests has the maximum value between -2 < *r* < -1.5 cm and has good agreement with New et al. [76]. The shear stress for triple jet tests has minus values where backflows are in presence. The magnitude is smaller than that of single jet tests and the maximum shear stress is obtained between -5 < *r* < -4 cm. Because the triple

jets occupy a wider space on the top surface the location of the maximum shear stress is expanded. As we can observe from Figure 6.44 (b), it is due to the fact that the slope of the normalized maximum radial velocity for single jet tests is steeper than triple jet tests, in other words the velocity gradient of the streamwise direction, i.e. $\partial u'_{\max} / \partial r$, changes faster than that of triple jet tests. Therefore in terms of shear stress distribution the triple jets is more beneficial to the dome structure of the upper plume however the higher temperature distribution can cause more serious damage to the system so careful investigation is needed.

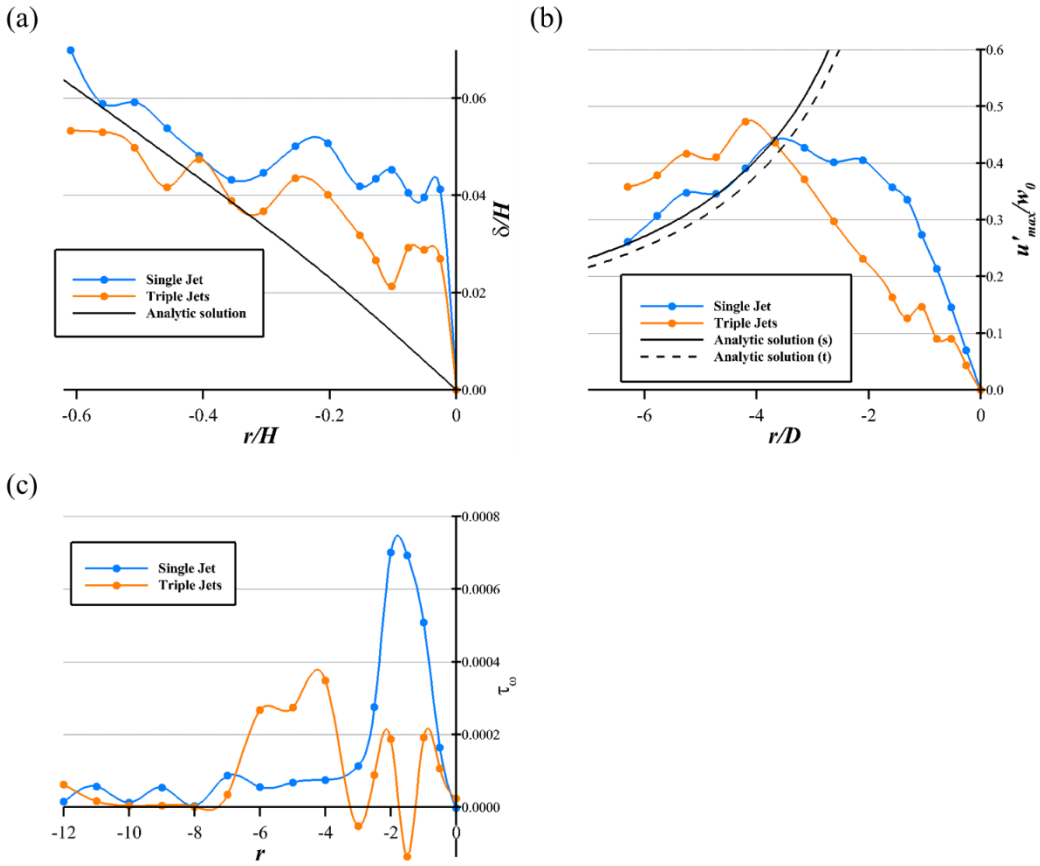

Figure 6.44. Characteristics of the jet wall region for single and triple jet tests. (a) Normalized length scale, (b) normalized maximum radial velocity profiles and (c) shear stress distributions.

7. CONCLUSION AND FUTURE WORK

The objectives of this research are to design and build a 1/16th scaled model of a very high temperature reactor and perform experiments that simulate a loss-of-coolant accident during a DCC event. This was achieved through the use of particle image velocimetry to analyze the velocity distribution, eddy structures and shear stress distributions of multiple turbulent buoyant jet mixings to provide the benchmark data for CFD validation. The experimental facility was successfully scaled down with the cooperation of INL and 1/16th scaled VHTR was constructed based on the geometrical length scaling with emphasis on the Reynolds and Richardson number, important dimensionless numbers to consider in order to properly simulate natural circulation in the prototype reactor. The test facility is completely water proof and a total of 10 kW heat capacity can be generated by multiple heating tape sections with 25 coolant channels. The particle image velocimetry is an ideal method to visualize the complex turbulent flow behavior in the upper plenum of the scaled VHTR. The pulsed laser, high speed camera, frequency generator and NI DAQ for thermocouples and the flowmeter are calibrated and synchronized to perform PIV tests.

Throughout the preliminary tests, it was determined that in order to obtain a statistically steady state result for the PIV data a thousand number of images were considered to be sufficient for first order statistics. PIV jet velocity profiles are validated with the data from the ultrasonic flowmeter and analytic flow rate equation. Furthermore the experimental test facility was modified to have the capabilities for individual control

for each heating pipe, the ability to block extraneous light to enhance the PIV performance and filtering out of fluorescent orange particles to reuse seeding particles. A Comparison between CFD and PIV shows that the Reynolds stress model performs the best to predict the velocity distribution and mixing of the turbulence among the three types of turbulent models (k-ε, k-ω and RSM) in Star-CCM+.

For the basis of the study, single buoyant jet tests are performed by operating the center coolant pipe only. The Reynolds number based on the pipe diameter ensures the buoyant jet is fully turbulent throughout the tests. Several PIV data validation methods are proposed to guarantee that the PIV results are statistically steady state and capture the detailed turbulent eddy structures. One of the most important parameters is Stokes number and the value ($St << 1$) indicates that our test condition is sufficient. Sensitivity analysis shows that 2,000 image guarantee statistically mean velocity profiles. Normalized root-mean-square deviation residual by the maximum axial velocity is the best suitable condition for testing the convergence and the value is determined to be 0.003. The mean velocity profiles show very symmetrical behavior along the axial axis. Self-similarity of the axial velocity is observed in the range of $0.57 < z/D < 9.43$. The self-similarity profiles of the Reynolds stress proves that the buoyant jet behaves like a plume as Morton et al. expected. The average entrainment coefficient is measured to be 0.0767, confirming its plume-like behavior and a constant spreading rate of 0.111 is obtained, confirming Morton's constant spreading rate hypothesis. Turbulent kinetic energy budget indicates some very important features of a single buoyant jet. The advection term is the major portion of the budget and is balanced by dissipation and diffusion terms. Near the jet

boundary the production term is most dominant. Within the jet the flow is not at local equilibrium. Q criterion identifies the four significant eddy structures in a single buoyant jet: RT vortices, KH vortices, secondary vortices and recirculated vortices. By applying the moving average velocity field and Q criterion, the mechanism of vortex-pair is explained. It is found that vortex-dipoles are influenced by centripetal forces generated by the concave surface. Depending on the location of these vortex-dipoles the mechanism can lead to either favorable or unfavorable interactions.

During the triple buoyant jet tests, the merging region prevails in the entire region of interest. Higher dominant characteristic puffing frequencies are obtained than single jet experiment due to the presence of two additional jets. Self-similarity is not observed in triple jet experiments. A similar turbulent eddy structure mechanism is observed in triple jet tests. The proper orthogonal decomposition provides another method for decomposing the eddy structures of turbulent flows. Triple jets contains higher energy in the first mode than a single jet but the logarithmic trend of the convergence is similar. There was no difference in identifying the eddy structure between the velocity magnitude, streamline, vorticity and Q criterion contours. The coordinate transformation allows us to extract the values along the concave surface and the shear stress distributions for the single and triple jet tests are obtained. The backflows are observed at r = -0.5 and 1.5 cm for triple jets but no backflows are presented in a single jet. Higher shear stress is measured in the single jet tests due to the turbulent jet mixing in triple jet experiments. Although the shear stress for triple jets is beneficial to the dome structure, a higher temperature gradient could inflict serious damage to the structure.

For future work, first and foremost CFD validation should be furnished. CFD is the only way to examine any local hot spot and high thermal gradient in the reactor vessel. The present experimental data can be used for the initial conditions in the validation. However, CFD validation is very hard to achieve since the behavior of jets are followed by the motions of plume. Their undulated and meandered motions are difficult to be captured by commercial CFD software since the energy equation should be properly solved and a well justified momentum equation with the Boussinesq assumption should be guaranteed. Higher order of turbulent modeling such as LES is needed to accurately predict the turbulent buoyant jet mixing.

In addition, experiments with different numbers of jets can be performed to investigate how they influence turbulent jet mixing. As turbulent jet phenomena is independent of Reynolds number geometrical effect is the most significant, different pitch-to-diameter experiments can be performed to compare the results with single and triple jet experiments. Also by replacing the water reservoir with a water pump system the scaled VHTR can simulate the PCC accident scenario. This will have much faster flowrate in the system and eventually high Reynolds number turbulent jet mixing will occur. Again, POD, wavelet and Q criterion will help to identify the eddy structure of turbulent jets. These experiment data will be used to provide benchmark data.

REFERENCES

1. *BP statistical review of world energy*. June 2015, BP, https://www.bp.com/content/dam/bp/pdf/energy-economics/statistical-review-2015/bp-statistical-review-of-world-energy-2015-full-report.pdf.
2. *Technology roadmap: nuclear energy*. 2015, International Energy Agency (IEA), http://www.iea.org/publications/freepublications/publication/Nuclear_RM_2015_FINAL_WEB_Sept_2015_V3.pdf.
3. A t*echnology roadmap for generation IV nuclear energy systems*. December 2002, Gen IV International Forum (GIF), https://www.gen-4.org/gif/upload/docs/application/pdf/2013-09/genivroadmap2002.pdf.
4. Doug Chapin, S.K., Jim Nestell, *The very high temperature reactor: a technical summary*. 2004: MPR Associates Inc., Alexandria, VA, USA, http://www.mpr.com/uploads/news/very-high-temperature-reactor.pdf.
5. Campbell, J., *Very high temperature reactor [VHTR]*, very-high-temperature-reactor.pdf, Editor., Idaho National Laboratory: Idaho National Laboratory.
6. Schultz, R.R., et al., *Studies related to the oregon state university high temperature test facility: scaling, the validation matrix, and similarities to the modular high temperature gas-cooled reactor*. 2010, Idaho National Laboratory (United States). Funding organisation: DOE-NE (United States).

7. KAERI, *A schematic of the VHTR*. 2009: Korea Atomic Energy Research Institute (KAERI), http://mdportal.kaeri.re.kr/materials-degradation/degradation-vhtr/149-d20120075.

8. PIRT, *Next generation nuclear plant phenomena identification and ranking tables (PIRTs).* 2008, http://info.ornl.gov/sites/publications/files/Pub7837.pdf.

9. Haque, H., W. Feltes, and G. Brinkmann, *Thermal response of a modular high temperature reactor during passive cooldown under pressurized and depressurized conditions.* Nuclear Engineering and Design, 2006. **236**(5–6): p. 475-484.

10. McIlroy, H., et al., *PIV experiments to measure flow phenomena in a scaled model of a VHTR lower plenum.* 2006, Idaho National Laboratory Report INL/INT-06-11740.

11. McVay, K.L., et al., *Preliminary tests of particle image velocimetry for the upper plenum of a scaled model of a very high temperature gas cooled reactor.* Progress in Nuclear Energy, 2015. **83**: p. 305-317.

12. Gauthier, J.-C., et al., *ANTARES: The HTR/VHTR project at framatome ANP*. Nuclear Engineering and Design, 2006. **236**(5–6): p. 526-533.

13. Chang, J., et al., *A study of a nuclear hydrogen production demonstration plant.* Nuclear Engineering and Technology, 2007. **39**(2): p. 111.

14. Condie, K., et al., *Development of an experiment for measuring flow phenomena occurring in a lower plenum for VHTR CFD assessment*. 2005, Idaho National Laboratory Report INL/EXT-05-00603.

15. Elder, R. and R. Allen, *Nuclear heat for hydrogen production: coupling a very high/high temperature reactor to a hydrogen production plant.* Progress in Nuclear Energy, 2009. **51**(3): p. 500-525.

16. Khamis, I. *Nuclear power plants can produce hydrogen to fuel the "hydrogen economy"*. in *ACS Press Conference*. 2012. San Diego, California: American Chemical Society

17. Chang, H.O., C. Davis, and R. Moore, *Development of safety analysis codes and experimental validation for a very high temperature gas-cooled reactor*. 2004, Idaho National Laboratory Report INL/EXT-06-01362.

18. Reyes Jr, J., et al., *Scaling analysis for the high temperature gas reactor test section (GRTS).* Nuclear Engineering and Design, 2010. **240**(2): p. 397-404.

19. Gougar, H. and C. Davis, *Reactor pressure vessel temperature analysis for prismatic and pebble-bed VHTR designs.* 2006, Idaho National Laboratory Report INL/EXT-06-11057.

20. Johnson, R.W., D.P. Guillen, and T. Gallaway, *Investigations of the application of CFD to flow expected in the lower plenum of the prismatic VHTR*. 2006, Idaho National Laboratory Report INL/EXT-06-11756.

21. Tung, Y.-H. and R.W. Johnson. *CFD calculations of natural circulation in a high temperature gas reactor following pressurized circulator shutdown*. in *ASME 2011 International Mechanical Engineering Congress and Exposition*. 2011. American Society of Mechanical Engineers.

22. Thielicke, W. and E.J. Stamhuis, *PIVlab–Towards user-friendly, affordable and accurate digital particle image velocimetry in MATLAB.* Journal of Open Research Software, 2014. **2**(1): p. e30.

23. Sanchez, T., et al., *Spontaneous motion in hierarchically assembled active matter.* Nature, 2012. **491**(7424): p. 431-434.

24. Booth-Gauthier, E.A., et al., *Force-induced changes in subnuclear movement and rheology.* Biophysical Journal, 2012. **103**(12): p. 2423-2431.

25. Leong, T., et al., *The role of surfactant headgroup, chain length, and cavitation microstreaming on the growth of bubbles by rectified diffusion.* The Journal of Physical Chemistry C, 2011. **115**(49): p. 24310-24316.

26. Mirsepassi, A. and D. Rankin, *Particle image velocimetry in viscoelastic fluids and particle interaction effects.* Experiments in Fluids, 2013. **55**(1): p. 1-7.

27. Piro, V., N. Piro, and O. Piro, *Characterization of intraventricular blood flow using a microbubble-contrast tracking echo-PIV technique.* Journal of the American College of Cardiology, 2012. **59**(13s1): p. E1139-E1139.

28. Xu, H. and E. Bodenschatz, *Motion of inertial particles with size larger than Kolmogorov scale in turbulent flows.* Physica D: Nonlinear Phenomena, 2008. **237**(14): p. 2095-2100.

29. Amini, N. and Y.A. Hassan, *Measurements of jet flows impinging into a channel containing a rod bundle using dynamic PIV.* International Journal of Heat and Mass Transfer, 2009. **52**(23–24): p. 5479-5495.

30. WebBook, N.C. *NIST Standard Reference Database*. 2016, http://webbook.nist.gov/chemistry/.

31. Pope, S.B., *Turbulent flows*. 2000: Cambridge University Press, New York, NY, USA.

32. McCreery, G.E., K.G. Condie, and R.R. Schultz, *Scaled rxperimental modeling of VHTR plenum flows,* in *Proceedings of the 15th International Conference on Nuclear Engineering (ICONE 15), Nagoya, Japan*. 2007.

33. Aldridge, R.J., *Scaling Study of the Depressurized Conduction Cooldown Event in the High Temperature Test Facility Using REAL5-3D/ATHENA,* in *Nuclear Engineering*. 2013, Oregon State University. Master's Thesis: p. 165.

34. Lee, J.H.W. and V.H. Chu, *Turbulent Jets and Plume: A Lagrangian Approach*. 2003: Springer Science+Business Media, New York, NY, USA.

35. Lee, J.H. and V. Cheung, *Generalized Lagrangian model for buoyant jets in current.* Journal of Environmental Engineering, 1990. **116**(6): p. 1085-1106.

36. Jirka, G.H. and R.L. Domeker, *Hydrodynamic classification of submerged single-port discharges.* Journal of Hydraulic Engineering, 1991. **117**(9): p. 1095-1112.

37. Roberts, P.J., A. Ferrier, and G. Daviero, *Mixing in inclined dense jets.* Journal of Hydraulic Engineering, 1997. **123**(8): p. 693-699.

38. Woods, A.W., *A model of the plumes above basaltic fissure eruptions.* Geophysical Research Letters, 1993. **20**(12): p. 1115-1118.

39. Chen, C.J. and W. Rodi, *Vertical turbulent buoyant jets: a review of experimental data.* NASA STI/Recon Technical Report A, 1980. **80**.

40. Hussein, H.J., S.P. Capp, and W.K. George, *Velocity measurements in a high-Reynolds-number, momentum-conserving, axisymmetric, turbulent jet.* Journal of Fluid Mechanics, 1994. **258**: p. 31-75.

41. Paillat, S. and E. Kaminski, *Entrainment in plane turbulent pure plumes.* Journal of Fluid Mechanics, 2014. **755**: p. R2.

42. Morton, B., G. Taylor, and J. Turner. *Turbulent gravitational convection from maintained and instantaneous sources*. in *Proceedings of the Royal Society of London A: Mathematical, Physical and Engineering Sciences*. 1956. The Royal Society.

43. Papanicolaou, P.N. and E.J. List, *Investigations of round vertical turbulent buoyant jets.* Journal of Fluid Mechanics, 1988. **195**: p. 341-391.

44. Phares, D.J., G.T. Smedley, and R.C. Flagan, *The wall shear stress produced by the normal impingement of a jet on a flat surface.* Journal of Fluid Mechanics, 2000. **418**: p. 351-375.

45. Wang, H. and A.W.-k. Law, *Second-order integral model for a round turbulent buoyant jet.* Journal of Fluid Mechanics, 2002. **459**: p. 397-428.

46. Dai, Z., L.-K. Tseng, and G. Faeth, *Structure of round, fully developed, buoyant turbulent plumes.* Journal of Heat Transfer, 1994. **116**(2): p. 409-417.

47. Peterson, P., *Scaling and analysis of mixing in large stratified volumes.* International Journal of Heat and Mass Transfer, 1994. **37**: p. 97-106.

48. Tritton, D.J., *Physical Fluid Dynamics*. 1977: Van Nostrand Reinhold Company, Molly Millars Lane, Wokingham, Berkshire, England.

49. Raffel, M., C.E. Willert, and J. Kompenhans, *Particle image velocimetry: a practical guide*. 2013: Springer, New York, NY, USA.

50. Adrian, R.J. and J. Westerweel, *Particle image velocimetry*. 2011: Cambridge University Press, New York, NY, USA.

51. Stanislas, M., J. Kompenhans, and J. Westerweel, *Particle image velocimetry: Progress towards industrial application*. Vol. 56. 2010: Kluwer Academic Publishers, Dordrecht, The Netherlands.

52. Pizer, S.M., et al., *Adaptive histogram equalization and its variations.* Computer Vision, Graphics, and Image Processing, 1987. **39**(3): p. 355-368.

53. Thielicke, W., *The Flapping Flight of Birds: Analysis and Application*. 2014, University of Groningen. Doctoral Dissertation: p. 255.

54. Huang, H., D. Dabiri, and M. Gharib, *On errors of digital particle image velocimetry*. Measurement Science and Technology, 1997. **8**(12): p. 1427.

55. Okamoto, K., et al., *Standard images for particle-image velocimetry.* Measurement Science and Technology, 2000. **11**(6): p. 685.

56. Soria, J., *An investigation of the near wake of a circular cylinder using a video-based digital cross-correlation particle image velocimetry technique.* Experimental Thermal and Fluid Science, 1996. **12**(2): p. 221-233.

57. Westerweel, J. and F. Scarano, *Universal outlier detection for PIV data.* Experiments in Fluids, 2005. **39**(6): p. 1096-1100.

58. O'hern, T., et al., *Experimental study of a turbulent buoyant helium plume.* Journal of Fluid Mechanics, 2005. **544**: p. 143-171.

59. Soteriou, M.C., Y. Dong, and B.M. Cetegen, *Lagrangian simulation of the unsteady near field dynamics of planar buoyant plumes.* Physics of Fluids, 2002. **14**(9): p. 3118-3140.

60. Cetegen, B.M. and T.A. Ahmed, *Experiments on the periodic instability of buoyant plumes and pool fires.* Combustion and Flame, 1993. **93**(1-2): p. 157-184.

61. Cetegen, B.M. and K.D. Kasper, *Experiments on the oscillatory behavior of buoyant plumes of helium and helium-air mixtures.* Physics of Fluids, 1996. **8**(11): p. 2974-2984.

62. Papanicolaou, P.N. and E.J. List, *Statistical and spectral properties of tracer concentration in round buoyant jets.* International Journal of Heat and Mass Transfer, 1987. **30**(10): p. 2059-2071.

63. Shabbir, A. and W.K. George, *Experiments on a round turbulent buoyant plume.* Journal of Fluid Mechanics, 1994. **275**: p. 1-32.

64. Ezzamel, A., P. Salizzoni, and G. Hunt, *Dynamical variability of axisymmetric buoyant plumes.* Journal of Fluid Mechanics, 2015. **765**: p. 576-611.

65. Paillat, S. and E. Kaminski, *Second-order model of entrainment in planar turbulent jets at low Reynolds number.* Physics of Fluids, 2014. **26**(4): p. 045110.

66. Carazzo, G., E. Kaminski, and S. Tait, *The route to self-similarity in turbulent jets and plumes.* Journal of Fluid Mechanics, 2006. **547**: p. 137-148.

67. Weisgraber, T. and D. Liepmann, *Turbulent structure during transition to self-similarity in a round jet.* Experiments in Fluids, 1998. **24**(3): p. 210-224.

68. Lumley, J.L., *Computational modeling of turbulent flows.* Advances in Applied Mechanics, 1978. **18**(123): p. 213.

69. Liu, J.-L., X.-Q. Feng, and G.-F. Wang, *Buoyant force and sinking conditions of a hydrophobic thin rod floating on water.* Physical Review E, 2007. **76**(6): p. 066103.

70. Panchapakesan, N. and J. Lumley, *Turbulence measurements in axisymmetric jets of air and helium. Part 1. Air jet.* Journal of Fluid Mechanics, 1993. **246**: p. 197-223.

71. Jeong, J. and F. Hussain, *On the identification of a vortex.* Journal of Fluid Mechanics, 1995. **285**: p. 69-94.

72. Hunt, J. *Vorticity and vortex dynamics in complex turbulent flows*. in *Canadian Society for Mechanical Engineering, Transactions (ISSN 0315-8977), vol. 11, no. 1, 1987, p. 21-35.* 1987.

73. Chong, M., A.E. Perry, and B. Cantwell, *A general classification of three-dimensional flow fields.* Physics of Fluids A: Fluid Dynamics (1989-1993), 1990. **2**(5): p. 765-777.

74. Landel, J.R., C. Caulfield, and A.W. Woods, *Meandering due to large eddies and the statistically self-similar dynamics of quasi-two-dimensional jets.* Journal of Fluid Mechanics, 2012. **692**: p. 347-368.

75. Rohlfs, W., et al., *Insights into the local heat transfer of a submerged impinging jet: Influence of local flow acceleration and vortex-wall interaction.* International Journal of Heat and Mass Transfer, 2012. **55**(25): p. 7728-7736.

76. New, T. and J. Long, *Dynamics of laminar circular jet impingement upon convex cylinders.* Physics of Fluids, 2015. **27**(2): p. 024109.

77. Adrian, J.R., T.K. Christensen, and Z.-C. Liu, *Analysis and interpretation of instantaneous turbulent velocity fields.* Experiments in Fluids, 2000. **29**(3): p. 275-290.

78. Lai, A.C. and J.H. Lee, *Dynamic interaction of multiple buoyant jets.* Journal of Fluid Mechanics, 2012. **708**: p. 539.

79. Sirovich, L., *Turbulence and the dynamics of coherent structures. Part I: Coherent structures.* Quarterly of Applied Mathematics, 1987. **45**(3): p. 561-571.

80. Liang, Y., et al., *Proper orthogonal decomposition and its applications—Part I: Theory.* Journal of Sound and Vibration, 2002. **252**(3): p. 527-544.

81. Nguyen, T.D., et al., *Proper orthogonal decomposition-based estimations of the flow field from particle image velocimetry wall-gradient measurements in the backward-facing step flow.* Measurement Science and Technology, 2010. **21**(11): p. 115406.

82. Graftieaux, L., M. Michard, and N. Grosjean, *Combining PIV, POD and vortex identification algorithms for the study of unsteady turbulent swirling flows.* Measurement Science and Technology, 2001. **12**(9): p. 1422.

83. Tu, C. and D. Wood, *Wall pressure and shear stress measurements beneath an impinging jet.* Experimental Thermal and Fluid Science, 1996. **13**(4): p. 364-373.

84. Ghaneeizad, S.M., J.F. Atkinson, and S.J. Bennett, *Effect of flow confinement on the hydrodynamics of circular impinging jets: implications for erosion assessment.* Environmental Fluid Mechanics, 2015. **15**(1): p. 1-25.

85. Schabel, W. and H. Martin, *G10 Impinging jet flow heat transfer*, in *VDI Heat Atlas*. 2010: Springer, Berlin, Germany. p. 745-752.

86. Zhe, J. and V. Modi, *Near Wall Measurements for a Turbulent Impinging Slot Jet (Data Bank Contribution).* Journal of Fluids Engineering, 2001. **123**(1): p. 112-120.

APPENDIX A FACILITY DRAWINGS

The following Figures show the schematics of a scaled model of a VHTR design done by SolildWorks. They do not include the inlet/outlet pipe and water reservoir. Note that dimensions are inches.

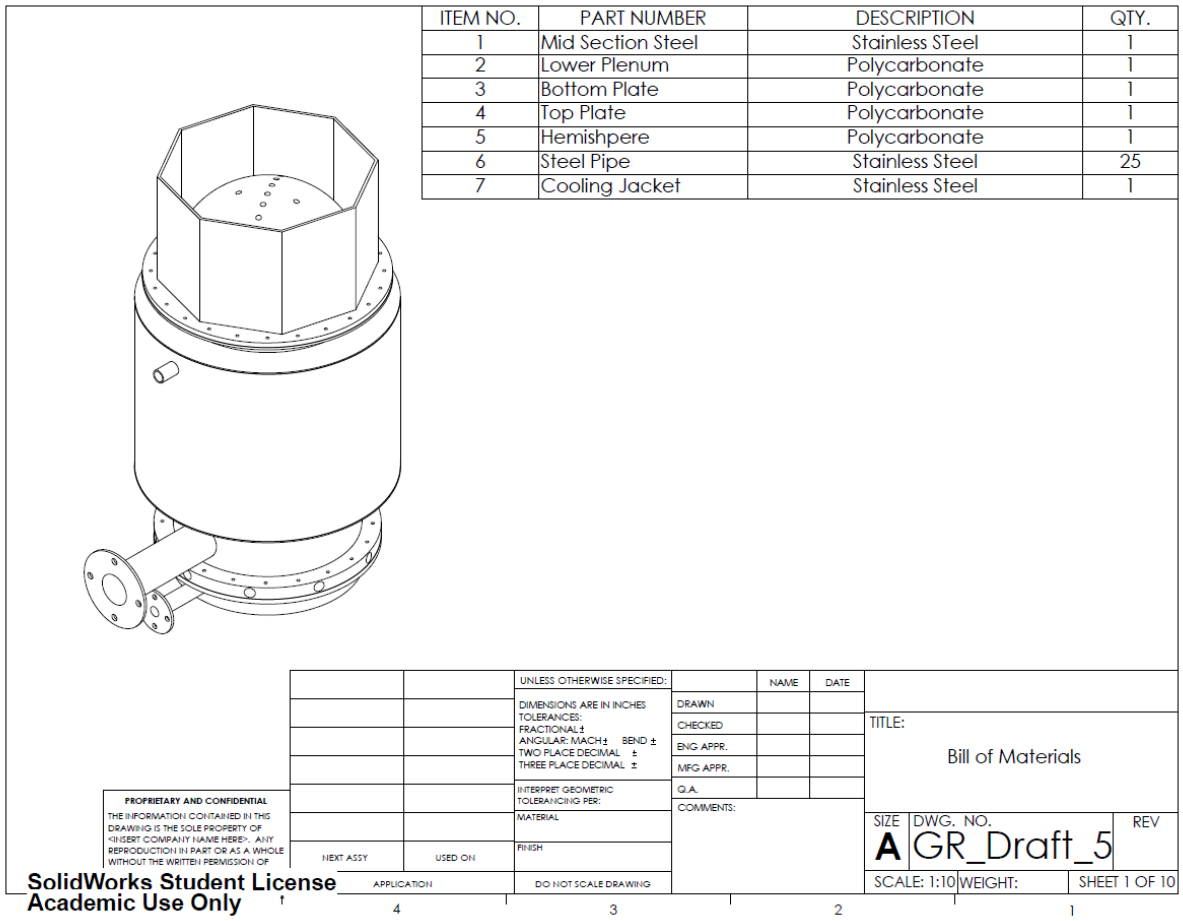

ITEM NO.	PART NUMBER	DESCRIPTION	QTY.
1	Mid Section Steel	Stainless STeel	1
2	Lower Plenum	Polycarbonate	1
3	Bottom Plate	Polycarbonate	1
4	Top Plate	Polycarbonate	1
5	Hemishpere	Polycarbonate	1
6	Steel Pipe	Stainless Steel	25
7	Cooling Jacket	Stainless Steel	1

Figure A.1. Fully assembled facility design (stainless steel and polycarbonate) with the list of part names.

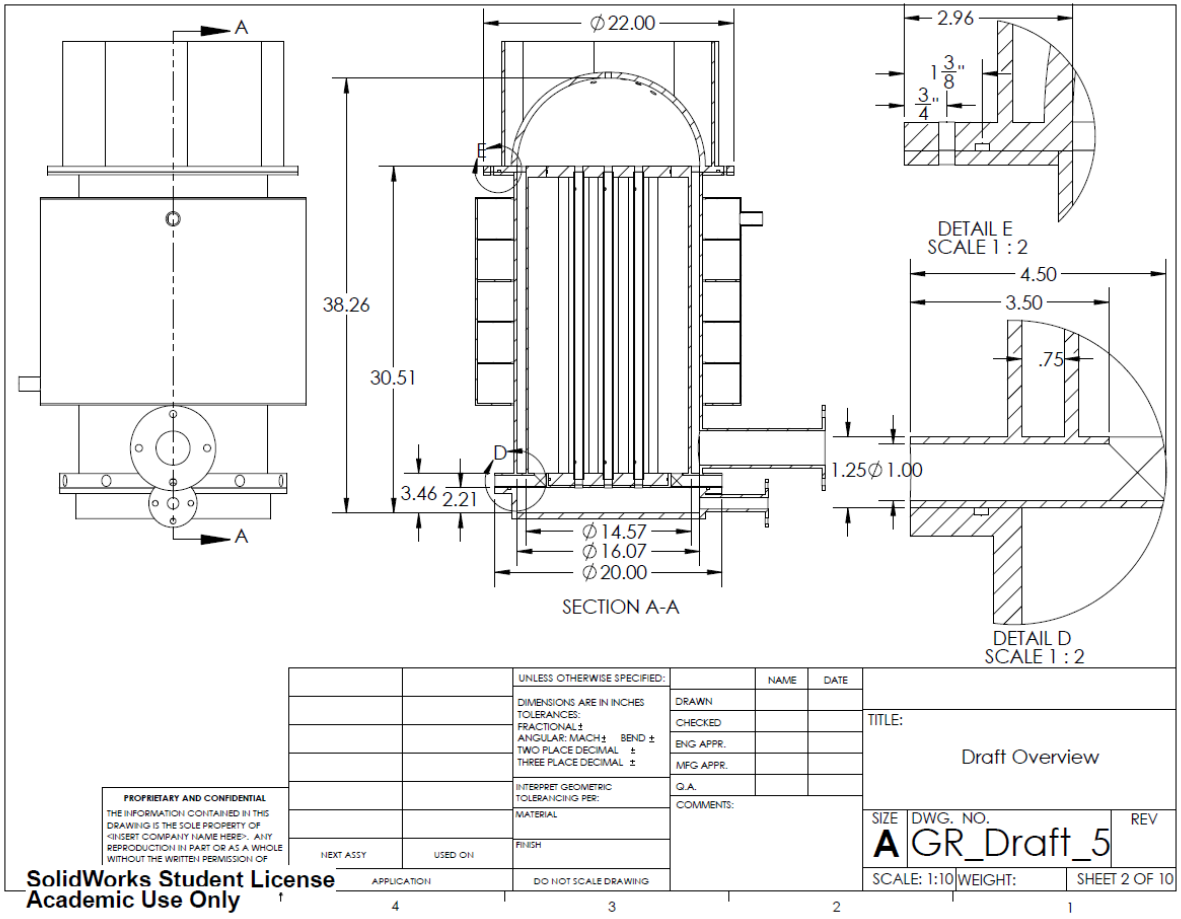

Figure A.2. Fully assembled facility design (stainless steel and polycarbonate): a cross section view with detail mid section view.

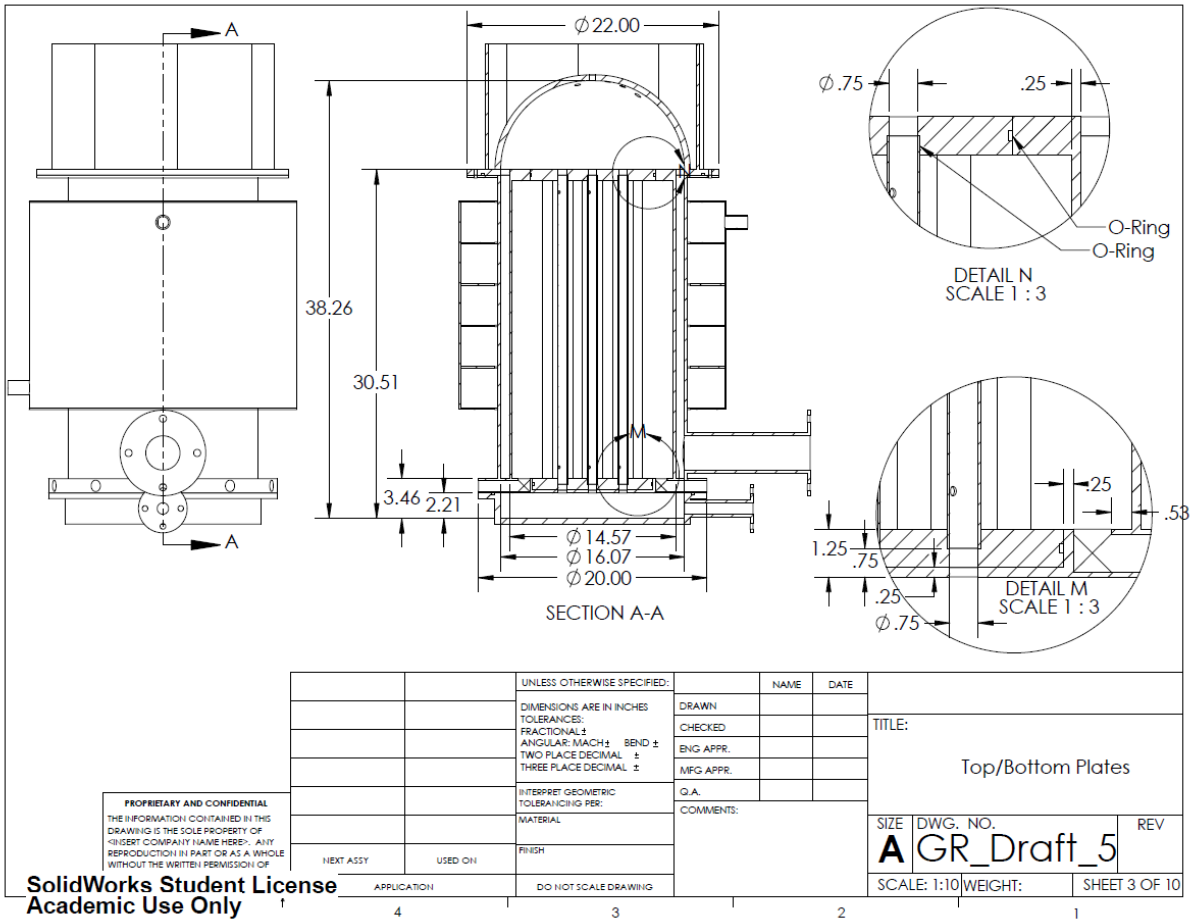

Figure A.3. Fully assembled facility design (stainless steel and polycarbonate): a cross section view with detail inside view.

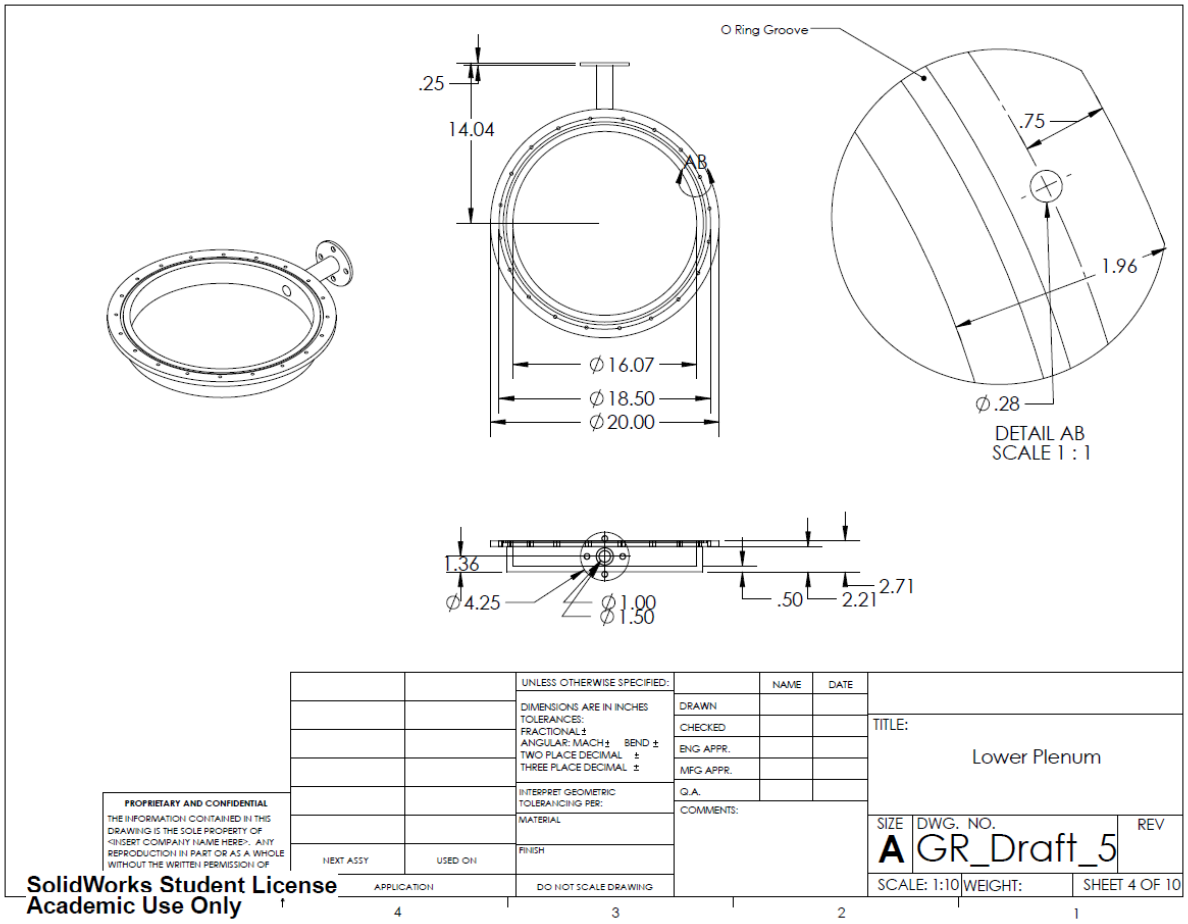

Figure A.4. Lower plenum (polycarbonate).

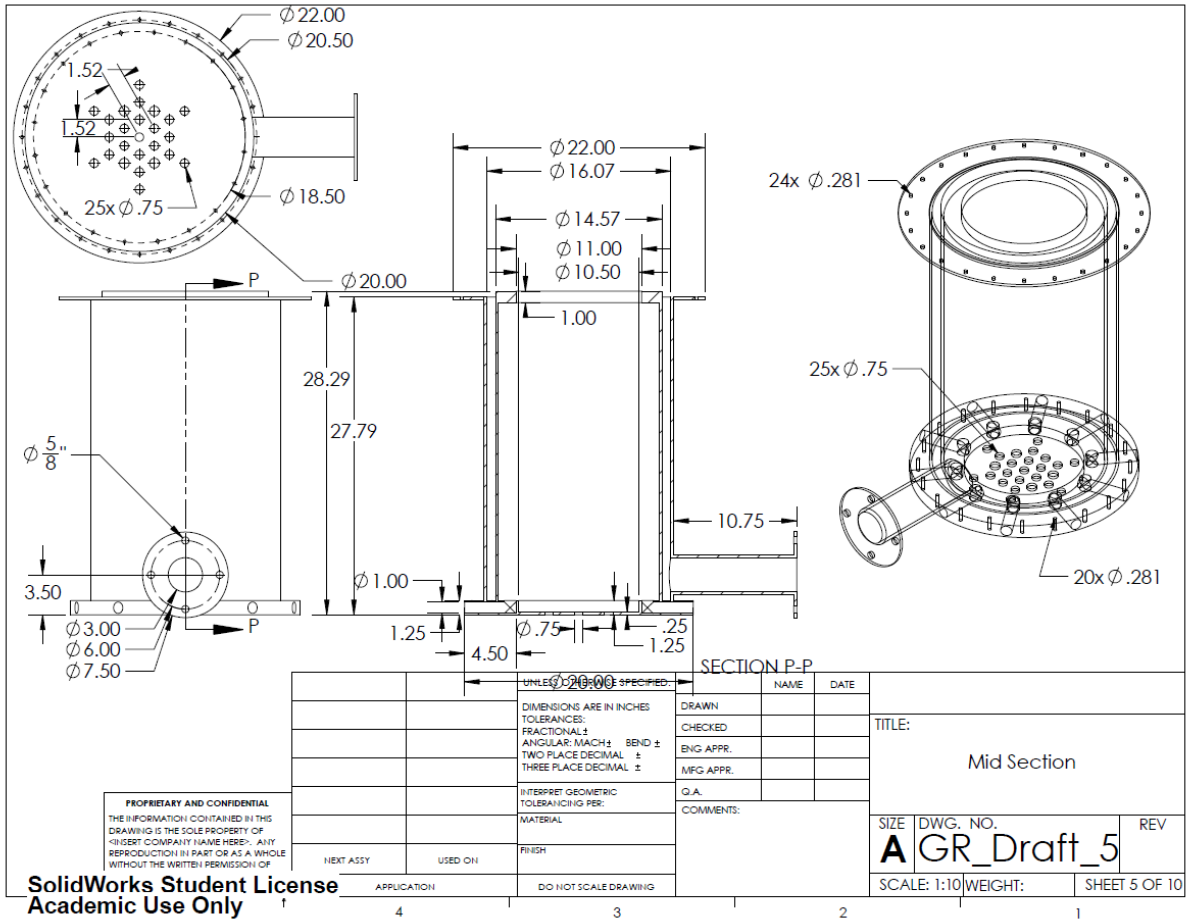

Figure A.5. Mid section (polycarbonate).

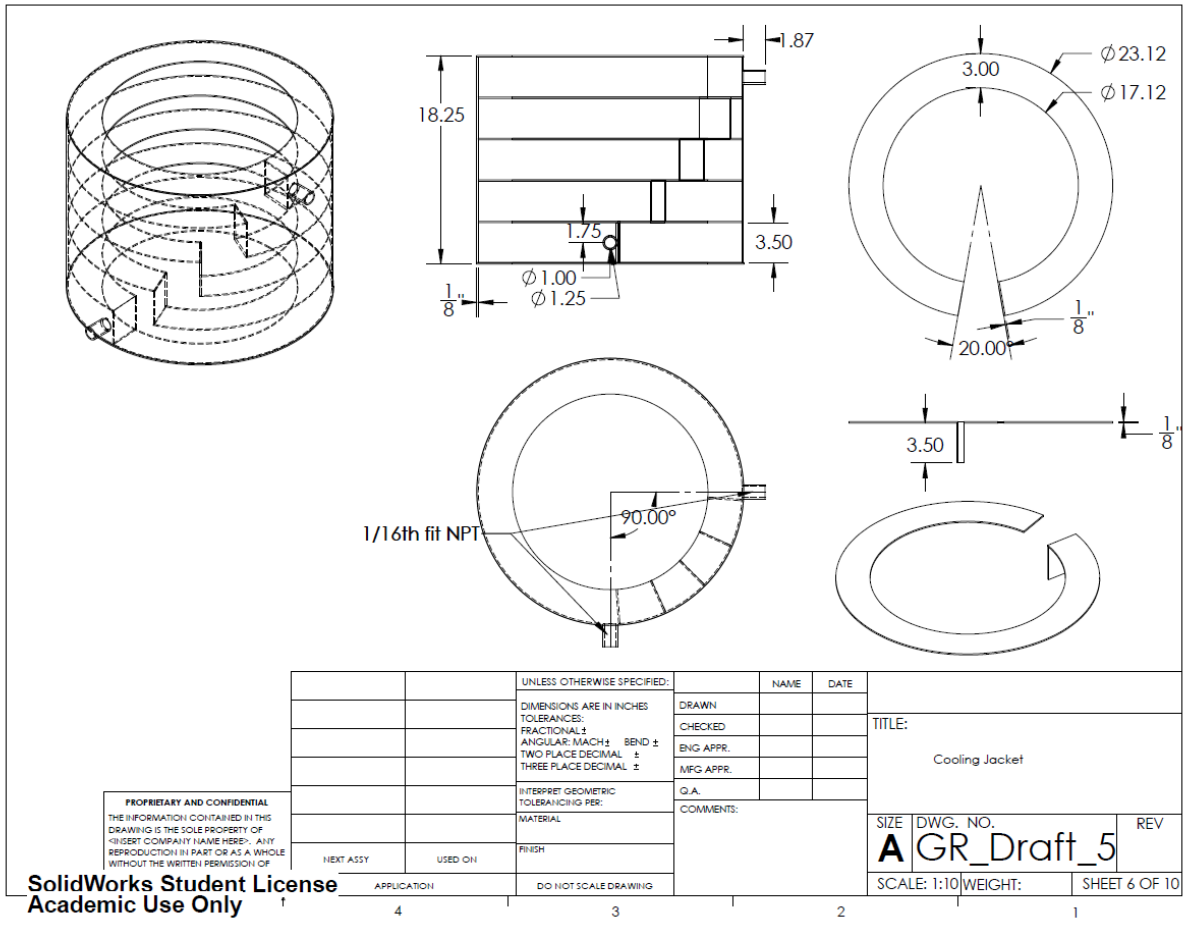

Figure A.6. Cooling jacket (stainless steel).

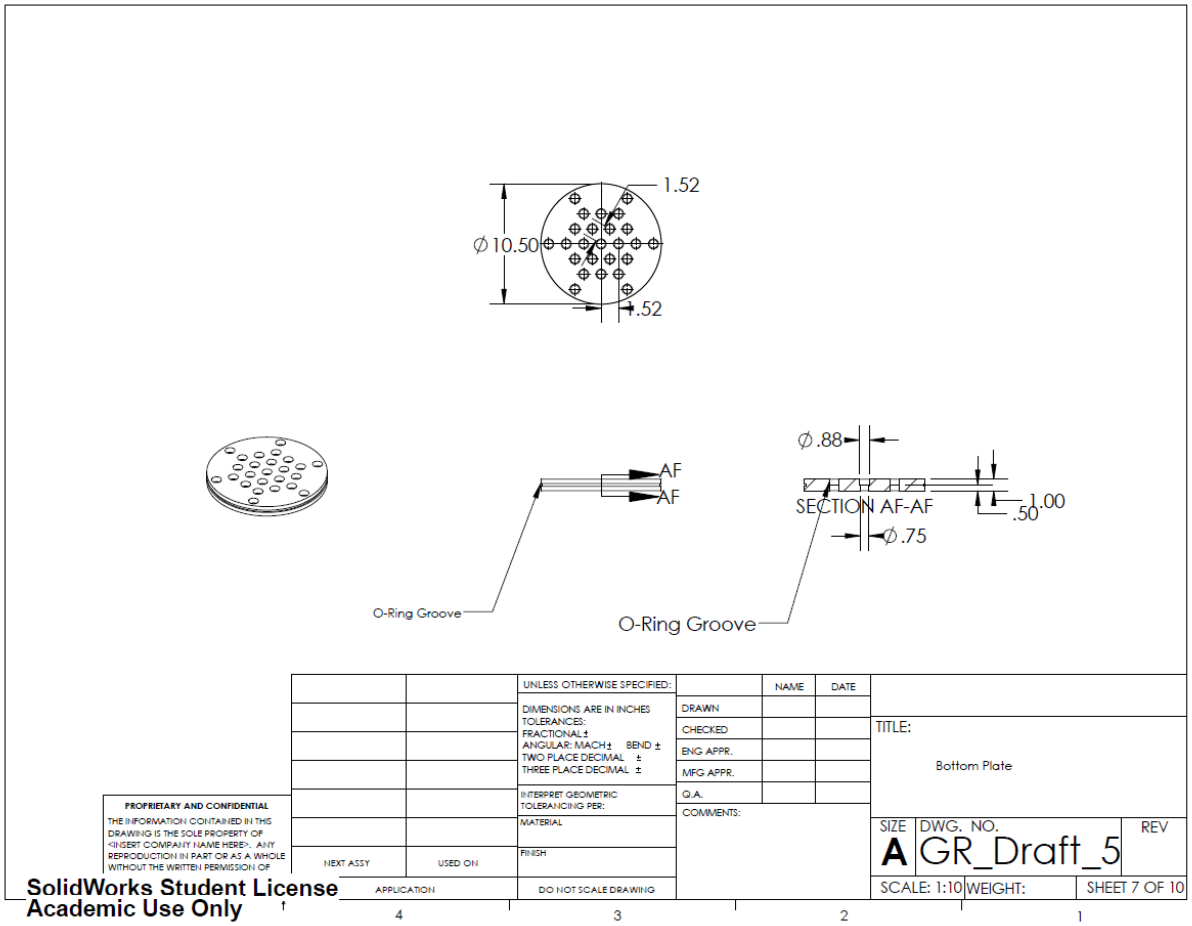

Figure A.7. Bottom plate (polycarbonate).

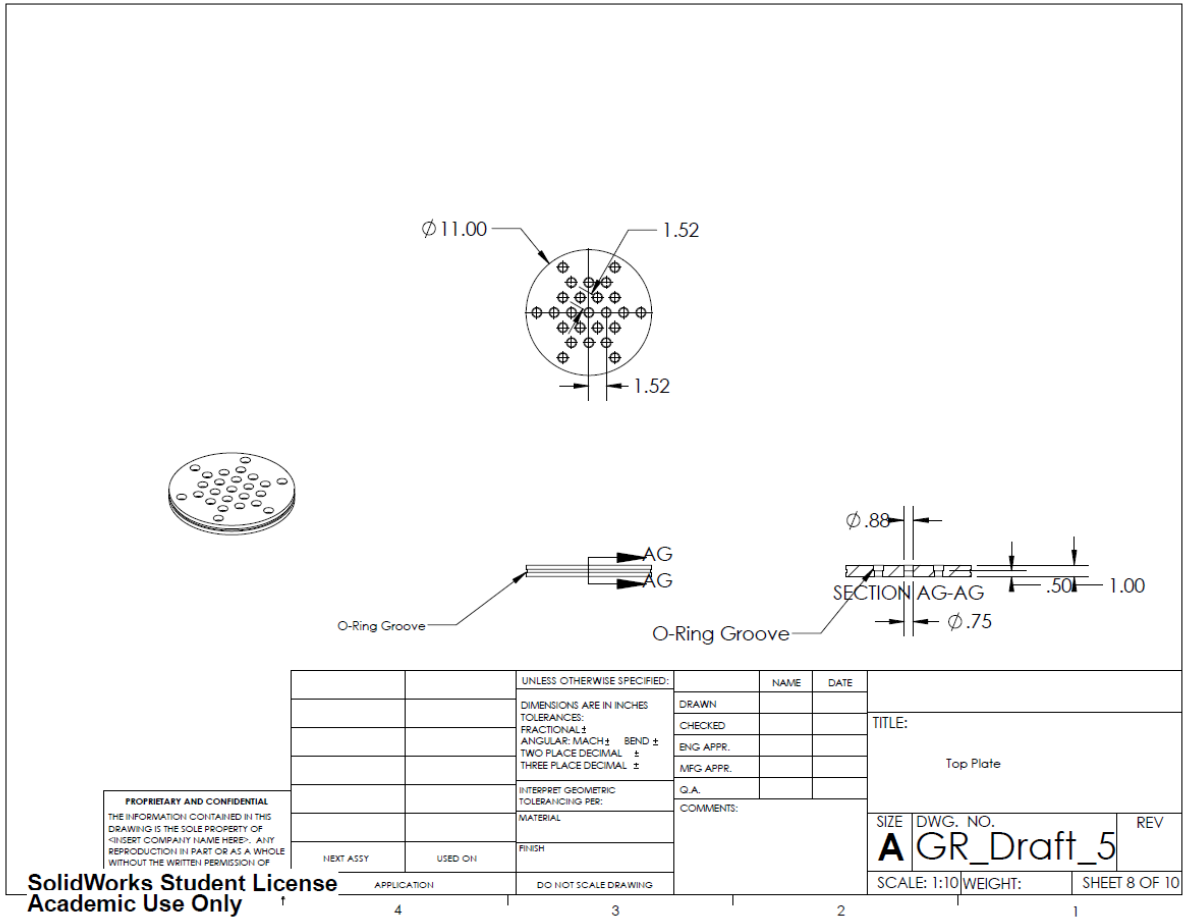

Figure A.8. Top plate (polycarbonate).

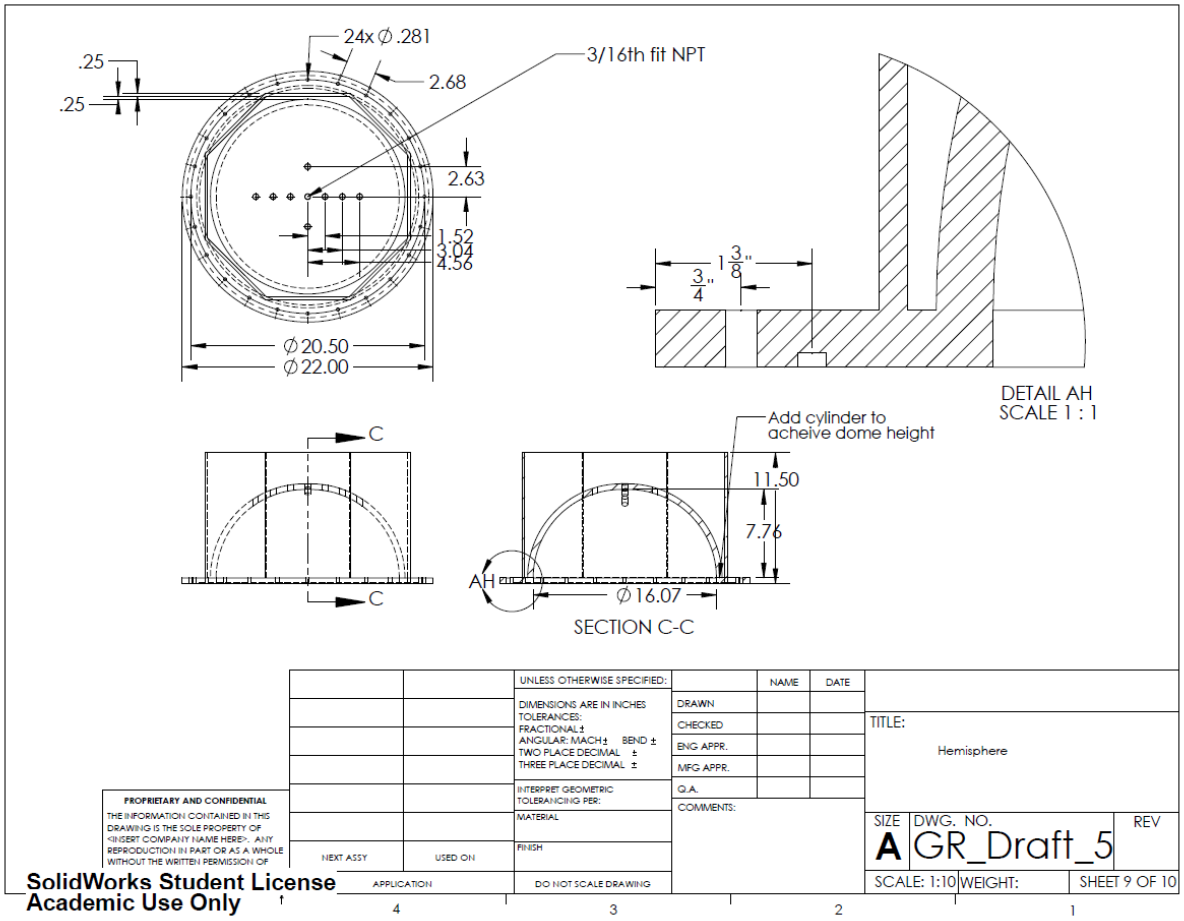

Figure A.9. Hemisphere (polycarbonate).

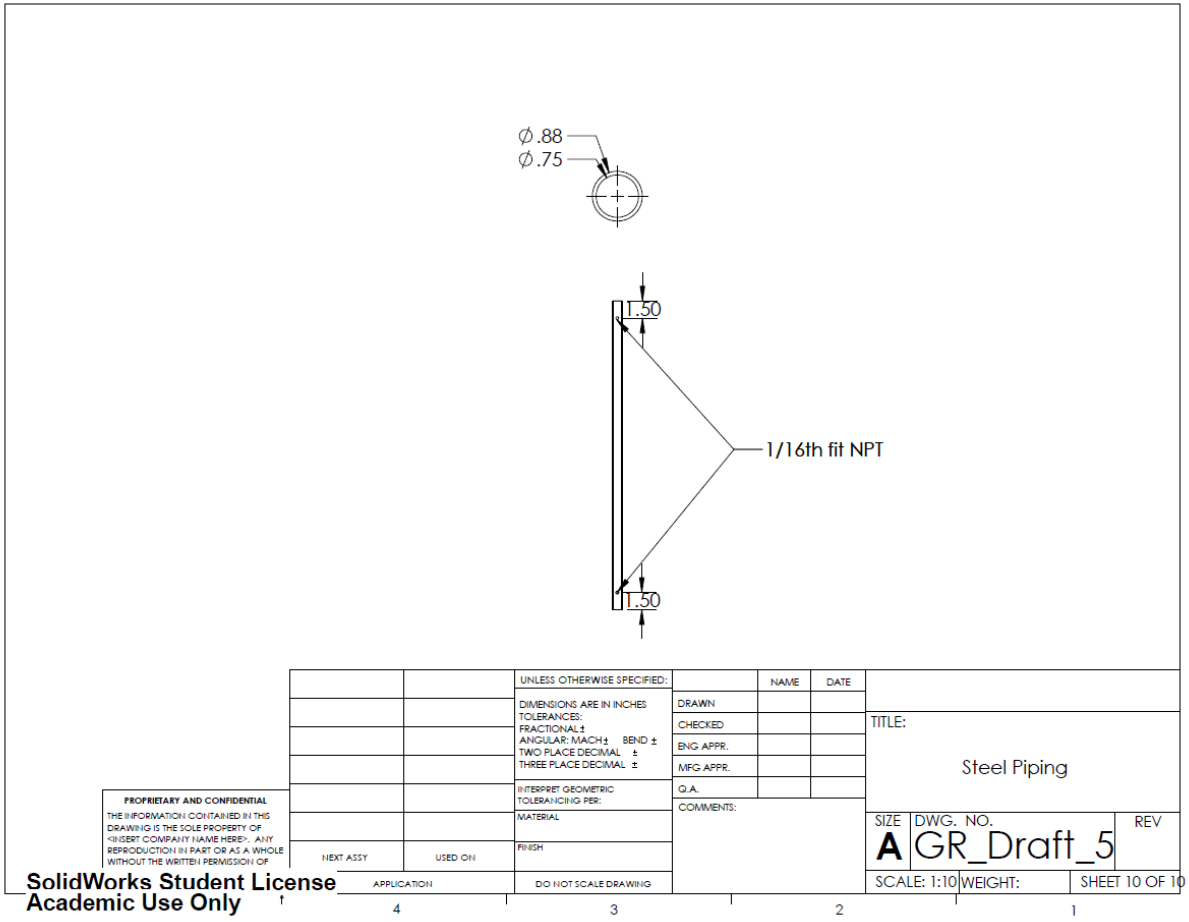

Figure A.10. Steel piping (stainless steel).